Technische Universität Dresden

BLIND SOURCE SEPARATION FOR THE PROCESSING OF CONTACT-LESS BIOSIGNALS

DANIEL WEDEKIND

von der Fakultät für Elektrotechnik und Informationstechnik
der Technischen Universität Dresden

zur Erlangung des akademischen Grades

DOKTORINGENIEUR
(Dr.-Ing.)

genehmigte Dissertation

Vorsitzender: Prof. Dr.-Ing. habil. Mehmet Ercan Altinsoy
Gutachter: Prof. Dr.-Ing. habil. Hagen Malberg
Gutachter: Prof. Dr.-Ing. habil. Niels Grabow
Gutachter: Assoc. Prof. Dr. Urban Wiklund
Prüfer: Prof. Dr.-Ing. Peter Birkholz

Tag der Einreichung: 07.09.2020
Tag der Verteidigung: 15.06.2021

DECLARATION

I hereby declare that the present work submitted to the examination board of the Faculty of Electrical and Computer Engineering at the Technische Universität Dresden with the dissertation entitled

Blind Source Separation for the Processing of Contact-Less Biosignals

was completely written by me, the signer and that I have not used any other document than the specified means, materials and references. All references and resources used by me in this work are properly cited within. This work was only possible due to the supervision and indirect contribution of:

- Prof. Dr.-Ing. Sebastian Zaunseder
- Prof. Dr.-Ing. habil. Hagen Malberg

Daniel Wedekind

ABSTRACT

(Spatio-temporal) Blind Source Separation (BSS) provides a large potential to process distorted multichannel biosignal measurements in the context of novel contact-less recording techniques for separating distortions from the cardiac signal of interest. This potential can only be practically utilized (1) if a BSS model is applied that matches the complexity of the measurement, i.e. the signal mixture and (2) if permutation indeterminacy is solved among the BSS output components, i.e the component of interest can be practically selected. The present work, first, designs a framework to assess the efficacy of BSS algorithms in the context of the camera-based photoplethysmogram (cbPPG) and characterizes multiple BSS algorithms, accordingly. Algorithm selection recommendations for certain mixture characteristics are derived. Second, the present work develops and evaluates concepts to solve permutation indeterminacy for BSS outputs of contact-less electrocardiogram (ECG) recordings. The novel approach based on sparse coding is shown to outperform the existing concepts of higher order moments and frequency-domain features.

ZUSAMMENFASSUNG

(Spatio-temporale) Blind Source Separation (BSS) eignet sich für die Verarbeitung von Multikanal-Messungen im Bereich der kontaktlosen Biosignalerfassung. Ziel der BSS ist dabei die Trennung von (z.B. kardialen) Nutzsignalen und Störsignalen typisch für die kontaktlosen Messtechniken. Das Potential der BSS kann praktisch nur ausgeschöpft werden, wenn (1) ein geeignetes BSS-Modell verwendet wird, welches der Komplexität der Multikanal-Messung gerecht wird und (2) die unbestimmte Permutation unter den BSS-Ausgangssignalen gelöst wird, d.h. das Nutzsignal praktisch automatisiert identifiziert werden kann. Die vorliegende Arbeit entwirft ein Framework, mit dessen Hilfe die Effizienz von BSS-Algorithmen im Kontext des kamera-basierten Photoplethysmogramms bewertet werden kann. Empfehlungen zur Auswahl bestimmter Algorithmen im Zusammenhang mit spezifischen Signal-Charakteristiken werden abgeleitet. Außerdem werden im Rahmen der Arbeit Konzepte für die automatisierte Kanalauswahl nach BSS im Bereich der kontaktlosen Messung des Elektrokardiograms entwickelt und bewertet. Neuartige Algorithmen basierend auf Sparse Coding erwiesen sich dabei als besonders effizient im Vergleich zu Standard-Methoden.

Too many strange faces, Tyrion thought, too many new players.
The game changed while I lay rotting in my bed,
and no one will tell me the rules.

— George R.R. Martin in *A Storm of Swords* p.255, A Song of Ice and Fire (2000)

ACKNOWLEDGMENT

First of all, I deeply thank the head of *Institut für Biomedizinische Technik* (IBMT), Prof. Dr.-Ing. habil. Hagen Malberg and the former group lead of IBMT's signal processing group Prof. Dr.-Ing. Sebastian Zaunseder for admitting me into IBMT and thus, allowing and promoting my research on Blind Source Separation (BSS). Furthermore, I'd like to emphasize both Prof. Dr.-Ing. Sebastian Zaunseder and Ass. Prof. Urban Wiklund for continuously sharpening my scientific writing while always providing formative and thorough feedback during all the publications we have written together. Urban Wiklund, I moreover thank very much for inviting me to Umeå University in northern Sweden in 2016 for a scientific exchange which have been a magnificent experience both from a scientific and human perspective. Important to mention are also my IBMT doctoral colleagues Alexander Trumpp, Fernando Andreotti, Martin Schmidt and Felix Gräßer with whom I connect a splendid and enriching period of time. Finally, I must not forget to thank my family and especially my love Isabell for backing me up especially since finishing this thesis started to claim our free time after I left IBMT for joining economy in 2017.

CONTENTS

LIST OF FIGURES

LIST OF TABLES

LIST OF ABBREVIATIONS

AC alternating current

ACC accuracy

aECG arrhythmia electrocardiogram

AF atrial fibrillation

ANCOVA analysis of covariance

ANOVA analysis of variance

AV atrioventricular

bpm beats per minute

BCG ballistocardiogram

BMI body mass index

BSS Blind Source Separation

BVP blood volume pulse

cbPPG camera-based photoplethysmogram

cdf cumulative distribution function

CCD charge-coupled device

cECG capacitive electrocardiogram

CI confidence interval

cICA constrained Independent Component Analysis

CMOS complementary metal-oxide-semiconductor

CMRR common mode rejection ratio

DC direct current

DFT discrete Fourier transform

ECG electrocardiogram

EEG electroencephalogram

EMG electromyogram

EVD eigenvalue decomposition

fICA frequency Independent Component Analysis

FIR finite impulse response

HF high frequency

HRE heartrate error

HRV heartrate variability

IBMT Institute of Biomedical Engineering

ICA Independent Component Analysis

IMRR isolation mode rejection ratio

IQR inter-quartile-range

ISI intersymbol interference

JADE Joint Approximate Diagonalization of Eigenmatrices

KF Kalman filter

LED light emitting diode

LF low frequency

MAP maximum a-posterior

MICA Multidimensional Independent Component Analysis

MLE maximum likelihood estimator

NIR near-infrared

OPV operational amplifier

PCA Principal Component Analysis

pdf probability distribution function

PI performance index

πCA Periodic Component Analysis

PPG photoplethysmogram

PPGI photoplethysmography imaging

RADICAL Robust, Accurate, Direct ICA aLgorithm

RGB red, green, and blue

RMSE root mean squared error

ROI region of interest

RRI beat-to-beat interval

RSA respiratory sinus arrhythmia

SNR signal-to-noise ratio

SOBI second-order blind identification

STD standard deviation

STFT short-time Fourier transform

SVD singular value decomposition

tECG textile electrocardiogram

LIST OF SYMBOLS

GREEK SYMBOLS

Symbol	Description	Dimension	Unit
τ	time lag	$\mathbb{R}^{1\text{x}1}$	-
η	viscosity	$\mathbb{R}^{1\text{x}1}$	$\mathrm{N \cdot s \cdot m^{-2}}$

ROMAN SYMBOLS

Symbol	Description	Dimension	Unit
Ag	silver (chemical element)	-	-
C	electrical capacity	$\mathbb{R}^{1\text{x}1}$	$\mathrm{A \cdot s \cdot V^{-1}}$
Ca	calcium (chemical element)	-	-
Cl	chlorine (chemical element)	-	-
CO_2	carbon dioxide (chemical compound)	-	-
F	Faraday constant	$9.65 \cdot 10^4$	$\mathrm{A{\cdot}s{\cdot}mol^{-1}}$
J	negentropy	-	-
K	potassium (chemical element)	-	-
Na	sodium (chemical element)	-	-
P	membrane permeability	$\mathbb{R}^{1\text{x}1}$	$\mathrm{cm \cdot s^{-1}}$
P	pressure	$\mathbb{R}^{1\text{x}1}$	$\mathrm{N \cdot m^{-2}}$
p	probability density	-	-
R	universal gas constant	8.314	$\mathrm{K^{-1} \cdot mol^{-1}}$
R	flow resistance	$\mathbb{R}^{1\text{x}1}$	$\mathrm{N \cdot s \cdot m^{-2} \cdot m^{-3}}$
R	electrical resistance	$\mathbb{R}^{1\text{x}1}$	$\mathrm{V \cdot A^{-1}}$
O_2	oxygen (chemical element/compound)	-	-
S	differential entropy	-	-
T	absolute temperature	$\mathbb{R}^{1\text{x}1}$	K
x	k-sample sensor signal vector	$\mathbb{R}^{1\text{x}\,k}$	-
$\mathbf{x}$	sensor signal matrix x	$\mathbb{R}^{n_1\text{x}\,k}$	-
y	k-sample estimated source signal vector	$\mathbb{R}^{1\text{x}\,k}$	-
$\mathbf{y}$	estimated source signal matrix y	$\mathbb{R}^{n_1\text{x}\,k}$	-
s	k-sample source signal vector	$\mathbb{R}^{1\text{x}\,k}$	-
$\mathbf{s}$	source signal matrix	$\mathbb{R}^{n_2\text{x}\,k}$	-

$\hat{\mathbf{s}}$	estimated source signal matrix	$\mathbb{R}^{n_2 \mathrm{x}\, k}$	-
$\mathbf{A}$	mixing matrix	$\mathbb{R}^{n_2 \mathrm{x}\, n_1}$	-
$\mathbf{W}$	demixing matrix	$\mathbb{R}^{n_1 \mathrm{x}\, n_2}$	-

Ser Jorah: "I would not linger here long, my queen.
I mislike the very smell of this place."
Dany smiled. "Perhaps, it's the camels you're smelling.
The Quarteen themselves seem sweet enough to my nose."

— George R.R. Martin in *A Clash of Kings* p.425, A Song of Ice and Fire (1998)

1

INTRODUCTION

1.1 BACKGROUND AND MOTIVATION

Telemedical monitoring provides major opportunities for reorganizing an increasingly expensive healthcare system. Moreover, the ambulatory monitoring of health and stress offers new applications regarding safety-critical tasks, e.g. driving vehicles [111, 271]. In this context, the contact-less acquisition of vital signs allows a convenient medical assessment and is of high interest.

Various systems and principles for contact-less measurements have been introduced in recent years [33, 308]. Thereby, the term "contact-less" refers to the usage of measurement techniques that cope without sensors strictly fixed to the body at defined measurement locations. In particular, one has to distinguish between non-contact techniques where no sensor is directly attached to the body surface, i.e. the skin, and minimum-contact techniques where e.g. a textile sensor integration ensures flexible skin contact [303].

Available measurement techniques include dry-contact (minimum-contact) and non-contact biopotential electrodes [51]. Electrode implementations like textile or polymeric electrodes for wearable sensing or capacitive electrodes for seat-integrated sensing through clothes have been successfully proven to record the electrocardiogram (ECG) [111, 271, 290]. However, the obtained ECG is of non-standard nature when compared to its clinical counterpart. Moreover, the minimal-conductive measurement principle, which allows flexible health monitoring, is strongly affected by movement artifacts [51]. The resulting decreased coverage and accuracy of a single channel can be addressed by exploiting the redundancy of a multichannel setup [15, 290].

Amongst the non-contact approaches, the usage of cameras, referred to as camera-based photoplethysmography or photoplethysmography imaging, is one promising solution to assess the cardiac pulse in a very user-friendly setting. The acquisition of the cardiac pulse using cameras was firstly demonstrated by Hülsbusch *et al.* [117] 2002. Meanwhile, many researchers have addressed the camera-based photoplethysmogram (cbPPG), most often to assess the heartrate [20, 55, 79, 113, 212, 265, 293]. The most important drawback

of the technique is its susceptibility to artifacts induced by movements and changes in illumination. Sophisticated image and signal processing techniques are required to cope with such factors and facilitate the camera-based assessment of the cardiac pulse even under real world conditions. Comparable to the contact-less ECG recording techniques, the cbPPG image sensor typically also serves a multichannel setup.

Blind Source Separation (BSS) is a signal processing technique suitable for multichannel processing meanwhile aiming at the separation of signal mixtures (e.g. mixtures of ECG or cbPPG and distortions) into its components [123]. Whereas the standard BSS such as Independent Component Analysis (ICA) determines a purely spatial filter for processing multiple (spatially distributed) channels, the spatio-temporal BSS adds finite impulse response (FIR) filters to the multichannel processing by adding a temporal dimension [203, 290]. In the research community, BSS techniques are widely applied to clinical and contact-less ECG recordings for the removal of artifacts and noise [49, 290]. Poh *et al.* [212] were the first to use BSS algorithms in the context of the cbPPG. Since then BSS algorithms became a core part of signal processing schemes to extract the heartrate from cbPPG recordings [55, 94, 95, 112, 113, 153, 166, 174, 181, 212, 213, 259, 297, 307].

Despite the frequent BSS use in the cbPPG domain and high capacity of BSS on the one hand, there is no consensus on performance improvements, i.e. signal quality improvements by using BSS techniques, on the other hand. In particular, Christinaki *et al.* [55], Kwon *et al.* [153] and Feng *et al.* [79] reported also oppositional findings for standard cbPPG BSS usage as proposed by Poh *et al.* [212].

Moreover, especially in BSS settings for electrophysiologic biomedical signal analysis, it is likely that the number of measured channels exceeds the number of underlying sources [131]. This is particularly relevant for multi-sensor setups of typcial contact-less recording techniques. Most common BSS algorithms compute a symmetrical transformation, i.e., ensure the same number of input and output channels [131]. Since BSS is typically only solved up to a permutation (i.e. separated components are available but the output is unordered which is referred to as permutation indeterminacy), the desired output component (e.g. the cardiac component) has to be selected automatically. This selection is particularly important when processing a large number of channels as in spatio-temporal ICA, which adds time-lagged channels during the processing [203, 204, 281].

Besides the existing diversified approaches to component selection [4, 70, 98, 101, 150–152, 189, 218, 222, 258, 290], the evaluation of their actual selection performance is rare. Moreover, the available approaches typically address component selection only in moderate selection scenarios, i.e. a very limited amount of output components. Identifying a robust component selector capable of handling also a large amount of output components would allow powerful techniques as spatio-temporal BSS to become applicable for multichannel biosignal processing.

1.2 AIM OF THIS WORK

The focus of this doctoral work is the development of algorithms for the beneficial utilization of Blind Source Separation for the processing of contact-less biosignal recordings for cardiac signal acquisition. The topic is here divided into two main aspects, which are addressed in this dissertation, as follows:

- BSS application aims at increasing the signal quality of the signals of interest, i.e the cardiac signal. In order to facilitate beneficial BSS usage, particular BSS algorithms and configurations need to be identified that match the characteristics of contact-less cardiac signal recordings and allow for improvements of the signal quality. Accordingly, available BSS algorithms are identified and characterized in the (cb)PPG domain.
- For the exploitation of any BSS potential (i.e. the improvement of signal quality) in practice, permutation indeterminacy needs to be solved. Specifically, an automated selection of the best available BSS output component is required. Accordingly, algorithms to solve permutation indeterminacy for contact-less biosignal recordings are developed and characterized in the ECG domain.

1.3 DISSERTATION OUTLINE

In Chapter 2, the medical background of cardiac activity is described. Further in Chapter 3, the current technical state-of-the-art of cardiac signal acquisition as well as of minimum-contact and non-contact measurement techniques is presented. Moreover, the processing of multichannel biosignal recordings by means of data fusion techniques is discussed where Blind Source Separation algorithms are presented in detail. In addition, the application of BSS to biomedical signals (i.e. ECG and (cb)PPG) is discussed. In Chapter 4, methods for characterizing BSS algorithms in the context of contact-less biosignal recordings are presented as well as novel methodologies for solving permutation indeterminacy are described. Chapter 5 presents the synthesized, recorded and collected data material used throughout this work for characterizing the selected methodologies. Chapter 6 depicts the results based on the experiments defined in Chapter 4 whereas Chapter 7 provides the according discussion. Last, conclusions are drawn for future works in Chapter 8.

1.4 COLLABORATORS AND CONFLICTS OF INTEREST

This thesis was written at the *Institut für Biomedizinische Technik* (IBMT), TU Dresden. During the development of this work, some collaborators contributed to the project. This section summarizes the role of each partner.

Our clinical partners from the University Hospital *Carl Gustav Carus* of Dresden respectively *Herzzentrum* (Univ.-Prof. Dr. med. habil. Klaus Matschke, Dr. med. Thomas Waldow, Dr. rer. nat. Katrin Plötze, Dr. med. Stefan Rasche, Frederik Gätjen) realized together with the IBMT team the recording and evaluation of the clinical data of the *CardioVisio* project.

A collaboration with *Volkswagen AG* (VW AG), Wolfsburg, active until 2014 under the control of Dr.-Ing. Thanh Binh To and Peter Mirwaldt investigated the usage of minimum-contact and non-contact biosignal measurement techniques in the car environment. The capacitive electrocardiogram data used within this work was recorded in 2014 on a VW AG test bench in a study conducted by the IBMT team. Moreover, the cascaded output selection algorithm (CASCSEL) presented later on in this work was developed based on data from the VW AG test bench.

Another automotive collaboration established in 2015 between the IBMT and *ALPS Electric Europe GmbH*, Unterschleißheim, under control of Sascha Kunzmann and Werner Ackermann also approached minimum-contact and non-contact measurement techniques in the car environment.

Furthermore, a cooperation with the Umeå University (Sweden) and especially Ass. Prof. Urban Wiklund was established during a 3-month research stay at the Umeå University in early 2016. In Umeå, together with Dr. Denis Kleyko and Prof. Evgeny Osipov from Luleå University of Technology (Sweden), ideas for sparse coding algorithms were developed that resulted in the automated Blind Source Separation component selection algorithms based on sparse coding, that are presented within this work. Moreover, the textile electrocardiogram data that were recorded by the Umeå group around i.e. Nils Östlund, Marcus Karlsson and Stefan Karlsson was provided by Urban Wiklund for the usage within this work.

Bran: When a man was hurt you took him to the maester, but what could you do when your maester was hurt?

— George R.R. Martin in *A Clash of Kings* p.967, A Song of Ice and Fire (1998)

2

MEDICAL BACKGROUND

Biosignal acquisition and processing addresses physiological processes and possible pathological changes for gathering information on a subject's health condition. This chapter provides background information on the physiological processes of interest and their expressions, on which this doctoral work is built. For that purpose, section 2.1 provides information on bioelectrical (electrophysiologic) and biomechanical (cardiovascular) phenomena and systems under normal healthy conditions, which work as a biological signal generator. Section 2.2 discusses pathological changes in the above described systems and how they affect the measured entities.

2.1 PHYSIOLOGY

2.1.1 *Cardiac Electrophysiology*

Electrophysiologic phenomena inside the human body facilitate muscle contractions responsible e.g. for the heart beat constitution. Such cell excitation processes are based on ions as charge carriers. These charge carriers form spatially separated intra- and extracellular ion concentrations thus generating potentials across ion-selective cellular membranes. Membrane potentials are altered by ion transport processes. On the one hand, this becomes possible by ion transport through the membrane and by electrochemical driving forces on the other hand. The chemical force thereby is given by the ion concentration gradient between intra- and extracellular area whereas the electrical force originates from the electrical potential difference across the membrane by the ionic charge carriers. Both driving forces can form an electrochemical equilibrium, if they coexist in opposite direction and equal level. At the equilibrium state the Nernst potential E_I determines the equilibrium potential of a given ion I

$$E_I = -\frac{\mathrm{R} \cdot \mathrm{T}}{z_I \cdot \mathrm{F}} \cdot \ln \frac{[I]_{\mathrm{intra}}}{[I]_{\mathrm{extra}}} \tag{1}$$

with $[I]_{\text{intra}}$ the intra- and $[I]_{\text{extra}}$ the extracellular ion concentration and R the universal gas constant, T the absolute temperature, F the Boltzmann constant, and z_I the ion valence. Primarily relevant ions for electrophysiologic equilibrium are the cations of sodium (Na^+) with main extracellular proportion and potassium (K^+) with main intracellular proportion. Anions are negatively charged proteins (mainly intracellular) and extracellular chlorine ions (Cl^-). At rest, the membrane's lipid bilayer is practically impermeable for ions. Despite ion channels for passive transport, special transmembrane transport proteins realize the ion transport for the constitution of the equilibrium state mostly for Na^+ and K^+. Thereby, they are responsible for the preservation of the imbalance of respective ions between intra- and extracellular area. Thus, Na^+ ions of the electrochemical ion influx are carried out whereas K^+ ions of the ion efflux are carried in. [120, p.21f],[208, p.49f]

The equilibrium potentials of all involved ions in membrane proximity form the resting potential of the membrane E_M. The Goldmann-Hodgin-Katz equation describes relevant ions together with the membrane's respective ion permeability P_I [208, p.91]

$$E_M = -\frac{\mathrm{R}\cdot\mathrm{T}}{\mathrm{F}}\cdot\ln\left(\frac{\mathrm{P}_{\mathrm{K}^+}\cdot[\mathrm{K}^+]_{\text{intra}}+\mathrm{P}_{\mathrm{Na}^+}\cdot[\mathrm{Na}^+]_{\text{intra}}+\mathrm{P}_{\mathrm{Cl}^-}\cdot[\mathrm{Cl}^-]_{\text{extra}}}{\mathrm{P}_{\mathrm{K}^+}\cdot[\mathrm{K}^+]_{\text{extra}}+\mathrm{P}_{\mathrm{Na}^+}\cdot[\mathrm{Na}^+]_{\text{extra}}+\mathrm{P}_{\mathrm{Cl}^-}\cdot[\mathrm{Cl}^-]_{\text{intra}}}\right). \tag{2}$$

Due to the relatively high membrane permeability for potassium ions at rest, the equilibrium potential of K^+ dominates E_M which causes a resting potential of around $-80\,\mathrm{mV}$ to $-60\,\mathrm{mV}$ for most cells ($E_M \approx -85\,\mathrm{mV}$ for the myocardium). [120, p.23],[208, p.89f,191]

Some cells (e.g. neural, sensual and muscle cells) are capable of rapidly changing their membrane potential by altering the ion permeability on short-term basis. This is referred to as action potential. During an action potential, membranes' voltage-dependent Na^+ channels open (causing a Na^+ influx) while K^+ channels close which cause a shift in the membrane potential (depolarization) due to the temporarily dominating equilibrium potential of Na^+. Heart muscle cells have a threshold potential of around $-65\,\mathrm{mV}$ for the initiation of this reaction. The potential shift also causes voltage-dependent calcium (Ca^{2+}) channels to open. In the myocardium, calcium influx causes a contraction of the heart muscle cells. As long as K^+ channels are inhibited during the action potential, the cell remains depolarized which is known as refractory period. Especially heart muscle cells show a distinct refractory period where the action potential develops a plateau phase before the repolarization. Figure 1 illustrates the indicated aspects of an action potential cycle of a myocardium cell. During the refractory period, a cell is not excitable, which allows for a structured conduction of the depolarization in larger groups of cells (e.g. the contraction of the myocardium). [120, p.23,52f],[208, p.92f,191f]

Specialized heart cells show no stable resting potential but exhibit spontaneous action potentials, whereby they drive a regular heart rhythm even without external depolarization. Such cells are denoted pacemaker cells whereas the human heart holds three levels. The first and fastest natural rhythm shows the sinus node located superior of the heart's

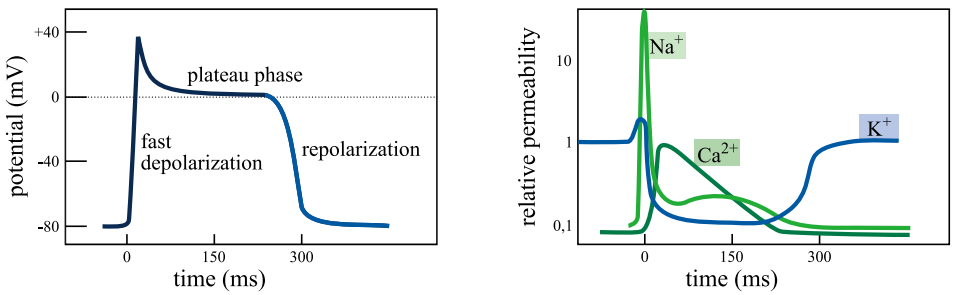

Figure 1: The action potential of a heart muscle cell and the cell membrane's predominant ion permeabilities (right side). Redrawn and modified from [208, p.191, Fig. 5.21].

right atrium which depolarizes about 70 times per minute. Further down in the plane between atrium and ventricles finds the secondary pacemaker atrioventricular (AV) node with an intrinsic pace of 40-50 beats per minute (bpm). Thus, in physiologic condition, the AV node gets depolarized through the stimulus originated from the sinus node before its intrinsic depolarization. The same holds for the third pacemaker (Purkinje fibers) located in the walls of the ventricle generating a pace of 25-40 bpm. [120, p.51f],[208, p.92,198f]

The stimulus conduction inside the heart is based on extracellular and intracellular propagation. The latter bases on gap junctions that ensure electrical coupling between the heart cells. Accordingly, one depolarization (e.g. of a pacemaker cell) progressively spreads across the whole heart. Moreover, there exist specialized heart structures that decelerate or on the other hand accelerate stimulus conduction. The connective tissue-based valve layer between atrium and ventricle can only be electrically passed at the AV node at lower conduction speed. Accelerating fibers like the bundle of His, Tawara branches and Purkinje fibers facilitate especially fast stimulus conduction in ventricles' branches and wall. These factors, which influence the stimulus conduction, ensure a coordinated contraction of heart muscle even in partly pathological conditions. Slow and restricted stimulus conduction at the AV node allows for temporally prior excitation of the atrium in physiological conditions (supporting the filling of the ventricle with blood previously accumulated in the atrium) and blocks too fast stimuli occurring e.g. under pathological conditions like atrial fibrillation (AF). Fast stimulus conduction through the bundle branches supports the uniform contraction of the working myocardium triggering the ejection performance of the heart. The whole stimulus conduction from the sinus node to the ventricle's myocardium lasts around 150 ms, which is clearly below the duration of the action potential of around 300 ms. This ensures that the stimulus conduction has finished before the end of the refractory period. [120, p.51f],[208, p.197ff]

During the depolarization of the heart muscle cell, the membrane potential gets commutated and thus, acts as a dipole from an intra- to extracellular perspective. Moreover, a functional and structural union of multiple heart muscle cells (e.g. a fiber) with depolarized cells as well as cells in rest acts as a dipole also from a purely extracellular perspective. A union of heart muscle cells or even the whole heart can be considered as one single dipole which forms a resulting overall electrical vector as a sum of the partial

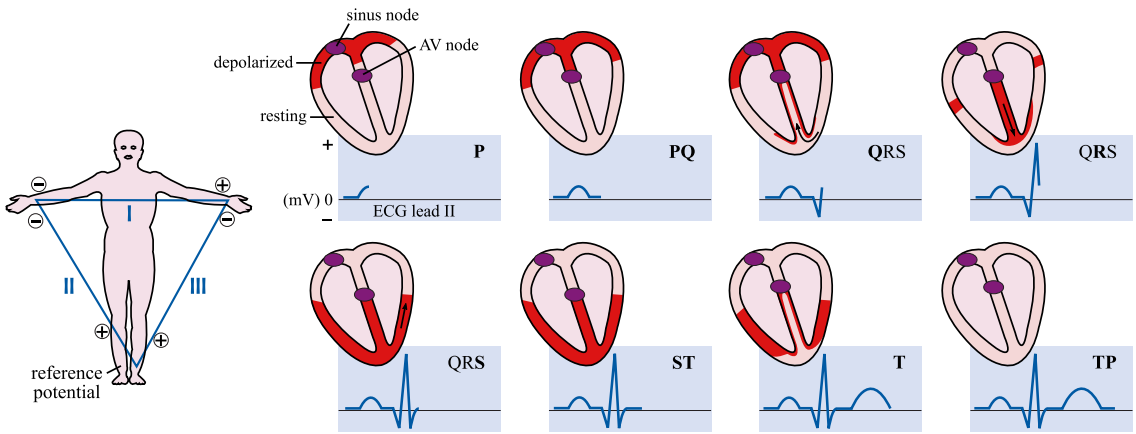

Figure 2: The stimulus conduction through the human heart (right side) as the source of the ECG waveform measured by a standard Einthoven lead (Einthoven lead system on the left side). Redrawn and modified from [120, p.56, Fig. 3.4] and [120, p.57, Fig. 3.6].

vectors (dipoles including its potential difference). The vector is quantified by the sum of its underlying potential differences. Thus, it equals zero, if all cells are simultaneously depolarized or in rest. The direction of the vector is constituted by the direction of the stimulus conduction. Around an electrical dipole, an electrical field develops. The electric field lines and respective isopotential lines are expressed according to the electric properties of the surrounding tissue. However, at the body surface the electrical field can be detected, which serves as basis of the superficial ECG. [120, p.55],[208, p.200f]

Figure 2 shows the stimulus conduction through the human heart alongside the ECG waveform as it is measured by the standard Einthoven limb lead II. The gathered partial and characteristic waveforms are denoted P-, QRS- and T-wave including its connecting sections PQ-, ST- and TP-segment. The P-wave characterizes the depolarization propagation of the atrium followed by the PQ-segment with fully depolarized atrium (showing no change in depolarization and thus, an isoelectric line) and the transition of the stimulus through the AV-node. The depolarization of the ventricle is characterized by an initial stimulus traveling in direction of the ventricle basis (Q-wave), being further directed to the ventricle apex (R-wave), and again upwards along the subepicardial parts especially of the left ventricle (S-wave). The QRS-complex is followed by the isoelectric ST-segment marking a fully depolarized ventricle. The T-wave further represents the ventricle repolarization whereas the TP-segment (sometimes showing an U-wave) comprises the phase until the next heart beat gets initiated. [120, p.56]

By using the Einthoven limb lead electrodes, as indicted in Figure 2, also the Goldberger lead system can be derived. Whereas the Einthoven leads are bipolar and measure a limb potential difference each between two limb locations (with respect to the reference potential gathered at the right leg), the Goldberger leads are unipolar. Accordingly, for each Goldberger lead (aVR, aVL, aVF) a pair of two limb potentials are interconnected to form an indifferent electrode, which is measured against the remaining limb potential. For instance, aVR constitutes the interconnected potentials of left arm and left foot

measured against the right arm. The limb leads are especially used to assess the heart rhythm and the heart's electrical axis. Furthermore, the unipolar chest leads of Wilson (V1-V6) are derived from electrodes directly placed at given chest locations, whereas the limb leads are interconnected to form the indifferent electrode. The Wilson leads depict the horizontal plane of stimulus conduction. Other supplementary ECG lead systems for special medical question are e.g. defined by Nehb addressing the heart's back wall and the corrected orthogonal lead system by Frank for a three-dimensional excitation assessment and vectorcardiographic questions [237, p.424f]. [120, p.55ff],[208, p.200ff]

2.1.2 *Cardiovascular System*

The cardiovascular system is a complex transport system of the human body which consists of the heart as main active blood pump and a network of blood vessels. Thereby, the heart delivers the cardiac output, which is fed into the vessel network. The cardiac output is the primary indicator of the functional capacity of the blood circulation to meet the demands of the supplied functional systems of the human body [54]. It is constituted of the stroke volume (the blood volume ejected by the heart during one stroke) and the heart rate. The transported blood volume realizes the mass transfer of gas (O_2, CO_2), nutrients and metabolic products between the blood and the organs. The transport mechanism is mainly passive (diffusion) and its main part takes place in the capillaries and the post-capillary venules each merging some capillaries. The capillaries are the blood vessels with smallest single diameter but highest cross sectional area taking into account the amount of vessels in parallel. There, respiratory gas molecules can easily pass the membranes of the vascular endothelium such that the diffusion is limited primary by the vessel perfusion. Other exchanged substances as fluids use other transport mechanism like filtration and re-absorption which are controlled by intra-/extra-capillary pressure ratios and membrane permeability. [120, p.82],[208, p.233]

Whereas the blood volume flow in the capillaries, which is mainly responsible for the mass transfer, is nearly continuous due to increasing flow resistance with decreasing vessel diameter [208, p.232], the blood volume is rhythmically fed into the vessel network by the heart's ejection.

The rhythm is controlled by the two main branches of the vegetative nervous system, the parasympathetic and the sympathetic nervous system. The parasympathetic system innervates the sinus and AV node as well as the atrium. By increasing the permeability for K^+ ions in these parts, the spontaneous sinus node depolarization rate and thus, the heart frequency gets decreased, the conduction time in the AV node gets increased and the general excitability decreases. An example for parasympathetic rhythm influence is the respiratory sinus arrhythmia (RSA), i.e. a respiration-synchronous heart rhythm alteration. Pressure receptors modulating the parasympathetic tone are involved in this mechanism. The sympathetic system innervates the whole heart including the ventricle. Its

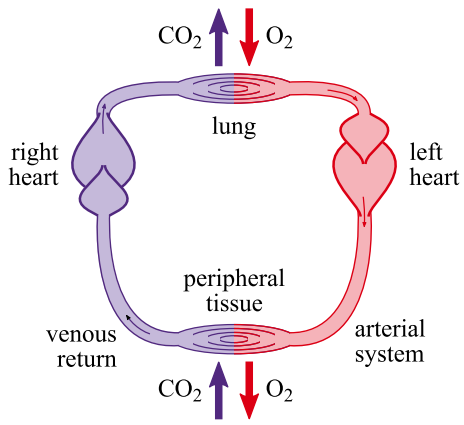

Figure 3: The cardiovascular circulatory system. Redrawn from [208, p.172, Fig. 5.2].

effect is based on the activation of Ca^{2+} channels that increase the contractile force while accelerating the muscle relaxation, which improves the transportation capacity. Moreover, the spontaneous sinus node depolarization rate (heart rate) gets increased, the conduction time of the AV node gets decreased and the general excitability increases. An example for sympathetic rhythm influence is the increase in organ's oxygen demand (e.g. by sports activities). [120, p.68],[208, p.180,206]

Along with the rhythm, the heart's pumping capacity and thus, the cardiac output is determined by active and passive mechanisms. Whereas the vegetative nervous system, as described above, actively affects the capacity by rhythm and contractile force, there also exist passive regulatory mechanisms. They can compensate for short-term alterations in pressure and volume most importantly to ensure equal blood volume ejection by both ventricles, which is necessary to prevent edema. Therefore, the Frank-Starling-mechanism regulates the heart's pre- and afterload. The preload represents the blood volume to be pumped, which has accumulated at the end of the ventricle's filling phase (diastole) and which is determined by venous filling pressure. Thereby an increased filling volume induces an increased pre-strain of the myocardium. During the ejection phase (systole), this enables the ventricle to increase the ejected volume (at equal afterload). The afterload represents the pressure in the subsequent vessels (i.e. the aorta) against which the heart pumps. The ventricle output valve to the aorta opens later in case of increased afterload. This reduces the ejected volume, which increases the remaining volume in turn affecting the preload of the next heart beat. Thus, the cardiac output can be kept constant up to a limited extent even for higher pressures. [120, p.67],[208, p.177ff]

As indicated above, each heartbeat's cycle involves processes altering the blood volumes and pressures inside the heart as well as in the appended vessels. The heart itself thereby functionally consists of two separate pumping systems, whereas both pumps are arranged in succession thus forming a circulatory system. See Figure 3 for an illustration. The right heart pumps the venous blood (deoxygenated, carrying CO_2) into the pulmonary circulation where gas exchange causes the re-oxygenation of blood and the expiration of CO_2

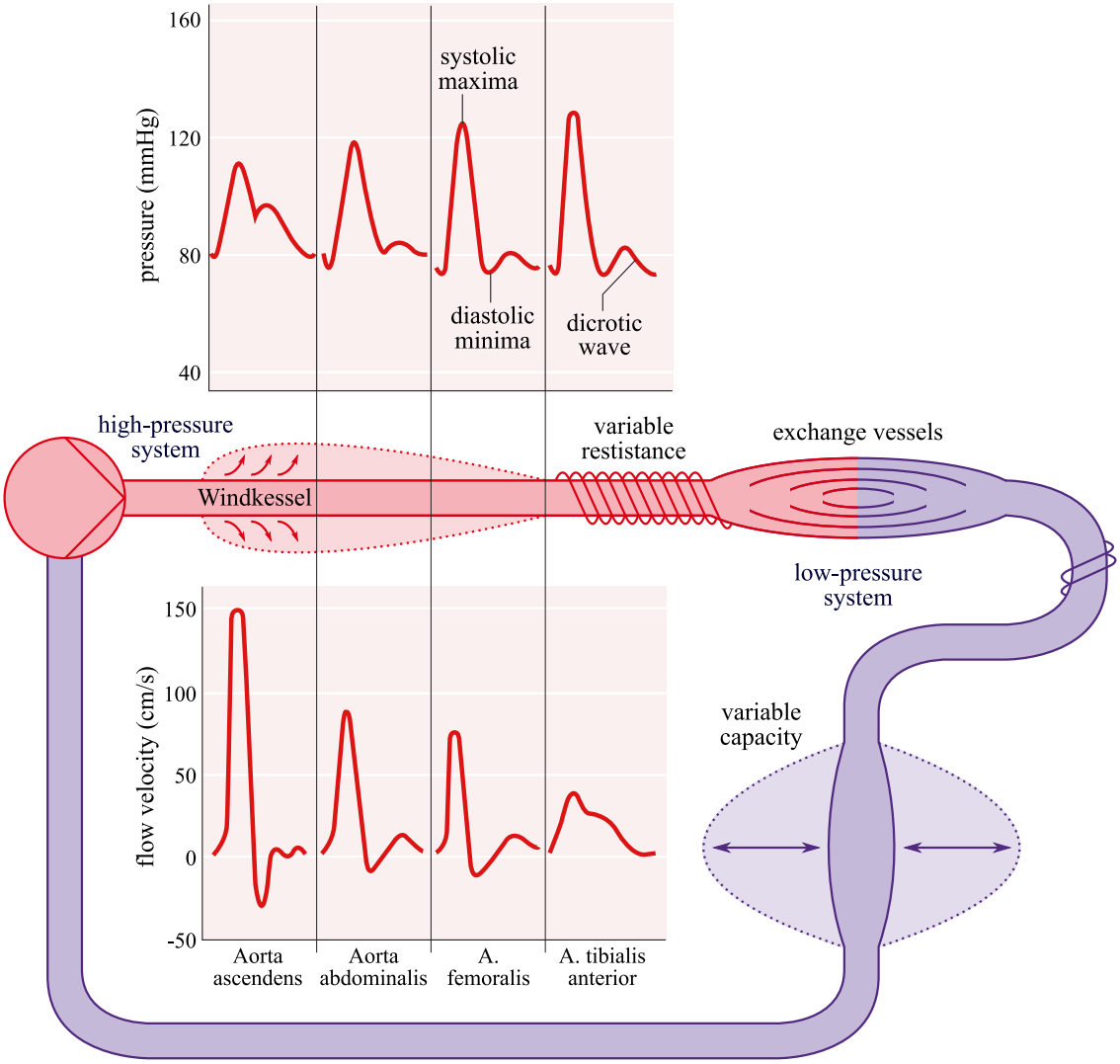

Figure 4: The high-pressure and low-pressure system of the body circulation system including blood pressure and blood flow velocity characteristics for the high-pressure system. Redrawn and modified from [120, p.78, Fig. 4.3] and [208, p.216, Fig. 6.1].

out of the lungs. The left heart pumps the oxygenated blood into the systemic circulation of the body supplying all (peripherally) connected tissues. Both heart parts contract simultaneously following the cycle first filling the ventricles during the diastole. There, the relaxing ventricles cause an decreasing ventricular pressure further causing a passive opening (by the pressure gradient) of the atrioventricular valves with subsequent blood volume transfer from the atria into the ventricles. Second, during systole and ventricle contraction the atrioventricular valves close again (preventing backflow of blood) and a ventricular pressure exceeding the arterial pressure behind passively opens the semilunar valves and leads to ejection of 60-70% of the ventricles' blood volume ($\approx$ 70–90 ml for both ventricles). When the ventricle pressure falls below the arterial pressure, the semilunar valves to close again. [120, p.62f],[208, p.171ff]

The overall circulatory system covers a blood volume of around 5 l. Accordingly, the volume ejected at each heartbeat only represents a small fraction of the overall volume. The main part of the blood volume ($\approx 85\%$) is buffered in the low-pressure system of the circulatory system, which comprises the capillaries, the complete venous system and the pulmonary circulation. Besides hydrostatically induced pressure increases, a mean pressure of 0-25 mmHg is typical and the blood vessels are thin-walled and highly dilatable (high compliance) such that volume changes barely effect the pressure. The left ventricle pumps blood into the high-pressure system. The high-pressure system consists of an arterial Windkessel by the aorta and the larger arteries and the subsequent resistance vessels (smaller arteries and arterioles) which supply the exchange vessels (capillaries). The pressure difference between high- and low-pressure system (arterio-venous pressure difference) drives the blood flow through the peripheral resistance. See Figure 4 for a graphical illustration of the high- and low-pressure system including the pressure and blood flow velocity conditions in the high-pressure system. The Windkessel function of the aorta and larger arteries is realized by relatively thick, highly elastic vascular walls. During systole, only half of the ejected blood volume flows directly into the arteries. The aorta buffers the remaining volume which is pressed into the arteries during diastole due to elastic resilience. This smooths flow and pressure peaks of the blood ejection. Subsequent to Windkessel and conduction vessels the resistance vessels are arranged. They reduce blood pressure before the blood flow's entrance into the capillary system. A flexible resistance thereby allows for demand-based blood supply in favor of certain organs, mainly by adjusting the vascular diameter in the arterioles by vascular muscle tone adaptation. Ohm's law and Hagen-Poiseuille law

$$\dot{Q} = \frac{\Delta P}{R} = \Delta P \cdot \frac{\pi}{8\,\eta} \cdot \frac{r^4}{l} \tag{3}$$

state the relationship between the flow volume per unit time (current $\dot{Q}$) and the driving pressure difference ΔP together with the flow resistance R, the vessel radius r and length l as well as the fluid (blood) viscosity η. The fourth power highlights the predominant role of the vessel diameter for the flow control. Moreover, changes in the flow resistance in the arterioles also effect the pressure difference across the resistance and thus, the pressure in the appended exchange vessels (capillaries). In addition to resistance control, precapillary sphincter can occlude single capillaries, which especially happens in rest to a large fraction of capillaries [156, p.34]. [120, p.77ff],[208, p.215-228]

At the junction of vessels as well at points of changing properties (wave resistance) of the vascular walls, the rhythmical blood pulse wave gets reflected. Reflected waves superimpose peripherally directed waves and cause addition of pressures pulses as well as subtraction of volumetric flow pulsation (see Figure 4). The superposition of the reflected pressure pulse causes an exaltation of the first causal pressure pulse in peripheral direction.

The reflected pulse wave again get's reflected in peripheral direction which cause a second less pronounced pulse wave (dicrotic wave). Because of the alternation of forward and backward pressure spread, the volumetric flow pulsation shows two positive peaks. Due to decreasing flow velocity, the volumetric flow pulsation also decreases in direction of the periphery. In the capillaries, the flow velocity reaches its minimum ($\ll$ 1 cm/s) and the volumetric flow pulsation is almost attenuated. On the contrary, the velocity of the pressure pulse (pulse wave velocity) is highest in the periphery ($\approx$ 800-1200 cm/s) because of the decreasing vascular profile with increasingly rigid vascular walls. Oscillations of the blood pressure within a single heart beat are referred to as first order blood pressure oscillations. Moreover, respiration and periodic peripheral tone oscillations induce short-term blood pressure oscillations of second and third order, respectively. [120, p.78f],[208, p.231f]

The circulatory system is centrally controlled by the circulatory center. Regulatory intervention addresses the regulation of blood pressure as well as the organ perfusion on a short-term (seconds up to minutes) or mid- to long-term basis. The short-term regulation, e.g. the preservation of a circulatory homeostasis, is realized by sympathetic vasoconstrictive fibers via nerval or humoral activation. Baroreceptors, which are mainly located in the aorta and carotid artery, operate as pressure sensors. They act both inhibitory on the sympathetic nervous system as well as with a parasympathetic activation upon increasing the transmural pressure. Thereafter, the heart frequency decreases together with the overall peripheral resistance and vessel tone of the low-pressure system. Accordingly, the low-pressure system can absorb more blood volume such that the filling pressure of the heart (preload) and the stroke volume decreases, which causes a decrease in blood pressure. On the contrary, reduced baroreceptor activity due to decreasing transmural pressure increases the sympathetic as well as decreases the parasympathetic tone. As a consequence, the heart rate and ventricle contractility gets increased as well as the total peripheral resistance and the tone of storage vessels of the low pressure system. That increases the mobilized blood volume and thus, the heart's preload and the blood pressure. Together with the baroreceptors, other sensors respond to mechanical effects (i.e. pressure/strain) at different locations (e.g. the atrium) or chemical indicators as pH-value or adrenaline level to regulate vasoconstriction as well as fluid balance. Whereas short-term circulatory regulation mainly operates on a sympathetic/parasympathetic and thus blood pressure-regulating basis, the mid-/long-term regulation mainly operates on the volume regulation by affecting the fluid and electrolyte balance. Thereby, the renin-angiotensin-aldosterone system and other humoral regulators affect the blood pressure by fluid and Na^+ retention and excretion via the kidney which is partly supplemented by vasoconstrictive effects. Besides the global regulation of blood pressure and volume, the local blood supply of every organ, which largely differs for different organs even in rest, is regulated by a large number of local neuronal and humoral regulatory mechanisms. Auto-regulative effects as vasoconstriction in case of increased transmural pressure ensure homeostatic

blood flow e.g. in the brain and the kidney. In the pulmonary artery, the auto-regulation works in opposite direction thus ensuring almost homeostatic blood pressure. An increased stroke volume accordingly causes a more-extensive lung perfusion. Such auto-regulative effects are myogenic or chemically mediated. Moreover, chemical regulation (e.g. partial pressure of O_2 and CO_2) together with humoral (e.g. adrenalin) and nerval (predominant sympathetic) regulation affect local supply differences as a consequence of demand. Nerval vasoconstrictive (sympathetic) activations thereby can be superimposed by stronger humoral vasodilative effects which e.g. can combine a sympathetically increased heart frequency with an improved organ perfusion by vasodilation. [120, p.83-89],[208, pp.238-251]

2.2 PATHOLOGY

2.2.1 *Electrophysiology of Cardiac Diseases*

As a consequence of temporary disturbance or pathological changes of the electrophysiologic processes in the heart, disorders of excitation formation, conduction and recovery occur and express themselves in the ECG. Thus, the ECG possesses a high informative value on electrophysiologic disorders, i.e. for the assessment of cardiac diseases. Common disorders of excitation formation and conduction significantly affect the heart rhythm and thus, are even properly apparent in simple ECG lead systems as the Einthoven leads also under modifiable measurement locations. Rhythm disturbance can be categorized into intermittent and persistent disturbances.

Intermittent rhythm disorders due to disturbed formation occur in case of depolarization originating not from the regular pacemakers but in ectopic pacemakers (e.g. perfusion-deprived myocardial cells). Supraventricular extrasystoles emerge superior from the bundle of His mostly from the atrium. Regular stimulus conduction through the AV node yields a regular QRS complex but reduced beat-to-beat interval (RRI). See Figure 5a1 for an example. A ventricular extrasystole emerges from the ventricle. The irregular stimulus conduction through the heart changes the QRS-morphology (see Fig. 5a2). If the irregular ventricle excitation state coincides with a subsequent regular (sinus) depolarization, the refractory period inhibits the regular excitation, which causes a compensatory pause (increased distance between the extrasystolic and the next regular QRS complex). Whereas a disturbed stimulus conduction in the ventricle (e.g. bundle branch block) not necessarily contributes to rhythm disorder but rather to QRS morphology changes [146, p.102], rhythm disorders due to disturbed stimulus conduction can originate from an abnormal atrioventricular stimulus conduction (AV-block). There is a distinction between three degrees of severity. The first degree denotes a prolonged atrioventricular stimulus conduction $> 0.2\,\mathrm{s}$ (see Fig. 5b1). An AV-block of second degree denotes an incomplete stimulus conduction such that not every atrial depolarization is conducted to the ventricle (see Fig. 5b2) and single P-waves appear. If the atrioventricular stimulus conduction is

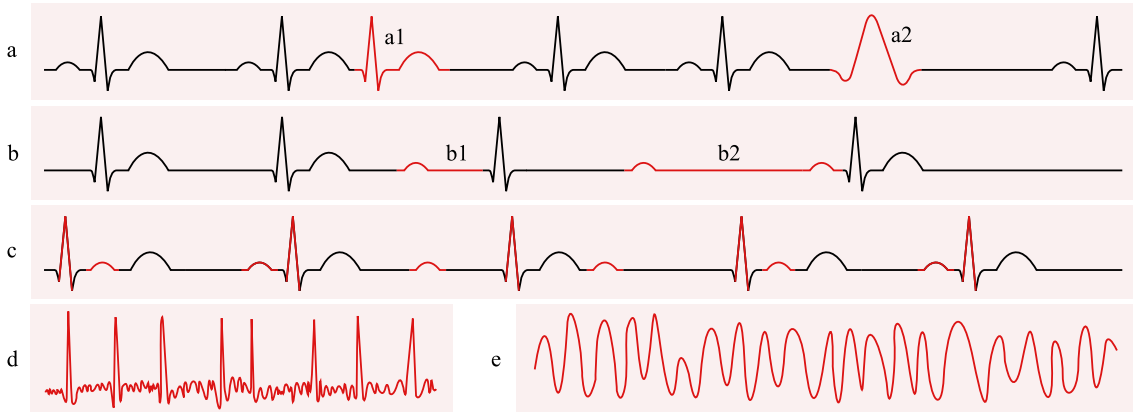

Figure 5: Arrhythmic ECG types. a: extrasystoles, a1: supraventricular extrasystole, a2: ventricular extrasystole, b: AV-block, b1: first degree, b2: second degree (Mobitz I), c: AV-block third degree, d: atrial fibrillation, e: ventricular fibrillation. Redrawn and modified from [120, p.60, Fig. 3.12 and p.61, Fig. 3.13 & 3.14].

completely inhibited (AV-block of third degree), both atrial and ventricular depolarization appear independently of each other regarding their respective pacemaker without rhythmic synchronization of P-Wave and QRS-complex (see Fig. 5c). [120, p.60f],[208, p.207f]

An AV-block of third degree might represent a persistent rhythm disorder that effects each heart beat constitution. Sinus bradycardia (heart frequency < 60 bpm) and sinus tachycardia (heart frequency > 100 bpm) are persistent rhythm disorders which are morphologically unobtrusive and pathological only for sudden (paroxysmal) and non-causal (e.g. tachycardia in resting condition) appearance [146, p.153f]. Fibrillation and flutter, however, represent critical rhythm disorders. In case of atrial flutter (depolarization rate 220-350/min.) and atrial fibrillation (depolarization rate 350-600/min.) the stimulus conduction is disturbed such that neighboring areas are depolarized independently of each other. Because of the frequency-selective stimulus conduction through the AV node, atrial depolarization is only irregularly conducted to the ventricle (see Fig. 5d). An absolute arrhythmia with irregular rhythm and a ventricle depolarization of around 120-150 bpm become apparent. During ventricular fibrillation, the ventricle depolarizes in a high-frequent uncoordinated fashion (see Fig. 5e). This is frequently caused by an extrasystole during repolarization (T-wave), where parts of the myocardium are already repolarized and another depolarization can induce a circulating depolarization between several ectopic excitation centers, which inhibits ventricle's filling and pump function. Functional, this is equivalent to a cardiac arrest. A ventricular fibrillation can be interrupted by defibrillation. [120, p.61],[208, p.208]

Disorders of excitation recovery can be categorized into primary and secondary disorders. While secondary excitation recovery disorders follow a disturbed excitation conduction, primary excitation recovery disorders occur independently. Specific primary disorders affect the ST-segment in terms of its elevation or depression and isolated changes of the

T-wave (e.g. negation), respectively. Such disorders are caused e.g. by myocardial infarction and its precursors as well as heart muscle inflammation (myocarditis, pericarditis). [146, p.132f]

2.2.2 *Cardiovascular Disorders*

Cardiovascular disorders typically originate from a loss of the circulatory system's ability to properly adapt to changing blood pressures and blood flow demands. They are often induced by sclerosis (induration) and stenosis of blood vessels. Induration of functionally elastic vessels as the aorta (Windkessel) increases the systolic blood pressure. Also, as indicated by equation (3), a vascular stenosis decreases the vascular radius and has a major effect on the blood flow resistance (increase). Impeded peripheral blood effluent increases the diastolic blood pressure. A prominent example for severe vascular stenosis is cardiac infarction, where blood perfusion in a coronary artery is inhibited (ischemia) by vascular occlusion. This causes the appended myocardial section to fail which decreases the pumping capacity of the heart and hampers the stimulus conduction in the affected area [208, p.208]. Thereby, the occlusion of arterial vessels can be caused by a progressive stenosis as well as a thrombus (embolism). The venous system can also be source of cardiovascular disorders. Venous valves physiologically close during venous pressure increase by inspiration or leg muscle contraction. This prevents peripherally directed venous blood flow and supports venous return. Also, peripheral blood is attracted by respiration-induced thoracic pressure changes. These functionalities provide 1/3 of the energy of the circulatory system with respect to the venous return and are disturbed by venous valve insufficiency. Valve insufficiency (reflux) besides valve stenosis (increased flow resistance) also has a major haemodynamic effect at the heart's four valves with respect to pressure and flow conditions characterizing the cardiac output [156, p.17f]. An arteriovenous fistula bypasses the arterioles and exchange vessels. Because of the pressure-dependence on the vascular resistance given a certain flow, such fistula decreases the arterial pressure. This has to be compensated by increased stroke volume (flow), however, the blood perfusion of downstream tissues behind the fistula nevertheless is decreased. [156, p.35ff]

Despite a physical modification of vascular properties, pressure sensors (e.g. baroreceptors) and volume sensors (e.g. in the atrium), which are operating in the short-term cardiovascular control, can be misaligned due to habituation effects under persistent irregular conditions. In this context, nerval control instants of the circulatory system which react to stress and fear can affect blood pressure increases and vascular dilation as reflexive "fight and flight reaction". A persistent increase in blood pressure (hypertension) again cause a physical harm of the vessels which impair e.g. long-term blood pressure regulation systems in the kidneys. [156, p.45f,53]

2.3 CHAPTER SUMMARY

In this chapter, the properties of two major human physiological signal generators, the heart's electrophysiological system and the cardiovascular system from a mechanical point of view, were discussed. The heart's electrophysiology causes rhythmic electric signals, showing charactristic waveforms due to depolarization and repolarization that are synchronous with the particular heart activity. Its causal effect is locally limited to the heart but it is measurable at the body surface. The signal morphology is indirectly affected by the measurement location due to projection. The cardiovascular system causes a rhythmic and pulsating mechanic signal characterized by blood pressure and blood volume flow. Its causal effect propagates over the the complete body but with changing morphology such that the morphology is directly affected by the measurement location. Both signals are physiologically and pathologically modulated in rhythm and morphology on different time scales.

Ser Jacklyn scratched at his cheek with his iron hand.
"Wise measures. Though I have no love for that alchemist's piss."
Tyrion: "Nor I, but I use what I'm given."

— George R.R. Martin in *A Clash of Kings* p.315, A Song of Ice and Fire (1998)

3

TECHNICAL STATE OF THE ART

Biosignal acquisition and processing addresses physiological processes and their possible pathological changes for gathering information on a subject's health condition. This chapter provides background information on the biosignal acquisition and processing techniques, on which this doctoral work is built. For that purpose, section 3.1 provides information on clinical and novel minimum-contact/contact-less acquisition techniques for bioelectrical (electrophysiological) and biomechanical (cardiovascular) phenomena. Section 3.2 discusses the fundamentals of processing multichannel biosignal recordings. From there, section 3.3 details Blind Source Separation as a particular multichannel processing technique. Finally, section 3.4 identifies the boundaries of Blind Source Separation's state of the art for the processing of the particular biosignal recording techniques described before.

3.1 CARDIAC DIAGNOSTIC AND MEASURING TECHNIQUE

3.1.1 *Clinical Cardiac Signal Acquisition*

3.1.1.1 *Biopotential Measurement*

Biopotential measurement typically addresses bioelectrical phenomena at the body surface by using metal-based electrodes. The activity measurable at the body surface thereby reflects ion-based bioelectrical excitation (e.g. through excitable cells of the heart muscle) from within the body whose electrical potentials are carried to the body surface because of the tissue's conductivity [92, 253]. Whereas the intra-corporal electrical processes originate from ion-based charge transport, at the body surface the stratum corneum forms a dry dielectric outer layer, which basically impairs the transfer of ions to electrons in the electrode. A moist electrolyte gel electrode is one possibility that facilitates an ion conductivity of the skin's dry outer layer [92]. Figure 6 shows the electrical equivalent circuit of the electrode-electrolyte system including the skin. The conductive electrolyte (R_c) is composed of sodium (NaCl) and/or potassium chloride (KCl) correspondingly ensuring

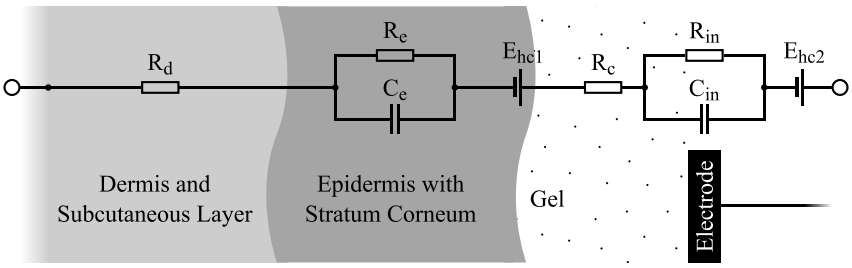

Figure 6: Electrical equivalent circuit of a biopotential electrode (adapted from [280, p.207]).

compatibility to the body fluids [253]. This solution buffers the electrolytic composition through the outer and inner layers of the skin [51] and forms two Nernst potentials on both sides of the electrolyte. The Nernst potential is described by the Nernst equation assessing the relative activity of ions on two sides of a semipermeable membrane [199, 253]. Gruetzmann *et al.* [92] denotes both potentials as half-cell potentials ($E_{hc1,2}$) whereas E_{hc2}, that is located on the electrode side of the electrolyte, serves the potential commonly known as half-cell potential. Since electrolytic solutions of different concentrations and ion mobilities in direct contact also exhibit a potential difference, E_{hc1} which is also known as liquid-junction potential gives the other Nernst potential [280, p.194f]. The processes (potential differences) at the two electrolyte boundaries (electrode, skin) are important for the biopotential measurement.

An electrode's half-cell potential E_{hc} is a consequence of the Helmholtz double layer formed of ions at the interface between electrode and electrolyte. This causes the electrolyte close to the electrode to establish a different electrical potential compared to the rest of the electrolytic solution. Without alteration of the charge distribution in the solution, the half-cell potential should be observable at the electrode [199]. Additionally, the ions at the electrode-electrolyte interface could be hydrated thus involving a layer of solvent molecules (adsorption of water) in the double layer [110, p.23f].

The drivers of the half-cell potential at the electrode-electrolyte interface are redox reactions. Thereby e.g. cathodic oxidation appears where a metal atom releases electrons as charge carrier inside the electrode and goes into solution as positively charged cation (e.g. for silver: $Ag \rightarrow Ag^{+} + e^{-}$). Reduction appears where ions are reduced (discharged onto the metallic surface) in reverse direction. Inverse processes appear with anions at the anode [199].

Without additional currents, redox reactions of cations and anions form an equilibrium at the electrode-electrolyte interface. However, there exists a difference between oxidation and reduction rates of $Ag \leftrightarrows Ag^{+} + e^{-}$ [61, p.21] causing a higher amount of cations close to the surface forming a double layer with anions (principal anion Cl^{-}) to be complexed from the electrolyte [280, p.190f,206].

If electrical fields/currents are added between electrolyte and electrode, charge-transfer processes involved in redox reactions are not always entirely reversible and deviations from equilibrium occur. The activation energy for the respective redox reaction not necessarily

equals each other, which causes either oxidation or reduction predominating the interface in case of imprinted currents. Moreover, currents affect the ion concentrations itself at the interface [280, p.191ff]. In that case, the Helmholtz double layer remains intact and no actual current passes the interface, whereas the change in the half-cell potentials is referred to as polarization and overpotential. The measured current is a displacement current [280, p.196]. Accordingly, such electrodes impose a highpass character based on the capacitive nature of the double layer (R_{in} and C_{in}) and are known as electrodes of the first kind [73],[110, p.24],[199],[280, p.203].

Non-polarizable electrodes allow current to pass freely without changing the charge distribution in the electrolytic solution adjacent to the electrode. A balanced electrochemical reaction is achieved by interfacing a metal to its salt e.g. a silver base structure coated with a layer of silver chloride, which itself is almost insoluble in aqueous solutions [199]. In this system, silver shows the tendency to oxidize as known from the polarizable electrode whereas the silver cation Ag^+ shows the tendency to form the ionic compound AgCl on the electrode surface together with the principal anion Cl^- from the electrolyte. This gives the balanced overall reaction $Ag + Cl^- \leftrightarrows AgCl + e^-$ [280, p.197]. Electrokinetic effects of such electrodes belong to the bulk charge induced by an applied field. Electrodes of this nature are known as electrodes of the second kind [73]. The silver-silver chloride-based electrode system behaves similar to a non-polarizable electrode and offers lowest and most stable half-cell potential [199, 253].

The half-cell potential of the electrolytic interface can cause electrode-based motion artifacts, when charge distributions adjacent to the electrode alter due to relative motion between electrode and electrolytic solution. A non-polarizable electrode is less affected by relative motion than a polarizable one.

The electrolyte-skin interface transduces the ionic currents of the body to currents measurable through the electrode-electrolyte interface. The impedance of the epidermis (R_e and C_e) is poorly defined and unstable [92] and the effect of instability can be minimized by the removal of the stratum corneum prior to the measurement [280, p. 207f]. However, the stratum corneum serves as membrane semipermeable to ions, which gives a potential difference (Nernst potential) based on differing ion concentrations between skin and the electrolyte gel [280, p.207]. The removal of the stratum corneum will still enable the manifestation of a half-cell potential (liquid-junction potential [280, p.194f]) at the electrolyte-skin interface. Time-variant ionic currents inside the body thus affect charge displacements covered by ions in the electrolyte which influence the electrokinetic phenomena at the electrode-electrolyte interface measurable at the electrode. In this context, ionic currents are altered by field potentials spread from the respective sources (e.g. the heart muscle) through the body as a volume conductor [280, p.135ff].

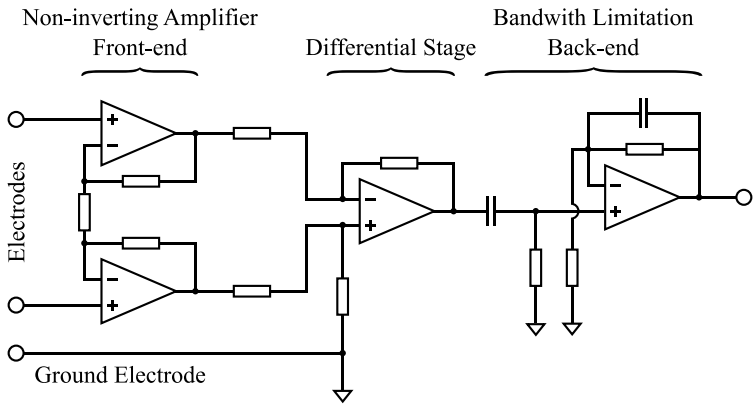

Figure 7: Basic circuit design of a biopotential amplifier based on an instrumentation amplifier (adapted from [253]).

3.1.1.2 *Biopotential Amplification*

Biopotential amplifiers provide amplification to low level potentials measured from the human body, typically ranging between 1 µV and 100 mV (the ECG shows a typical amplitude difference of 1 mV [253]). They must simultaneously guarantee protection from electrical shock and damage for both subject and electronic equipment [197]. Due to the high source impedances and high levels of interferences typical for biopotential measurements, they address features like high differential gain, low common mode gain, high common mode rejection ratio (CMRR) and high input resistance as well as a linear amplification to not distort the measured signal [197, 253]. Common mode rejection thereby refers to suppressing content showing only very small amplitude and phase differences between the measuring electrodes thus appearing only between input and ground [197].

A typical circuit design of biopotential amplifiers involves the design of the instrumentation amplifier as depicted in Figure 7. It is composed of a differential first stage consisting of two non-inverting operational amplifiers (OPVs) followed by a second stage differential amplifier and back-end bandwidth limitation with highpass and lowpass filter [253].

The preferable high differential gain is distributed over the first two stages as the gain factor of the first stage is limited because of the amplitude mismatch between a relatively high electrode half-cell potential compared to the amplitude of the measured biosignal. However, the two-stage combination can achieve high common mode rejection and high input resistance realized by the non-inverting amplifier front-end. Nevertheless, the common mode rejection always is limited by the equivalence requirement of the source impedances at the respective electrodes [197]. An ECG amplifier further may limit the bandwidth of the signal (back-end) to its relevant content of around 0.05 - 100 Hz whereas distortions of the signal by highpass filters needs to be avoided [253].

Further interference suppression can be achieved by negative feedback of the common mode signal into its lead by a driven-right-leg circuit. Electromagnetic shielding and other filtering and guarding approaches and related technical solutions (e.g. by automatic

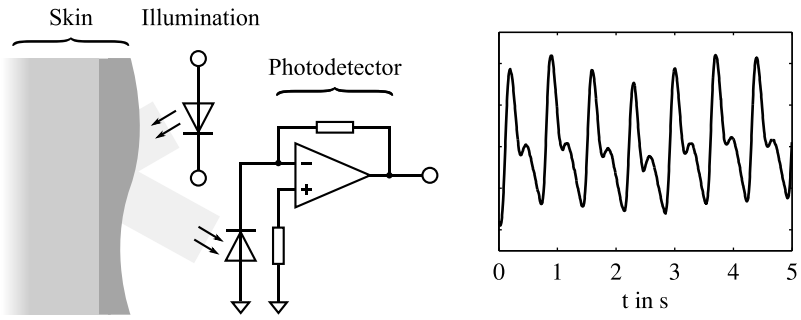

Figure 8: Basic recording principle (based on reflection) for optical measurement of the cardiac volume flow by photoplethysmography (adapted from [6]) including an exemplary PPG signal excerpt.

discharging of a high-pass capacitor of the back-end amplifier for baseline restoration in case of amplifier saturation) are applied. [253]

To ensure subject safety, very small leakage currents (µA) of the amplifier are allowed and electrical isolation from the power line is required to prevent current between instrumentation, subject and the earth ground, respectively. Transformers or opto-couplers are common techniques to provide galvanic isolation. Their performance is characterized by the isolation mode rejection ratio (IMRR). Moreover, equipment protection against high voltages e.g. by defibrillation and electrosurgical instrumentation is achieved by using diodes or providing alternative paths to ground for high voltages like low pressure gas discharge tubes. [197, 253]

3.1.1.3 *Optical Measurement of Blood Volume Changes*

The non-invasive measurement of absolute blood volume involved in cardiac processes is a rather complex task. Two-dimensional or Doppler echocardiography estimates relevant cross sections (e.g. the aortic cross section by measuring the aortic diameter) and further estimates velocities through the respective cross section or otherwise directly measures end-systolic and end-diastolic left-ventricular volumes using ventricular models [54, 71].

However, if one is less interested in absolute volume measurement, the assessment of the pulsatile component of the cardiac volume flow, i.e. the rhythmic changes in the blood flow through the human body, is available via a simple non-invasive measurement principle, the photoplethysmography [6].

Whereas its main clinical purpose is the measurement of blood's oxygen saturation, the photoplethysmogram (PPG) is an optical measurement technique that also can detect blood volume changes in the microvascular bed of tissue, thus allowing for non-invasive measurements at the skin-surface. It is opto-electronically realized by two basic components, a light source to illuminate the tissue and a photodetector (e.g. a photodiode) to measure variations in the light intensity associated with the blood volume in the tissue. Figure 8 shows the measurement principle. The technique is applied to acquire the peripheral pulse wave (for a signal example see also Figure 8). [6]

Based on the optical measurement principle addressing the light modulation within the human tissue, the optical processes scattering, absorption, reflection, transmission and also fluorescence contribute to the PPG. These processes are mainly affected by blood volume and blood vessel wall movement. Dependent whether the light irradiation works mainly through the tissue (i.e. from the opposite side of the photodetector) or indirect (i.e. adjacent to the photodetector), transmitted or reflected light (each containing proportions of scattered light) is measured at the sensor, whereas absorption modulates the total amount of light. Water as the main constituent of body tissue (and melanin) thereby strongly absorbs short (e.g. ultraviolet) and long (e.g. longer infrared) wavelengths, what refers to as optical water window. In the visible and shorter infrared wavelength spectrum, hemoglobin as blood component shows significant absorbency which causes a pulsatile blood volume to rhythmically change the amount of absorbed (and measured) light. The absorption also differs for oxygenated hemoglobin (HbO_2) and reduced hemoglobin (Hb) despite for isobestic wavelengths (e.g. 805 nm). Moreover, light of different wavelength penetrates and consequently gets absorbed in tissue of different depth with different blood vessel structure. The gathered signal accordingly shows a pulsatile (alternating current (AC)) component with fundamental frequency depending on the heart rate plus a direct current (DC) component affected by the measured tissue with its average blood volume and some quasi-DC contributions due to respiration and other low-frequency phenomena. [6]

The measurement of the peripheral PPG from humans was firstly described in 1936 by Molitor *et al.* [193]. Nowadays, PPG sensors use light emitting diodes (LEDs) of green [74, 301] or red and/or near-infrared (NIR) wavelength [6, 76, 301]. One distinguishes between the transmissive irradiation of the finger-tip or earlobe and the reflective irradiation at all suitable sorts of body locations. Although the concept of the PPG does not necessarily require direct contact between photodetector and the recording location, direct contact with moderate contact pressure improves the pulse amplitude and suppresses light reflected at the skin surface as source of disturbance [107]. However, also non-contact/remote PPG has been studied more recently [42, 233]. Besides single location use, PPG measurements have also been conducted simultaneously at multiple locations [7, 76].

3.1.2 *Minimum-contact/Contact-less Cardiac Signal Acquisition*

3.1.2.1 *Capacitive ECG*

The capacitive electrocardiogram (cECG) represents a mean to measure the electrical excitation of the heart muscle cells in a minimum-contact or even limited non-contact fashion. The coupling to the subject is established capacitively and does not require any galvanic contact. However, the differential bioelectrical signal is equivalent to the standard conductive ECG [33] . The electrical field at the body surface is measured via the displacement current in the electrode [110, p.30],[238]. Figure 9 shows the electrical equivalent front-

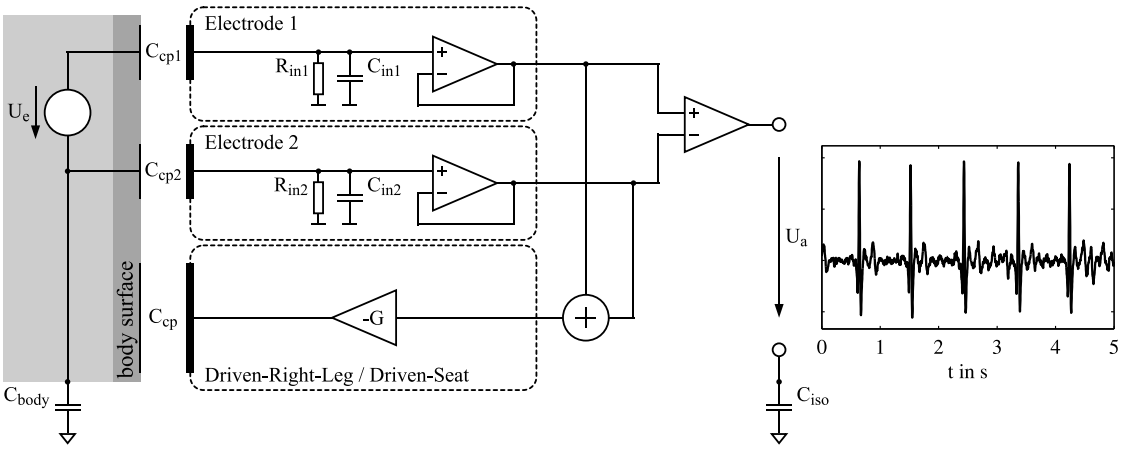

Figure 9: Electrical equivalent front-end circuit of a cECG measurement system (adapted from [33, 238],[110, p.32]) with a sample cECG-excerpt recorded using a cECG seat cushion.

end circuit of a cECG measurement system. The coupling between the subject and the electrodes is characterized by the coupling capacitances C_{cp}. The electrodes possess an input impedance (R_{in}, C_{in}) which is adapted by an impedance converter (OPV). The input impedance must be much larger than the source impedance imposed by C_{cp} to avoid signal attenuation [238]. The capacitive voltage divider formed by C_{cp} and C_{in} acts as a high-pass filter which causes a minimization of C_{in}, especially because removing the mechanical contact between electrode and body surface while inserting an air gap or clothing largely decreases C_{cp} [110, p.33],[238]. On the other hand, the large input impedance increases the influence of external interferences [170]. Because of the lacking galvanic contact between subject and measurement system, common mode interferences are likely to occur which can saturate the impedance converter of the electrodes. Active reference potential control by Driven-Right-Leg/Driven-Seat can help to suppress common mode interferences e.g. caused by differing coupling capacitances C_{cp1} and C_{cp2} [110, p.41f]. Also, increasing the electrode size decreases the coupling impedance meanwhile minimizing common mode interference [160]. DC common mode interferences like electrostatic charge of the subject due to e.g. triboelectricity [277] cannot be suppressed by capacitive reference potential control [110, p.42]. Noise coupling by electrical fields, in turn, was not found to induce a larger impact on insulated electrodes compared to wet electrodes [230]. A sample cECG excerpt can be seen in Figure 9 (recorded with a cECG seat cushion and Driven-Seat).

The measurement of a capacitively coupled ECG was first demonstrated by using insulated electrodes by Richardson [220],[221] in 1967 and 1968, respectively. However, the research interest regarding this technique for cardiac monitoring grew not until the 2000s. Then, new applications of the cECG addressing long-term and everyday ECG monitoring were presented e.g. by integrating capacitive electrodes into a chair [18, 145, 169]. Also, other types of seats, e.g. car seats utilizing multiple capacitive electrodes and a Driven ground (Driven-Right-Leg/Driven-Seat) [164, 165, 271, 281] and a ground level obtained

from the steering [44, 180] were studied as well as toilet seats [17, 144] and an airplane seat [227].

Besides seats, the use of cECG in beds has been under consideration, which could facilitate a less obtrusive sleep medical cardiovascular assessment. Lim *et al.* [170] used eight aluminum-shielded cECG electrodes with reference level measured through a large conductive textile ground sheet all covered by a cotton sheet. Later, the group added a Driven ground to the system [171]. Fully flexible electrodes of highly conductive textile material in a bedsheet with cotton bedcover were used together with a capacitive Driven-Right-Leg circuit of Wu *et al.* [294] and Lee *et al.* [160]. Chamadiya *et al.* [45] utilized actively guarded electrodes driving the guarding layer with a common mode voltage for hospital beds. The usage of capacitive electrodes in mattresses have also been adapted to the monitoring of neonates [140].

More applications of the cECG are in bathtubs [172], a portable multichannel unit as presented by Oehler *et al.* [201] as well as multimodal electrodes also including optical sensors for the usage e.g. on the operating theater table [276].

3.1.2.2 *Textile (Wearable) ECG*

Another possibility to measure an ECG without preparation of the skin like the cECG is the usage of dry-contact electrodes. The conductive electrode material itself is brought into contact with the skin. Since the dry-contact electrode directly aims at ionic charges altered by bioelectrical processes, the mandatory electrolytic layer responsible for transducing ionic currents into electric currents by redox (oxidation-reduction) reactions is constituted by sudor [110, p.25f],[199]. Sudor contains Na^+, K^+ and Cl^- ions [280, p.208] but has a lower ion conductivity compared to gel used in wet electrodes [92]. The initialization of the interface may require a settling time of a few minutes before achieving readable signals [186].

Because of the higher input impedance compared to wet electrodes and the partly-polarizable nature of the dry electrode, the half-cell potential of the electrode-electrolyte interface is affected by relative movements between electrode and skin inducing artifacts [87, 92],[110, p.22,26],[199]. Similar electrical equivalent circuits as presented in Figure 9 can be used for dry-contact active and passive (no impedance conversion) electrodes adding a coupling resistance in parallel to the coupling capacitance C_{cp} [51].

The interplay between coupling resistance and capacitance determines the limits of noise sensitivity [51]. Analogue to cECG (varying coupling capacitance), the coupling impedance alters during moistening of the skin under the electrode (e.g. shunting the coupling capacitance) [87].

Common mode interference expresses differently in dry-contact electrodes compared to wet-electrodes. Searle *et al.* [230] found that dry-contact (as well as insulated) electrodes show less interference according to non-stationary electrical fields than wet electrodes. Especially, the two limiting cases, i.e. infinite coupling conductance (dry-contact electrode,

zero resistance) or infinite coupling impedance of the electrode (cECG, infinite resistance), are optimal for low-noise signal reception [51]. Artifact levels through relative motions between subject and electrode were found significantly higher than by using wet electrodes [230] and should be addressed by mechanical design considerations [51, 87].

Dry-contact electrodes allow for reusable wearable devices and smart clothing and also facilitate long-term physiological monitoring [92, 186, 205]. Special interest for dry-contact electrodes arises from disadvantages of common gel-based electrodes going along with dermatological responses to the gel or recording in gel-sensitive areas as well as reliance on an electrolyte which decreases the signal quality while the gel dehydrates [186, 230].

Dry electrodes build from silver plates [205] and stainless steel plates or silver foil as well as with active impedance conversion [206] have been used. The reduction of necessary wires to connect active dry electrodes and size of the active electrodes was addressed in [68].

Mechanically adaptive electrodes have been addressed by electrically conductive foam with silver surface and titanium adhesion layer [92]. Moreover, polymeric structures have been proposed utilizing conductive nanoparticles in a elastic polysiloxane connected to a textile (belt/shirt) [111] as well as a thin metallic layer on a polysiloxane base structure as electrode on a wristband [19]. Conductive polymer transducers for active electrodes with impedance conversion has also been used for limb leads [27] and flexible non-woven fabric-based electrodes [139] with imprinted conductive inks [300].

The highest formability of a dry-contact electrode can be obtained by a textile integration. However, the structured surface of a textile reduces the contact surface by forming cavities and interstices which affects the coupling impedance [110, p.26f]. This property is compensated by increased electrode adhesion through moistening of the skin [209]. Practical realizations are given by knitted stainless steel textile electrodes (stainless steel wires twisted around a yarn) in a garment or belt to obtain multichannel ECG [41, 290] partly covering the metal electrode with a hydrogel membrane [209, 228]. Also a bed has been equipped by large-area electrodes from electrically conductive carbon and nickel-plated fibers [128]. In this work, the term textile electrocardiogram (tECG) refers to as dealing with ECG derived by textile forms of dry-contact electrodes.

3.1.2.3 *Camera-based Photoplethysmogram*

The cbPPG represents an opportunity to measure the PPG, i.e. time-variant changes of the cardiac volume flow in conceptually contact-less fashion. Additionally, it offers the acquisition of two-dimensional information. As utilized in the PPG concept, the basic idea is to measure the light radiated from illuminated tissue using an image sensor [242]. Figure 10 illustrates the basic recording principle.

The cbPPG concept originally denoted as photoplethysmography imaging (PPGI) was first described 1996 in a patent application by Vladimir Blažek and others [29] and later on taken up by his group members in 2000 and 2002 [117, 295]. It utilizes polychromatic il-

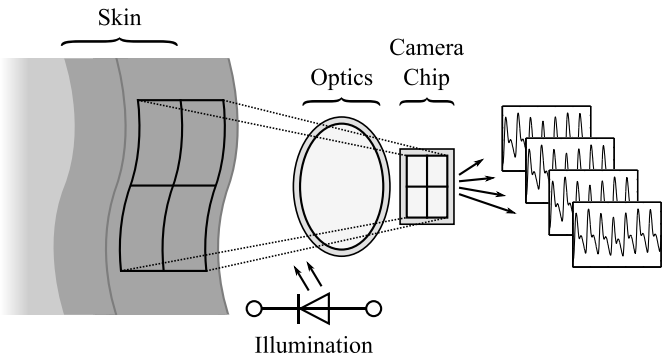

Figure 10: Basic recording principle for optical measurement of the cardiac volume flow by camera-based photoplethysmography.

lumination and an actively cooled charge-coupled device (CCD) sensor for two-dimensional assessment of the dermal blood perfusion at human limbs. Venous blood perfusion and its functional test [29, 295] as well as wound healing [117] was addressed by the pioneer researchers. The relationship between arterial hemodynamics, also accessible by this technique, and the heart synchronous blood volume pulse and heart frequency, respectively, was additionally outlined by the group.

A growing community of researchers has taken up the cbPPG technology since than. Following its introduction, other pioneering works continued to use high-quality experimental/industrial cameras [114, 118, 289] based on CCD and complementary metal-oxide-semiconductor (CMOS) technology. Such cameras were also utilized later on in clinical investigations [2, 217, 251, 302] and other rather fundamental research questions [93, 95, 137, 138, 147, 232]. Simple webcams, either laptop-integrated [55, 212, 213] or external [63, 79, 86, 112, 166], soon augmented the scope of suitable measurement technology. Comparisons between webcams and high-sensitivity CMOS camera showed comparable performance on simpler cbPPG post-processing tasks like heart and breathing rate estimation [231, 244]. Standard consumer level cameras like camcorders [113, 246], digital compact [265] or single-lens reflex cameras [181] have also been used. In addition, the application of cell phone cameras has been examined [134, 153, 184, 214, 229]. A special application utilized a camera integrated into a mobile service robot [241]. The measurement scenarios applied to cbPPG have been rather limited and restricted. The most typical scenario involve healthy subjects sitting at a table including the measurement technique which acquires video data from parts of the upper body and head in a resting condition [55, 63, 93, 95, 112, 113, 147, 153, 166, 174, 181, 213, 231, 244, 246, 252, 265, 273, 307]. Less frequent, larger subjects' movement (i.e. head movement) is allowed or forced according to a protocol in such sitting scenarios [77, 79, 86, 241]. Another typical scenario comprises video data acquisition from parts of the limbs (e.g. palm, arm, foot) [34, 42, 114, 117, 118, 138, 192, 245, 289, 295]. Actual motion scenarios involving subjects using fitness devices like bike,stepper or treadmill are rare and conducted mostly with few subjects [95, 243, 275]. Challenging scenarios like driver monitoring [30, 215, 292, 305] are rarely addressed

and, if at all, with very few subjects. Despite monitoring healthy subjects, the clinical usage of cbPPG finds applications in patients with atrial fibrillation [62, 184], general cardiovascular patients [217], dialysis patients [251], migraine patients [302], and neonates [2].

The basic components of the cbPPG technology consists of a camera sensor chip and optics. Typical sensor types comprise pixels of CCD or CMOS technology. Part of the sensor is also a color filter, which controls the wavelengths gathered at each sensor pixel. Horizontal (e.g. Bayer filter, RGBE) and vertical (e.g. Foveon X3) structures of wavelength separation are available. Each single pixel of a gathered image typically consists of the red, green, and blue (RGB) color channels, each color channel covering a certain range of wavelengths of the respective color. Orange or cyan color channels can also be found in the cbPPG context [181] as well as monochrome cameras [243]. The quantization of each color value for each pixel is described by the bit depth per color (8 bit [265], 10 bit [163], 12 bit [141] or 14 bit [295]). A sensor comprises an absolute number of pixels, which can be combined on the sensor side referred to as binning [295]. The optics of a cbPPG system include adjustment possibilities by aperture, shutter speed (length of exposure), focal length, and the use of additional spectral and other optical filters limiting the bandwidth [86] or polarization [192] of the measured light. [182]

Many cbPPG applications do not make use of spezialized illumination but instead work with ambient lightning conditions [182]. Thereby, the accomplishments of measurements at ambient light came along the first applications of consumer level cameras for cbPPG of Takano *et al.* [246] and Verkruysse *et al.* [265]. In the lightning context, Sun *et al.* [244] also reported, that the pulsatile (AC) component of the volume pulse measured by cbPPG shows no correlation with the ambient light intensity while the DC component does. However, lightning variations can induce severe distortions in cbPPG. Strategies to cope with such interferences aim at separately measuring the ambient light for later subtraction to obtain an illumination rectified cbPPG [10, 168]. Such cbPPG applications, which comprise active illumination use LEDs of green wavelength [136, 138] or red [10], respectively, both red and NIR [118, 289, 295] wavelength or even diffuse halogen [9] and full spectrum bulb illumination [77].

Despite each single camera sensor pixel can deliver a cbPPG signal (given a technically adequate illumination and exposure and a measurement at a suitable skin region), the consolidation of multiple pixels by averaging is known to improve the signal-to-noise ratio (SNR) of the cbPPG [243, 265]. The amount of spatially distributed pixels, typically containing suitable regions for gathering the cardiac pulse, is referred to as region of interest (ROI). The cbPPG further is extracted by only considering (i.e. typically averaging [252]) the pixel values inside the ROI for each frame. Thereby, single ROIs [212] or the usage of multiple ROIs at once [181, 252] are considered. The ROI selection besides the measured wavelength is critical due to different dominance of the underlying effects and according

waveforms measured at different sites of the skin, i.e. the blood volume pulse (BVP) or the ballistocardiogram (BCG) [191, 232, 257].

The BVP is mostly covered by conventional PPG theory underlying an altering amount of blood in the measured volume (additional theories had been formulated by Kamshilin *et al.* [138] and Sidorov *et al.* [234]). Thereby, it is worth noting that the cbPPG is expected to measure light reflected from less penetration depth compared to conventional PPG. I.e., the PPG signal is mainly composed by processes of the arterial vasculature, whereas the cbPPG serves a mixture of processes within the upper skin layers. BCG effects, however, are particularly characteristic for cbPPG. One distinguishes between global BCG effects, i.e. the movement of the measurement region due to a distant effect (e.g. head movements while blood ejects into the aorta), and local effects (e.g. the movement of the measurement area due to a pulsating artery below the measurement area). [304]

3.2 PROCESSING OF MULTICHANNEL BIOSIGNAL RECORDINGS

Unobtrusive and minimum-contact/contact-less biosignal measurement techniques as the above described tECG, cECG and cbPPG offer increased measurement comfort and widespread measurement scenarios. However, these techniques are susceptible to disturbances (i.e. they show low SNR). Compared to the fixed contact sensors used in conventional ECG and PPG, these disturbances are likely to arise from relative movements between sensor and subject for instance as motion artifacts. Biosignals from single sensors thus contain episodes incorporating no valid or only hidden information. One approach to overcome this problem is the fusion of biosignals obtained from multiple sensors and/or modalities, where all sensor measurements of interest originate from the same mutual source (i.e. the heart). [15]

Multi-sensor data fusion aims at improving four major performance categories of data usage. The data representation is improved either by increasing the degree of abstraction or increasing the level of detail. Second and third, the certainty of data as well as the accuracy (standard deviation) is improved. Fourth, increased redundancy and concordance improves the coverage (completeness). [190, p.4f]

Data fusion can be handled using three basic types of fusion architecture. If the original sensor data consists of observations of the same or similar physical quantity (commensurate data), which also can be properly associated and aligned with each other (e.g. temporal alignment of signals, spatial alignment of images), the raw sensor data can be fused. This approach is also termed data-level fusion. If the sensor fusion addresses non-commensurate data, e.g. ECG and PPG showing differing morphology and relative peak locations while exhibiting equal beat-to-beat interval [15], other fusion architectures have to be applied. Feature-level fusion addresses the combination of several feature vectors extracted from multiple sensor data to a single concatenated feature vector for further

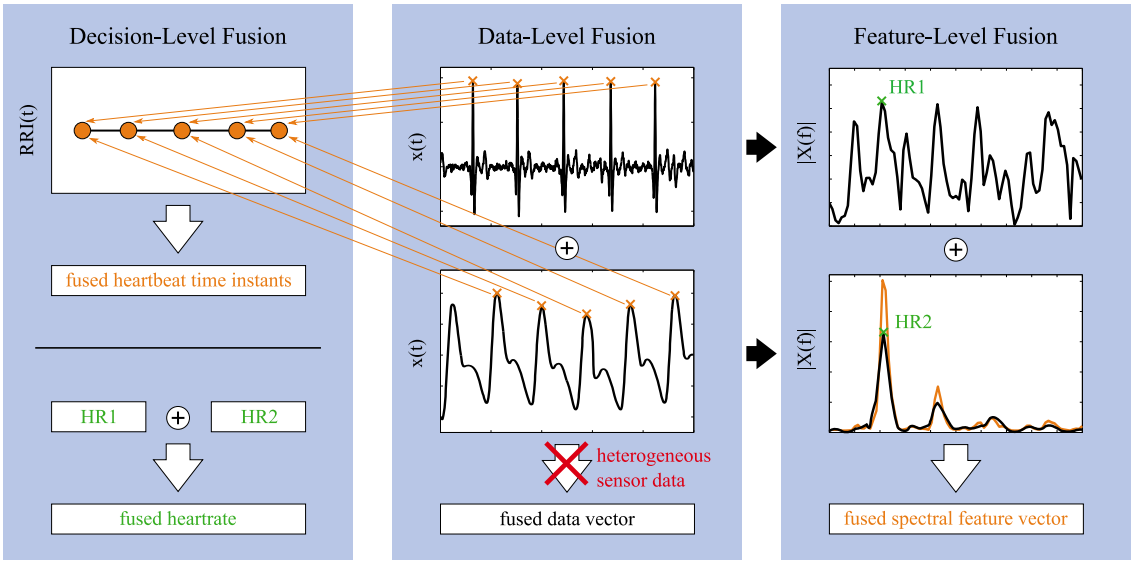

Figure 11: Exemplary data fusion strategies for biosignal processing: The cECG and cbPPG signal (middle box) aren't suitable for data-level fusion because of their noncommensurate nature. Feature-level fusion (right box) e.g. by calculating the cross spectrum out of the single spectra |X(f)| is possible (see orange curve). Decision-level fusion (left box) combines estimates of heartbeats time instants from both signals or heartrate estimates from both spectra.

processing. Decision-level fusion combines preliminary estimates of an entity's location or attribute. [96],[97, p.21f]

Figure 11 exemplarily depicts fusion architectures in the context of cardiac biosignal processing. Whereas data-level fusion is appropriate only for homogeneous sensor data as measured by redundant and equivalent sensor networks (e.g. multichannel cECG), heterogeneous data as measured by applying different measurement principles (capacitively, optical) can be fused by feature-level and decision-level fusion. Thereby, target decisions of a heterogeneous biosignal fusion process are e.g. a robust heartrate estimate [278] or single most accurate heartbeat time instants [239] giving a time series of beat-to-beat-intervals for analyzing heartrate variability (HRV) [3]. Because of cardiac biosignals' periodic nature, e.g. the frequency domain gives an appropriate feature space for either estimating preliminary decisions (e.g. heartrates) or enabling feature-level fusion e.g. using the cross spectrum [23]. Feature-level and decision-level fusion naturally applies also to features and decisions derived from homogeneous sensor data.

3.2.1 *Feature-Level Fusion*

The possibilities of fusing multichannel biosignal data on the feature-level are diverse due to a practically unlimited feature space. However, its application to improve the robustness of target biosignal processing decisions (e.g. heartrates, beat-to-beat intervals) is less common. Yet, since the Fourier spectrum presents a widespread feature space for

biosignal analysis, the cross spectrum serves its data fusion counterpart. Analogous to the spectral density $\mathrm{S}(f)$ which is given by the Fourier transform of the auto-correlation function, the cross spectral density $\mathrm{S}_{xy}(f)$ is defined by the Fourier transform of the cross-covariance function [158]. The cross covariance thereby is the second moment of the joint probability density of the variables. In this context, the coherence $\mathrm{Coh}_{xy}(f)$, which involves the cross spectral density is useful if spectral components between two signals are significantly correlated [196]:

$$\mathrm{Coh}_{xy}(f) = \frac{|\mathrm{S}_{xy}(f)|^2}{\mathrm{S}_x(f) \cdot \mathrm{S}_y(f)} \tag{4}$$

Cross spectra have been applied for assessing (patho-)physiological relation and interaction between heterogeneous biosignals [16, 23]. The application of averaging spectral information is presented in [148] where multichannel logarithmic spectra are averaged for the calculation of the average cepstrum.

3.2.2 *Decision-Level Fusion*

Common concepts of decision-level fusion involve simple voting techniques, probabilistic fusion (i.e. Bayes fusion) and evidential belief reasoning (e.g. Dempster-Shafer fusion) [97, p.21],[142] and are widely applied to biosignal processing. Besides this methodological classification, Šprager *et al.* [239] categorized decision-level fusion for biosignal processing into multichannel (multiple homogeneous sensors), multisensor (multiple heterogeneous sensors, e.g. [56],[32]) and multimethod (one sensor, multiple extraction methods) fusion.

3.2.2.1 *Voting Techniques*

Voting techniques aim at the selection of a single best sensor among multiple sensors. A selection of a single sensor can be based, e.g., on a sensor quality index [278]. Together with the arithmetic mean, the median also serves a simple and frequently applied selector under the assumption, that measurements (e.g. heartrates) in the considered window are samples of the same measurement level [298]. Orphanidou *et al.* [202] applied a voting to judge amongst respiration-related poles of auto-regressive models from different measurements and subsequently selected the pole with highest magnitude. A "hybrid" median involving recent and previous measurements (temporal) from different sensors (spatial) and previous estimates was applied [298]. A weighted average that negatively judges high relative sensor value innovation between two sensors was introduced by Tarassenko *et al.* [250] and further developed by a signal-quality scaled innovation judgment [167]. Weighted decisions of separately measured atrial and ventricular activity were fused in [106]. Physiological limits and prior average heartrate estimates were used for exclusion of RRIs in a multisensor setting [90].

3.2.2.2 *Bayesian Inference*

Bayesian inference treats all quantities as random variables characterized by a probability distribution. Thereby, conditional probability distributions model the likelihood of observed data given a hypothesis (e.g. a certain heartrate) and further take into account (non-)informative priors, i.e. the probability of the hypothesis. One obtains a posterior probability distribution of the hypothesis given the data, which facilitates the maximum a-posterior (MAP) approach aiming at the most probable posterior probability and hypothesis, respectively. [43],[190, p.115ff]

The according formalism applicable to digital biosignal processing and its k discrete-time observations comprises

y_k : the actual state (e.g. true heartrate) at time k
x_k : the observation of the state (e.g. measured heartrate) at time k
X_k : all observations of the state $\{x_1, x_2, \ldots, x_k\}$ up to time k.

The notation P(A|B), the probability of event A given event B, and, i.e. P(A, B), the probability of two coincident events A and B gives the posterior probability of a single sensor by using Bayes' rule

$$P(y_k|X_k) = P(y_k|x_k, X_{k-1}) = \frac{\overbrace{P(x_k|y_k, X_{k-1})}^{\text{likelihood}} \cdot \overbrace{P(y_k|X_{k-1})}^{\text{prior probability}}}{\underbrace{P(x_k|X_{k-1})}_{\text{normalization}}} \tag{5}$$

where the normalization can be neglected in relative comparisons of hypothesis probabilities. [43]

The particular solution needs to take into account the respective (in-)dependence of multiple sensors and single measurements x_k [50] and further needs to select appropriate probability distributions to be modeled by the assessed data [190, p.119ff].

While applying the Bayesian framework to biosignal processing, a MAP estimate not necessarily comes along with determining the state of highest likelihood because of the influence of prior probabilities. However, a maximum likelihood estimator (MLE), which aims at the highest probability of observing certain data given a state hypothesis, becomes relevant for fusing annotations (e.g. beat-to-beat intervals, heartbeat time instants) with help of features as signal quality or precision measures. The expectation-maximization (EM) algorithm by Dempster *et al.* [69] is one solution that facilitates a weighted judgment of annotations by multivariate regression using aforementioned features and can be applied independently [309].

Informative priors for fusing homogeneous multichannel biosignals have been proposed by [306] assessing the similarity of QRS morphology and [299] evaluating the peak height and their intervals for calculating a channel priority. The Bayesian inference was adapted

to multichannel heartrate fusion (MAP) by Wartzek *et al.* [278] by modeling prior probability distribution using the prior fusion result and estimating the likelihood of the recent heartrate estimates given a time frame of prior measurements.

A sophisticated multisensor fusion approach comparable to Bayesian inference was proposed by Ebrahim *et al.* [75] and Feldman *et al.* [78]. Physiological limits were used to eliminate heartrates. The consensus of the remaining heartrates (sensors against each other, sensors against past fused heartrate) was evaluated to select a maximum likelihood hypothesis (which sensor(s) contain reliable heartrates respectively, the past prediction should be further used) by assessing Gaussian-modeled errors. Accordingly, selected heartrates and their prediction is fused by a Kalman filter (KF) acting as a weighted averager.

Multimethod fusion comprises strategies to combine multiple annotations of different human (e.g. addressing a consensus among multiple expert annotations) or technical annotations derived from biosignal processing on the same quantity. An expectation maximization approach evaluating the human annotator precision by linear regression of the annotation using a feature vector (containing signal quality and heartrate features) was presented by Zhu *et al.* [309]. Šprager *et al.* [239] proposed a MLE of independent detectors moreover using priors from physiological limits and prior RRI together with detection characteristics of each detector to derive a MAP approach for heartbeat annotations from multiple detectors.

3.2.2.3 *Dempster-Shafer Fusion*

Compared to Bayesian inference which is based on the concept of probabilities, the Dempster-Shafer fusion still addresses the weighting of sensors but by so-called "masses" m measuring the degree of belief. The Dempster-Shafer theory introduces a state "unknown" combining alternative states and thus defining a (momentary) non-zero intersection between states. Masses can be combined by Dempster's rule of combination hereafter given for three abstract states A,B and C and masses associated with the recent sensor measurement m_s and masses from prior existing evidence m_o:

$$m(C) = \frac{\overbrace{\sum_{\mathrm{A}\cap\mathrm{B}=\mathrm{C}} [m_s(\mathrm{A}) \cdot m_o(\mathrm{B})]}^{\text{joint belief of sources}}}{1 - \underbrace{\sum_{\mathrm{A}\cap\mathrm{B}=\varnothing} [m_s(\mathrm{A}) \cdot m_o(\mathrm{B})]}_{\text{conflict between sources}}}. \tag{6}$$

Accordingly, the numerator involves mass products associated with the target state C as well as combinations of C with "unknown", whereas the denominator involves mass products of definite (non-"unknown") and non-equal states. Recent and prior information sources (measurement masses m_s and m_o) can also be replaced by two simultaneously measuring sensors or can be extended to a larger number of sensors. [43, 142]

3.2.3 *Data-Level Fusion*

Data-level fusion gives the most accurate fusion technique for proper sensor association and alignment [96]. This is because it aims at improving the quality and reliability of the data before any feature or decision is derived. Because the fused data in this context is typically measured by spatially distributed sensors (e.g. pixels), the term spatial data fusion is also used. In classical data fusion literature, which is dominated by military applications, data-level fusion, if considered at all, mostly deals with fusion of image data on the pixel-level. The fusion of image data is also important for the large variety of medical imaging techniques [65, 177]. [97, ch.4]

However, considering the redundant multichannel measurement of biosignals (as e.g. cECG and tECG) in the data fusion context, data-level fusion became an important signal processing strategy for combining multichannel data. Correspondingly, Luo *et al.* [175] define a "*signal-level fusion*" as a "*combination of the signals of a group of sensors with the objective of providing a signal that is usually of the same form as the original signals but of greater quality*". Methods for data-level-fusion comprise the weighted average as simplest method as well as the Kalman filter (KF) which estimates optimal weights in a statistical sense. The KF is designed to combine redundant information provided by a group of sensors not only on the signal level under the assumption (given a two-sensor example) that discrete measurements $x_1(k)$ and $x_2(k)$ are constituted by $y(k)$, the discrete state of interest and $n_1(k)$ and $n_2(k)$, independent zero-mean Gaussian random variables:

$$x_1(k) = y(k) + n_1(k) \quad \text{and} \quad x_2(k) = y(k) + n_2(k) \tag{7}$$

Thus, the system is assumed that it can be linearly modeled (otherwise the extended Kalman filter serves an alternative). Based on a state-space representation of the underlying system (see equation (9)), an optimal combination $\hat{y}(k)$ of the state prediction $y(k|k-1)$ and its recent measurement $x(k)$ is given by

$$\hat{y}(k) = y(k|k-1) + \mathbf{K}(k)[x(k) - \mathbf{H}(k) \cdot y(k|k-1)] \tag{8}$$

$$y(k+1|k) = \mathbf{F}(k) \cdot \hat{y}(k) + \mathbf{B}(k) \cdot u(k) \tag{9}$$

with $\mathbf{K}$ the Kalman gain assessing the noise influences (process noise, measurement noise) and its covariances, $\mathbf{H}$ the measurement matrix transforming the predicted state into the measurement space of x, $\mathbf{F}$ the state transition matrix, and $\mathbf{B}$ together with u the deterministic influence of external inputs on the state y. This framework can easily be applied to data-level fusion of homogeneous data e.g. by considering one sensor the prediction and another the measurement [175, p.44]. For linear systems and also strictly speaking decision-level fusion of e.g. heartrates [12], the KF provides straightforward estimates of

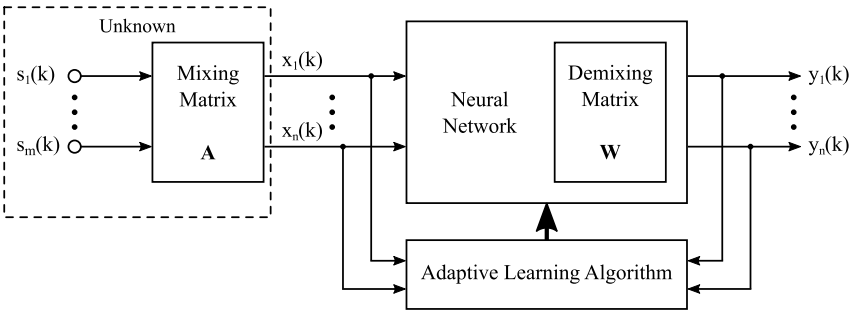

Figure 12: Schematic Blind Source Separation. Redrawn and modified from [58, Fig. 1].

statistically weighted data. However, considering actual data-level fusion for nonlinear biosignals as the ECG [59, p.171ff], applying the KF requires extensive dynamic modeling of the underlying biosignals [225],[269]. Based on the model incorporated by equation (7), the idea of consensus sensors (identifying sensors measuring the same quantity) is also applied to data-level fusion by Bayesian estimation [176] and statistical decision theory [183]. In this context, it can be shown, that adding more redundant sensors improves the (data-level) fusion result [219]. [175]

With respect to the aforementioned definition of data-level fusion also more recent signal processing techniques as Blind Source Separation (BSS) can be conciliated. These techniques are less-restrictive on assumptions regarding noise distribution and also require far less modeling on the source signals y while maintaining the assumption [219] of statistical independence between noise and noise-free measurements. In this context, noise sources are considered as another equivalent state vectors y_i i.e. as independent and separable components [49] such that the model underlying equation (7) is extended to a multitude of weighted (w_i) states/sources $x = \sum_i w_i \cdot y_i$. In the following, BSS techniques will be considered in more detail.

3.3 BLIND SOURCE SEPARATION

The blind separation of sources tackles the problem of estimating and separating primary sources (original input signals) from an array of sensors and their measurements without knowing the transmission channels, i.e. the mapping of original sources onto the observable mixtures of sources. The term "blind" indicates the unsupervised and self-normalizing nature of this procedure. As depicted in Figure 12, the problem is addressed by developing a neural network together with an adaptive learning algorithm for reversing the unknown mixing process constituting the i-th observed measurement $x_i(k)$ out of m weighted original sources $s_j(k)$

$$x_i(k) = \sum_{j=1}^{m} a_{ij} \cdot s_j(k) \tag{10}$$

$$\mathbf{x} = \mathbf{A} \cdot \mathbf{s} \tag{11}$$

$$\mathbf{s} \simeq \mathbf{y} = \mathbf{W} \cdot \mathbf{x} \simeq \mathbf{A}^{-1} \cdot \mathbf{x} \tag{12}$$

with $\mathbf{y} = [y_1(k), y_2(k), \ldots, y_n(k)]^T$ the estimate of the original source signals. In this context, one distinguishes between Blind Separation or Blind Source Separation (BSS) and Blind Signal Separation, respectively, whose object are the separated sources s and Blind Identification whose object is to estimate the mixing process $\mathbf{A}$. Blind Identification thereby addresses Blind Beamforming for estimating the location of sources or their directional vectors, respectively. [39],[58],[124]

Equation (10) and (11) in this context is a simplification of the actual mixing process $\mathbf{x}(k) = \mathbf{f}\{\mathbf{s}(k)\} + \mathbf{n}(k)$ with $\mathbf{f}$ any unknown function and $\mathbf{n}$ additive sensor noise in order to generate a more tractable (linear) separation problem. [131]

Separation techniques dealing with more complex mixing processes allowing sources to differently enter the mixing process at multiple delays are termed Blind Deconvolution or convolutive BSS [210]. This links to BSS based on signals' state space representation by delay reconstruction [59, p.181].

Typical Blind Source Separation algorithms attempt to identify an independent set of vectors/axes onto which the measured data is projected to fulfill the transformation's target properties $\mathbf{y}$ being intrinsically uncorrelated (Principal Component Analysis) or statistically independent (Independent Component Analysis). [59, p.149]

3.3.1 *Principle Component Analysis*

3.3.1.1 *Principle Component Analysis*

PCA is a transformation technique which decorrelates data by its projection onto orthogonal axes, thus ensuring a diagonal covariance matrix $\mathbf{Cov}(\mathbf{y}) = E\{\mathbf{y}\mathbf{y}^T\} - \mu_y \mu_y^T$. Thereby, the observed multivariate data $\mathbf{x} = [x_1(k), x_2(k), \ldots, x_n(k)]^T$ with $k \in [1, K]$ can be decomposed by singular value decomposition (SVD)

$$\mathbf{x}^T = \mathbf{U} \cdot \mathbf{\Lambda} \cdot \mathbf{\Gamma}^T \tag{13}$$

with $\mathbf{\Lambda}$ a non-square $K \times n$ matrix with zero entries except the leading diagonal with $\mathbf{\Lambda}_{ii} = \sqrt{\lambda_i}$ the square roots of the eigenvalues λ_i (i.e. the singular values) of the covariance matrix $\mathbf{Cov}(\mathbf{x})$ arranged in descending order of their magnitude, also $\mathbf{\Gamma}$ a $n \times n$ matrix

of column vectors representing the eigenvectors γ_i of $\mathbf{Cov}(\mathbf{x})$ and, $\mathbf{U}$ a $K \times K$ matrix of projections of $\mathbf{x}^T$ onto the eigenvectors. [59, p.149]

Noise-reduction in the measurement domain ($\mathbf{x}$) using the above-described SVD is realized by truncating the decomposition (13) by retaining only the most significant eigenvectors. Moreover, Principal Component Analysis (PCA) can be reformulated to resemble a neural network problem to solve SVD by a multilayer perceptron [59, p.151f].

Alternatively, the covariance matrix $\mathbf{Cov}(\mathbf{x})$ can be decomposed by eigendecomposition (or eigenvalue decomposition (EVD)) into

$$\mathbf{Cov}(\mathbf{x}) = \mathbf{\Gamma} \cdot \mathbf{D} \cdot \mathbf{\Gamma}^T \tag{14}$$

with $\mathbf{D}$ a square $n \times n$ diagonal matrix of eigenvalues λ_i sorted in descending order and γ_i of $\mathbf{\Gamma}$ having unit norm (for uniqueness of the solution [60]). Also, EVD can by reformulated to be solved by neural networks [58].

Finally, the source signal estimates $\mathbf{y}$ of PCA are obtained by setting $\mathbf{W} = \mathbf{\Gamma}^T$ which diagonalizes the covariance matrix $\mathbf{Cov}(\mathbf{y})$ [58]

$$\mathbf{y}_{PCA} = \mathbf{\Gamma}^T \cdot \mathbf{x}. \tag{15}$$

Thereby, PCA projects the data on an orthogonal basis and retains the maximum amount of variance among all linear projections inside the projected space [49].

3.3.1.2 *Whitening*

Whitening is a special case of PCA which ensures the covariance matrix of $\mathbf{y}$ equaling the identity matrix $\mathbf{Cov}(\mathbf{y}) = \mathbf{I}$. This realizes a "white" vector $\mathbf{y}$ being intrinsically uncorrelated and each variable y_i having unit variance. Using the EVD as described above (equation (14)), whitened source signal estimates y can be obtained by [124]

$$\mathbf{y}_{White} = \mathbf{\Gamma} \cdot \mathbf{D}^{-1/2} \cdot \mathbf{\Gamma}^T \cdot \mathbf{x}. \tag{16}$$

3.3.1.3 *Time-Structure Based Methods*

Time-structure based methods capture temporal consequences of the relations between independent signals together with the spatial relations both arising from independence between separated sources s_i. Whereas common PCA or Whitening only covers spatial decorrelation between sensors/sources, this approach extends the decorrelation to a spatio-temporal decorrelation. Temporal structure which is relevant for periodic signals as biomedical signals is covered accordingly and can improve the BSS performance [130]. The temporal dependency is addressed by assessing correlation at different time lags τ. Thus, a

stack of covariance matrices $\mathbf{Cov}^{\tau}(\mathbf{x})$ with respect to the time lag τ is formed and a joint diagonalizer $\mathbf{W}$ is searched

$$\mathbf{Cov}^{\tau}(\mathbf{y}) = \mathbf{W} \cdot \mathbf{Cov}^{\tau}(\mathbf{x}) \cdot \mathbf{W}^{T} \tag{17}$$

which optimizes the overall diagonality of the stack $\mathbf{Cov}^{\tau}(\mathbf{y})$ for instance by minimizing the sum of squared off-diagonal elements. The time-delayed covariance matrix is of the form $\mathbf{Cov}^{\tau}(\mathbf{x}) = E\{\mathbf{x}(k)\mathbf{x}^{T}(k-\tau)\}$. [131]

Further approaches introduce a symmetric stack-metric $\mathbf{C}(k_i, \tau_j)$ of the i-th (non-overlapping) time window and the j-th time lag for joint diagonalization [53]:

$$\mathbf{Cov}_x(k_i, \tau_j) = \frac{1}{n} \sum_{k=k_i}^{k_i+n-1} \mathbf{x}(k)\mathbf{x}^{T}(k-\tau_j) \tag{18}$$

$$\mathbf{C}(k_i, \tau_j) = \frac{1}{2}[\mathbf{Cov}_x(k_i, \tau_j) + \mathbf{Cov}_x^{T}(k_i, \tau_j)] \tag{19}$$

Methods for solving the joint diagonalization problem include the usage of Jacobi angles [40, 311] as well as joint approximate diagonalization by MLE [211] or least-squares optimization [312]. A positive effect of joint diagonalization is the removal of the influence of white noise on the diagonalization of a multisensor measurement such that a robust whitening can be derived [53].

The joint diagonalization of time-lagged covariance matrices is also known as second-order blind identification (SOBI) by Belouchrani *et al.* [26]. Despite basing the joint diagonalization on pre-whitened inputs, Belouchrani further defines conditions to select time lags τ in order to obtain a unique solution for the demixing matrix $\mathbf{W}$. Namely, a set of non-zero time lags τ should be selected such that $\mathbf{W} \cdot \mathbf{Cov}^{\tau}(\mathbf{x}) \cdot \mathbf{W}^{T} = \mathbf{Diag}^{\tau}(d_1, \ldots, d_n)$ suffices $d_i \neq d_j$ for $\forall\, 1 \leq i \neq j \leq n$ for all τ.

The appropriate choice of the number of time lags τ can be addressed e.g. by fitting an autoregressive model to each channel [131] or assessing the autocorrelation function [21].

Other methods based on time-structure which do not utilize temporal correlations as described above, work with cross-correlations between frequency sub-bands or joint diagonalization in cross time-frequency distributions of multiple signals. [131]

3.3.2 *Independent Component Analysis*

Independent Component Analysis (ICA) is a transformation technique aiming at statistical independence between outputs $\mathbf{y}$ such that the joint probability distribution function (pdf) $p(\mathbf{y}) = p(y_1, y_2, \dots y_n)$ of the source estimates $\mathbf{y}$ is factorizable by its marginal pdfs [124]:

$$p(\mathbf{y}) = \prod_{i=1}^{n} p(y_i) \tag{20}$$

Because the joint pdf of two (or more) Gaussian random variables is completely symmetric and thus, independent of any orthogonal transformation of the random variable, the applicability of this principle (i.e. ICA) is restricted to random variables $\mathbf{y}$ containing at most one Gaussian variable y_i. Otherwise, the problem would lack the identifiability of the problem's solution [124]. Another important restriction that applies to ICA is the assumption on uncorrelated (i.e. white) and thus orthogonal outputs $y_i \in \mathbf{y}$. This guarantees an unique solution such that each independent component is only estimated once.

While the algorithmic principle for solving this problem was already introduced in 1986 by Herault and Jutten [105], the term Independent Component Analysis was introduced by Jutten and Herault in the first place in 1991 [135]. Since then, typical algorithms utilize measures derived from information theory to judge statistical independence. These measures are essentially based on mutual information or entropy [296], respectively. A widely applied key to statistical independence thereby is the non-Gaussianity of the ICA output which derives as a consequence of the central limiting theorem. Accordingly, sums of independent random variables rather tend toward Gaussian distributions [124].

Whereas the amount of algorithms and their variations proposed to solve the ICA problem are manifold, we restrict the following descriptions to fundamental ICA solutions and such which are commonly applied to biomedical signal processing.

3.3.2.1 *Projection Pursuit*

Since Independent Component Analysis is subject to blindly identifying the underlying independent components of multivariate data, Projection Pursuit can be regarded as first approach towards the solution of an ICA separation problem. Projection Pursuit was designed to determine low-dimensional projections of multivariate data in order to reveal salient features of the high-dimensional data. These low-dimensional projections can linearly be obtained by the rotation of the coordinate system/axes and data projection (visualization) onto the planes/axes of the new coordinate system. [84]

The problem of Projection Pursuit now is to identify interesting projections among the large number of possible projections. Whereas Friedman *et al.* [84] first developed an index characterizing projections following the idea of visual clustering (small inter-point distances together with large overall data spread), which is rather applicable to process

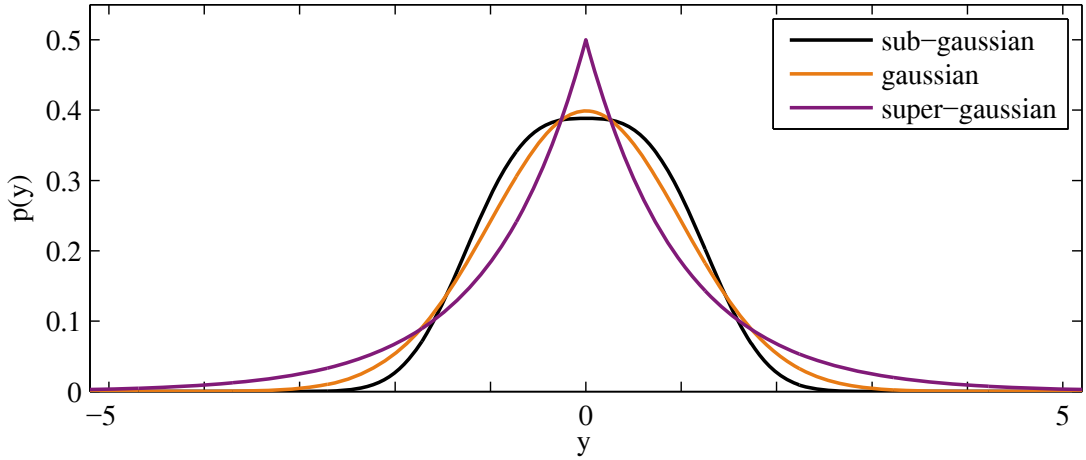

Figure 13: Exemplary (sub-/super-)gaussian probability densities $p(y)$ drawn from the exponential power family of density functions $p(y) = c_1 \cdot \exp(c_2 \cdot |y|^\alpha)$ with c_1, c_2 normalization constants and α the parameter to define the (sub-/super-)gaussian shape [123].

point clouds than biosignals as ECGs, Huber [116] and Friedman [83] afterwards proposed the idea of using non-Gaussianity which later on served as a major concept for addressing statistical independence [60]. In the context of Projection Pursuit, these projections were considered least interesting, which show normal (Gaussian) probability distribution of the projected data. This is because sums tend to be normally distributed such that most linear combinations (views on the data based on the rotated coordinate system) will be approximately normally distributed. Given fixed variance, normal distributions also have the maximum information, which is tried to be separated and thus, minimized by interesting projections. [83, 116]

Non-Gaussianity in a probability distribution is tractable via non-normal deviations in the tails (e.g. heavy tails measurable by cumulants) or even the main body and center of the distribution. Typical non-Gaussian distributions as super- and sub-Gaussian distributions relevant for biosignals [222] show characteristic behavior with respect to both distributions' tail and center. Whereas super-Gaussian distributions exhibit sharp and narrower centers together with stronger pronounced tails, sub-Gaussian distributions show a larger mass proportion concentrated in their center compared to normal distributions [162] (see Fig. 13 for exemplary probability densities). Friedman [83] developed a projection index focusing on the main body of the distribution. After Whitening of the input data, projections (ensuring $\mathbf{w}_n \mathbf{w}_n^T = 1$)

$$z_n = \mathbf{w}_n \cdot \mathbf{y}_{White} \tag{21}$$

are transformed by the cumulative distribution function (cdf) of a normal distribution Φ and scaled to the interval [-1,1]

$$\Phi(z_n) = \frac{1}{\sqrt{2\pi}} \int_{-\infty}^{t=z_n} \mathrm{e}^{-1/2t^2} \, \mathrm{d}t \tag{22}$$

$$R_n = 2\Phi(z_n) - 1 \tag{23}$$

A standard normal distributed transformation z_n will cause a uniform distributed R_n. Measuring the non-uniformity of R_n corresponds to a measure of non-Gaussianity of z_n. The non-uniformity is measured by the integral-squared distance δ_u between the pdf of R_n, $p(R_n)$ and the uniform density $p_u = \frac{1}{2}$

$$\delta_u = \int_{-1}^{1} [\, p(R_n) - \frac{1}{2} \,]^2 \mathrm{d}R \tag{24}$$

The probability density $p(R_n)$ is measured by expanding the density into Legendre polynomials P_j up to J terms which gives the projection index $I(\mathbf{w}_n)$

$$I(\mathbf{w}_n) = \sum_{j=1}^{J} (2j+1) E\{P_j(R_n)\}^2 \tag{25}$$

$$I(\mathbf{w}_n) = \frac{1}{2} \sum_{j=1}^{J} (2j+1) \left[\frac{1}{N} \sum_{k=1}^{N} P_j(R_n(k)) \right]^2 \tag{26}$$

The obtained projection index is subject to optimization (maximization) which is addressed by computing $\frac{\delta I}{\delta \mathbf{w}_n}$. Moreover, Projection Pursuit requires a removal of the obtained structure from the data in order to be able to compute another interesting projection. This removal is realized by transforming the obtained projection z_n inside the whitened data $\mathbf{y}_{White} \rightarrow \mathbf{y}'_{White}$ such that this particular projection becomes standard normal distributed and the newly computed projection index optimization will neglect the prior solution. [83]

3.3.2.2 *Minimum Mutual Information*

The ICA algorithm proposed by Comon [60] is based on minimizing the mutual information of the output components. Mutual information is invariant under transformations like scaling and permutation as well as component-wise monotonic, nonlinear transforms [296]. The mutual information thereby is derived by evaluating both sides of equation (20) which defines statistical independence. Specifically, assessing the difference of both

pdf components $p(\mathbf{y})$ and $\prod_i p(y_i)$ becomes possible by the *Kullback-Leibler* divergence, namely the divergence between two probability densities $p_1(\mathbf{u})$ and $p_2(\mathbf{u})$:

$$\delta(p_1(\mathbf{u}), p_2(\mathbf{u})) = \int p_1(\mathbf{u}) \log \frac{p_1(\mathbf{u})}{p_2(\mathbf{u})} \, \mathrm{d}\mathbf{u}. \tag{27}$$

This gives the mutual information $I(\mathbf{y})$ of the ICA output components $\mathbf{y}$:

$$I(\mathbf{y}) = \int p(\mathbf{y}) \log \frac{p(\mathbf{y})}{\prod_i p(y_i)} \, \mathrm{d}\mathbf{y} \tag{28}$$

which only vanishes if the output components of $\mathbf{y}$ are statistically independent. Comon [60] derives the mutual information and *Kullback-Leibler* divergence, respectively, by using higher-order cumulants. Accordingly, the mutual information is alternatively expressed as a function of the differential entropy $S(p(\mathbf{y}))$ or the corresponding negentropy $J(p(\mathbf{y}))$, respectively. This quantities are defined as

$$S(p(\mathbf{y})) = -\int p(\mathbf{y}) \log p(\mathbf{y}) \, \mathrm{d}\mathbf{y} \tag{29}$$

$$J(p(\mathbf{y})) = S(\phi(\mathbf{y})) - S(p(\mathbf{y})) \tag{30}$$

with $\phi(\mathbf{y})$, a gaussian pdf of same mean and variance as $\mathbf{y}$ and $S(\phi(\mathbf{y}))$ the largest of possible entropies. The decomposition of the logarithm in equation (28) together with the relation of differential entropies of an output $\mathbf{y}$ and its whitened version $\mathbf{y}_{White}$

$$S(p(\mathbf{y})) = S(p(\mathbf{y}_{White})) - \frac{1}{2} \log \det \mathbf{Cov}(\mathbf{y}) \tag{31}$$

gives the rewritten mutual information [60]

$$I(\mathbf{y}) = J(p(\mathbf{y})) - \sum_{i=1}^{n} J(p(y_i)) + \frac{1}{2} \log \frac{\prod_i \mathbf{Cov}_{ii}(\mathbf{y})}{\det \mathbf{Cov}(\mathbf{y})}. \tag{32}$$

Since pre-whitening of the mixed signals $\mathbf{x}$ or continuous whitening of the output $\mathbf{y}$, respectively, will cancel the last term of equation (32), the minimization of the mutual information will refer to maximizing the second term of the right side of this equation [123] by utilizing cumulants of orders three and four [60]. Namely, the pdfs $p(\mathbf{y})$ necessary to calculate the negentropies are expanded in neighborhood of their respective gaussian densities $\phi(\mathbf{y})$ (i.e. the term $\frac{p(\mathbf{y})}{\phi(\mathbf{y})}$ is expanded) by using *Edgeworth* expansion. Because only the second term of equation (32) depends on the de-mixing matrix $\mathbf{W}$ (for whitened output), this sum of marginal negentropies is represented by cumulant tensors as a func-

tion of $\mathbf{W}$ (see [60] section 3.1) which serves the contrast to be maximized. Comon also derives the pairwise independence which provides the relation that given $\mathbf{y} = \mathbf{C} \cdot \mathbf{s}$ with $\mathbf{C}$ an orthogonal square matrix $\mathbf{C} = \Lambda \cdot \mathbf{P}$ with Λ diagonal and $\mathbf{P}$ a permutation matrix, the output components $y_i \in \mathbf{y}$ are pairwise independent, if $\mathbf{s}$ is a matrix of independent components including at most one Gaussian component. This simplifies the computation by the fact that now, only pairwise cumulants need to be considered. Accordingly, the optimization (i.e. the calculation of $\mathbf{W}$ by contrast maximization) is conducted each using pairs of signals and their respective elements of $\mathbf{W}$. Moreover, unit variance components/-sources ensures identifiability of the solution. [60]

3.3.2.3 *FastICA*

The popular FastICA algorithm proposed by Hyvärinen [123] realizes the mutual information minimization solution to ICA (described above as proposed by Comon [60]) by replacing the cumulant-based entropy estimation with a new approximation of differential entropy [122] together with a performant optimization. Thereby, it follows the idea of addressing statistical independence by maximizing non-Gaussianity of the output components by using negentropy. Abstaining from cumulant-based estimators/contrasts compensates for the cumulant-related drawbacks of outlier-sensitivity and their limitation to tail characteristics of the respective distributions [122]. The new entropy approximation is based on the maximum entropy method, namely approximating the maximum entropy that is compatible with the measurement of the random variable. In order to measure the relevant characteristics (i.e. the pdf) of a scalar random variable u, one can estimate expectations $E\{G_i(u)\}$ of u given a test function G_i such that the information on the density $p(u)$ becomes the form

$$E\{G_i(u)\} = \int p(u) \cdot G_i(u) \, \mathrm{d}u = c_i \quad \text{for } i \in [1, n]. \tag{33}$$

Together with equation (29) it is obvious that one exactly measures the differential entropy in the case G_i equals minus the logarithmic pdf $p(u)$ of u [122, 123]. However, since the pdf typically is not known a priori in our BSS setup, equation (33) only gives an ambiguous solution because multiple densities $p(u)$ can correspond to the obtained measurements each showing different entropies. An unambiguous solution is given by the density of maximum possible entropy. Further assuming the density being near the Gaussian density $\phi(u)$, i.e. $p(u) = \phi(u)(1 + \delta(u))$ (because $\phi(u)$ itself shows the maximum entropy but we are looking for non-Gaussian densities to address statistical independence), the maximum entropy pdf is of the form

$$p(u) = \phi(u)(1 + \sum_{i=1}^{n} c_i \cdot G_i(u)) \tag{34}$$

which can be used to approximate the entropy of the output component y [122]:

$$S(y) \approx S(\phi(y)) - \frac{1}{2}\sum_{i=1}^{n} c_i^2 \tag{35}$$

Whereas multiple G_i can simultaneously be used to measure the entropy of a random variable (guidelines for assembling G_i can be found in [121–123]), FastICA typically refers to use only one single G to estimate the negentropy J_G [123] as a function of the demixing matrix $\mathbf{W}$ or one demixing-vector $\mathbf{w}$ and $y_i = \mathbf{w}^T \cdot \mathbf{x}$, respectively.

$$J_G(\mathbf{w}) = \Big[E\{G(\mathbf{w}^T \cdot \mathbf{x})\} - E\{G(\phi(\mathbf{w}^T \cdot \mathbf{x}))\}\Big]^2 \tag{36}$$

Maximizing the sum of negentropies $\sum_i J_G(\mathbf{w}_i)$ realizes the solution to minimize the mutual information as proposed by Comon [60] (see equation (32)). The optimization (maximization) of the negentropy-based contrast can be realized by common stochastic gradient descent (simplified one unit: $\mathbf{w}_{n+1} = \mathbf{w}_n - \eta \cdot \nabla J(\mathbf{w}_n)$ with η the learning rate). However, Hyvärinen also proposes a fixed-point algorithm (simplified one unit: $\mathbf{w}_{n+1} = \mathbf{w}_n - \eta \cdot \frac{J(\mathbf{w}_n)}{\nabla J(\mathbf{w}_n)}$) such that the learning rule becomes (see [123] for further stabilized versions and modifications of the learning rule)

$$\begin{aligned} \mathbf{w}_{n+1}^* &= E\{\mathbf{x} \cdot g(\mathbf{w}_n^T \mathbf{x})\} - E\{g'(\mathbf{w}_n^T \mathbf{x})\}\mathbf{w}_n \\ \mathbf{w}_{n+1} &= \mathbf{w}_{n+1}^* / \parallel \mathbf{w}_{n+1}^* \parallel \end{aligned} \tag{37}$$

with g' the derivative of g and g the derivative of G. [123]

3.3.2.4 *Maximum Entropy*

Inspired by neural networks, the Infomax approach to BSS as proposed by Bell *et al.* [25] aims at maximizing the mutual information $I(g(\mathbf{y}), \mathbf{y})$ that a g-transformed output $g(\mathbf{y})$ contains about its input $\mathbf{y}$ (i.e. the transformation input is given by the ICA output) by maximizing the entropy $S(p(g(\mathbf{y})))$. Accordingly,

$$I(g(\mathbf{y}), \mathbf{y}) = S(p(g(\mathbf{y}))) - S(p(g(\mathbf{y})|\mathbf{y})) \tag{38}$$

where $S(p(g(\mathbf{y})|\mathbf{y}))$ represents the entropy of $g(\mathbf{y})$ which does not originate from $\mathbf{y}$. Moreover, Bell *et al.* [25] considers only a gradient of this quantities with respect to some parameter $\mathbf{w}$ (i.e. $\mathbf{y} = \mathbf{w}^T \cdot \mathbf{x}$) such that equation (38) becomes

$$\frac{\delta}{\delta \mathbf{w}} I(g(\mathbf{y}), \mathbf{y}) = \frac{\delta}{\delta \mathbf{w}} S(p(g(\mathbf{y}))) \tag{39}$$

with $S(p(g(\mathbf{y})|\mathbf{y}))$ not depending on $\mathbf{w}$ ($\frac{\delta}{\delta \mathbf{w}} S(p(g(\mathbf{y})|\mathbf{y})) = 0$) because of its additive noise character. Considering the one-dimensional case, the parameter w weights the input x before the output y is passed through an invertible function $g(y) = g(w \cdot x)$. If one passes y (i.e. its pdf) through g, one maximizes both $I(p(g(y), y))$ as well as $S(p(g(y))$ by aligning high density parts of y with highly sloping parts of g. The pdfs of $g(y)$ and y are related accordingly:

$$p(g(y)) = \frac{p(y)}{|\delta g(y)/\delta y|} \tag{40}$$

Following the definition of differential entropy (eq. (29)), the output entropy can be derived by [25] and equation (40)

$$S(p(g(y))) = -E\{\log p(g(y))\} = E\{\log \left| \frac{\delta g(y)}{\delta y} \right| \} - E\{\log p(y)\} \tag{41}$$

where only the first term of the right side of equation (41) is considered to be affected by the parameter w. Applying a stochastic gradient descent to maximize the entropy with $\Delta w = w_{n+1} - w_n$ will give

$$\Delta w \propto \frac{\delta S(p(g(y)))}{\delta w} = \frac{\delta}{\delta w} \left(\log \left| \frac{\delta g(y)}{\delta y} \right| \right). \tag{42}$$

See also Amari *et al.* [8] for a natural gradient realization of this approach.

Utilizing a nonlinear function g (resp. its Taylor series expansion, see also [135]) to yield statistical independence is possible since g accesses higher order terms to measure mutual information. However, Bell *et al.* [25] underlines the importance of the choice of the non-linearity. Namely, in a multi-dimensional case (e.g. a two-dimensional case)

$$S(p(g_1(y_1), g_2(y_2))) = S(p(g_1(y_1))) + S(p(g_2(y_2))) - I(g_1(y_1), g_2(y_2)) \tag{43}$$

maximizing the joint entropy $S(p(g_1(y_1), g_2(y_2)))$ requires the maximization of individual entropies $S(p(g_1(y_1)))$ and $S(p(g_2(y_2)))$ plus the minimization of mutual information $I(g_1(y_1), g_2(y_2))$ in order to obtain statistical independence between the outputs y_i. A

non-linearity (approximately) matching the cdf of the respective source signals will ensure the maximization of entropies as well as an actual minimization of mutual information. On the other hand, locally correct solutions are nevertheless obtained by zero-mean outputs or sources, respectively. [25, 296]

3.3.2.5 *JADE*

The Joint Approximate Diagonalization of Eigenmatrices (JADE) algorithm, which has been frequently used in scientific BSS applications was firstly proposed by Cardoso *et al.* [39] in 1993.

As the previously described ICA approaches do more explicitly, also cumulant approaches as JADE implicitly utilize knowledge about the source distributions (in comparison only Comon [60] introduces a distribution-assumption-free concept based on the *Kullback-Leibler* divergence of marginal and joint densities but anyway realize the contrast by exploiting cumulants) [38]. In particular, second-order and fourth-order cumulants were used where e.g. fourth-order cumulants of the random variables $x_1, x_2, x_3, x_4 \in \mathbf{x}$ with $\tilde{x}_i = x_i - E\{x_i\}$ estimates as

$$\begin{aligned}&\mathrm{Cum}(x_1, x_2, x_3, x_4) = \\ &\quad E\{\tilde{x}_1\tilde{x}_2\tilde{x}_3\tilde{x}_4\} - E\{\tilde{x}_1\tilde{x}_2\}E\{\tilde{x}_3\tilde{x}_4\} - E\{\tilde{x}_1\tilde{x}_3\}E\{\tilde{x}_2\tilde{x}_4\} - E\{\tilde{x}_1\tilde{x}_4\}E\{\tilde{x}_2\tilde{x}_3\}\end{aligned} \tag{44}$$

and cumulants involving only one variable x_i with $i = \mathrm{const}\,\forall\, x_i$ are called auto-cumulants or cross-cumulants otherwise. Using $R_{ij} = \mathrm{Cum}(x_i, x_j)$ and $Q_{ijkl} = \mathrm{Cum}(x_i, x_j, x_k, x_l)$, the *Kullback-Leibler* divergence from equation (27) (as well as other ICA entropy-based contrasts) can be approximated [38], i.e.

$$\delta(p_1(\mathbf{u}), p_2(\mathbf{u})) \approx \frac{1}{4}\sum_{ij}\left(R_{ij}^{p_1(\mathbf{u})} - R_{ij}^{p_2(\mathbf{u})}\right)^2 + \frac{1}{48}\sum_{ijkl}\left(Q_{ijkl}^{p_1(\mathbf{u})} - Q_{ijkl}^{p_2(\mathbf{u})}\right)^2. \tag{45}$$

Moreover, cumulants show a multilinearity property such that the fourth-order cumulants of the output $y_i = \sum_p w_{ip} \cdot x_p$ are obtained

$$\mathrm{Cum}(y_i, y_j, y_k, y_l) = \sum_{pqrs} w_{ip}w_{jq}w_{kr}w_{ls} \cdot \mathrm{Cum}(x_p, x_q, x_r, x_s) \tag{46}$$

which can be exploited for the linear ICA model. The statistical independence addressed by computing a transformation $w \in \mathbf{W}$ brings in the diagonalization such that the fourth-order cumulant matrix $Q^{p(\mathbf{s})}$ of statistically independent source signals $\mathbf{s}$ is a diagonal matrix of kurtoses and thus, all cross-cumulants equaling zero.

Because a fourth-order cumulant matrix would be a four-dimensional matrix, cumulant matrices are further expressed in terms of a set of two-dimensional matrices such that the entry Q_{ij} of this matrix which is based on random variables x_i of sensors $i \in [1, n]$ is calculated as [263, p.488]

$$Q_{ij} = \sum_{k,l=1}^{n} \mathrm{Cum}(x_i, x_j, x_k, x_l). \tag{47}$$

In order to capture a large amount of fourth-order information in a set of two-dimensional matrices, an additional matrix M is involved to generate a two-dimensional cumulant matrix. If one defines a set of cumulant matrices $\{Q^{p(\mathbf{x})}(M)\}$ with respect to an arbitrary $n \times n$ matrix M, the entry Q_{ij} is obtained

$$[Q^{p(\mathbf{x})}(M)]_{ij} = \sum_{k,l=1}^{n} \mathrm{Cum}(x_i, x_j, x_k, x_l) \cdot M_{k,l}. \tag{48}$$

Using the multilinearity property from equation (46) will arrange the cumulant matrices involved in the ICA model $\mathbf{x} = \mathbf{A} \cdot \mathbf{s}$ according to

$$Q^{p(\mathbf{x})}(M) = \mathbf{A} \cdot \mathbf{D}(M) \cdot \mathbf{A}^T \tag{49}$$

$$\mathbf{D}(M) = \mathbf{Diag}\left(Q_{1111}^{p(s_1)} \cdot \mathbf{a}_1^T M \mathbf{a}_1, \ldots, Q_{nnnn}^{p(s_n)} \cdot \mathbf{a}_n^T M \mathbf{a}_n\right) \tag{50}$$

with $\mathbf{a}_i$ the i-th column of $\mathbf{A}$ and $Q_{iiii}^{p(s_i)}$ the kurtosis of s_i. The underlying diagonalization problem is similar to EVD in PCA (see section 3.3.1). However, in this case one searches for a joint diagonalizer of a set of matrices. Cardoso [38] gives guidance to construct such sets. Thereby, a maximal set of cumulant matrices $\{Q^{p(\mathbf{y}_{white})}(M)\}$ is constructed to guarantee an equivariant estimate[1] of the diagonalization by involving a large number of fourth-order statistics. Actually, a set of eigenmatrices of $\{Q(M)\}$ with non-zero eigenvalues is used to compute a joint diagonalization. The respective set of matrices is jointly diagonalized by a product of plane rotations based on Jacobi angles (Jacobi rotations) as proposed by Cardoso *et al.* [40].

By using diagonalization of higher-order (fourth-order) cumulant tensors analogous to the second-order cumulant tensor covariance matrix (PCA), JADE is considered very efficient for a small number of observations [101], while it is not for a large number of observations [38]. An advantage coming alongside the usage of Jacobi angles for the computation of the transformation is superseding the necessity for gradient descent optimization (i.e. its sensitivity to local optima). [38, 39]

1 An equivariant estimator preserves the structure of the parameter estimation problem (i.e. finding the diagonalizer of the fourth-order cumulant matrix) while using only sample estimates.

3.3.2.6 *RADICAL*

The Robust, Accurate, Direct ICA aLgorithm (RADICAL) as well as the other following approaches are relatively new ICA developments, which were proposed after the fundamental ICA approach statements during the 1990s.

As multiply exploited in the ICA domain, RADICAL bases on the concept of expressing mutual information by entropies or negentropies, respectively, as described in equation (32). Accordingly, minimizing mutual information essentially equals minimizing marginal differential entropies $\sum_i S(p(y_i))$ or maximizing negentropies, respectively. In order to solve this minimization problem, Learned-Miller *et al.* [159] propose a new entropy estimator thus giving an alternative solution to the minimum mutual information principle by Comon [60].

The according entropy estimator is based on order statistics. Namely, if one considers an ordered random variable y^* which is ordered with respect to the sample value $y^*(1) \leq y^*(2) \leq y^*(N)$ an m-spacing is defined $y^*(i+m) - y^*(i)$ and m is limited by N (and can be a function of N such that one typically considers a m_N-spacing). The entropy estimator is defined as

$$S_{m_N}(p(y)) = \frac{1}{N - m_N} \sum_{i=1}^{N-m_N} \log\left(\frac{N+1}{m_N}(y^*(i+m_N) - y^*(i))\right) \tag{51}$$

with $m_N \approx \sqrt{N}$ such that the expectation of the corresponding density $p(y)$ centers around its probability mass, which lowers the variance of the estimator. In order to improve the performance of the optimization regarding false optima especially in case of small sample sizes $N \leq 2000$, the algorithm further uses replicates y' of the original samples with added spherical Gaussian noise ($\mathcal{N}(y, \sigma_R^2)$) at R samples to augment the original data prior to entropy estimation. Given a pre-whitened output $\mathbf{y}_{White}$ the residual rotation aiming at statistical independence while maintaining whiteness is computed. In the two-dimensional case, the global optima can easily be computed with a given resolution and the rotation range $[0, \pi/2]$ suffices since every 90° will result in the same independent component. In the multidimensional case, the optimization is successively calculated for a series of $\{y_i, y_j\}$ pairs by utilizing Jacobi rotations always affecting only the two respective components. Accordingly, the overall rotation is not calculated at once but in sweeps of pairs i, j with $1 \leq i \neq j \leq n$ for $\mathbf{y}_{White}$ consisting of n random variables.

Thus, the RADICAL approach uses no explicit nor implicit density estimation. Moreover, its entropy estimator is robust against outliers, however the required pre-processing i.e. whitening is not. The utilized global optimization also is robust compared to gradient descent methods because sticking to local optima is avoided. [159]

3.3.2.7 πCA

In biosignal processing with BSS, the (pseudo-)periodic structure and information inherent in many biosignals is typically not exploited. Periodic Component Analysis (πCA) utilizes such periodic structure of signals. A measure ϵ of periodicity to be minimized (to maximize the periodicity of the output y) in the BSS context was proposed by Saul *et al.* [226]:

$$\epsilon(\mathbf{w}, \tau) = \frac{\sum_k |y(k+\tau) - y(k)|^2}{\sum_k |y(k)|^2} \tag{52}$$

with $y(k) = \mathbf{w}^T \cdot \mathbf{x}(k)$. Thereby, $\mathbf{w}$ is further allowed to be complex in order to compensate for phase differences among the outputs s and the originally real-valued signals $x(k)$ are transformed to analytic signals with imaginary parts computed by the Hilbert transform.

Whereas the above mentioned contrast ϵ refers to a constant time lag τ, Sameni *et al.* [224] extend the πCA concept to deal with changing τ as typical for physiologically fluctuating distances between successive heart beats in biosignals. Specifically, R-peaks in the input ECG are detected and a phase signal $\varphi(k) \in [-\pi, \pi]$ is extracted which serve as a basis to a time-adaptive τ_k

$$\tau_k = \min \{\tau | \varphi(k+\tau) = \varphi(k), \tau > 0\} \tag{53}$$

Also, Sameni *et al.* [224] works with real-valued variables and transformations. Moreover, the output y in equation (52) is reformulated such that ϵ becomes

$$\epsilon(\mathbf{w}, \tau_k) = 2\left(1 - \frac{\mathbf{w}^T \cdot \mathbf{Cov}_{\tau_k}(\mathbf{x}) \cdot \mathbf{w}}{\mathbf{w}^T \cdot \mathbf{Cov}(\mathbf{x}) \cdot \mathbf{w}}\right). \tag{54}$$

3.3.2.8 *Constrained ICA*

Given an already existing notion of the source signals of interest which should be extracted out of the measured signal mixtures $\mathbf{x}$, one can impose a constraint to the ICA optimization problem which works alongside the maximization of statistical independence. Since these notions are typically seizable in form of temporal information on the source signal's course (e.g. additional sensors access time instances of heartbeats), temporally constraints are common in constrained Independent Component Analysis (cICA). Typical implementations [129, 161, 173, 187, 189, 259] apply these constraints to the FastICA algorithm. To measure the closeness $f(\mathbf{w})$ to the constraint $r(k)$ (typically a rectangular

function resembling the temporally important features), a correlation coefficient can be applied such that equation (36) becomes

$$\begin{aligned} &\text{Maximize: } J_G(\mathbf{w}) = \Big[E\{G(\mathbf{w}^T \cdot \mathbf{x})\} - E\{G(\phi(\mathbf{w}^T \cdot \mathbf{x}))\}\Big]^2 \\ &\text{Subject to: } f(\mathbf{w}) = \xi - E\{r(k)\,\mathbf{w}^T \cdot \mathbf{x}(k)\} \leq 0 \end{aligned} \tag{55}$$

with ξ a threshold and both variances $E\{y^2\}, E\{r^2\} = 1$. This constrained optimization problem can be addressed by the Lagrange multiplier method (see [173] for details) with the new Lagrangian objective function $\mathcal{L}$ including the constraints

$$\mathcal{L}(\mathbf{w}, \mu, \lambda) = -J_G(\mathbf{w}) + f(\mathbf{w}, \mu) + h(\mathbf{w}, \lambda) \tag{56}$$

with μ and λ the Lagrange multipliers and h modeling the above mentioned variance constraint (h can be omitted in case of pre-whitening). The crucial choice belongs to the threshold ξ which can be done empirically [129, 189]. Namely, ensuring the optimization to generally as well as exactly converge to the desired output $y_i \neq y_j$, ξ needs to be chosen $\xi \in [f(y_i, r), \min f(y_j, r)]$ [173]. Accordingly, Mi [187] serves an algorithm to adapt ξ based on detecting the desired convergence behavior.

3.3.2.9 *Frequency Domain ICA*

The classical instantaneous ICA model does not hold for convolutive mixtures $x_i(k) = \sum_{j,\tau} a_{ij}(\tau) \cdot s_j(k - \tau)$. Despite convolutive mixtures can be handled by BSS models including delay-reconstruction [240] and spatio-temporal FIR filters [203], respectively, the convolutive model can also be approached in the frequency domain. Accordingly,

$$X_i(f, k) = \sum_{j=1}^{N} A_{ij}(f) \cdot S_j(f, k) \tag{57}$$

denotes the ICA model for each frequency bin $X(f)$ and $X(f, k)$, respectively $S(f, k)$ is the time-frequency representation, e.g. the short-time Fourier transform (STFT) of $x(k)$ and $s(k)$ at the frequency bins f [188]. $A_{ij}(f)$ designate the discrete Fourier transform (DFT) coefficients of the FIR filters $a_{ij}(\tau)$ of the mixing matrix $\mathbf{A}$. This model needs to be solved by ICA algorithms capable of complex-valued data.

Complex ICA extensions to facilitate frequency Independent Component Analysis (fICA) have been proposed e.g. for the infomax (maximum entropy) approach by Smaragdis [235] and Anemüller *et al.* [14]. Also, FastICA has been modified to deal with complex data

in a fICA setting by Milanesi *et al.* [188]. Thereby, the FastICA learning rule depicted in equation (37) is adapted as

$$\mathbf{w}_{n+1} = E\{\mathbf{x} \cdot g^*(\mathbf{w}_n^H \mathbf{x})\} - E\{g^{*\prime}(\mathbf{w}_n^H \mathbf{x})\}\mathbf{w}_n \tag{58}$$

where g^* is the complex extension of g, e.g. for the commonly applied $g(\mathbf{y}) = \tanh(\mathbf{y})$ such that $g^*(\mathbf{y}) = \tanh(\Re\{\mathbf{y}\}) + \mathrm{i} \cdot \tanh(\Im\{\mathbf{y}\})$ as already proposed in [235].

Under the model defined above, each considered frequency bin requires an ICA computation. Before back-transformation of the obtained output components into the time domain, the components of each frequency bin need to be associated with their matching components from other bins. Inter-frequency correlation can be used to solve this indeterminacy since different spectral envelopes of the same source should show highest correlation among the possible combinations [14, 189].

3.3.3 *Quantification of BSS Performance*

A direct sample-by-sample comparison between a single estimated source signal y and true source signal s given the solved permutation indeterminacy is obtained by [310]

$$D = \min \left\| \frac{y}{\|y\|} \pm \frac{s}{\|s\|} \right\|^2 \tag{59}$$

a $\boldsymbol{L}_2$-normalized version of a squared distance to address the gain indeterminacy. However, this measure serves a poor contrast for distinguishing between solutions $y \approx s$ and badly solved permutation indeterminacy [268].

Other measures directly comparing source signal estimates y with their respective true source s (and the noisy measured signal x) are given by the noise reduction factor[2] (with $\langle f \rangle$ the mean of a function f):

$$\chi = \sqrt{\frac{\langle x - s \rangle^2}{\langle y - s \rangle^2}} \tag{60}$$

and the cross-correlation coefficient between the true source and its estimate (mean μ and standard deviation σ)[3] [59, p.179]

$$\rho = \frac{\langle [s - \mu_s][y - \mu_y] \rangle}{\sigma_s \sigma_y}. \tag{61}$$

2 [189] defines a similar (inverse) measure of a quadratic error
3 [189] defines a similar morphology recovery coefficient which is limited to the immediate QRS vicinity

Defining a BSS model including a source-to-sensor filter $a_{ij}(\tau)$ that depends on embedding time lag τ, the i-th measurement x_i with $i \in [1, m]$ is mixed out of n source signals s_j by

$$x_i(k) = \sum_{j=1}^{n} \sum_{\tau=0}^{+\infty} a_{ij}(\tau)\, s_j(k-\tau) + \epsilon_{ni}(k) \tag{62}$$

with $\epsilon_{ni}(k)$ additive sensor noise at the i-th sensor.

Assuming a time-invariant linear mixing system $\mathbf{A}^\tau$: $\{\mathbf{A}(\tau)|\tau \in [0, +\infty]\}$ and the according demixing system $\mathbf{W}^\tau$ one obtains the global system $\mathbf{B}^\tau = \mathbf{W}^\tau \cdot \mathbf{A}^\tau$ which can be evaluated in an experimental setting given a previously known mixing system $\mathbf{A}^\tau$. The intersymbol interference (ISI) of $\mathbf{B}^\tau$ defined as [155]

$$\mathrm{ISI} = \frac{\sum_{\tau=0}^{+\infty} |\mathbf{B}(\tau)|^2 - \max_{\tau\in[0,+\infty]} |\mathbf{B}(\tau)|^2}{\max_{\tau\in[0,+\infty]} |\mathbf{B}(\tau)|^2}. \tag{63}$$

ISI is insensitive to overall gain and group delay (unlike the mean square error). It is measured row-wise as row ISI[4] [57, p.373],[155, 268] (dropping the summation over τ for simplicity)

$$\mathrm{ISI}_j = \frac{\sum_{i=1}^{m} |\mathbf{B}_{ji}|^2}{\max_{i\in[1,m]} |\mathbf{B}_{ji}|^2} - 1 \tag{64}$$

or as combined performance index (PI) of all $j \in [1, n]$ rows[5] [57, p.161],[248]

$$\mathrm{PI} = \frac{1}{n(m-1)} \sum_{j=1}^{n} \sum_{i=1}^{m} \left(\frac{|\mathbf{B}_{ji}|}{\max_{i\in[1,m]} |\mathbf{B}_{ji}|} - 1 \right). \tag{65}$$

Similar approaches estimate a SNR of the transformation obtained by the system $\mathbf{B}^\tau$ together with the source signals $\mathbf{s}$ [247]

$$\mathrm{SNR}_j^\tau = 10 \log_{10} \frac{\sum_{k=1}^{K} |\sum_{\tau=0}^{+\infty} \mathbf{B}_{jj}(\tau) s_j(k-\tau)|^2}{\sum_{k=1}^{K} |\sum_{\tau=0}^{+\infty} \mathbf{B}_{jn}(\tau) s_n(k-\tau)|^2} \tag{66}$$

considered as noise source s_n and source of interest s_j with its SNR_j^τ, respectively. These measures cannot be applied to underdetermined ($m < n$) BSS problems [268].

4 [57] extends this measure with an analogue column-wise ISI. [155] uses another indexing for evaluating the inverse system $\mathbf{B}^{-1} = \mathbf{A} \cdot \mathbf{W}$

5 [57] extends this measure with an analogue column-wise assessment

A generalized model for the decomposition of source signals obtained by BSS was proposed by Vincent *et al.* [268] in the context of BSS performance quantification for audio source separation. Estimated sources are decomposed into a true source part plus error terms corresponding to interferences by other sources, additive noise and algorithmic artifacts. The decomposition is based on orthogonal projections of the estimated source signals y onto vector subspaces spanned by the true sources s. Numerical performance criteria (i.e. signal-to-noise/interference/artifacts-ratio) are derived from this decomposition.

3.3.4 *General Practical Limitations of ICA Usage*

Common ICA algorithms as presented above assume a properly chosen nature of the mixing problem to be solved. This for instance involves a well-determined mixing relation between mixtures and sources, i.e. the number of sources m to be estimated being less or equal the number of measured mixtures n. Also, the amount of samples per measured mixture needs to be sufficient to ensure reliable contrasts and avoid artifacts. In the following, some problems and related approaches addressing practical conditions beyond the typical ICA assumptions are highlighted.

ARTIFACTS OF ICA In ICA (and BSS) insufficient sample sizes can lead to the generation of artefactual sources due to over-fitting. These specific artifacts have been termed *spikes* and *bumps* by Hyvärinen *et al.* [126]. Considering the extreme case, where the number of measurements n equals the number of samples $(\mathbf{x}, \mathbf{A} : n \times n)$, it is obvious that a perfect candidate $\mathbf{y}$ of non-Gaussian output components under the whiteness constraint is a permutation (and sign-change) matrix of *spikes*.

If the original source signals are not independent and identically distributed but show strong time-dependencies (e.g. periodic signals), the spikes are rather be expressed in a lowpass-filtered fashion, i.e. as *bump* artifacts even for larger sample sizes. This is because the periodic signal of sample size N consists of k-times repeated segments such that the actual sample base for ICA optimization only is of size N/k and *bumps* of size k can be generated. Accordingly, sample size and sampling rate as well as compression (e.g. batch processing) approaches should be considered with care. [126]

UNDER-/OVERDETERMINED ICA Most ICA algorithms consider the symmetric case of l source component estimates $\mathbf{y}$ obtained after inverting the mapping of m source signals $\mathbf{s}$ onto n mixtures $\mathbf{x}$ with $l = m = n$. While facing a more generalized ICA problem, one defines the underdetermined $m > n$ as well the overdetermined $m < n$ case. Whereas the latter may effectively be addressed by PCA pre-processing, the underdetermined case is troublesome. An underdetermined ICA may result in output components itself resembling a mixture of the original source signals while anyway being statistically independent [173].

Many approaches to the underdetermined case utilize the sparseness of source signals [67], for instance Georgiev *et al.* [88] propose the concept of a sufficiently sparse source signal. A sparse source signal thereby contains as few as possible non-zero elements. While real-world time-domain sources rather not resemble sparse sources at first glance, a linear sparseness-improving transformation (e.g. the wavelet packet transform, see also [310] for BSS based on a signal dictionary) may be able to generate a sparse representation. Moreover, constraining

1. the $n \times m$ matrix $\mathbf{A}$ to be non-singular also regarding its $n \times n$ sub-matrices
2. the source signals $\mathbf{s}$ to contain at most $n-1$ non-zero elements
3. $\mathbf{s}$ nevertheless being sufficiently rich (contain a sufficient amount of independently distributed non-zero entries, see [88] for details),

the underdetermined source separation problem can be uniquely solved by a hyperplane evaluation of the columns of $\mathbf{x}$. Another approach to underdetermined ICA basically works with the concept of virtual sensors (see e.g. De Lathauwer *et al.* [67],[66]), which are generated in the context of cumulant matrices and their simultaneous diagonalization to achieve statistically independent output components (as used in SOBI an JADE).

On the contrary, Joho *et al.* [133] investigated the overdetermined ICA problem in a subsequent PCA→ICA setup. The authors showed by simulations, that adding sensors can improve the output signal quality for both the virtual sensors obtained by PCA as well as the ICA outputs. In particular, the PCA profits of an increased sensor number, since singular values (resp. eigenvalues) and thus, the SNRs of the original source signals are improved. The effect of an increased SNR for a larger sensor number then also shows in the ICA output. Additionally, more sensors decrease the condition number of $\mathbf{A}$ (i.e. the influence of small changes like noise in the sensor of $\mathbf{x}$ on the estimate of $\mathbf{s}$ by $\mathbf{A}^{-1}$). However, sensor noise is the limiting factor since for instance a dimension reduction by PCA is typically based on singular values (resp. eigenvalues), thus excluding outputs associated with small singular values. Moreover, the commonly applied whiteness constraint in ICA eventually increases the noise power after being passed through PCA.

SEPARABILITY OF SOURCES The question whether the l estimated independent output components $\mathbf{y}$ represent actually separated source signals $\mathbf{s}$ is strongly connected to underdetermined ICA. The problem of separability of independent sources is stated by Cao *et al.* [36][6] such that after the mixing process $\mathbf{x} = \mathbf{A} \cdot \mathbf{s}$ we estimate a demixing process $\mathbf{y} = \mathbf{W} \cdot \mathbf{x}$ which still leaves the indeterminacy $\mathbf{y} = \mathbf{B} \cdot \mathbf{s}$ with $\mathbf{B} = \mathbf{W} \times \mathbf{A}$ a $l \times m$ matrix. Typically, one does only have partial control of $\mathbf{B}$ because $\mathbf{A}$ is unknown. The question of separability arises, if one can obtain a $\mathbf{W}$ such that each row of $\mathbf{B}$ contains only one single non-zero entry. In this context, the Darmois-Skitovich theorem states that

6 The term *separability* in [36] specifically refers to the existence of $\mathbf{A}$ however, by using this term within this doctoral work, the relation between $\mathbf{y}$ and $\mathbf{s}$ is considered.

given a m-dimensional source vector $\mathbf{s} = (s_1, \ldots, s_m)^T$ of mutually independent sources and further two pairwise independent output components y_1 and y_2

$$\begin{aligned} y_1 &= b_{1,1} \cdot s_1 + b_{1,2} \cdot s_2 + \ldots + b_{1,m} \cdot s_m \\ y_2 &= b_{2,1} \cdot s_1 + b_{2,2} \cdot s_2 + \ldots + b_{2,m} \cdot s_m \end{aligned} \tag{67}$$

show $b_{1,i} \neq 0$ and $b_{2,i} \neq 0$, then s_i has a Gaussian distribution. While this theorem has no limiting consequence in the case $l = m$ and the ICA restriction regarding at most one Gaussian source, the case $l < m$ has consequences for a full column rank matrix $\mathbf{A}$. Then, a matrix $\mathbf{W}$ can be computed that separates m source signals into l non-empty disjoint groups of source signals (i.e. independent components which are anyway pairwise independent). Also, Cao *et al.* [36] derive consequences for the structure of $\mathbf{B}$ in case of the number of Gaussian sources (noises) exceeding one.

RELIABILITY OF BSS One problem of unsupervised learning algorithms as common BSS arises from the fact that the respective algorithm will always give a solution within its model class, e.g. PCA will give an orthogonal separation independent of the actual orthogonality of the original sources. Given the knowledge of both $\mathbf{s}$ the true sources and $\mathbf{y}$ the estimated sources, one can calculate the actual separation error E_i of the i-th component as the angle difference between the true direction of source and the estimated source [185]

$$E_i = \arccos\left(\frac{\mathbf{e}_i \cdot \mathbf{f}_i}{\| \mathbf{e}_i \| \cdot \| \mathbf{f}_i \|}\right) \tag{68}$$

with $\{\mathbf{e}_i\}$ the canonical basis of the true sources and $\{\mathbf{f}_i\}$ the basis of the estimated sources.

One approach towards estimating the BSS reliability blindly is given by Meinecke *et al.* [185]. It considers the reliability of BSS projections by application of re-sampling. Namely, an ICA solution $\mathbf{y}$ is computed which is used to re-sample surrogate data by using Bootstrap. The ICA algorithm again is used to compute the rotation which separates the surrogate data (after respective whitening). The uncertainty of the original i-th ICA projection is assessed by evaluating the variance of the rotations (angles).

Thereby, a rotation in $\mathbb{R}^n$ is defined through a plane, i.e. a plane rotation in the (i, j)-plane. The overall n-dimensional rotation can be decomposed by the product of plane rotations of all principle planes $1 \leq i, j \leq n$. A (i, j)-plane rotation is given by the

identity matrix $\mathbf{I}$ except the contributions in (i, j) with $R_{i,j}(\alpha)$ the (i, j)-rotation matrix of angle α and exemplarily one gets [72]

$$R_{i,j}(\alpha) = \begin{bmatrix} 1 & 0 & 0 & 0 \\ \cos\alpha & 1 & -\sin\alpha & 0 \\ \sin\alpha & 0 & \cos\alpha & 0 \\ 0 & 0 & 0 & 1 \end{bmatrix} \text{ for } (i, j) = (2, 3) \tag{69}$$

which is a principle, that is also utilized in the joint diagonalization of matrices [40]. However, in the new estimate of $\mathbf{W}^*$ separating the surrogate data, the (i, j)-plane rotations are already mixed. Nevertheless, it can be expected that $\mathbf{W}^*$ will be close to the identity matrix, since it separates surrogate data from already separated data. Based on that, the rotation angles between the identity matrix $\mathbf{I}$ and $\mathbf{W}^*$ are assessed for single components (rows of $\mathbf{W}^*$) with respect to the vectors forming the (i, j)-plane of each i-th component by using $\cos\alpha = \frac{a_1 \cdot a_2}{|a_1| \cdot |a_2|}$ with $a_1 \in \mathbf{I}$ and $a_2 \in \mathbf{W}^*$ the vectors defining the plane's axes. Namely, the variance of the rotation angles α of the i-th component among the surrogate samples is computed. Accordingly, first the variance of $\alpha_{i,j}$ ($\mathrm{Var}(\alpha_{i,j})$) given a pair (i, j) is estimated for all surrogate samples (i.e. the instability of the rotation with respect to a rotation in the (i, j)-plane). Afterwards, the uncertainty U_i with respect to the i-th component is computed by determining the maximum variance among the j contributions to the i-th component by [185]

$$U_i = \max_j \mathrm{Var}(\alpha_{i,j}). \tag{70}$$

This gives the maximum variance of the angle which bounds the reliability of the direction of the ICA estimate y_i.

NONLINEAR ICA The previous descriptions on ICA underlay a linear mixing process model $\mathbf{x} = \mathbf{A} \cdot \mathbf{s}$ which has to be critically examined in real-world measurement scenarios. Refining the ICA model in order to be capable of dealing with a nonlinear mixture will give

$$\mathbf{x} = \mathbf{f}(\mathbf{s}) \tag{71}$$

with $\mathbf{f}$ an unknown function from $\mathbb{R}^n$ to $\mathbb{R}^n$ (a linear $\mathbf{f}$ equals the classical ICA model). However, it can be shown [125], that while it is always possible to find a function $\mathbf{h}$ with $\mathbf{y} = \mathbf{h}(\mathbf{x})$ giving statistically independent outputs, this solution is highly non-unique. Specifically, by incrementally building $\mathbf{h}$ using a Gram-Schmidt-like orthogonalization pro-

cedure, one can always form a set of n variables y_i which are jointly uniformly distributed in the unit cube $[0,1]^n$ and thus, independent. However, this solution will be non-unique since $\mathbf{y}' = \mathbf{h}'(\mathbf{M} \cdot \mathbf{x}) \neq \mathbf{y}$ for a linear transformation $\mathbf{M}$. According to this, the nonlinear ICA solution will leave an indeterminacy comparable to that solved by standard linear ICA. Only under very strong assumptions (i.e. a two-dimensional mixing problem, $\mathbf{f}$ a conformal mapping, source densities with known bounded support), unique solutions can possibly be obtained. [125]

3.3.5 *Limitations of BSS for Processing Biomedical Signals*

Multichannel biomedical signals derived from a (at least partly known) spatial distribution of sensors with respect to the human body provide temporally and spatially correlated measurements. These measurements are additionally contaminated by disturbances either of physiological or environmental origin. In order to analyze the measured biomedical signals, the measurements needs to be unmixed into its constituent physio-/pathological components and separated from disturbances. Moreover, information about the number of distinct sources [279], their spatial distribution and temporal changes are to be provided. BSS methods at least partially aim at automated data-driven solutions for these requirements. [131]

In the following, the general application of BSS to biomedical signals is discussed in the context of the aforementioned limitations defined by the assumptions underlying practically relevant BSS models.

SEPARABILITY OF BIOSIGNALS AND DISTURBANCES Typical environmental disturbances in biomedical signal acquisition arise from common mode interferences in biopotential measurement. Common mode interferences express themselves as technically originating baseline wander and power-line interference or non-technical contamination like muscle activity and motion-related signal changes [49]. Despite already been addressed by common biopotential amplification technique, even an ideal amplifier with infinite common mode rejection ratio is limited due to a common mode signal being dependent on equal source impedances [197], i.e. the impedances characterizing the distances between the human body's signal generator(s) and each electrode. However, due to the nature of common mode interferences spreading very similarly on differential leads, BSS provides a suitable technique to cope with such interferences in multichannel (multi-lead) settings.

Also, the model of the BSS input, i.e. how the measured signal mixture is constituted by the underlying source signals, affect its separability by means of BSS. The dipole model of the ECG, i.e. one of the physiological models utilized for biosignal measurements, fulfills one of the fundamental BSS assumptions such that the ECG recording is a linear mixture of bioelectrical signals. The explicit manifestation of the linear mixture depends on the measurement location [264]. In the cbPPG domain, the measurement model differs with

respect to the utilized wavelengths. A cbPPG can be measured at different locations (i.e. pixels or ROIs) using a single wavelength (monochrome approach, [64, 154, 252]) or alternatively at a single location using different wavelengths (multispectral approach, [265]). The most widespread approach originating from Poh *et al.* [212] processes multispectral measurements of the blood volume pulse. Thereby, each color sensor measures a mixture of the photoplethysmographic effect alongside disturbances like changes in ambient light or motion artifacts. This approach neglects the two-fold mixture problem apparent in this measurement setup. One the one hand, light of different wavelength penetrates to different depth of the human skin [265], which possess different properties [24] (e.g. absorption properties). The blood volume pulse then is formed as an individual mixture of multiple wavelengths [95], which gives the first mixture. Additionally, the mixture of the measured color changes is superimposed by disturbances. It has to be questioned whether all types of disturbances (e.g. changing ambient light brightness) express themselves homogeneously for the different wavelengths and thus can be effectively separated by linear BSS. Alternatively, the BSS model of [64, 154] in the context of the cbPPG utilizes different spatial sensors of the same wavelength (monochrome approach). According to that model, melanin and hemoglobin differently reflect the light such that the observed signals serve as a mixture of these two contributions. Thus, this model covers the reflection and absorption of light in different depths of the skin [24] but for the same wavelength. Whereas the amount of melanin can be considered constant in time, the amount of hemoglobin is periodically affected by the blood volume pulse. The separation of these signals by ICA should be possible by processing a pair of signals from two skin locations [64, 154]. However, the underlying assumptions in this case comprise the measurement of a homogenous blood volume pulse with respect to the two locations together with two locations measured at the same color (regardless its brightness). The assumption on a homogeneous (linear) superposition of disturbances (e.g. the relative change of brightness) in this model seems realistic for common scenarios.

Moreover, in biosignal processing, clinical information and noise share similar properties as commonly used for linear biosignal analysis like time- and frequency-domain features. Whereas BSSs' mixing models typically base on linear models in the time-domain, processing approaches as Independent Component Analysis (ICA) do not rely on the linear assumptions (a linear spectral superposition of biosignal and disturbance sources) applied for spectral filtering. [49],[59, p.171] Therewith, they suit better to nonlinear spectral data structure and have been associated with biological systems from the early beginning of ICA algorithm developments on [131, 135]. Among the BSS algorithms, ICA is considered superior to e.g. PCA for the nonlinear data structure of biosignals [49]. In addition, compared to spectral filters, BSS does not cause a reduction of amplitudes of important biosignal waveforms as the QRS complex of the ECG [101].

Typically, the linear stationary mixing paradigm underlying the ICA ensures the separability of sources. For instance, a cardiac source signal which rotates through the abdomen

due to respiration together with stationary located noise sources induces a nonlinear mixing process [59, p.165]. However, this can also be understood as a problem of missing stationarity [131] of an actually linear mixing process which may be addressed by segmentation of the data. Basically, the assumption of a linear mixing process in biomedical multichannel measurements serves a reasonable hypothesis in most cases.

BSS MODEL SELECTION Despite the common instantaneous mixing model which is addressed by a standard linear BSS model in the time domain, other BSS models e.g. utilizing signals' state space reconstruction, have been discussed in the context of biomedical signal processing.

Nonlinear dynamics can be described by a state space reconstruction [240]. Under the assumption that the biosignal dynamics evolve from an attractor[7] (as reasonable for biosignals like the ECG [82] and PPG [46]), a replica state space using delay vector reconstruction is given

$$\mathbf{x}(k) = [x(k), x(k+d), \ldots, x(k+(m-1)\cdot d)]^T \in \mathbb{R}^m \tag{72}$$

with m the reconstruction dimension and d the sample (time) delay. Appropriate choices for m should consider the box counting dimension/Minkowski dimension D_0 according $m > 2 \cdot D_0$ of the nonlinear dynamics and d can be selected e.g. by the first minimum in the mutual information of the signal. In practice, the selection of m of d can be realized by accuracy optimization of the connected nonlinear filtering technique. [59, p.173]

The state space representation can be used for filtering by ICA even given a single univariate ECG lead [59, p.173f,181f]. Filtering based on delay reconstruction representations can also be understood as FIR filter. Processing multivariate inputs based on a delay reconstruction state space extends the standard temporal filter to a spatio-temporal FIR filter [203]. According to Stögbauer *et al.* [240], BSS based on delay reconstruction in general serves the more appropriate choice for biosignal processing since it accounts for the multidimensionality of a source originating from a chaotic dynamical system as the human heart.

The FIR filter perspective of ICA using delay reconstruction state space is basically equivalent with convolutive ICA performed in the frequency domain (fICA), i.e. the computation of the ICA for time courses of band-limited frequency bands (short-term Fourier transform). Accordingly, ICA inputs are formed each of the same frequency bands from different input signals. Since ICA is only solved up to a permutation the components from several frequency-bands need to be associated. This is addressed by inter-frequency-band correlation to construct grouped frequency domain components for back transformation

7 An attractor serves a subset of the phase space, i.e. a limited set of conditions, which a dynamical system (approximately) does not leave over time. An ECG won't express an arbitrary form but instead follows limited dynamics and expresses an attractor (see e.g. [178]).

into the time domain [189]. Convolutive BSS algorithms do not necessarily contribute to an improved separation performance compared to standard instantaneous algorithms. For instance, Vayá *et al.* [264] showed a better performance of instantaneous time domain ICA for extraction of atrial activity during AF compared to convolutive methods. Milanesi *et al.* [189] on the contrary reported lesser quadratic errors of the waveform compared to the ECG reference, better QRS morphology recovery (higher correlation with reference) and increased R peak detection accuracy for fICA. Whereas in fICA two indeterminacies (association of frequency bands to one component, permutation of multiple components) are to be solved, convolutive BSS by delay reconstruction solved in the time domain only possess the permutation of multiple output components. Applying such spatio-temporal ICA showed performance improvements compared to instantaneous ICA for wearable ECG recordings [290].

Nevertheless, instantaneous mixing (without embedding delay-reconstruction) is commonly assumed and holds for certain biomedical applications [131, 222]. Another simplification, assuming a noiseless mixing in the linear model, is less realistic but still allows for the separation of sources yet contaminated by measurement noise. [131]

Another important limitation of the BSS model is introduced by common BSS algorithms that are based on (higher-order) statistics and treat the observations $\mathbf{x}$ as random variables where temporal ordering is irrelevant. On the contrary, temporal structure is relevant in biosignals and could be exploited as less-common approaches like time-structure based methods do (see section 3.3.1). In the context of separation from maternal and fetal ECG, a periodic component analysis was proposed by Sameni *et al.* [224] which replaces classical independence of ICA by a periodical temporal structure criterion. However, this approach wasn't developed up to a level applicable for unsupervised data-driven usage. Temporally constrained methods (see section 3.3.2) also incorporate time-structure. In contact-less multichannel measurement setups as the cECG, however, temporal a priori information as necessary for the temporally constrained ICA is typically not available. Clinical setups recording an ECG alongside and electroencephalogram (EEG), on the other hand, can provide temporal information to separate EEG disturbances originating from the ECG [98]. Even data-driven temporal constraint determination requires carefully determined thresholds [189] and thus training which inhibits the transferability to other data sets. Besides temporal information, also spatial information or topographical maps (a priori knowledge about spatial projections e.g. in the EEG) can be included in the ICA estimation as constraints. [131]

CONSEQUENCE OF OVERDETERMINED BSS Increasing the number of ICA inputs by increasing m (for delay vector reconstruction in equation (72)) or the number of sensors complicates the permutation indeterminacy, which is one of the major problems and antagonism of ICA. While adding inputs allow for fusion-performance improvements on the one hand [219], it hampers the exploitation of the performance increase on the other hand.

Because BSS is only solved up to permutation, a selection of interesting sources among $\mathbf{y}$ after BSS application is mandatory. In order to highlight the selection necessity, ICA is a context-dependent transformation driven by the data within the analysis window such that no clinically relevant biosignal (e.g. ECG) is obtained by its application. For clinical use and diagnosis, the back projection of non-noise sources (by $\mathbf{W}^{-1}$ and setting noise-source-related columns to zero) after their respective selection is necessary and overcomes the scaling ambiguity. The according permutation problem for handling back projection is rather complicated but needs to be solved regardless ICAs usage with or without back projection to anyway make use of the separation performance. [59, p.162ff]

The assumption of square mixing (the number of measurements equals the number of estimated sources) is a commonly applied commitment in BSS application trying to avoid model order selection and making BSS more tractable. This assumption is in particular relevant for overdetermined mixtures because it is less likely in large multichannel setups. Overdetermined mixtures can be addressed by data-reduction techniques like prewhitening. These techniques, however, show a potential weakness to guaranty that the sources of interest are contained in the subspace spanned by dominant principle components (dominant eigenvalues, respectively amount of expressed variance). Other enumeration approaches are also based on eigenvalues [91, 261] or aim at sequential source separation [108]. Together with the common square mixing assumption and thus, the number of sources to be extracted, the assumption of decorrelation or statistical independence is utilized for the computation of the BSS solution. In the light of an actual biomedical multichannel setup, also the question arises how many actually independent sources can be extracted by given sensors. In general, the question whether independence is actually achieved by a transformation and to which degree (e.g. assessed by mutual information) is seldomly addressed in the ICA context [240]. [131]

While being based on common ICA algorithms, an alternative view onto ICA with respect to the square mixing problem is given by Multidimensional Independent Component Analysis (MICA). MICA extends the conventional ICA approach by aiming at independent subspaces (sub-matrices of $\mathbf{A}, \mathbf{W}$) while allowing for dependencies within the sub-matrices [48, 254]. Thus, multidimensional components $\mathbf{y}$ are determined by combining one-dimensional non-independent source signal estimates [37]. This connects a relaxed independence assumption of the relation between output components y with the anyway applied practical realization of ICA, which aims at estimating components that are merely as independent as possible. [35],[37]. Essentially, MICA serves an alternative interpretation of the results obtained by common ICA.

RELIABILITY OF BSS OUTPUTS As indicated above in context of the BSS's permutation indeterminacy, signal morphology retention by BSS is another issue which needs to be considered carefully regarding the actual signal processing task [59, p.162]. For instance, PCA has shown to perform worse with respect to signal morphology in the back

projection case (noise canceling by column-cleaning in $\mathbf{W}^{-}1$) compared to ICA, especially when using ICA with delay reconstruction. Still, PCA is described to maintain diagnostic morphology in the projected space [49]. In addition, compared to other data-driven non-linear noise filtering techniques, ICA showed to perform best in reducing noise and worse in maintaining morphology (correlation to original signal). This rather recommends ICA for ECG processing tasks as the estimation of beat-to-beat intervals (RRIs), i.e. the precise location of R-peaks [48],[59, p.185].

In general, one needs to consider that BSS techniques compute data transformations based on measures taken from the given data characteristics which are captured by contrast functions. The used contrast function, in turn, affects the output component morphology. For instance, the separation of atrial and ventricular activity addresses components of different nature (i.e. sub-Gaussian atrial and super-Gaussian ventricular [222, 264]) which possibly is not properly addressed by applying one single contrast function for all components in the BSS optimization. Also the measurement of component characteristics can be challenged regarding the question if all samples of the whole input data segment can contribute to an useful transformation. One respective approach is given by using parametrized BSS inputs. For instance, only R-peak values or values sampled from the ST-segment have been extracted as parameters of the measured signals, characterizing the signal as a subset of the available samples as input for BSS [47],[249].

3.4 APPLICATION OF BSS FOR PROCESSING ECG AND (CB)PPG SIGNALS

3.4.1 *BSS for ECG Processing*

3.4.1.1 *Applications of BSS to ECG*

Since its first application by Barros *et al.* [22] (1998), Blind Source Separation techniques have been applied in the ECG domain mostly to standard (contact-electrode) ECG recordings of standard clinical lead systems. Different PCA and ICA algorithms have been used to process three ECG leads with subsequent back-transformation of independent components resembling the cardiac components to obtain a noise-/artifact-free ECG in the measurement space [49, 101]. Atrial and ventricular activity have been separated by ICA in clinical 12-lead ECG of patients showing AF [222]. Several lead subsets of a standard clinical 12-lead ECG were processed with FastICA in [150]. Moreover, 12-lead ECGs have been reconstructed from independent components of a reduced three-lead ECG [258]. Also, the influence of typical noise types for processing standard ECG have been simulated on two-lead recordings from PhysioNet MIT databases. Specifically, beat detection accuracy in ECG originating from MIT arrhythmia and normal sinus rhythm database plus added simulated noise with and without JADE ICA have been investigated [151, 152]. FastICA has been applied in this context to MIT ECGs with added simulated noise by [4, 218]. Also, customized lead-sets were used as origin for ECG processing with BSS. Whereas [291] pro-

cessed an eight-lead thoracic ECG with ICA, standard ICA was compared to fICA and cICA on customized two-lead ECG [189].

Besides BSS's application to standard ECG, standard ICA as well as spatio-temporal ICA have been utilized for the processing of wearable tECG recordings of healthy subjects [290]. Moreover, abdominal ECG recordings are processed with PCA, [70], FastICA [262] and cICA [161] for facilitating the extraction of the fetal ECG.

In general, there is consensus on the benefit of processing ECGs signals with BSS methods in order to reduce noise and allow for the recovering of specific ECG features as the R-peak and RRIs. [47].

3.4.1.2 *Permutation Indeterminacy for ECG Processing*

In the context of ECG processing and ECG identification, the permutation indeterminacy has been addressed by two major strategies. The first strategy aims at identifying the undesired components (i.e. artifacts) for exclusion. Thus, it indirectly obtains the desired ECG component. This strategy has mostly been applied in setups with only a small amount (two/three) of BSS output components. Thereby, one can exploit, that higher order moments as kurtosis suits as ECG signal quality indicator with typical values higher than these of (Gaussian) noise [167]. Accordingly, pre-calculated kurtosis thresholds (lower bound) to identify noise in combination with intra-segment variance thresholds (upper bound) to identify artifact components (i.e. abrupt changes) have been applied [49],[101]. Components' periodicity by means of auto-correlation was exploited in [189]. Also, decision trees were used to classify artifacts in [152].

The second strategy aims at directly identifying the desired component (i.e., the ECG). Again, higher-order statistics have been utilized since e.g. kurtosis has been proposed as target of ICA optimization for ECG processing [291]. The selection of single channels by higher order moments was addressed in [218, 290]. Multiple ECG candidates as input of a multichannel post-processing were identified by utilizing kurtosis in [151]. Kurtosis ordering of heart activity components after ICA was used in [222]. Other approaches used template matching for single channel selection [4, 150, 258] and the amplitude of detected heartbeats [70].

Despite directly measuring signal statistics and features, the ECG develops a characteristic and distinct waveform, i.e. the QRS complex. The periodic nature of this waveform under physiological conditions offers an indirect way of identifying the ECG component within a BSS output by assessing detections of QRS waveforms (peaks). The maternal ECG of an abdominal ECG recording after BSS was identified by comparing pre- and post-BSS QRS detections [11] or the assessment of QRSs' periodicity [262]. A simple periodicity criterion was also applied to identify the ECG component inside the BSS output of an electroencephalogram (EEG) by using QRS detections in [98].

The identification of the cardiac component becomes unnecessary in case of using temporally constrained ICA, because only one single component may be extracted which

matches the given temporal reference. James and Gibson [129] identified the ECG component in the EEG ICA output by QRS time instants extracted from another simultaneously recorded signal. Lee *et al.* [161] realized the identification of the maternal ECG component from an abdominal ECG by using temporal a priori information. In this context, the signal covering the temporal constraint does not have to match the exact temporal behavior but should point the algorithm in the direction of the target component [131].

3.4.2 *BSS for cbPPG Processing*

3.4.2.1 *Applications of BSS to cbPPG*

Poh *et al.* [212] were the first to use BSS algorithms in the context of the cbPPG. Since then BSS algorithms became a core part of signal processing schemes to extract the heart rate from cbPPG recordings. Common approaches [94, 95, 99, 112, 153, 166, 212, 213, 260, 305] use different color channels (typically RGB) extracted from ROI, typically the face, as input to PCA or JADE. FastICA has also been applied to RGB signals [55, 166, 307] and achieved a slightly better performance in comparison to other ICA algorithms [55]. Tsouri *et al.* [259] proposed a constrained ICA for RGB information of a face ROI. Other researchers have further developed the idea of applying multispectral cbPPG to PCA and ICA but have used alternatives to RGB, namely combinations of RGB with orange and cyan channels or chrominance as well as hue, infrared and LAB color space based signals, respectively [81, 95, 113, 127, 174, 181, 273, 297].

In addition to wavelength-based considerations, more selective ROI choices like reducing the face ROI to a more concise area have been outlined in the context of BSS [55, 79, 112, 166, 181, 243]. These approaches seek to exclude regions that are not supposed to contribute with useful signals but can introduce distortions, e.g. by mouth movements during speaking/smiling or blinking eyes [166, 252]. Approaches, which are described in literature, typically rely on a spatial preselection and use multispectral information RGB as input to BSS techniques. Moreover, a monochrome cbPPG, extracted from the forehead, was used as input for spatio-temporal ICA [243]. Wang *et al.* [273] alternatively addressed spatial selection without using explicit face detection. The authors utilized the temporal behavior of pixel traces to distinguish skin-like areas showing temporally periodic content from motion-like content. Even Guazzi *et al.* [93] pursued the idea of spatially selecting ROIs according to the local distribution of signal quality. Qi *et al.* [216] simultaneously processed multiple ROIs by using Joint BSS.

Despite the frequent multispectral BSS use, there is no consensus on performance improvements by using BSS techniques with multispectral inputs. In particular, Kwon *et al.* [153] described a blurred spectral peak after applying RGB ICA as well as an increased heart rate error. Christinaki *et al.* [55] identified only subtle improvements but similar heart rate errors with/without using RGB ICA. Feng *et al.* [79] as well as Hassan *et al.* [99]

and Holton *et al.* [112] showed a lack of robustness by applying standard approaches that use ICA with RGB channels.

3.4.2.2 *Permutation Indeterminacy for cbPPG Processing*

Different approaches for addressing permutation indeterminacy while processing cbPPG with BSS have been outlined. Some approaches simply select a fixed (namely the second) component after transformation of the RGB channels [112],[113],[153],[212],[305] or even consider fixed position principle components [260] (e.g. the third [174]). Only two of these works briefly assess the results obtained for this selection [153, 174]. Some approaches address a distinct peak in the spectrum (caused by the cardiac pulse) by selecting the component with the maximum peak [55],[94],[213],[179],[181] or the maximum spectral SNR [20, 28], respectively. Alternatively, component selection based on cross correlation with an assumed heart rate [79] or other source signals in the Joint BSS context [216] was described. Others neglect an automated component selection [99],[143],[166],[243]. Excluding the artifact component instead of selecting the pulse component has also been proposed [149]. Another approach assesses the similarity of the de-mixing matrix to the expected composition of a pulse component from the RGB signals [95]. Also, [64, 154] do not propose an actual selection of the desired component but combine a sample of several randomly collected ICA results from several locations of the subjects face and the respectively derived heartrates for majority voting among the heartrates. A multitude of components is also combined in [267], where the first three PCA components of video-based respiration signals from different ROIs are selected for further combination.

3.4.3 *Problem Description*

During the extensive application of BSS to biosignal processing and the proposal of a large variety of BSS algorithms, many researches have addressed algorithmic comparisons in order to highlight performance differences between certain BSS algorithms on given datasets composed of ECG [49, 131, 189, 290] or cbPPG data [55, 94, 100, 112, 127, 154, 179, 216, 259, 288]. The essential benefit of applying BSS with respect to the input data, however, is not addressed as standard. Yet, in the ECG domain Milanesi *et al.* [189] uses a performance measure, which takes into account the sensor signal and a reference signal for the measurement of the BSS effect and also compares performance indices to the raw sensor data. [101],[129] and [290], on the other hand, provide only qualitative (signal) examples of comparisons between original sensor and cleaned signals. In the cbPPG domain, pre-/post- BSS assessment of signal quality or rather typical heart rate accuracy are more frequent [55, 99, 112, 153, 154, 174, 212]. Nevertheless, the characterization of BSS performance limits, i.e. the examination of beneficial and unfavorable conditions for its application, remains rare. One of the few exceptions for instance investigates the influence of technical parameters on cbPPG BSS performance [179]. Also, in the ECG domain, adding

simple simulated noise types (baseline wander, powerline interference and electromyogram (EMG)) to standard ECG recordings to e.g. assess beat detection accuracy is addressed by some researchers [4, 152, 218] in the BSS context.

Moreover, approaches to one of the major problems to harness any potential of BSS application, i.e. the permutation indeterminacy, have been proposed for several particular ECG and cbPPG applications. Still, these approaches typically merely appear as algorithm description without a quantitative evaluation of their actual selection performance.

Therefore, this work will focus on two main aspects (1) how can a particular BSS routine be applied to achieve a benefit by its application and what are the factors limiting its performance for contact-less biosignal processing and, (2) how can such benefits of BSS application anyway be exploited, i.e. how can permutation indeterminacy be solved. Thus, this work is laying the foundations for the practical application of BSS in innovative biosignal processing applications.

3.5 CHAPTER SUMMARY

Classical biosignal recording techniques as ECG or PPG are nowadays supplemented by contact-less recording techniques as cECG, tECG or cbPPG which allow for new (e.g. non-clinical) biosignal measurement scenarios. Related problems like non-standard signal nature or even decreased signal quality can effectively be addressed by exploiting the redundancy of multichannel measurements which are processed by data fusion techniques. Despite fusing features or parameters (e.g. heartrates) of multiple redundant channels, fusion on the raw data level serves an approach aiming at the improvement of the biosignal data quality prior to parameter extraction. Despite the Kalman filter approach, Blind Source Separation represents a data level fusion approach, which requires less modeling of both useful and noise signals compared to KF.

Typical BSS approaches are either based on second-order statistics which involve diagonalization of single or multiple covariance matrices (e.g. PCA), or are based on higher-order statistics (e.g. ICA). ICA approaches utilize the concept of statistical independence to separate multiple source signals. Original methods use minimum (mutual) information or maximum entropy approaches which are based on cumulant measures or neural network approaches. Subsequent ICA developments as πCA, cICA and fICA refine the ICA concepts in the context of particular applications as biomedical signal processing.

In the biomedical signal processing community, BSS techniques are frequently applied. However, it remains unclear, which inputs are beneficially processed by BSS application, i.e. under which circumstances the output signal quality or output parameter (e.g. heartrate) accuracy is improved by BSS. Also, the BSS's permutation indeterminacy requires an automated selection of the component of interest after the BSS processing. This problem is only unsatisfactorily (i.e. marginally) solved.

Tyrion: "My most trusted advisers are a eunuch and a sellsword, and my lady is a whore. What does that say about me?"

— George R.R. Martin in *A Clash of Kings* p.602, A Song of Ice and Fire (1998)

4

EXPLOITING THE POTENTIAL OF BSS FOR BIOSIGNAL PROCESSING

Given the principal applicability of a Blind Source Separation algorithm to separate source signals from signal mixtures, the practical outcome of applying this signal processing technique depends on, first, the selection of suitable input data capable of being handled by the respective BSS algorithm and, second, the ability to exploit the results of BSS i.e. by reliably selecting the source component of interest. This chapter provides descriptions of the experiments and algorithms conducted and developed to address the underlying characteristics and solve the two above stated problems. Contents of this chapter partially appeared already in own publications, i.e. [281, 282, 284, 286, 287]. Specifically, section 4.1 provides the experiments and algorithms related to the effect of BSS inputs on the BSS performance. Thereby, this work develops a new framework to assess BSS algorithm efficiency in the context of cbPPG. Section 4.2 describes the experiments and algorithms related to automated BSS output selection. Novel algorithms to solve permutation indeterminacy in the context of contact-less ECG recordings are presented. Finally, section 4.3 links the two problems input selection and output select-ability together by providing a joint evaluation.

4.1 SELECTION OF BSS INPUT DATA

Whereas in the ECG processing domain, the positive effect of applying BSS for signal quality enhancement and cardiac source separation (see section 3.4.1.1, p.63ff) is largely uncontroversial with permutation indeterminacy presenting the main problem of BSS's application, in the cbPPG domain, it is not [55, 79, 99, 112, 153]. Moreover, in the cbPPG domain it turned out that e.g. commonly applied BSS methods show weak performance on other databases than the ones proposed alongside the algorithms [100]. Accordingly, this doctoral work in the first part aims at figuring out whether BSS serves an appropriate processing tool for enhancing the cbPPG signal quality. Beneficial BSS variants for its application to cbPPG are to be designed. To this end, the following sections define investigations addressing the effect of BSS input characteristics on the outcome of the BSS application. First, simulated test data is constructed in order to model borderline cases of the BSS

model (see section 3.3.4, p.54ff) in the context of cbPPG. Employing such data intends to identify potential origins of BSS failure in cbPPG processing. Second, experiments for real cbPPG data are defined, which address controlled conditions for BSS input characteristics. Especially, input conditions are constructed which deal with the linearity assumption of the standard BSS model.

4.1.1 *BSS Benchmark Testing*

In order to test, whether certain input conditions in the context of cbPPG, respectively, BSS negatively affect the BSS performance (i.e. decrease the signal quality), simulated cbPPG data is constructed to meet specific borderline cases of the BSS model. Also selected real PPG data is added as a supplement. Three general aspects of BSS inputs are examined in this context namely, (1) the characteristics of the original source signals underlying the processed mixtures, (2) the characteristics of the mixtures to be separated by BSS and, (3) the effect of modifying the mixtures prior to processing by BSS. In the following, brief descriptions of these aspects are given as well as the according data creation is described.

SOURCE SIGNAL CHARACTERISTICS Common BSS algorithms restrict their outputs to be uncorrelated/white. Besides computational advantages, this restriction typically is motivated by ensuring the identifiability of the outputs, i.e. the uniqueness of the BSS solution. Moreover, the concept of statistical independence of the estimated source signals implies uncorrelated sources. This approach to source separation is also known as the "orthogonal approach" [38]. However, one has to challenge whether the source signals to be separated actually meet the orthogonal approach and what will be the result of a model violation (e.g. by cross-correlated sources [310]). Meinecke *et al.* [185] proposes a measure of reliability of the BSS result, which should be used to assess whether the underlying BSS model holds. This measure is tested alongside some controlled source signal characteristics which in part violate the standard BSS model.

In a cbPPG measurement scenario, the PPG typically serves the source signal of interest. However, also other source signals like sensor noise [200, 255] or different kinds of disturbances entering the measurement section, are simultaneously measured by a cbPPG. Specifically, any lack of explicit control of the lightning conditions during the recording induces a source signal characterized by the changing amount of light (e.g. ambient light) [10]. Moreover, subject motion with respect to the sensor induce motion artifacts originating from ROI fluctuation or alternating radiant flux at the measurement location [80]. Those additional source signals do not necessarily form an orthogonal system as imposed by the orthogonal approach. The influence of typical disturbance sources onto the BSS processing of cbPPG is to be investigated with special regard to deviations from the orthogonal approach. Since typical disturbances due to alternating light conditions and

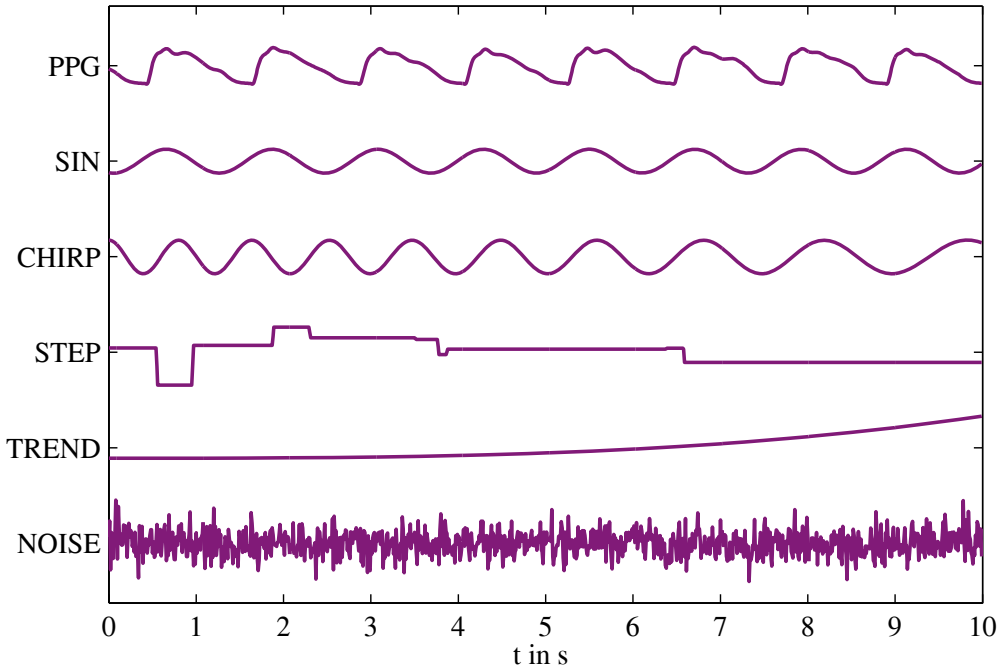

Figure 14: Exemplary artificial disturbance source signals for testing the dependency of BSS performance on source signal characteristics. From top down: PPG shows an exemplary synthesized PPG signal without distortion (see section 5.1.1), SIN shows a sinus function that is adapted to the PPG in phase and frequency, CHIRP shows a quasi-periodic chirp signal, STEP shows a random multi-step function, TREND shows a random monotonic third-power trend and NOISE shows a white Gaussian noise signal.

motions in the cbPPG context can be of different frequency and even periodic nature, the disturbance source signals are modeled by:

- periodic or quasi-periodic (non-monotonic) baseline alternation
- step functions or continuous (monotonic) baseline alternation
- white gaussian noise to model image respectively sensor noise [255]

Exemplary disturbances can be seen in Figure 14. Those signals are generated according to the following steps to obtain signals of 10 s duration. The periodic and quasi-periodic disturbance signals are partly phase-aligned with the PPG signals. This approach addresses a distinct violation of the orthogonal BSS approach. For each PPG segment, the peaks are detected by using a simple maximum search detector [223]. These peak detections are further used to extract the minimum, mean and maximum RRI in this segment. A sinus function is generated which matches the mean RRI. Moreover, this sinus function is phase-shifted to align the first maximum of the first PPG beat with a sinus maximum and thus, generate some violation of the orthogonal approach of BSS (see Figure 14 - SIN). The quasi-periodic disturbance signal is formed by a chirp signal generated with start frequency 3/2 times the maximum local heart frequency (minimum inverse RRI) and

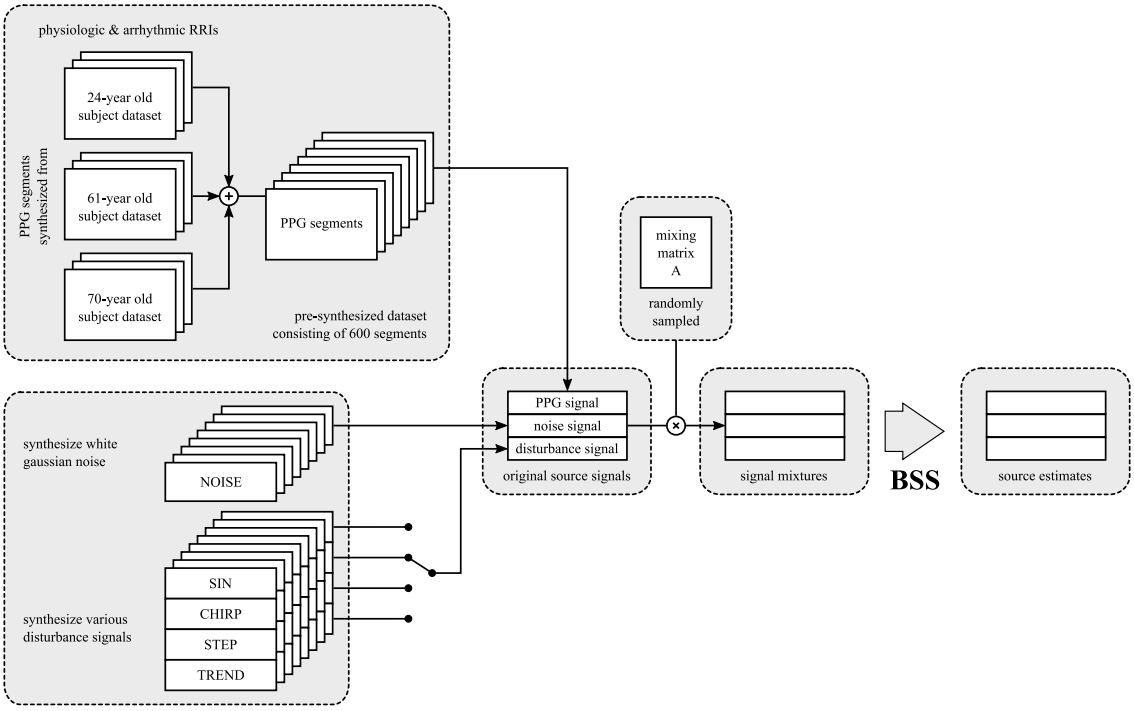

Figure 15: Test scenario for testing BSS source signal characteristics. Always, one synthesized PPG segment is assembled together with one white gaussian noise segment and one artificial disturbance signal. For each combination (with respect to the different disturbance signals SIN,CHIRP,STEP,TREND) one mixture matrix $\mathbf{A}$ is sampled to generate the mixture signals, i.e. four times 600 signal mixtures.

end frequency 2/3 times the minimum local heart frequency (maximum inverse RRI, see Figure 14 - CHIRP). In contrast to the (quasi-)periodic disturbances, the step functions and monotonic functions are completely random based. In order to generate a random step function, an integer $i \in [1, 10]$ representing the step number is sampled as well as the matching amount of real-valued step locations $x_i \in [0.1, 9.9]$. Finally, step heights for subsequent addition are randomly sampled from a normal distribution and the step function is sampled out of accordingly parametrized and scaled Heaviside functions (see Figure 14 - STEP). The monotonic trend function (see Figure 14 - TREND) is randomly sampled by parametrizing the third-power function $y = a \cdot x^3 + b$ by drawing two random points $y_1(x = 0\,\mathrm{s})$ and $y_2(x = 10\,\mathrm{s})$ from a uniformly distributed interval $[-1, 1]$. Lastly, a white Gaussian noise vector is sampled (see Figure 14 - NOISE).

The PPG signals utilized as source signals are synthesized to generate 10 s segments by using physiological and pathological RRI series as described in section 5.1.1. Accordingly, 600 different segments are available, which were down-sampled to sampling frequency $f_s = 100\,\mathrm{Hz}$. This sampling frequency serves a technically feasible frame rate for cbPPG recording which finds its application in methodological and clinical cbPPG studies (e.g. [217],[256]). Moreover, the real-world cbPPG data analyzed later (see also section 5.1.3.1, p.98ff) was recorded with $f_s = 100\,\mathrm{Hz}$. The segment length of 10 s serves a compromise between a proposed stationarity of the segment statistics while likewise ensuring extract-

ability of cardiac parameters from a single segment. This segment length also finds scientific application (e.g. [217],[256]).

The PPG segments each are assembled alongside disturbance source signals. Figure 15 depicts the general scheme of assembling combinations of original source signals. Because it is assumed that sensor noise is always present in the cbPPG measurement scenario, every PPG segment is assembled with one white gaussian noise signal plus another disturbance source. One obtains every combination out of PPG + NOISE + one disturbance source (i.e. SIN,CHIRP,TREND,STEP). The noise and disturbance sources are newly sampled for each PPG segment.

For each PPG segment, also one mixing matrix $\mathbf{A}$ is randomly sampled (from a Gaussian distribution) to obtain a symmetric BSS problem (the number of signal mixtures equals the number of sources, i.e. $m = n = 3$). The obtained signal mixtures are processed with the respective BSS methods (see also section 4.1.4, p.79f) whereas FastICA is configured to work on three different conditions, i.e. by using a sub-Gaussian, a standard (flexible) and a super-Gaussian contrast by adapting the FastICA's tanh non-linearity according to [123].

MIXTURE SIGNAL CHARACTERISTICS Signal mixtures are composed out of source signals by applying a designated mixture (i.e. $\mathbf{A}$) that induces a certain mixture signal characteristic.

Cao *et al.* [36] defines the concept of a decomposable mixture in the context of BSS such that the mixture signals have to meet some particularly geometrical criteria in order to be separable by BSS algorithms. Also, the mixture itself can define an underdetermined problem, which can only be handled under strong assumptions [67, 88], respectively lead to statistically independent mixtures which are not further separable [173]. A potential origin is given by phase differences in the signal mixtures that can violate the applied BSS model (e.g. the instantaneous mixture) from a temporal perspective. Moreover and especially in biosignals, which are measured by flexible non-standard minimum-contact systems, the measured mixtures (multichannel measurements) are likely to contain variable morphology. In addition, this morphology differences can be further amplified by the nonlinear system dynamics underlying the biosignals (i.e. the ECG and PPG [46, 82]), which are measured at different sensor locations. This variable morphology may express itself similar to phase differences or even show signals of different origin (with actual phase differences). For instance, the blood volume pulse and ballistocardiogram are available side by side in neighboring measurement locations [232, 257] in the cbPPG. In order to create underdetermined mixtures, simulated data including phase differences is constructed. The performance of standard BSS algorithms as well as time-structure based methods (like SOBI [26, 131]) potentially capable of compensating for phase differences is assessed on those mixtures.

Thereby, the typical application of BSS for cbPPG processing involves a fixed amount of input sensors (i.e. three color space based sensors - RGB) [213, 274]. Thus, the recorded mixtures are likely to represent an underdetermined mixture, i.e. less mixture signals than source signals recorded in the mixture are available. An underdetermined signal mixture is simply synthesized by applying a non-symmetrical mixture matrix $\mathbf{A}$ as

$$\mathbf{x} = \mathbf{A} \cdot \mathbf{s} \quad \text{with } \mathbf{A} \text{ a } \mathbb{R}^{n_2 \mathrm{x}\, n_1} \text{ matrix and} \quad n_2 > n_1. \tag{73}$$

Besides directly underdetermined mixtures, phase differences between sensors can introduce time-lagged versions of the same source signal which represent an indirectly underdetermined mixture because an artificial source signal is generated by the the time-lagged signal version. This behavior can be synthesized straightforward. For both above-mentioned signal mixture manipulations, the synthesized signals (PPG and noise/disturbances) described above are utilized.

Moreover, recorded signals which originate from the same source process (e.g. cardiac volume flow propagation) while showing different morphology and phase behavior at different measurement locations can introduce unsuitable mixture characteristics. Thereby, they can show mixed characteristics of the underdetermined mixtures described above. The real-world multisensor mattress data (described in section 5.1.2, p.97f) are utilized for testing such heterogeneously underdetermined mixtures.

MIXTURE SIGNAL MODIFICATION Before applying BSS to signal mixtures, signal mixtures might get modified to match a certain BSS model.

Non-stationary mixtures violate the standard linear BSS model. However, the measured mixture signals can be modified to meet the model. For instance batch-processing is a technique to modify mixtures by applying sub-sampling to collect only suitable data interesting for the de-mixing [47, 249]. Nevertheless, reducing the sample size especially in temporally structured signals increases the risk of artifacts [126]. Tests are conducted to verify the usage of batch-processing for cbPPG signal mixtures. Since it is previously unknown, which samples of a particular segment are suitable, tests are conducted, which randomly select certain amounts of samples from each segment.

Moreover, spatio-temporal BSS have successfully been applied to ECG [240, 290]. Despite its particular usage in Sun *et al.* [243], an application for cbPPG is rare. Accordingly, tests are designed to assess, whether forming spatio-temporal BSS inputs presents a meaningful mixture modification for the processing of cbPPG signals. Spatio-temporal BSS adds additional (time-lagged) versions of each measured signal to the BSS input [290] in order to achieve a higher BSS performance capable of deconvolution by building a delay vector reconstruction of each mixture signal. The amount of sample-wise time-lagged versions added to the input can be determined by considering the involved system dynamics of

interest. For instance, Sun *et al.* [243] states the reconstruction dimension m (see equation (72)) to be chosen as

$$m \geq f_s / f_{low} \tag{74}$$

with f_s the sampling frequency and f_{low} the lowest frequency of interest. Since the conducted tests are based on segments of 10 s length, Traube Hering Mayer waves are considered as lowest interesting frequency ($f_{low} = 0.1\,\text{Hz}$) which gives $m \geq 10 \cdot f_s$. However, for the utilized sampling rate $f_s = 100\,\text{Hz}$, $m \geq 1000$ serves a computationally unfavorable setup, i.e. convergent solutions to ICA becoming unlikely. Moreover, since only 1000 samples are provided for each 10 s segment given $f_s = 100\,\text{Hz}$ and BSS works on full-rank signal matrices $\mathbf{x}$, all time-lagged signals are shortened until full-rank matrices are present with respect to each time-lagged component. Thus, spatio-temporal dimensions $dim > 100$ are considered less useful in this setup and tests are performed starting from $m = 1$ (no time-lagged input signal) up to $m = 100$.

For both mixture signal modification tests, the synthesized signals (PPG and noise/disturbances) described above are utilized.

4.1.2 *Evaluation Metrics*

In order to assess the deviation of the BSS problem from the orthogonal BSS model $d_\perp$, the covariance matrix of the original sources $\mathbf{Cov}(\mathbf{s})$ is evaluated. For further simplification, the absolute deviations from an equally sized identity matrix $\mathbf{I}$ are summed up:

$$d_\perp = \sum_{i=1}^{n} \sum_{j=1}^{n} |\mathbf{Cov}_{ij}(\mathbf{s})| - \mathbf{I} \tag{75}$$

Since the simulated BSS problem is symmetric and all contributors (original signals, mixing matrix $\mathbf{A}$) are known, the BSS performance parameter ρ_{sy}, i.e. the cross correlation coefficient between y_{PPG} and s_{PPG} of the PPG component is computed. Also, *Meinecke's* online reliability measure U_i (see equation (70)) and further U_{max}, i.e. the maximum variance of all contributions U_i to the PPG component is calculated.

Moreover, to test other common context-specific quasi-online measures of the BSS performance, the spectral SNR [94] is computed for original signals, signal mixtures and BSS outputs. By using this measure, the strength of the cardiac pulse in the spectrum is assessed. First a binary spectral mask BM is computed

$$\mathrm{BM}^{f_{\mathrm{PPG}}}(f) = \begin{cases} 1 \text{ if } f \in [f_{\mathrm{PPG}} \pm 5 \text{ bpm}] \\ 1 \text{ if } f \in [2 \cdot f_{\mathrm{PPG}} \pm 5 \text{ bpm}] \\ 0 \text{ otherwise.} \end{cases} \tag{76}$$

$\mathrm{BM}^{f_{PPG}}$ sustains the spectral indices of the heart rate f_{PPG} as well as its first harmonic. The precision $\pm$ 5 bpm refers to the accuracy demanded for heart rate meters specified in ANSI/AAMI EC13:2002 [1]. Finally, the SNR is calculated from a given amplitude spectrum $X(f)$ by

$$\mathrm{SNR}^{f_{\mathrm{PPG}}} = 10 \log_{10} \left(\frac{\sum_{f=30\mathrm{bpm}}^{240\mathrm{bpm}} \mathrm{BM}^{f_{\mathrm{PPG}}}(f) \cdot X(f)^2}{\sum_{f=30\mathrm{bpm}}^{240\mathrm{bpm}} (1 - \mathrm{BM}^{f_{\mathrm{PPG}}}(f)) \cdot X(f)^2} \right). \tag{77}$$

Further, $\Delta\mathrm{SNR}_{orig}$ is defined as the difference between $\mathrm{SNR}_y^{f_{\mathrm{PPG}}}$ and $\mathrm{SNR}_s^{f_{\mathrm{PPG}}}$, i.e. the difference between the strength of the cardiac pulse in the BSS output y_{PPG} and the original source s_{PPG}.

4.1.3 *Experiments Definition*

SOURCE SIGNAL CHARACTERISTICS Three hypotheses are examined to investigate the impact of source signal characteristics on the BSS performance which are as follows.

(1-1) The orthogonality $d_\perp$ of the original source signals $\mathbf{s}$ which is defined by the disturbance source types SIN, CHIRP, TREND and STEP, does affect the BSS output parameters SNR, U_{max} and ρ_{sy}.
(1-2) Different BSS algorithms show different performance (i.e. SNR, U_{max} and ρ_{sy}) on different noise types SIN, CHIRP, TREND and STEP.
(1-3) The reliability of the solution $\mathbf{W}$ (U_{max}) and the reliability of the solution $\mathbf{y}$ (ρ_{sy}) does affect the practically relevant parameter SNR, i.e. the strength of the cardiac pulse.

For PCA, no U_{max} is calculated because a PCA itself is part of the U_{max} calculation and thus, $U_{max} \stackrel{!}{=} 0$.

MIXTURE SIGNAL CHARACTERISTICS The characteristics of the mixture signals are simulated to meet three different kinds of underdetermined mixtures.

(1) Common (directly) underdetermined mixtures are generated by using the same data and procedure as described above. However, this time underdetermined conditions are achieved by (a) assembling each of the 600 synthesized PPG segments with one NOISE signal and two randomly selected disturbance signals (SIN,CHIRP,TREND,STEP) and

mixing these four signals with a random mixing matrix $\mathbf{A}$ of dimension $\mathbb{R}^{3x4}$ ($\mathbf{W}$ is computed symmetrically - $\mathbb{R}^{3x3}$). Alternatively, (b) each of the 600 synthesized PPG segments is assembled alongside another randomly selected PPG signal from the data plus one NOISE and one randomly selected disturbance while again mixing these signals by a $\mathbb{R}^{3x4}$ matrix $\mathbf{A}$. As utilized above, the SNRs and ρ_{sy} are calculated as well as *Meinecke's* online reliability measure U_{max}. The hypothesis pursued by (1)(a) and (b) is:

(2-1) Different BSS algorithms show different performance (i.e. SNR, U_{max} and ρ_{sy}) on underdetermined mixtures ($\mathbf{s} : \{s_i \,|\, 1 \leq i \leq M\}, \mathbf{y} : \{y_j \,|\, 1 \leq j \leq N\}$ with $M > N$).

---

(2) In order to test indirectly underdetermined mixture conditions due to phase shifts between the original source signals, two test cases are conducted. (a) To test phase shifts in well-determined mixing scenarios, input signals are assembled by one PPG signal plus its phase shifted copy (phase shift $\tau \in [0, 100$ samples$]$ with step size 5 samples) and one NOISE signal. (b) The actually underdetermined case is modeled as described in (a) but by additionally adding one randomly selected disturbance signal and mixing the original sources with $\mathbf{A} \in \mathbb{R}^{3x4}$. The phase shift experiments are conducted on 100 randomly selected PPG segments out of the 600 overall segments. Since phase shifts are potentially covered by time-structure based methods like SOBI utilizing time-lagged covariance matrices, the SOBI algorithm is added to the BSS algorithm selection for these particular experiments by using SOBI with 10 time-lagged covariance matrices (see the convergence behavior of the SOBI performance in [26] to justify this configuration). The assessment measures are computed as described above. The following hypothesis is examined by these experiments (a) and (b).

(2-2) Phase shifts among BSS input signals (i.e. phase shifts within PPG signal mixtures) do affect the strength of the cardiac pulse (i.e. the SNR), the reliability of the solution $\mathbf{W}$ (U_{max}) and the reliability of the solution $\mathbf{y}$ (ρ_{sy}).

---

(3) For testing heterogeneous underdetermined conditions, i.e. combinations of directly (1) and indirectly (2) undetermined mixtures, real-world signals from the multisensor mattress (see section 5.1.2, p.97f) are processed with BSS. Specifically, 100 signal pairs each of one PPG and one coincident BCG segment are processed without additional mixing. It is assumed, that PPG and BCG originate from the same source process but show different phase and morphology and at least sensor noise is present such that both indirectly and directly underdetermined mixture characteristics are present in the measured signals. As evaluation metrics, pre- and post-BSS SNRs are calculated alongside *Meinecke's* online reliability measure U_{max}. The difference between post- and pre-BSS SNR is defined as ΔSNR_{BSS}. Accordingly, the following hypothesis is addressed.

(2-3) Different BSS algorithms perform different on heterogeneous (underdetermined) mixtures with respect to the SNR and the reliability of $\mathbf{W}$.

MIXTURE SIGNAL MODIFICATION The experiments addressing the effect of modifying signal mixtures prior to BSS application are based on the same synthetic data (PPG, NOISE, disturbances) as described above. Processing modified mixtures thereby implies the application of a mixture (i.e. $\mathbf{A}$) to original synthetic source signals and further modifying the obtained mixtures $\mathbf{x} = \mathbf{A} \cdot \mathbf{s}$. The two tested scenarios involve (1) the processing of only a partial amount of the mixture samples and on the contrary (2) generating additional data out of the mixtures and process the augmented data, both to achieve a higher BSS performance.

(1) Batch processing is realized by selecting batches each including a given percentage $\in \{10, 25, 50, 75, 90, 100\}$ % of randomly selected samples of each signal of the mixtures (i.e. a random sample of segment indices with respect to the batch size is computed and equally applied to each of the three mixture signals). Thereby, the mixtures are obtained by assembling each one of the 600 PPG segments together with one NOISE and one randomly selected disturbance (from SIN,CHIRP,TREND,STEP) and mixing symmetrically with $\mathbf{A} \in \mathbb{R}^{3\text{x}3}$. Afterwards, the de-mixing matrix $\mathbf{W}^*$ is calculated based on the batch of $\mathbf{x} : \mathbf{x}^*$ and the previously introduced performance measures SNR and ρ_{sy} (except U_{max} which is computed during BSS) are computed from the non-batch outputs $\mathbf{y} = \mathbf{W}^* \cdot \mathbf{x}$. Accordingly, the following hypothesis is examined.

(3-1) Batch processing of BSS inputs (i.e. processing only a partial amount of input signal samples $\mathbf{x}$ to compute $\mathbf{W}$) does affect the strength of the cardiac pulse (i.e. the SNR), the reliability of the solution $\mathbf{W}$ (U_{max}) and the reliability of the solution $\mathbf{y}$ (ρ_{sy}).

---

(2) Spatio-temporal BSS is realized by forming augmented inputs $\mathbf{x}^\tau$ out of sample-wise time-lagged copies of each signal of $\mathbf{x}$ with $\tau = dim - 1$ (with dim the spatio-temporal dimension) and $dim \in \{1, 2, 5, 10, 20, 50, 100\}$ (i.e. experiments are conducted individually for each dim resp. τ). Since the spatio-temporal BSS for cbPPG in [243] is based on [132], FastICA is used to solve the spatio-temporal BSS problem. Also, JADE is applied as a second algorithm because of its popularity in cbPPG processing. However, since JADE becomes impractical on large data dimensions [38], i.e. only non-convergent solutions are found, spatio-temporal dimensions $dim > 10$ are skipped for JADE. Again, the underlying mixtures $\mathbf{x}$ are obtained by assembling each one of the 600 PPG segments together with one NOISE and one randomly selected disturbance (from SIN, CHIRP, TREND, STEP) and mixing symmetrically with $\mathbf{A} \in \mathbb{R}^{3\text{x}3}$. Moreover, only the SNR is assessed as BSS performance measure, since first, unequal dimensions of original source signals and output

signals as originating from the above described construction of spatio-temporal inputs prohibits the calculation of sample-wise comparisons and second, the assessment of the variance of rotation angles (i.e. U_i) from artificially augmented inputs/generated outputs is considered being of limited use. The following hypothesis is examined.

(3-2) The spatio-temporal dimension *dim* of BSS inputs does affect the strength of the cardiac pulse (i.e. the SNR).

In addition, two experiments based on spatio-temporal BSS are conducted which especially violate the assumptions of the standard linear BSS model, i.e. by applying non-instantaneous mixtures. By applying the above described experiment configuration of spatio-temporal BSS first, a convolutive mixture is simulated by applying a random mixture $\mathbf{A} \in \mathbb{R}^{3\text{x}30}$ to time-lagged original source signals $\mathbf{s}^{\tau}$ with $\tau \in [0, 9]$. I.e. the three original source signals $\mathbf{s}$ each are ten-fold present (but with different time lag) prior to their mixing with $\mathbf{A}$. After the mixing, again three mixture signals $\mathbf{x}$ are available which represent the convoluted sources. Second, a non-stationary mixture is simulated by composing the mixture out of a fixed component plus a sample-wise varying component $\mathbf{A} = \mathbf{A}_{\text{stat}} + \mathbf{A}_k$ where $\mathbf{A}_k$ is sampled for each discrete sample $\mathbf{x}(k) = (\mathbf{A}_{\text{stat}} + \mathbf{A}_k) \cdot \mathbf{s}(k)$ from a standard normal distribution with standard deviation $\sigma = 0.05$ and $\mathbf{A}_{\text{stat}}$ is once sampled from a standard normal distribution with standard deviation $\sigma = 1$. The following hypotheses are founding these two experiments.

(3-3) The spatio-temporal BSS can compensate for convolutive mixtures, i.e. it unmixes a convolutive mixture and provides an output component y_{PPG} of comparable strength of the cardiac pulse (i.e. the SNR) as present in the original source s_{PPG}.
(3-4) The spatio-temporal BSS can compensate for non-stationary mixtures, i.e. it unmixes a non-stationary mixture and provides an output component y_{PPG} of comparable strength of the cardiac pulse (i.e. the SNR) as present in the original source s_{PPG}.

4.1.4 *BSS Algorithm Selection*

As presented in section 3.3 (p.36ff), there exists a multitude of algorithmic principles for solving the BSS problem. To cover this range, five BSS algorithms are selected as a algorithm base which represent the fundamental approaches behind BSS. Second-order approaches are to be represented by PCA. SOBI, which can also be understood as an multidimensional PCA is additionally used in the particular context of phase-delayed inputs. The concepts behind ICA are represented by FastICA, JADE and RADICAL. Despite being deduced from the minimum mutual information principle, FastICA can also be understood as an example of the maximum entropy approach because of its application of the test

functions G. The JADE algorithm represents the usage of cumulants to access higher order information in the context of statistical independence. Finally, RADICAL serves an actual application of the minimum mutual information principle. Spatio-temporal BSS inputs are also processed with the above named standard ICA algorithms. Other approaches as πCA, cICA or fICA are not further considered because of their strong dependency of additional context-specific configuration, e.g. πCA and cICA require additional information on the expected periodicity of the signal, which is typically not available.

4.1.5 *Spatial (Contextual) BSS Input Selection*

Whereas the previous investigations are mainly based on simulated data in order to allow for fully controlled input conditions, real cbPPG data can provide inputs to BSS which are controlled at least to some extent (i.e. selected parameters under consideration). The following section depicts the algorithms used for clustering real cbPPG data to investigate the influence of BSS input characteristics. Specifically, the spectral homogeneity of inputs is utilized to cover characteristics which influence the linearity of the mixing problem to be handled by standard linear BSS models. The following investigations have also been reported in Wedekind *et al.* [283],[286].

In order to evaluate BSSs' benefit in consideration of varying (in)homogeneous inputs, different BSS input sets S are defined for the cbPPG data available from the CardioVisio study (see section A.2, p.162f). Each input set contains three input signals to reflect the common number of input channels when RGB videos are used. The input sets differ regarding the wavelength(s) to be used and the frequency content of chosen ROIs (see section 5.1.3.1, p.98ff for available ROIs). Regarding the wavelength, it is distinguished between using the green channel or using RGB channels (monochrome vs. multispectral approach). Regarding the frequency content, it is distinguished between using ROIs, which show equal dominant frequencies and using ROIs, which show differing dominant frequencies (*dominant frequency* refers to the location of the global maximum in the fast Fourier transform

Table 1: **Definition of input sets S for BSS.** Set IDs refer to MC - monochrome, MS - multispectral, R - random SNR and standard ROI sets from F - Face and FhC - Forehead and Cheeks. *Note that in case of equal dominant frequency, three different input sets were evaluated for the three most occurring dominant frequencies.

SET ID	WAVELENGTH	FREQUENCY CONTENT	SELECTION	OVERALL SIZE
MC1	green	equal dominant frequency*	highest SNR	3 x (32x32)
MC2	green	differing dominant frequencies	highest SNR	3 x (32x32)
MS1	RGB	equal dominant frequency*	highest SNR	3 x (32x32)
MS2	RGB	equal dominant frequency*	highest SNR	3 x [3 x (32x32)]
MCR	green	equal dominant frequency*	random choice	3 x (32x32)
MSR	RGB	equal dominant frequency*	random choice	3 x (32x32)
F	RGB	n/a	ROI_F	whole face
FhC	RGB	n/a	ROI_{FhC}	suitable regions

of the cbPPG signal from a ROI after applying a Hanning window and zero padding to 4096 points). To select each three ROIs it is further distinguished between a deterministic choice and a random choice. The deterministic choice selects three ROIs which show the highest signal quality (SNR). For the random selection three ROIs, which possess the desired frequency content, are chosen randomly (independently of its signal quality). To give an example, the selection "equal dominant frequency + deterministic choice" means that ROIs are firstly ordered according to their dominant frequency. Afterwards the ROIs, which show the highest SNRs within the desired dominant frequencies, are selected. Note that it has to be defined, which dominant frequency is the desired one. As there is no unambiguous answer to this question, input sets are created for the three most often occurring dominant frequencies (i.e. for "equal dominant frequency" always three different input sets were used). A detailed mathematical definition of equal/differing dominant frequency and the definition of signal quality is described in the Appendix A.2, p.162f. Table 1 summarizes the resulting input sets.

The cbPPG signal of every set is normalized by a three-step procedure. The signal is linearly detrended followed by 0.5 Hz highpass filtering (fifth order Butterworth) to limit low frequency content below an expected heart rate [1]. Furthermore, the signal amplitude is normalized by subtracting its mean and dividing the result by signal's standard deviation. Every set S is further processed with PCA and ICA, respectively. The FastICA algorithm is chosen because Christinaki *et al.* [55] have shown a superior performance of FastICA compared to JADE for processing cbPPG to extract the heart rate. The FastICA is initialized with a fixed random demixing matrix $\mathbf{W}$ which is used as starting point for every processed segment. The FastICA is symmetrically conducted for dimension preservation between $\mathbf{x}$ and $\mathbf{y}$. The standard tanh-nonlinearity is applied as contrast function which supports super-Gaussian source extraction [123] as indicated for the PPG signal [259]. Simultaneously, it does not aim at highly super-Gaussian signals, which is a consequence of Morris *et al.* [195] selecting the PPG component after ICA by using the lowest kurtosis of the components.

The application of the above defined cbPPG sets investigates the performance of BSS to enhance the cardiac pulse from cbPPG in dependency to varying input data characteristics. To that end, the following hypotheses are examined.

(4-1) Varying BSS input sets S provide cbPPG of different SNR.

(4-2) cbPPG input sets of varying constitution and quality cause BSS to provide source estimates $\mathbf{y}$ of different quality (SNR), i.e. BSS application show an effect on the SNR that depends on the input set S.

(4-3) Different BSS algorithms show different output SNR performance on different input sets S.

4.2 APPROACHES TO PERMUTATION INDETERMINACY

In the previous section, the capacity of various BSS algorithms neglecting permutation indeterminacy was tested. I.e. it was addressed, whether a benefit in signal quality can be achieved by BSS processing. The matter of the following section, however, is to make use of the BSS achievements and present algorithms to solve permutation indeterminacy for BSS in the ECG and (cb)PPG domain. In the understanding of this doctoral work, there is no primary reason that a successful solution to permutation indeterminacy (i.e. select the best available BSS output of interest) is affected by differing BSS algorithms given that the BSS algorithms stick to equal conditions, e.g. a symmetrical BSS model. Consequently, the following algorithms solving permutation indeterminacy are based on outputs of one single BSS algorithm, namely FastICA, which is commonly applied to both ECGs [189, 290] and cbPPGs [55, 307].

Moreover, spatio-temporal BSS has been identified as suitable approach to the processing of nonlinear, temporally structured biosignals as the ECG [59, p.181ff] with motivations derived from the underlying nonlinear chaotic system dynamics [240] or the convolutive filter perspective [189, 203, 290]. However, the application of spatio-temporal BSS renders solving permutation indeterminacy even more complicated due to the large increase of output components in the case of standard symmetric BSS processing. Therefore, spatio-temporal BSS outputs serve a challenging task for algorithms to solve permutation indeterminacy. Spatio-temporal FastICA thus is utilized in the following to generate the BSS output for the processing of biosignals. The selection of the number of time-lags used for spatio-temporal BSS is kept constant, however, the relation between the delay-embedding dimension (i.e. the number of in-/outputs) and the select-ability of the component of interest is addressed in the next section.

4.2.1 *Permutation Indeterminacy for ECG Signals*

Below (sections 4.2.1.1, 4.2.1.2, 4.2.1.3), several algorithms to solve permutation determinacy for BSS processing of ECGs are described. The performance of the algorithms for BSS output channel selection is assessed using real ECG data of different origin (standard ECG, textile ECG, capacitive ECG), including recordings from both normal sinus rhythm and arrhythmia). See section 5.2 (p.101ff) for the description of the according data.

Each channel of each segment of the ECG data was normalized for further processing by subtracting its mean and division through its standard deviation. Time-delayed versions of the original signals were added as additional inputs to the multichannel filter. Spatio-temporal BSS using FastICA algorithm with the skewness maximization and 10 added time lags [281] ($k \in [0, 10]$ samples) was symmetrically applied to seven textile or capacitive ECG leads which resulted in 77 output components per segment. Two ambulatory ECG leads of the arrhythmia database were processed similarly producing 22 output

components per segment. In this context, the concept of skewness maximization by BSS refers to generating spike train signals out of the ECG which show distinct QRS spikes and a low noise level. The Figures 16(a) and 17(a) show examples of respective output components (labeled with "BSS"). Among the BSS output components of each segment, each one single component is selected by the respective selection algorithms.

The performance of the selection is assessed by the heartbeat detection accuracy (ACC) of the selected BSS output component for each segment. The accuracy was obtained by comparing the manual QRS annotations from the reference ECG with the QRS detections estimated from the component as follows:

$$ACC = \frac{TP}{TP + FP + FN} \tag{78}$$

In the case of the arrhythmia electrocardiogram (aECG), the pathologic beats are also expected to contribute to the true positive (TP) detections and were considered false positive (FP) or false negative (FN) otherwise (no true negative beats allowed). By comparing the different component selection algorithms, the following hypothesis is examined.

(5-1) Subsequent to a BSS processing by spatio-temporal FastICA, different BSS component selection algorithms automatically select components of different heartbeat detection ACC with respect to the underlying data tECG, cECG and aECG.

4.2.1.1 *Cascaded Output Selection*

In order to depict a component selection strategy based on traditional features of the time-/frequency domain, a novel cascaded selection algorithm (termed CASCSEL) is introduced. It combines two approaches: on the one hand to exclude unsuitable components (by identifying artifact components), and on the other hand to select single suitable components among the residual components. The following algorithm has also been reported in Wedekind *et al.* [281],[287]. The cascaded output selection is realized in three steps.

PRIMARY OUTPUT COMPONENT EXCLUSION A primary artefact exclusion is implemented by calculating the ratio of high frequency (HF) power $P_{HF}^{(1)}$ and low frequency (LF) power $P_{LF}^{(1)}$ of each output channel. $P_{HF}^{(1)}$ and $P_{LF}^{(1)}$ are derived from power spectral density $\mathrm{S}_X(f)$ estimate which has been calculated using periodogram. A high HF-power is expected for usable channels as maximizing skewness can be obtained by strengthening waveforms belonging to QRS complexes which contain a marked high frequency content (up to 40 Hz [5], see Figure 16(b) (black curve) for an expected $\mathrm{S}_X(f)$ behavior after applying spatio-temporal ICA). The upper bound of the investigated frequency range was set to 40 Hz. LF-power and HF-power are determined in the range of 0.1–5 Hz and 5–40 Hz,

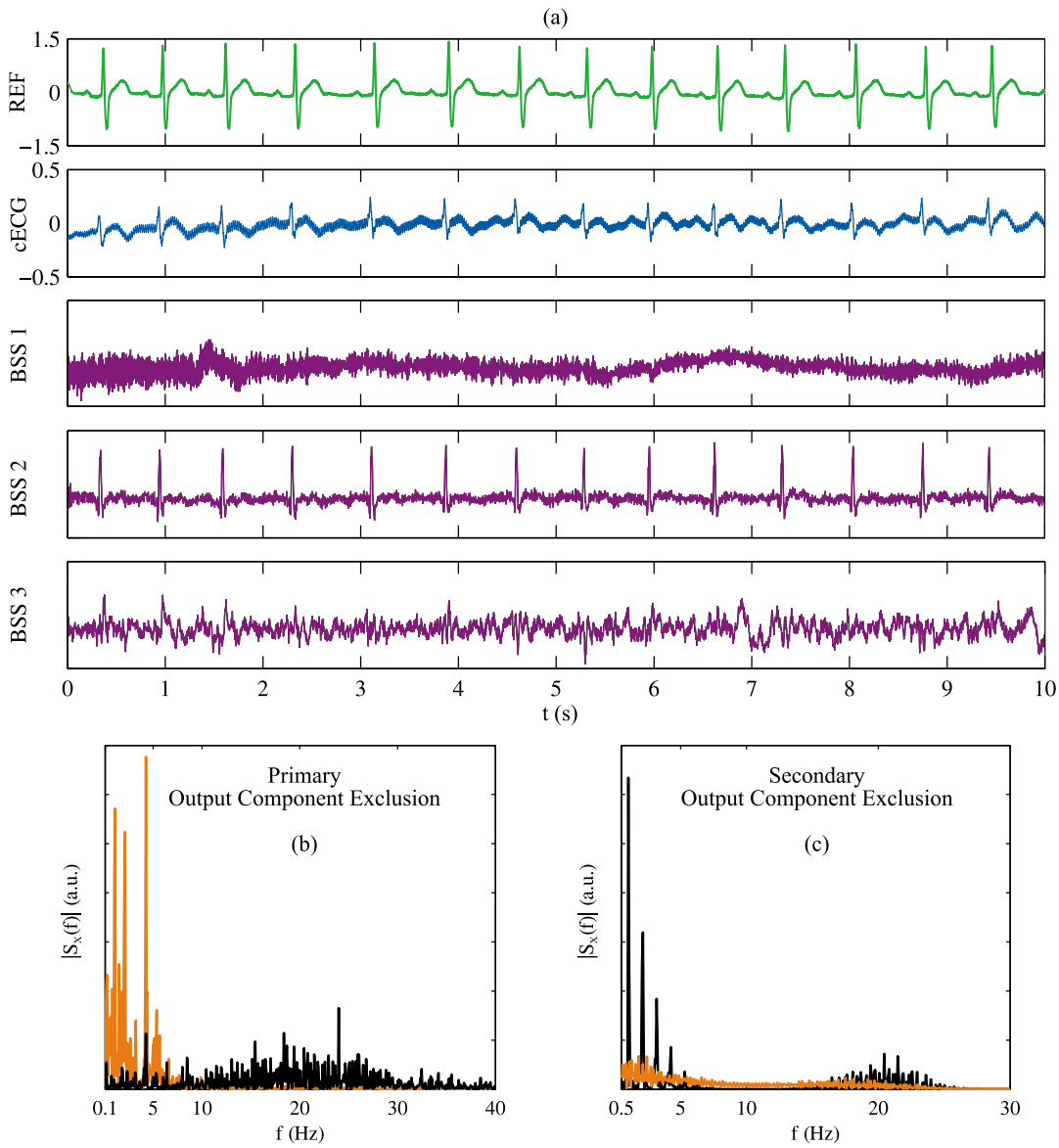

Figure 16: (a): Signal examples for cECG processing. Top panel: reference ECG REF (mV). Second panel: exemplary cECG channel (mV). Three bottom panels: Spatio-temporal ICA output component examples BSS 1-3 (a.u.). (b): Power spectral density $S_X(f)$ estimate for $CASCSEL$ primary output component exclusion (black curve shows $S_X(f)$ of BSS 2, orange curve shows $S_X(f)$ of BSS 3). (c): Power spectral density estimate $S_X(f)$ for $CASCSEL$ secondary output component exclusion (black curve shows $S_X(f)$ of BSS 2 and orange curve shows $S_X(f)$ of BSS 1, respectively after Pan Tompkins filtering). Figure contents appeared in [281].

respectively. The 5 Hz bound was introduced to separate potentially desired output signals from low frequency powered noise. At that stage, output channels are regarded as usable if it holds $P_{HF}^{(1)}/P_{LF}^{(1)} \geq 1$.

SECONDARY OUTPUT COMPONENT EXCLUSION A secondary channel exclusion is performed after post-processing of the remaining output channels from the first step. Application of a bandpass filter between 5–11 Hz, smoothed derivative filtering and squaring which is based on Pan and Tompkins QRS detection algorithm [207] aims at maximizing of QRS energy and reintroduces fundamental oscillations which are typically contained in an ECG (i.e. spectral peaks at the heart rate). An expected $\mathrm{S}_X(f)$-behavior can be seen in Figure 16(c) (black curve). Channels containing a relatively high LF-power are assumed to present desired waveforms. Consequently, power ratio estimation is performed on post-processed channels by now estimating LF-power in the range of 0.5–5 Hz, which encloses a recommended range for heart rate monitoring [1] and ensures the inclusion of expected harmonic oscillations of the heart rate inside $\mathrm{S}_X(f)$. HF-power is determined in the frequency range 5–30 Hz. A decreased upper frequency bound (30 Hz) compared to primary output channel exclusion is applicable due to limiting the high frequency content of the signals using the bandpass filter according to Pan and Tompkins. $P_{LF}^{(2)}/P_{HF}^{(2)} \geq d$ is used as criterion for a channel to be judged as usable. The initial threshold was set to $d = 1$ and allowed to decrease in the case of removing every remaining output channel with a given d.

BEST COMPONENT SELECTION After removing all potentially corrupted channels, $\mathrm{S}_X(f)$ (following post-processing based on Pan and Tompkins) is used to choose the best channel among the remaining output channels. Assuming distinct fundamental and corresponding harmonic oscillations containing the heart rate inside the frequency band 0.5–5 Hz of the desired signal (see also the black $\mathrm{S}_X(f)$ inside Figure 16(c)), the root mean squared error (RMSE) referring to the median of the $\mathrm{S}_X(f)$ inside this frequency band is calculated. A desired $\mathrm{S}_X(f)$ is expected to have a distinct deviation from its median inside the range of 0.5–5 Hz which contributes to a large RMSE. The channel with maximum RMSE is chosen to be the single desired output component.

4.2.1.2 *Sparse Coding Algorithm*

Whereas the above described procedure directly assesses feature representations of the signals, component selection can also be based on more abstract signal representations. For instance, the ECG develops a characteristic and distinct waveform (the QRS complex) which marks the main excitation of the heart muscle and can serve as a basis of an abstract signal representation. After all, the periodic nature of this particular waveform under physiological conditions results in the ECG's sparse nature [48]. This offers an indirect way of identifying the ECG component within a BSS output by assessing detections of QRS waveforms (peaks). The following investigations have also been reported in Wedekind *et al.* [285],[287].

Two novel approaches (termed *RCODE* and *PeriodTest*) to solve permutation indeterminacy aim at directly identifying ECG components in BSS outputs based on a sparse

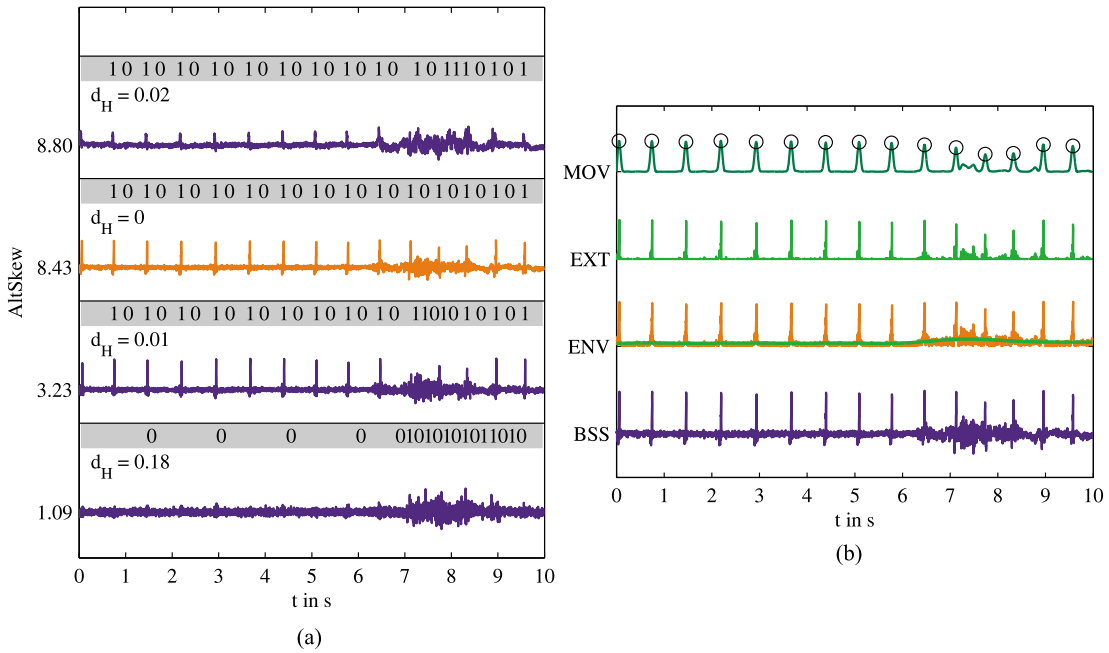

Figure 17: (a): Spatio-temporal BSS output components (excerpt) for tECG signals. Components are vertically ordered according to the alternative skewness measure ($AltSkew$). The modified Hamming distance d_H as well as the sparse code sequence of each output component are shown in grey bars. The $RCODE$ selection is marked by orange color and $d_H = 0$. (b): Data processing steps prior to the coding. Spatio-temporal BSS output channel (BSS) including its envelope (orange) and the lowpass-filtered (green) envelope (ENV), the extracted signal (EXT) and its moving window integrated version (MOV) including peak detections (black ∘). [285, 287].

representation of each component. The sparse representation itself, features QRS waveforms and their temporal behavior, expressed in the form of 'spike trains' typical for the spatio-temporal BSS on ECG [290]. Specifically, heartbeat detections derived from such spike trains serve as the input to the component selection. A component selection which is based on heartbeat detection consists of three major steps:

1. detection of peaks (both heartbeats and other peaks as large artifacts) in the output components
2. interpreting the temporal behavior of the peaks of each component
3. selecting one single component based on the above interpretation which most likely resembles the noise-free ECG component

Note that the second step requires an analysis of heartbeat dynamics that includes both false positive and false negative detections.

Before the peak detection, each component is pre-processed by highpass-filtering (0.5 Hz, 5th-order Butterworth) and lowpass-filtering (40 Hz, 5th-order Butterworth), a subsequent normalization (subtraction of the mean and division by its standard deviation) and an optional sign-change to ensure consistent positive heartbeat peaks.

PEAK DETECTION IN BSS OUTPUT COMPONENTS The main function of the peak detection in this context is to serve the basis for a sensitive subsequent interpretation, thus achieving a balance between sensitivity to distortions and likewise the ability to detect peaks in the presence of distortions. The essential processing steps prior to peak detection are shown in Figure 17(b). First, the envelope (ENV) is calculated for each BSS component using Hilbert transformation. A spike train signal is formed by extracting (EXT) the signal content above the lowpass-filtered (0.5 Hz, 5th-order Butterworth) envelope. This procedure intends to suppress distortions typical for relative motions between electrode and body surface in minimal-conductive ECG recordings. Peaks are further consolidated by moving window integration (MOV) using a 0.1 s Hamming window (considered as QRS length [52]). Finally, peaks are detected by applying a customized QRS-detector of the combined maximum-search [223] and the Pan-Tompkins [207] logical detection principle on MOV. In this context, the 'spike trains' typical for spatio-temporal BSS processing are robustly addressed by the detection principle of the simple maximum search detector [223]. However, the broad range of heart rates covered by the data as well as the arrhythmic events render the fixed heart rate guess of the maximum search detector to be impractical. Therefore, the maximum search detector is combined with the beat-to-beat decision logic and threshold-adaption of the Pan-Tompkins QRS-detection algorithm detecting one beat after another [207].

Whereas for the later assessment of the component selection (final heartbeat detection) a refractory period of 0.3 s is utilized on the original BSS component, the QRS-detector's refractory period is decreased to 0.05 s prior to the selection on MOV to achieve high sensitivity to artifacts in terms of a contrast for the component selection.

INTERPRETATION OF PEAK DETECTIONS I (RCODE) In order to interpret the peak detections from the above procedure, two different algorithms are applied. The first delivers a quasi-continuous measure between the expected behavior of a cardiac component consisting of peak detections followed by a reasonable time between subsequent peaks and differently pronounced deviations from this behavior up to a lack of multiple detections. This measure refers to as modified Hamming distance d_H. It is derived from a sparse code representation of the peak detections. The distance is calculated for each component's peak detections at times t_i ($i \in [1, I]$, I is the number of peak detections) by coding according to the dictionary {peak - 1, no peak - 0} together with physiological temporal a-priori information. The cardiac refractory period Δt_R is considered as 0.3 s [11], whereas the maximum peak-to-peak distance Δt_{max} is considered as 1.5 s (i.e. a minimum heart rate of 45 bpm [55]). Accordingly, a sequence $(x) \in \{0, 1\}$ is obtained as follows.

1. $(x_i) = 1$ with $i \in [1, I]$
2. add $\lceil (t_{i+1} - t_i)/\Delta t_{max} \rceil$ zeros between x_i and x_{i+1} if $t_{i+1} - t_i > \Delta t_R$
3. add $\lfloor (t_1)/\Delta t_{max} \rfloor$ zeros to (x) at $t < t_1$
4. add $\lfloor (10 - t_I)/\Delta t_{max} \rfloor$ zeros to (x) at $t > t_I$

The sequence (x) of final length L is further evaluated by the modified Hamming distance d_H which is designed to indicate the distance from the expected code behavior assuming a perfect ECG component with code $(x) = 1, 0, 1, 0, \dots$ or $(x) = 0, 1, 0, 1 \dots$, respectively.

However, subjects with very low heart rate (≈ 45 bpm) or arrhythmia even under perfect peak detection (ACC $= 1$) can feature sparse code patterns like $(x) = \dots, 1, 0, 0, 1, \dots$ or $(x) = 0, 0, 1, \dots$ and $(x) = \dots, 1, 0, 0$ at the beginning/end of the code sequence, respectively. To avoid negatively judging codes of such origin, these patterns are identified in each output component of a segment. Moreover, if there is temporal coincidence of these patterns (< 50 ms) in multiple components of the same segment, very low heart rate or arrhythmia is considered to be apparent in the segment. One "0" of the respective (0,0) code pairs is removed from the sequence (x) of the affected components in the case that none of the other components has already shown perfect ($(x) = 1, 0, 1, 0, \dots$) behavior.

After completing the code generation and manipulation, the modified Hamming distance distinctly evaluates single code pairs whether they show desired or non-desired patterns with respect to the expected cardiac pattern. Contrary to that, a common Hamming distance would serve a simultaneous distance measure between all code elements and the expected binary pattern. The modified measure d_H consists of two factors

$$d_H = w_d \cdot d_{10} \tag{79}$$

where d_{10} forms a distance to the expected behavior assessing only pairs of two subsequent code elements (x_i, x_{i+1}) each. It is defined by the ratio between the amount of non-desired code pairs (0,0) or (1,1) and the total amount of code pairs

$$d_{10} = \frac{|\{(x_i, x_{i+1}) | (x_i, x_{i+1}) = (0,0) \cup (1,1)\}|}{L - 1} \tag{80}$$

with $i \in [1, L-1]$.

w_d factors the length of the longest continuous sequence $(x_i, x_{i+1}, \dots) \subseteq (x)$ of the expected ECG code behavior where all pairs of subsequent code elements suffice $(x_i, x_{i+1}) = (1,0) \cup (0,1)$. Accordingly,

$$w_d = 1 - \frac{l_{10}}{L - 1} \tag{81}$$

where l_{10} is the length of the longest continuous sequence. If $I = 1$, d_H is set to 1. Examples of code sequences (x) and derived distance measures d_H are shown in Figure 17(a).

INTERPRETATION OF PEAK DETECTIONS II (PERIODTEST) The second algorithm is a simple periodicity test (PeriodTest) based on the peak detection evaluation proposed by Hamaneh *et al.* [98] which aims at the binary classification into periodic and non-periodic detections. It consists of the following three conditions for classifying a series of peak detections at times t_i ($i \in [1, I], I$ the number of peak detections) and the series of the according inter-beat intervals (Δt in s) with $\Delta t_i = t_{i+1} - t_i$ and its median Δt_{med} as periodic (and non-periodic otherwise) [98]:

1. $1/\Delta t_{med} \geq 2/3$
2. $1/\Delta t_{med} \leq 3$
3. $|\{\Delta t_i | \Delta t_i < 0.75 \cdot \Delta t_{med} \cup \Delta t_i > 1.25 \cdot \Delta t_{med}\}| < 0.2 \cdot (I - 1)$

Besides the frequency limitation with respect to the median peak-to-peak interval, the amount of single peak-to-peak intervals deviating more than 25% from their median is limited to 20%. The result of the periodicity test is given as Hamaneh criterion HC = 0: periodic peak detections (cardiac component candidate) or otherwise HC = 1: non-periodic peak detections (other component).

SELECTION The component with the minimal d_H or Hamaneh criterion HC = 0 is selected as $RCODE$ or $PeriodTest$ output, respectively. In the case of obtaining multiple components with equal minimum d_H or HC, a further selection is necessary to obtain a single output component for each selection routine. The application of spatio-temporal BSS with skewness maximization aims at 'spike trains' as cardiac output components. In order to evaluate the quality of the spike train in cardiac component candidates, a measure similar to skewness but focused on the peaks only is applied. A peak energy vector E_p is formed by the maximum peak value of the preprocessed component around each peak detection $E_{p,i} = \max_{t_i \pm 25\,\mathrm{ms}}(BSS)$. The $AltSkew$ measure assesses the average absolute peak energy of $E_{p,i}$ divided by its standard deviation:

$$AltSkew = \frac{\frac{1}{I}\sum_{i=1}^{I} |E_{p,i}|}{\sqrt{\frac{1}{I-1}\sum_{i=1}^{I}(E_{p,i} - \overline{E_p})^2}}. \tag{82}$$

Accordingly, highly energetic peaks of similar amplitude provide a high $AltSkew$. Examples can be seen in Figure 17(a) where components are vertically ordered with respect to $AltSkew$. Among the components with equal minimum d_H or HC, the single component with the maximum $AltSkew$ is selected.

4.2.1.3 *Standard Approaches to ECG Component Selection*

In order to facilitate a comparison to traditional BSS component selection methods using higher-order statistics [101, 151, 218, 222, 290], a single component selection based on skewness and kurtosis, respectively, is also applied. To achieve measures which are less affected by outliers, an outlier-removal using Walsh's non-parametric outlier test [270] was performed on each component prior to selecting the component with the highest skewness ($SKEW$) or highest kurtosis ($KURT$). This investigation is also part of Wedekind *et al.* [287].

4.2.2 *Permutation Indeterminacy for PPG Signals*

As described in section 3.4.2.2 (p.66), permutation indeterminacy for cbPPG is only unsatisfactorily solved, too. Wedekind *et al.* [284] already reported some initial investigations and discussions about permutation indeterminacy for cbPPG. However, this doctoral work will not continue on this topic and instead focus on permutation indeterminacy for ECGs. Transferability of the ECG algorithms to cbPPG permutation indeterminacy is discussed later on.

4.3 LINKING INPUT COMPOSITION AND OUTPUT PERFORMANCE OF BSS

While there exist theoretic guidelines to choose a delay-embedding dimension (i.e. the number and maximum time-lag used for spatio-temporal BSS input construction), the actual choice in practice is subject to accuracy optimization in the output of the filter technique (e.g. BSS) [59, p.173]. However, any obtained accuracy improvement in the output is only exploitable in practice, if the maximum accuracy output can also be selected by a given algorithm solving permutation indeterminacy. Accordingly, the relation between the number of added time-lags with the achieved maximum output accuracy/quality together with its select-ability (i.e. the ability of automatically selecting the best available output) is investigated. Because the positive effect of BSS for ECG is unambiguous, this test is performed for ECG data and the above described ECG-based algorithms for solving permutation indeterminacy (see section 4.2.1, p.82ff).

Accordingly, the respective algorithmic and data framework of section 4.2.1 is used to examine whether the spatio-temporal dimension *dim* affects first, the maximum accuracy $\mathrm{ACC}_{\mathrm{max}}$ of the BSS output components, and second, the relative accuracy of the automatically selected output $^{\mathrm{ACC}_{\mathrm{sel}}}/_{\mathrm{ACC}_{\mathrm{max}}}$. The hypotheses are as follows.

(6-1) The spatio-temporal dimension *dim* of BSS inputs affects the maximum reachable heartbeat detection accuracy $\mathrm{ACC}_{\mathrm{max}}$ of the BSS output.
(6-2) The spatio-temporal dimension *dim* of BSS inputs affects the relative heartbeat detection accuracy $^{\mathrm{ACC}_{\mathrm{sel}}}/_{\mathrm{ACC}_{\mathrm{max}}}$ of the selected BSS output component.

4.4 CHAPTER SUMMARY

A positive effect of BSS for multichannel biosignal processing depends on either how well the signal mixture, that is processed with BSS, fits the underlying BSS model or how well the particular BSS algorithm tolerates model violations. Moreover, in a practical processing setup using BSS, any improvement of signal quality can only be harnessed, if the particular output of improved quality can be extracted out of the BSS output, i.e. permutation indeterminacy can be solved.

This chapter defined a set of experiments which on the one hand address the first aspect of characterizing BSS methods given different conditions. These experiments are based on simulated as well as real-recorded (cb)PPG data and highlight the influence of certain characteristics of original signal sources, (recorded) signal mixtures and specific BSS models on the performance of BSS in terms of signal quality and the reliability of the BSS solution. On the other hand, algorithms are proposed that solve permutation indeterminacy for multichannel ECG processing with spatio-temporal BSS. Experiments are defined that apply these algorithms in the context of contact-less ECG recordings and arrhythmia. Also, this data and algorithm framework is used to investigate the relation between the BSS model configuration (input characteristics) and the usability of potential BSS-based signal quality improvements regarding their select-ability in terms of a solution to permutation indeterminacy.

Jamie: Not a great host, all in all, fewer than a thousand men in total.
Numbers were the last thing needed in Riverrun.

— George R.R. Martin in *A Feast for Crows* p.562, A Song of Ice and Fire (2005)

5

DATA MATERIAL

This chapter provides descriptions of the data that is utilized to address the above raised scientific questions. For that purpose, section 5.1 describes the generation of simulated (cb)PPG data as well as the data collected from healthy and clinical subjects. Section 5.2 accordingly describes the ECG data which were assembled from contact-less ECG recording techniques applied to healthy subjects as well as the pathological ECG data used for the experiments. Contents of this chapter partially appeared already in own publications, i.e. [286, 287].

5.1 CBPPG DATA

5.1.1 *Synthesized PPG Data*

PPG WAVEFORM MODEL The photoplethysmographic waveform is composed of a pulsatile "AC" component depending on the heartrate and its variability plus other influences as stroke volume and vessel properties and a "DC" component which relates to the tissue and average blood volume at the measurement location. The AC component is characterized by two phases, i.e. the anacrotic[1] and the catacrotic[2] phase. Moreover, the DC component slowly varies due to respiration and other low-frequency regulatory processes as e.g. Traube Hering Mayer waves. [6]

Synthesizing a PPG waveform has the advantage, that the true signal-to-noise ratio can be computed. On the contrary, any real (recorded) PPG waveform will already contain an amount of noise. The generation of synthetic PPG waveforms e.g. to verify measurement equipment can be based on hardware oscillators [266]. Also, software modeling has been applied to PPG including arrhythmia [115, 119, 236, 272].

Huotari *et al.* [119] models the peripheral PPG waveform by five log-normal functions (log-normal refers to $\log(\mathbf{x})$ being normally distributed) which resemble the percussion (systole, left ventricle contraction), tidal (systole, elasticity of the aortic wall), dicrotic

1 upstroke phase of the PPG beat during systole
2 downstroke phase of the PPG beat during diastole together with wave reflections, i.e. a dicrotic notch

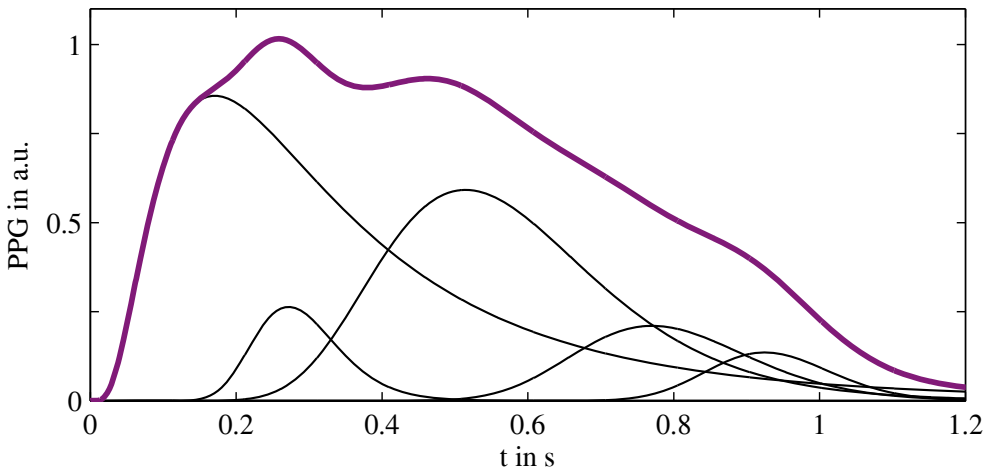

Figure 18: Synthesized PPG sample beat (purple) using the PPG model of [119]. The waveform consists of five log-normal components (shown in black). Model parameters are sampled from the parameter distributions of the 61-year old male subject in [119] (see also Table 4 in the appendix A.1, p.161).

(diastole, reflection from lower body bifurcation), and two pre-systolic components (re-reflections during the end of diastole). The i-th component s_i is given by

$$s_i(t) = \frac{a_i}{\sqrt{2\pi} \cdot \sigma_i \cdot t} \cdot \exp\left(-\frac{(\log(t/\mu_i))^2}{2 \cdot \sigma_i^2}\right) \quad \text{with} \quad i \in [1, 5] \tag{83}$$

with a_i a factor, μ_i the mean and σ_i the standard deviation. The resulting weighted, time-shifted, and time-scaled components further are linearly summed up. Huotari *et al.* [119] also present detailed parameter estimates for the respective five components of three male subjects (age 24, 61, 70). This serves an advantage compared to other contributions which combine two Gaussian functions with one Gamma function [115] or utilize an adaptive amount of multiple Gaussians alone [272] to model the BVP (i.e. the PPG), because these parameter estimates can directly be used to synthesize realistic waveforms. Accordingly, the Huotari-model [119] is used to generate PPG waveforms by applying the documented parameter estimates which can be found in the appendix (see A.1 Table 4, p.161). A sample synthesized PPG using this model is shown in Figure 18.

Whereas the model mentioned above have been used to analyze recorded BVP waveforms and thus work on a given (i.e. recorded) rhythm, the synthesis of PPG waveforms requires an additional modeling of the rhythm for combining multiple PPG beats. In this context, Sološenko *et al.* [236] propose a PPG model based on RR interval (RRI) information. Specifically, the authors develop a distinct scaling of amplitude and phase for the systolic and diastolic part of each single PPG beat which depends on the RRI of the preceding beat. Each single beat $s_k(t) = \sum_i s_{k,i}(t)$ formed of the i components is divided into a systolic ($t < t_p$) and a diastolic part ($t \geq t_p$) with t_p the time of the largest positive peak.

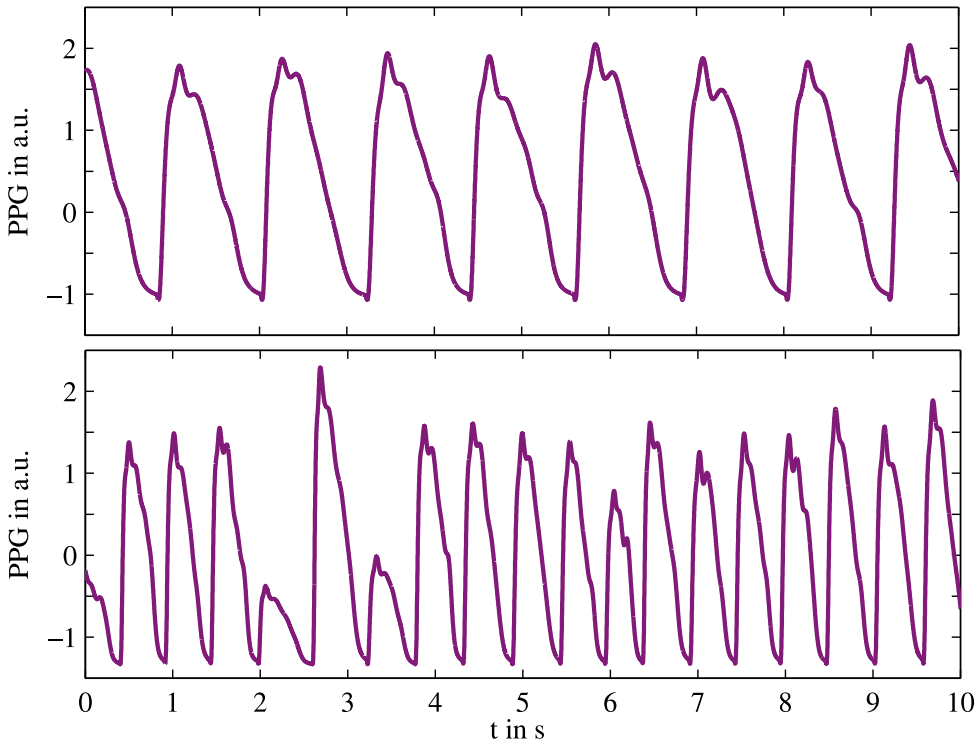

Figure 19: Synthesized PPG segments using the PPG model of [119] and the amplitude and phase scaling of [236]. The PPG model parameters are sampled from the parameter distributions of the 61-year old male subject in [119] (see also Table 4 in the appendix A.1, p.161). A physiological example (upper panel) and an arrhythmic example (lower panel) is shown. The underlying rhythm of the arrhythmic PPG is sampled from PhysioNet [89] MIT-BIH Arrhythmia Database [194] recording 215.

The scaling is performed by (compared to [236], these equations are adapted to work with positive time only):

$$s_k^*(t) = \begin{cases} b_k \cdot s_k(c_{s,k} \cdot t) & 0 < c_{s,k} \cdot t < t_p \\ b_k \cdot s_k(t_p + c_{d,k} \cdot (t - t_p)) & t_p \leq t < \infty \end{cases} \tag{84}$$

with b_k the amplitude scaling factor and $c_{s,k}$ the systolic and $c_{d,k}$ the diastolic phase scaling factor, of the k-th beat (see [236] for details on how to calculate the scaling factors). The scaled beats afterwards are lined up with respect to the RRI series. Figure 19 shows two examples of 10 s PPG segments using the above described amplitude and phase scaling. Given are a physiological (upper panel) as well as a arrhythmic (lower panel) PPG example where the latter was generated with RRI intervals from the PhysioNet [89] MIT-BIH Arrhythmia Database [194].

DATASET GENERATION Using the PPG waveform model of Huotari *et al.* [119] as well as the PPG amplitude and phase scaling model of Sološenko *et al.* [236] as described above, the synthetic dataset generation consisted of (1) sampling single PPG beats, (2) sampling

RRI series, (3) assembling PPG signals by scaling and stringing single beats together with respect RRI series obtained in the previous step and (4) sampling 10 s segments from the PPG signals.

Since Huotari *et al.* [119] described their PPG model together with the explicit statistics of three subjects (i.e. a 24,61 and 70-year old male subject), the synthetic dataset was generated by separately using these three model distributions. Specifically, the described PPG model utilizes five log-normal distributions to model a single PPG pulse, whose model parameters were given in [119] and are documented in Table 4 (appendix A.1, p.161). In order to synthesize a single beat, parameter sets for the five components of each beat were sampled randomly from the given model parameter distributions. For each of the three subjects model parameters, N = 100 beats were synthesized at a sampling frequency f = 1000 Hz. Figure 20 shows the accordingly generated beats for each subject's model.

The PPG model of Sološenko *et al.* [236] allows for assembling single PPG beats by underlying RRI series. The synthetic PPGs were generated from normal as well as arrhythmic RRI series. The physiological RRI series were obtained by randomly sampling RRIs from a standard normal distribution with a standard deviation of 30 ms (see [3], the distribution mean was selected 1000 ms for the model based on the 24 and 70-year old subject resp. 1200 ms for the 61-year old subject). Moreover, respiration (12 bpm) as well as Traube Hering Mayer waves (0.1 Hz) [6] were sinusoidally superimposed to the RRI intervals each with a standard deviation of 30 ms. Finally, the RRI series were re-normalized to meet the specified mean and standard deviation. The pathological RRI series were sampled from the PhysioNet [89] MIT-BIH Arrhythmia Database [194], namely the recordings 107,210 and 215. From the PhysioNet-given beat annotations, those segments were randomly selected that contain as many as possible premature beat annotations of any kind. For both physiological and pathological RRI series, segments were build/extracted to allow for generating PPG signals each consisting of N = 100 subsequent beats.

By applying the model of Sološenko *et al.* [236], the single PPG beats from the first step now were aligned (and scaled in amplitude and phase) with the RRI series derived in the second step. Figure 19 serves one excerpt each from a physiological and a pathological PPG signal. Specifically, the N = 100 single beats sampled from each subject's model distribution were utilized to generate PPG signals consisting of 100 subsequent beats by using first, one physiological RRI series and second, one pathological RRI series (MIT-BIH recording [194] assignment for pathological signals with [119] beat model pursuant (24 years old subject: RRI from recording 107, 61 years old subject: RRI from recording 215, 70 years old subject: RRI from recording 210). Moreover, the transitions of the scaled subsequent beats were smoothed by a ten-sample moving average filter applied to ±15 samples of the transitions between each two subsequent beats. Thus, six PPG signals each consisting of 100 PPG beats were obtained.

Finally, N = 100 segments of 10 s duration were randomly sampled from the six continuous PPG signals generated in the previous step. Accordingly, a total amount of 600 seg-

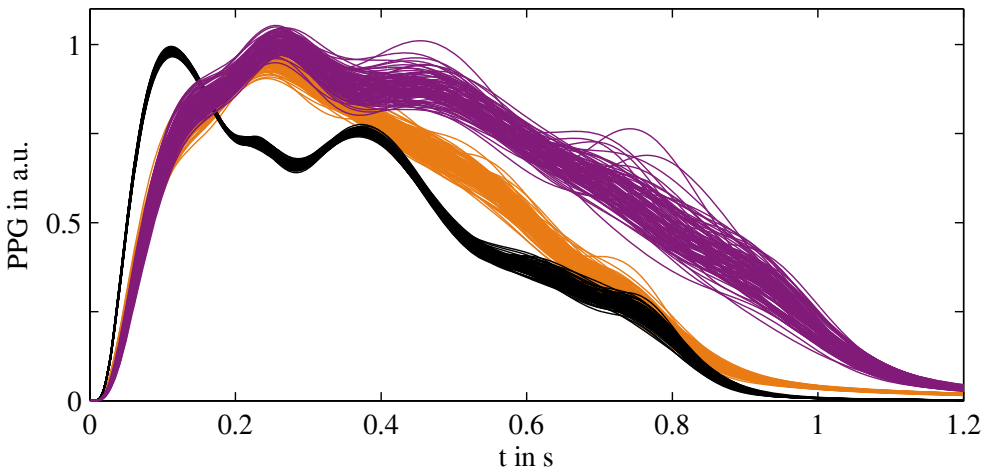

Figure 20: Synthesized PPG beats using the PPG model of [119]. Shown are N = 100 beats each sampled from the model parameter distributions of the 24-year old (black), the 61-year old (purple) and the 70-year old subject (orange). The model parameters can be found in Table 4 in the appendix A.1, p.161).

ments were synthesized based on the model distributions of three subjects together with six RRI series (three physiological and three pathological series).

5.1.2 *Data from Healthy Volunteers*

BVP DATA FROM THE MULTISENSOR MATTRESS In measurements setups addressing the BVP by cbPPG, BCG signals (mechanical expression of heart activity) are available in regions close to those showing PPG waveforms [232]. Thus, while processing multiple ROIs from e.g. facial videos, heterogeneous signals can be expected which simultaneously or alternately contain characteristics of both waveforms. A dataset with signals of both origins is used to model effects of alternating signal characteristics in the context of BSS for cbPPG processing.

In experiments measuring supine subjects with a multisensor mattress Hetzel [109] and Henning [103] utilized a piezo film to gather a dorsal BCG similar to common BCG (which is measured in longitudinal fashion) [103, p.65f,p.72f]. Simultaneously, a PPG was measured both dorsally and using an ear clip [103, p.98ff],[109, p.33]. The measurements obtained from this setup are based on a protocol comprising breathing maneuvers and motion tasks [109, p.35]. For this thesis, data was extracted from these experiments from a motion-less phase with spontaneous breathing. Figure 21 shows a signal excerpt from this dataset.

The multisensor mattress data were recorded during the master thesis of Hetzel [109] at the Institute of Biomedical Engineering (IBMT), TU Dresden. The mattress comprised sensors for recording cECG, BCG (piezo film, [103, p.68f]), PPG (dorsal MLT1020PPG sensor and ear clip MLT1020EC, ADinstruments, Dunedin, New Zealand) as well as antennas for radar-based sensing and a microphone for the recording of the phonocardiogram. The

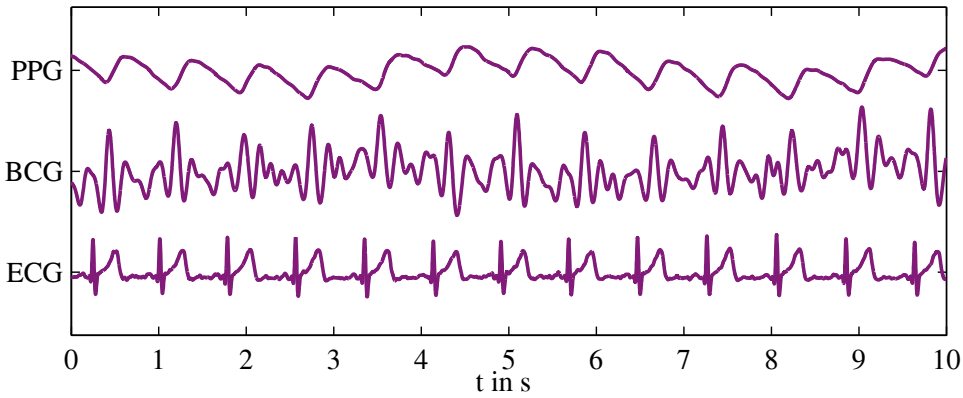

Figure 21: Sample data segment from multisensor mattress ([103],[109]). Shown is the dorsal ballistocardiogram (BCG) recorded with an piezo film and a dorsal photoplethysmogram (PPG) alongside the reference ECG.

data was sampled at a sampling frequency of 2 kHz by using a PowerLab 16/35 biosignal data acquisition system (ADinstruments). Moreover, a reference ECG was recorded using a Bio Amp (ADinstruments) differential biological amplifier. [109, p.33f]

Data were acquired from 18 healthy supine subjects (age: 26.7 $\pm$ 3.7 years, BMI: 24.8 $\pm$ 5.3 kg/m^2) lying on the multisensor mattress. The measurement protocol consisted of several breathing and motion maneuvers. Followed by an initial resting phase with spontaneous breathing, alternating breathing maneuvers consisting of spontaneous breathing, abdominal breathing and breath-holding were conducted. [109, p.35]

For this doctoral work, data from the first 45 s spontaneous breathing phase after the initial (familiarization) phase were extracted. Data excerpts from four subjects were selected among the overall data due to very good signal quality. Specifically, the BCG and PPG data were chosen alongside the reference ECG (for evaluation purposes). Afterwards, the BCG and PPG data were filtered (zero-phase) by a 10 Hz lowpass (5th-order Butterworth) and 0.1 Hz highpass (3th-order Butterworth) filter. From each of the four subjects' 45 s segments, 25 subsegments of 10 s duration (maximum overlap 9 s) were randomly selected and down-sampled to 100 Hz. Each segment was normalized to possess zero mean and unit variance. Overall, a total amount of 100 segments (with 10 s duration) were collected from the multisensor mattress data.

5.1.3 *Clinical Data*

5.1.3.1 *CardioVisio*

The cbPPG data was gathered within the scientific project *CardioVisio - Contactless aquisition of vital parameters*. Measurements were carried out at the cardiac surgical intensive care unit at the Heart Center Dresden, University Hospital Carl Gustav Carus, TU Dresden, Dresden, Germany. The project was approved by the Institutional Review Board

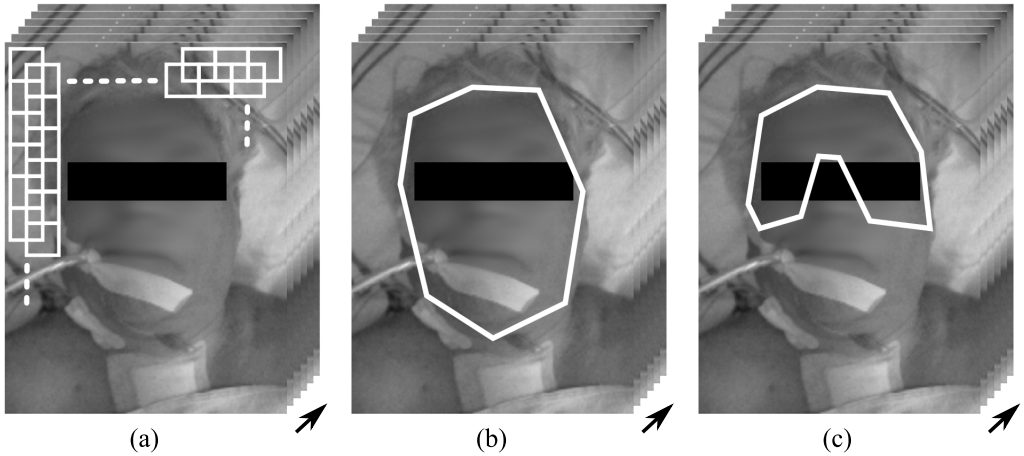

Figure 22: cbPPG ROI selection. White lines indicate ROI borders. (a): Evenly distributed 32x32 pixel ROIs with 50 % overlap. (b): Manually annotated ROI including the face ROI_F. (c): Manually annotated ROI including forehead and cheeks ROI_{FhC}. [286]

of the TU Dresden (IRB00001473, EK168052013). Patients after elective cardiac surgery were included if they gave written, informed consent prior to surgery. Video data was recorded during the immediate recovery from surgery after admission at the intensive care unit [217]. Postoperative care followed clinical standards including mechanical ventilation and external cardiac pacing by temporal atrial and ventricular wires adjusted to intrinsic cardiac rhythm and haemodynamic needs. Four-lead ECG and finger PPG were simultaneously recorded at 300 Hz and used to derive the reference heart rate. Specifically, manual beat annotations of the ECG are used to extract the ground truth heart rate out of the spectral representation (i.e. the peak best matching the ECG derived heart rate) of the PPG that is further used to compute SNRs of the cbPPGs.

Video data was recorded using an industrial camera (IDS UI-3370CP-C-HQ, IDS Imaging Development Systems GmbH, Obersulm, Germany, 100 fps, 420x320 pixels, RGB 3x12 bit). The camera was placed at a distance of approximately 60 - 100 cm to patients' faces. Clinical ceiling fluorescent lamps served as primary illumination source. However, the luminous color, intensity and homogeneity of the illumination varied across the measurements due to varying patient positions with respect to the illumination, varying room geometries and entering daylight. Therefore, a broad range of illumination characteristics is covered by the data.

In order to use only suitable data for further analysis, data segments were selected which showed high quality reference PPGs to correctly identify the true heart rate. Furthermore, data segments with severe cardiac disorders were excluded. Only continuous segments with a minimum length of 500 s (one per patient) were considered for further processing. Based on such criteria, overall recordings of 18 patients (13 male, 5 female; 30 minutes per recording) were selected from a larger collective of 70 patients (age: 70.3 $\pm$ 11.4 years, BMI: 28.8 $\pm$ 4.1 kg/m^2). The selected material includes a total of about 6 h video data

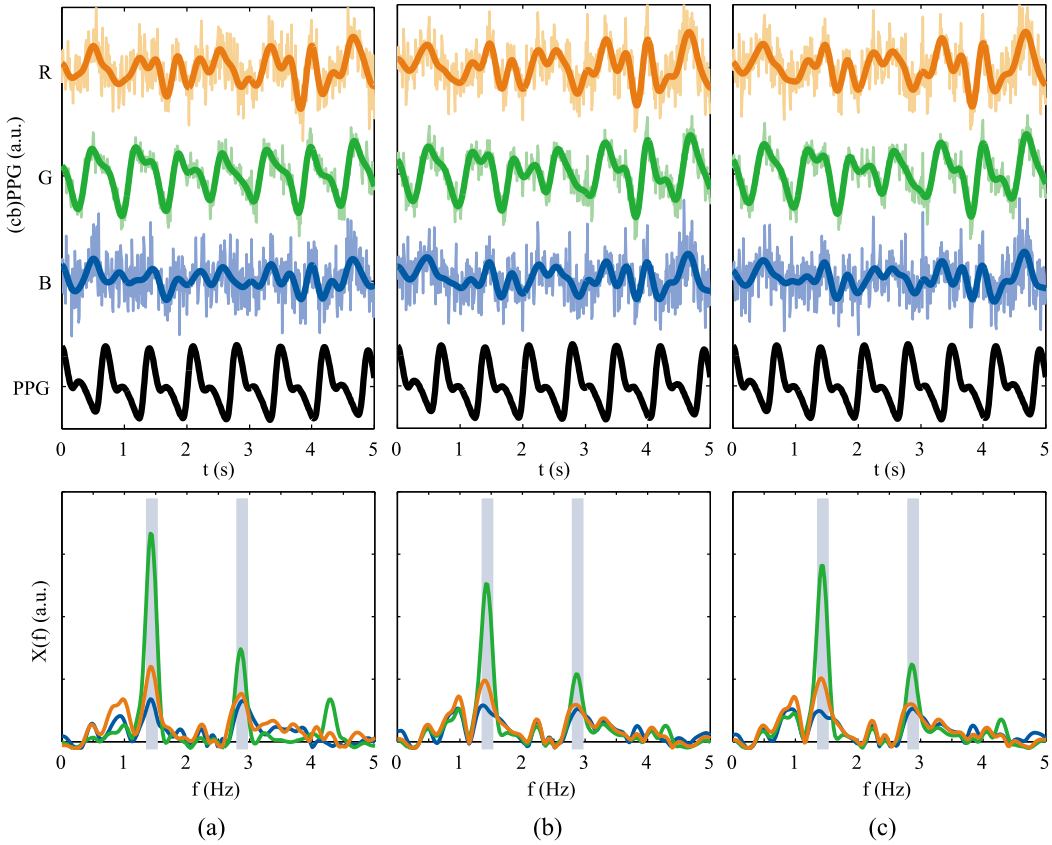

Figure 23: Sample cbPPG signal excerpts (normalized and normalized + 4 Hz lowpass filtered (bold signal) versions) and amplitude spectra from different ROIs. (a): 32x32 pixel ROI. (b): Manually annotated ROI including the face. (c): Manually annotated ROI including forehead and cheeks. The true heart rate and its harmonic (± 5 bpm) is indicated by the colored areas in the back of the spectra. Colors of the respective spectra are according to the time signals. [286]

(average length 1200 ± 400 s per patient). The selection did not consider video quality, i.e. slight patient motion as well as illumination inadequacies (changes or insufficient lightning) persisted in the dataset.

The selected video data was processed in segments of 10 s length resulting in 2197 segments (106 ± 37 per patient). The cbPPGs were extracted in three ways as illustrated in Figure 22. To allow a spatial selection of desired ROIs, every video frame was covered by 25 x 19 overlapping square ROIs (50 % overlap at each direction) of 32 x 32 pixels. The ROI placement is indicated in Figure 22(a). The ROI size was chosen since own prior investigations addressing the relationship between ROI size and signal quality (SNR) using a comparable technical setup (i.e. camera sensor, image resolution and camera distance to subject) showed that no higher signal quality can be obtained by further increasing the ROI size[3]. In order to compare the spatial ROI selection to standard ROI selection prior to BSS [55, 181, 212], manually annotated ROIs were used to extract the cbPPG of the com-

3 Other investigations [251], which showed an appropriate ROI size for pulse wave extraction to be larger (100-150 pixels ROI side length), used a higher image resolution.

plete face (ROI_F) and the forehead-cheeks region (ROI_{FhC}), respectively. See Figure 22(b) and 22(c) for exemplary ROI annotations. cbPPG were extracted from each ROI_n (with n = 1,2,...,475) as well as from ROI_F and ROI_{FhC} at every wavelength by averaging its pixels values [265] for each frame. See Figure 23 for exemplary signals together with the reference PPG.

5.2 ECG DATA

5.2.1 *Data from Healthy Volunteers*

5.2.1.1 *Capacitive ECG Data*

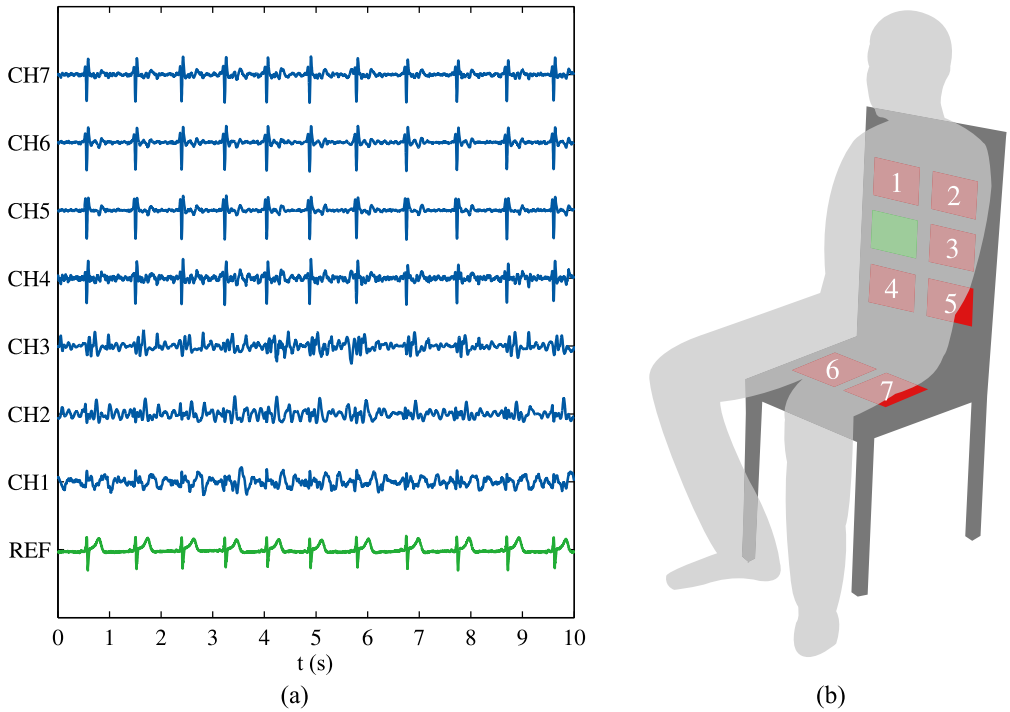

Figure 24: Capacitive data (cECG) and recording. (a) Input data example of the capacitive data. REF indicates the conductive reference ECG and CH1-7 the ECG leads obtained from the driver's seat electrodes. (b) Electrode placement of the cECG setup. The numbered electrodes each define a bipolar lead (CH) together with the green (unnumbered) electrode. [287]

The cECG recordings consist of data from ten healthy subjects (age structure with approximate range [25,45] years) seated at a driver's seat equipped with eight capacitive electrodes. The capacitive system was provided by Capical GmbH (Capical Medical Solutions, Braunschweig, Germany) and has been integrated into a driving test station [31]. The data was recorded by the doctoral candidate at the Volkswagen development site in Wolfsburg, Germany. The measurement protocol comprised a resting phase and a passive

motion phase, where the seat was moved impulse-like from outside at a given period of time. Bipolar ECG leads were obtained using a fixed bipolar reference electrode in chest height. See Figure 24(b) for an illustration of the electrode placement of the cECG system. Seven ECG leads obtained from the driver's seat (sampling rate 500 Hz) were processed in subsequent 10 s segments (1 s segment shift). A total of 523 ± 11 segments per subject containing both, resting and motion phases, were considered. The reference ECG recorded simultaneously using conductive electrodes together with manual annotations served as the ground truth. See Figure 24(a) for an example of a recording without a motion artifact.

5.2.1.2 *Wearable ECG Data*

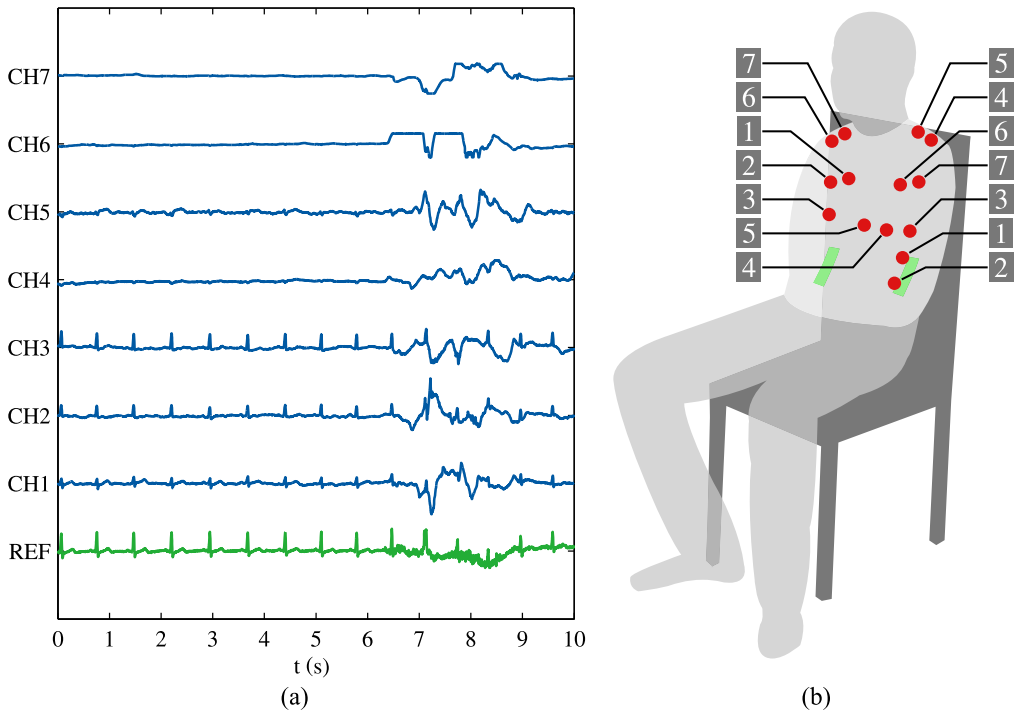

Figure 25: Wearable data (tECG) and recording. (a) Input data with heavy distortions and a large motion artifact. REF indicates the conductive reference ECG and CH1-7 the ECG leads derived from the textile electrodes. Due to the normalization of signals, QRS complexes are not visible in the upper channels. (b) Electrode placement of the tECG garment. The numbered electrodes indicate pairs of bipolar leads (equivalent to CH in (a)) and the reference potential measurement is marked green near the waist. [287]

The tECG recordings consist of data from ten healthy subjects (average age 30 years, range [21,47] years) wearing a garment with integrated textile electrodes [290] while performing a protocol of motion and non-motion phases (sitting, standing, sitting down, standing up, walking, flexing chest muscles). Seven bipolar ECG leads obtained from the garment (sampling rate 500 Hz) using a reference potential near the waist were processed in subsequent 10 s segments (1 s segment shift). A total of (mean ± standard deviation) 536 ± 9 segments per subject were considered. Manual annotations in a reference

ECG recorded simultaneously using conductive electrodes served as the ground truth. See Figure 25(a) for a data example including a large motion artifact as well as Figure 25(b) for an illustration of the electrode placement in the tECG garment.

5.2.2 *Clinical Data*

5.2.2.1 *PhysioNet MIT-BIH Arrhythmia Database*

Since no arrhythmia data were available for the used tECG and cECG techniques, pathological aECGs were assembled out of the PhysioNet [89] MIT-BIH Arrhythmia Database [194]. To match the data amount and the structure of the textile and capacitive ECGs, 100 segments (10 s duration, minimum 1 s segment shift, sampling rate 360 Hz) were randomly sampled out of each of the database's 48 two-channel recordings. Based on the expert beat annotations available with the database, first, segments containing non-normal beats (i.e. premature and block beats, no escape beats) were extracted. If 100 different segments containing pathological beats could not be sampled for a single patient, segments containing only (quasi-)physiological beats (sinus or paced beats) are added. By applying this procedure, 74 ± 41 of 100 segments for each patient containing pathological beats were obtained. The expert beat annotations also served as the ground truth regardless of their beat type.

5.3 CHAPTER SUMMARY

The data assembled for this doctoral work consists of synthesized (cb)PPG data as well as a broad variety of real-recorded (cb)PPG and ECG data incorporating contact-less measurement techniques as well as (clinical) standard measurement techniques. The synthesized (cb)PPGs allow for advanced analyses in the context of BSS (e.g. morphology retention) because the signals' ground truth is known. For the patient data, ground truth measurements are not available but instead more abstract ground truth parameters as the heartrate or heartbeat location are used. These data allow for BSS related analyses of according parameters (e.g. SNR, ACC, heartrate error (HRE)).

Jamie: "Oh, it's truth you want? Be careful, my lady. Tyrion says that people often claim to hunger for truth, but seldom like the taste when it's served up."

— George R.R. Martin in *A Clash of Kings* p.792, A Song of Ice and Fire (1998)

6

RESULTS FOR DATA ANALYSIS

This chapter provides the results of the experiments conducted to address the above raised scientific questions. It presents descriptive and graphical overviews of the results. The related complete numerical results are mostly described in the appendix. Section 6.1 describes the results of the (cb)PPG experiments on the influence of the BSS input data on BSS performance. Section 6.2 describes the results gained by the experiments on solving the major BSS output indeterminacy, i.e. permutation indeterminacy. Finally, section 6.3 provides the results for the comprehensive experiment about linking BSS inputs and output indeterminacy. Contents of this chapter partially appeared already in own publications, i.e. [286, 287].

6.1 SELECTION OF BSS INPUT DATA

In the following, the results and statistical evaluation of experiments, first, using mostly simulated PPG data and disturbances and, second, using real cbPPG data, are presented.

For the simulated data, ΔSNR_{orig}, U_{max} and ρ_{sy} are selected as results. ΔSNR_{orig} represents the difference between SNRs of the BSS output $\mathbf{y}_{\text{PPG}}$ and the original source signal $\mathbf{s}_{\text{PPG}}$ and thus is expected to be non-symmetrically (non-normally) distributed with a central mass close to 0 dB and a skewness towards negative values. Also, ρ_{sy} (limited by 1) and U_{max} (distributed over magnitudes of different order) are expected to be distributed non-normal. That is why non-parametric statistical tests, i.e. rank based tests are utilized for the statistical assessment of the simulated data. Moreover, the effect size measure Cohen's U1 [104] is chosen to characterize the effect size of potentially significant differences. Since it assesses relative amounts of group elements being larger/smaller than opposing group maxima/minima, respectively, its interpretation is straightforward. A maximum effect (U1 = 1) is achieved if every group element of one group is larger than all elements of another group. No effect equals U1 = 0.

For the cbPPG data, absolute SNR values respectively, a difference ΔSNR between the output $\mathbf{y}_{\text{PPG}}$ and the input $\mathbf{x}_{\text{PPG}}$ is assessed. These measures are expected to resemble a normal distribution. Accordingly, analysis of variance (ANOVA)/analysis of covari-

ance (ANCOVA) statistics and related post-hoc tests are applied. Hedges g [85] serves as effect size measure. g represents a standardized mean difference between groups. Given a comparable confidence interval (CI), the larger g, the bigger the impact of the experimental variable [198]. However, contextual information is required to interpret g in terms of absolute values. To define which effects are relevant for further discussion, instead the concept of CI consistency is introduced: an effect is regarded as consistent, if the CI of a given g is completely positive or negative, respectively.

Furthermore, to avoid large sample sizes to determine the statistical results [157], subjects' and methods' means are calculated and used as basis for the statistical analysis.

6.1.1 *Source Signal Characteristics*

Hypothesis 1-1:
The orthogonality $d_\perp$ of the original source signals $\mathbf{s}$ which is defined by the disturbance source types SIN, CHIRP, TREND and STEP, does affect the BSS output parameters SNR, U_{max} and ρ_{sy}.

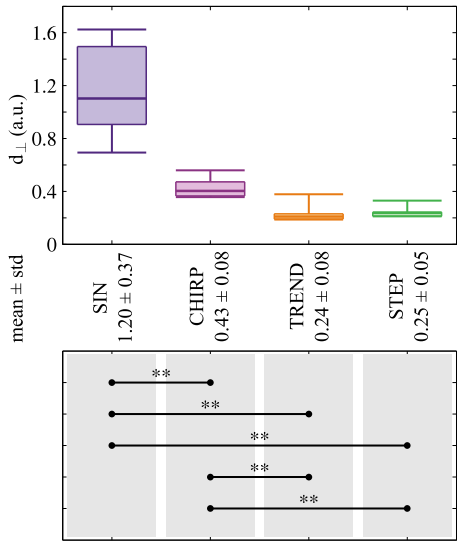

Figure 26: Deviations from the orthogonal BSS approach for different disturbance signals SIN, CHIRP, STEP, TREND measured by $d_\perp$ (in a.u., subject-wise averaged, N = 6, whisker lengths 10 % and 90 % percentile). Horizontal lines in the lower box indicate pairwise significant post-hoc tests between the disturbance types ($^*p \leq 0.05$, $^{**}p < 0.01$, $^{***}p < 0.001$).

In order to examine, whether different disturbance types actually cause different deviations from the orthogonal approach, $d_\perp$ is compared amongst the disturbance types. The independent samples of $d_\perp$ are subject-wise averaged to ensure statistical independence (i.e. each 100 segments sampled using three physiological and three pathological RRI series

give N = 6 averaged values per disturbance type). The Kruskal-Wallis test by ranks to log-scaled $d_{\perp}$ values (to ensure homoscedasticity by Brown-Forsythe-test) shows highly significant differences ($p < 0.001$) between the disturbance types. Mann-Whitney U tests confirm significant differences between most of the pairs. See Figure 26 for the results. Also, see additional results in section A.3.1 (p.165).

In order to illustrate exemplary source-, mixture- and BSS output signals of the experiment conducted on synthesized cbPPGs, Figures 27 and 28 show respective input and mixture signals for the applied noise categories SIN, CHIRP, TREND and STEP as well as the BSS output components resembling the PPG component for the different BSS algorithms which has been selected based on maximum correlation with the original PPG signal.

It is worth noting that regardless the disturbance type (SIN, CHIRP, TREND, STEP), the PCA is not capable of fully separating the white gaussian noise from the PPG in presence of the another disturbance signal, whereas all ICA algorithms show qualitatively noise-free sources. Moreover, even for qualitatively heavily distorted PPG signals from a morphological point of view (see CHIRP disturbance mixtures in Figure 27b), all ICA algorithms are capable of separating PPG signals for the given simple linear three-signal-mixtures. However, RADICAL shows a strong qualitative influence (altered signal morphology of the PPG component after BSS) of sinusoidal disturbances on the morphology of the BSS output components (see Figure 27a) whereas the other ICA algorithms do not.

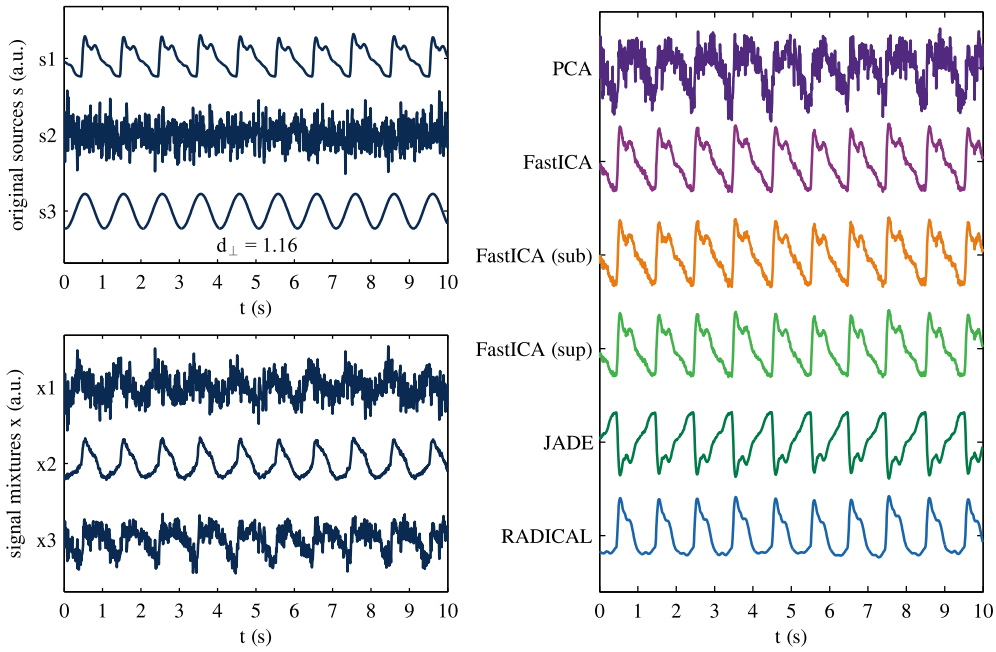

(a)

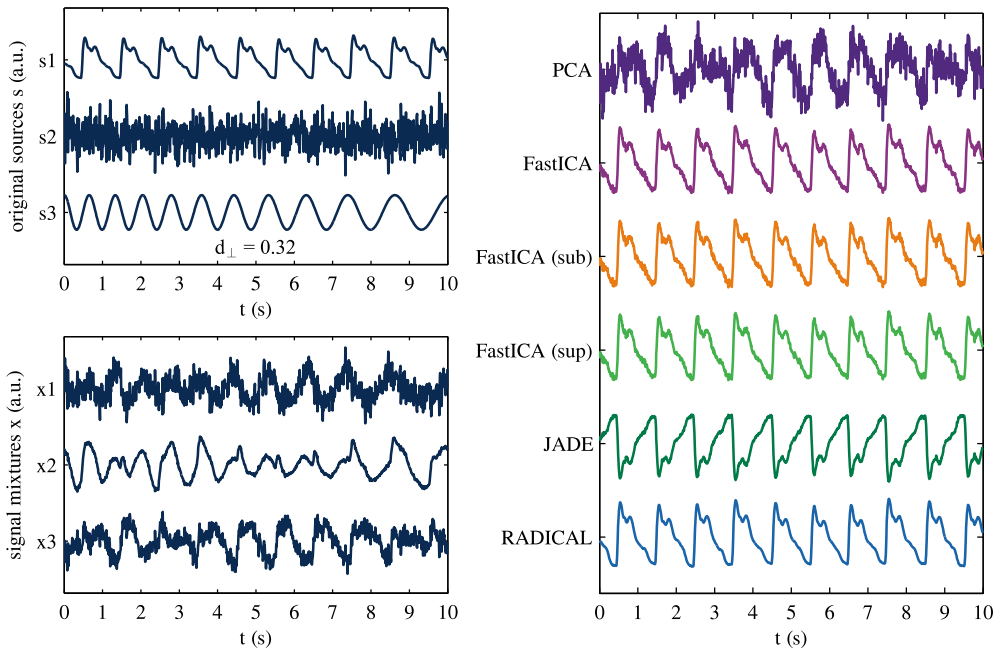

(b)

Figure 27: Exemplary signals showing the BSS performance of different algorithms on PPG signals mixed with (a) sinusoidal (SIN) and (b) quasi-periodical (CHIRP) disturbances. Shown are the original source signals $\mathbf{s}$ (upper left plot), the signal mixtures $\mathbf{x}$ (lower left plot) and the BSS output components y resembling the PPG component (right plot).

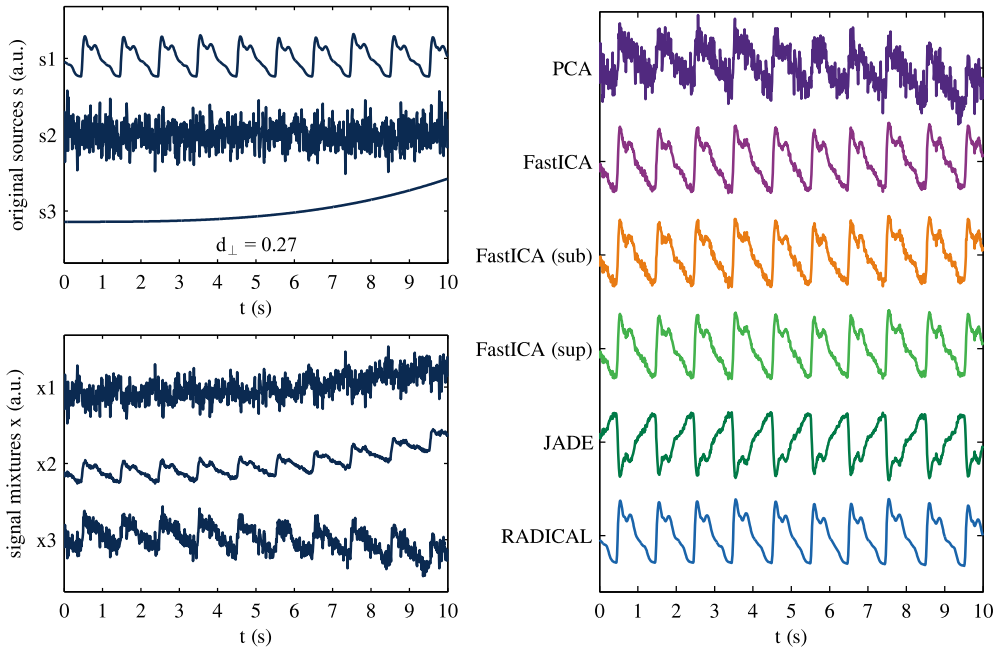

(a)

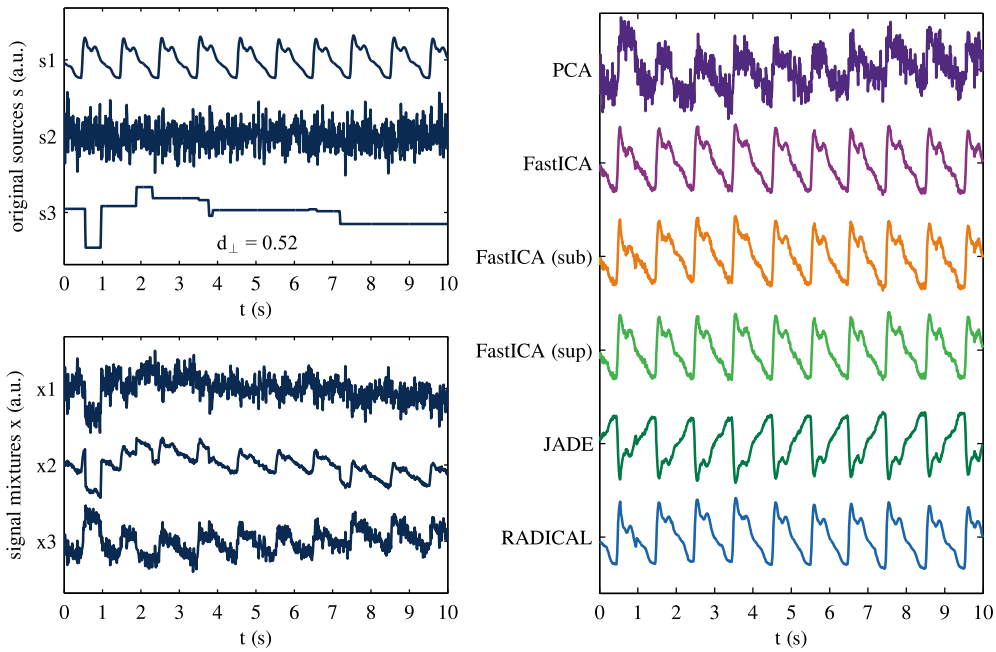

(b)

Figure 28: Exemplary signals showing the BSS performance of different algorithms on PPG signals mixed with (a) monotonous trend (TREND) and (b) volatile (STEP) disturbance. Shown are the original source signals $\mathbf{s}$ (upper left plot), the signal mixtures $\mathbf{x}$ (lower left plot) and the BSS output components y resembling the PPG component (right plot).

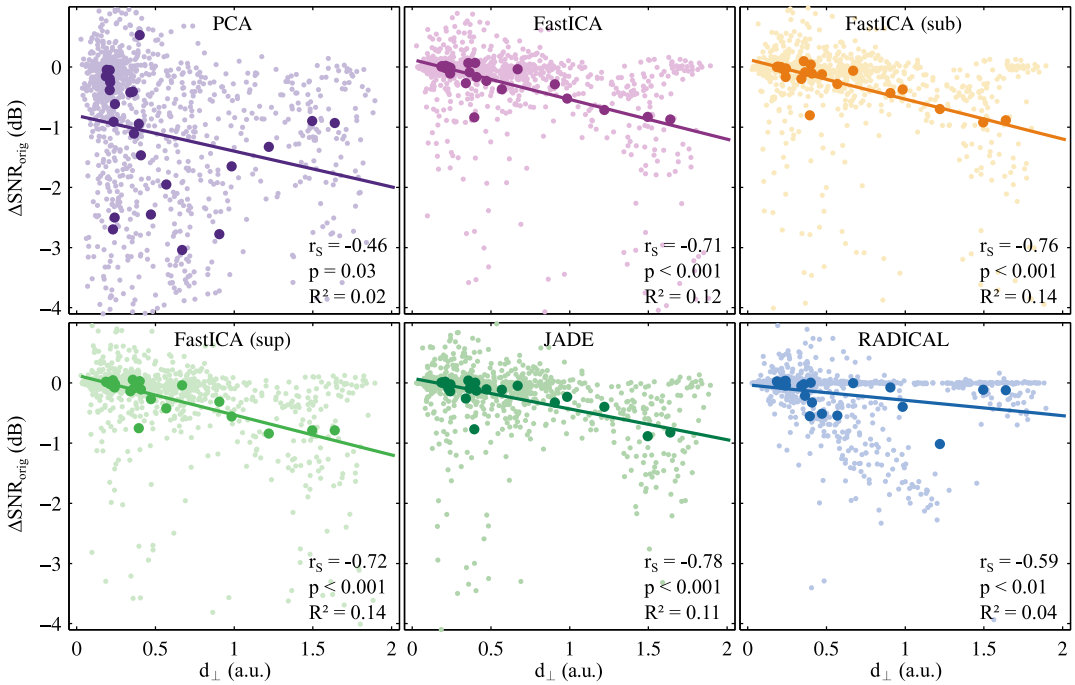

Figure 29: Relation between $d_\perp$ and ΔSNR_{orig} for different BSS algorithms. Full data distribution is shown in faint color, subject- and disturbance-type-wise averaged data (N = 24) is shown in bright color. An exemplary linear regression (incl. R^2) is calculated and drawn, if Spearman's rank partial correlation coefficient r_S (controlling for the disturbance type) indicates a significant correlation ($p \leq 0.05$).

Furthermore, the relation between ΔSNR_{orig}, U_{max} and ρ_{sy}, respectively, and $d_\perp$ is assessed by Spearman's rank partial correlation coefficient r_S. The correlation is calculated on subject- and disturbance-type-wise averaged values (N = 24) by controlling for the disturbance type. If r_S is significant ($p \leq 0.05$), an exemplary linear regression is calculated and rated by R^2 (variance resolution for non-averaged data). Figure 29 shows the data and statistics for the relation between ΔSNR_{orig} and $d_\perp$ each for the respective BSS algorithm. While only expressing a small amount of variance by the linear regression (2–14 %), all BSS algorithms show a significant negative correlation between ΔSNR_{orig} and an increasing deviation from the orthogonal approach $d_\perp$. Note that $\Delta\text{SNR}_{orig} = 0$ equals an optimal BSS outcome with respect to the SNR, i.e. a signal y matching the SNR of the original source signal s has been extracted from the signal mixture $\mathbf{x}$. Figure 30a and 30b show the relation between the deviation from orthogonality of the original source signals and U_{max} and ρ_{sy}, respectively. The reliability of $\mathbf{W}$, i.e. U_{max} is significantly correlated only to standard and super-Gaussian FastICA. The reliability of $\mathbf{y}$, i.e. ρ_{sy} instead, shows significant negative rank-based correlations for all ICA algorithms. Especially for RADICAL, together with the high negative correlation coefficient $r_s = -0.83$, the exemplary linear regression shows a high variance resolution of 76 %.

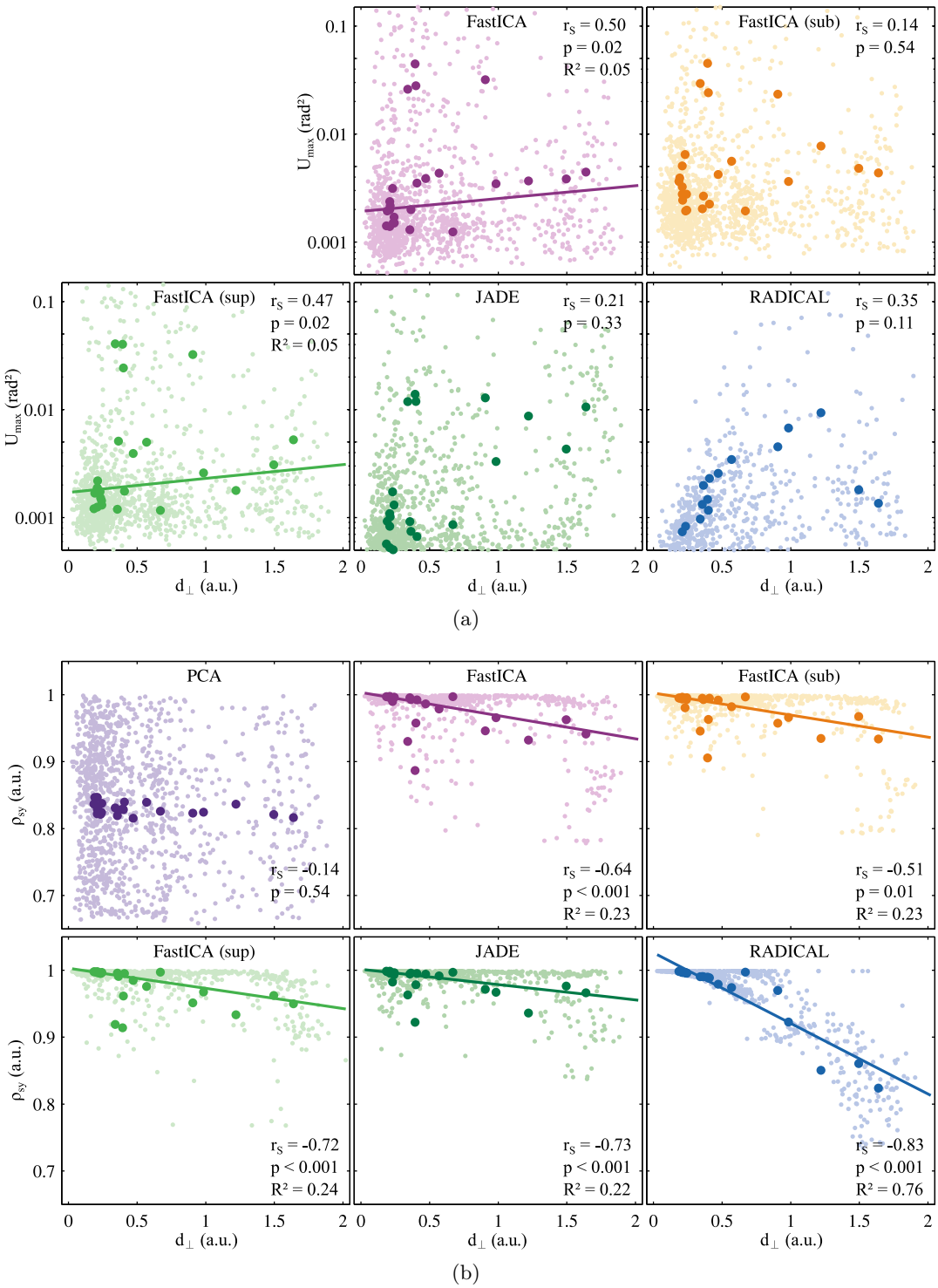

Figure 30: Relation between $d_\perp$ and U_{max} and ρ_{sy}, respectively, for different BSS algorithms. Full data distribution is shown in faint color, subject- and disturbance-type-wise averaged data (N = 24) is shown in bright color. An exemplary (log-)linear regression (incl. R^2) is calculated and drawn, if Spearman's rank partial correlation coefficient r_S (controlling for the disturbance type) indicates a significant correlation ($p \leq 0.05$).

Hypothesis 1-2:
Different BSS algorithms show different performances (i.e. SNR, U_{max} and ρ_{sy}) on different noise types SIN, CHIRP, TREND and STEP.

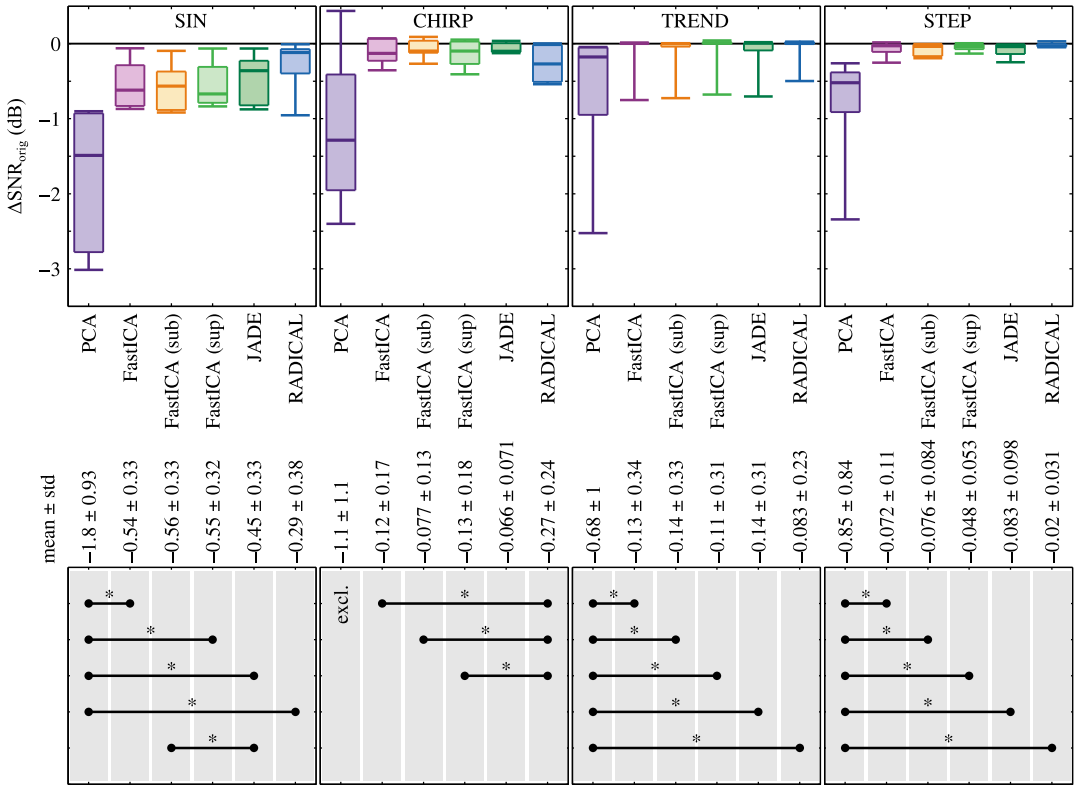

Figure 31: The SNR performance with respect to the BSS algorithm and disturbance type measured by ΔSNR_{orig} (in dB, subject-wise averaged, N = 6, whisker lengths 10 % and 90 % percentile). Horizontal lines in the lower boxes indicate pairwise significant post-hoc tests between the BSS algorithms ($^{*}p \leq 0.05$, $^{**}p < 0.01$).

The performance of the different BSS algorithms with respect the disturbance types using the BSS output measures ΔSNR_{orig}, U_{max} and ρ_{sy}, respectively, is assessed. The dependent samples of ΔSNR_{orig}, U_{max} and ρ_{sy}, respectively, are subject-wise averaged to ensure statistical independence (i.e. each 100 segments sampled using three physiological and three pathological RRI series give N = 6 averaged values per disturbance type). First, the homoscedasticity is validated by Brown-Forsythe-test. To ensure homoscedasticity, PCA was excluded from ΔSNR_{orig} on CHIRP disturbances and RADICAL was excluded from ρ_{sy} on SIN disturbances. The Friedman test further tests for significant differences between the BSS algorithms (which holds for all comparisons except for U_{max} on SIN disturbances). After full-filling these preconditions, Wilcoxon's signed rank test serves as post-hoc test to confirm significant differences amongst the pairs. See the Figures 31, 32a and 32b for the results.

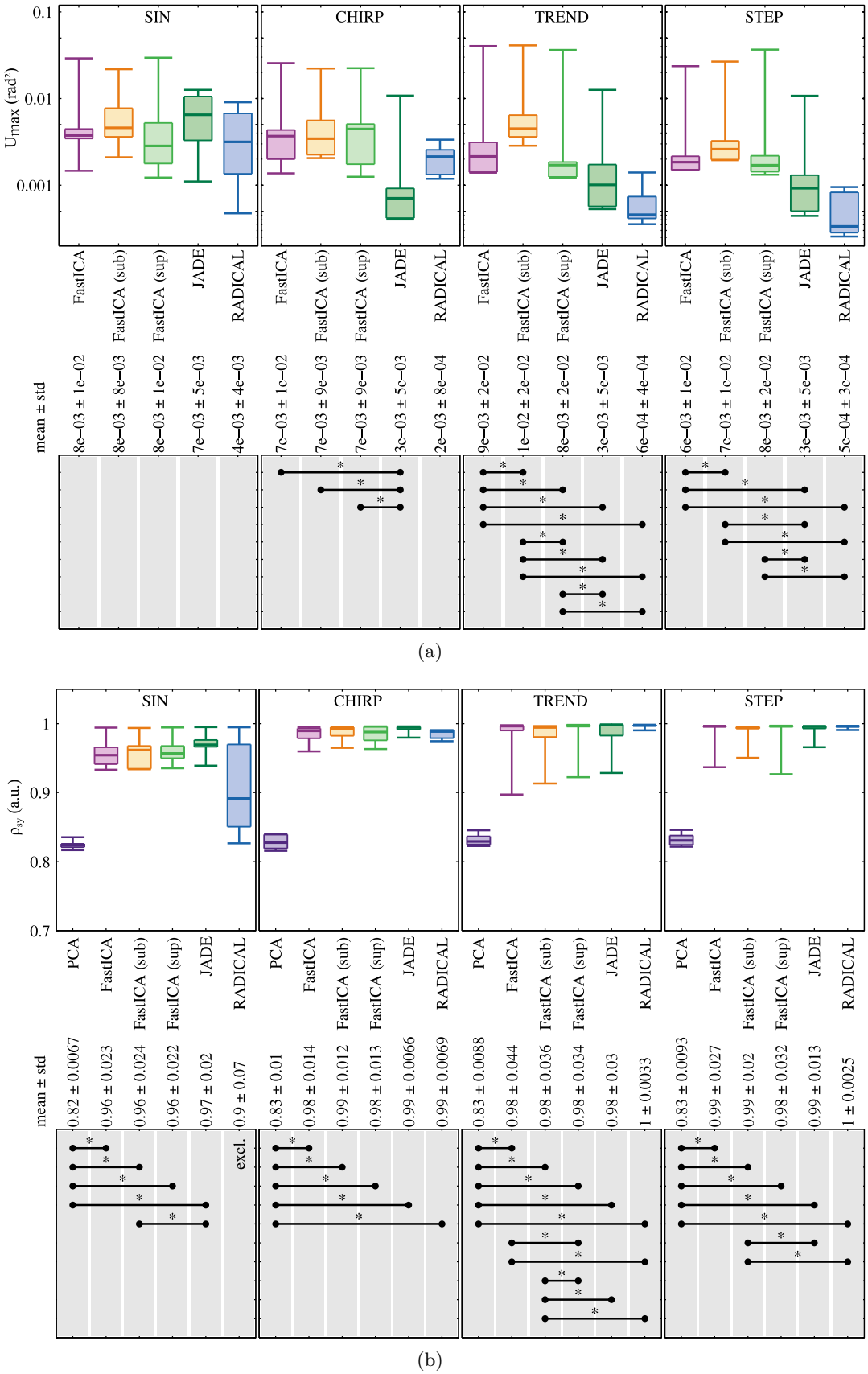

Figure 32: The reliability performance with respect to the BSS algorithm and disturbance type measured by U_{max} (rad^2) and ρ_{sy} (a.u.), respectively (subject-wise averaged, N = 6, whisker lengths 10 % and 90 % percentile). Horizontal lines in the lower boxes indicate pairwise significant post-hoc tests between the BSS algorithms ($^*p \leq 0.05$, $^{**}p < 0.01$).

It is worth noting that, while most ICA algorithms perform similar, the PCA performs worse, i.e. shows significantly lower SNRs and $\mathbf{y}$ reliability ρ_{sy}. Also, there occurs a significant difference in the reliability (variance) of $\mathbf{W}$, i.e. U_{max} for most of the BSS algorithms.

See numerical results in section A.3.1, p.165.

Hypothesis 1-3:
The reliability of the solution $\mathbf{W}$ (U_{max}) and the reliability of the solution $\mathbf{y}$ (ρ_{sy}) does affect the practically relevant parameter SNR, i.e. the strength of the cardiac pulse.

Spearman's rank partial correlation controlling for the disturbance type again is used to measure the relation of the SNR to the BSS reliability measures. Figures 33a and 33b show the relation between the relative strength of the cardiac pulse ΔSNR_{orig} and the BSS's reliability measures U_{max} and ρ_{sy}, respectively. The SNR is significantly negatively correlated to the reliability of $\mathbf{W}$, i.e. U_{max} for standard and super-Gaussian FastICA as well as RADICAL . It is also positively correlated to the reliability of $\mathbf{y}$, i.e. ρ_{sy} for all ICA algorithms. Accordingly, the output SNR decreases while (at least for some ICA algorithms) the reliability of $\mathbf{W}$ decreases. Moreover, the output SNR increases while (for all ICA algorithms) the reliability of $\mathbf{y}$ increases. For the calculated rank-based correlation coefficients r_s, a linear regression model shows a weak variance resolution.

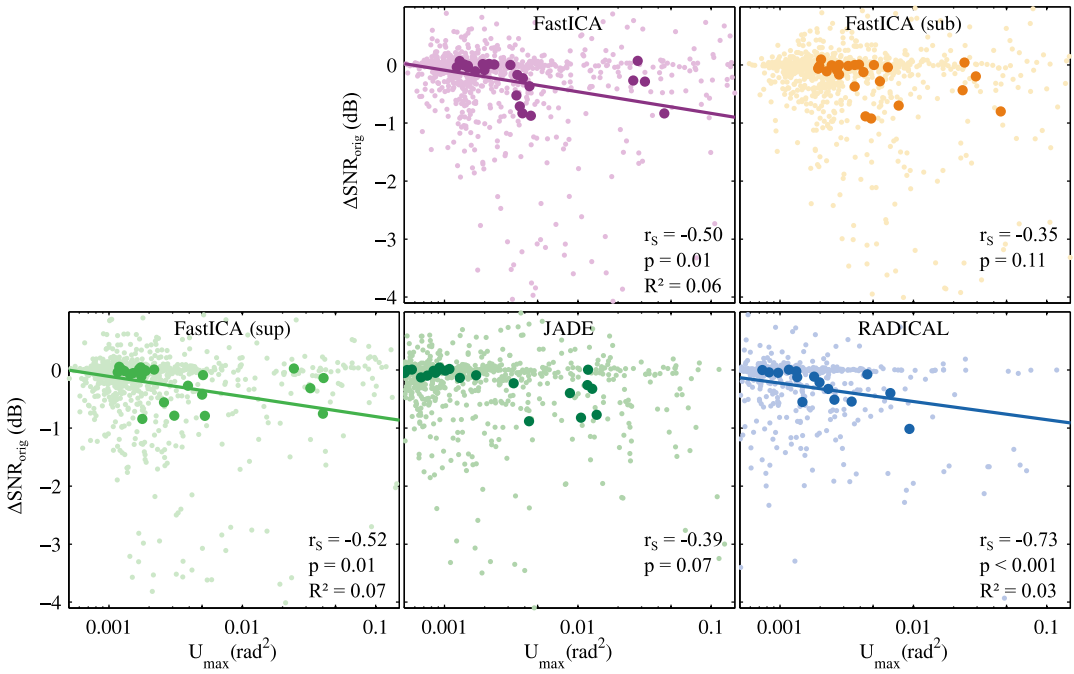

(a)

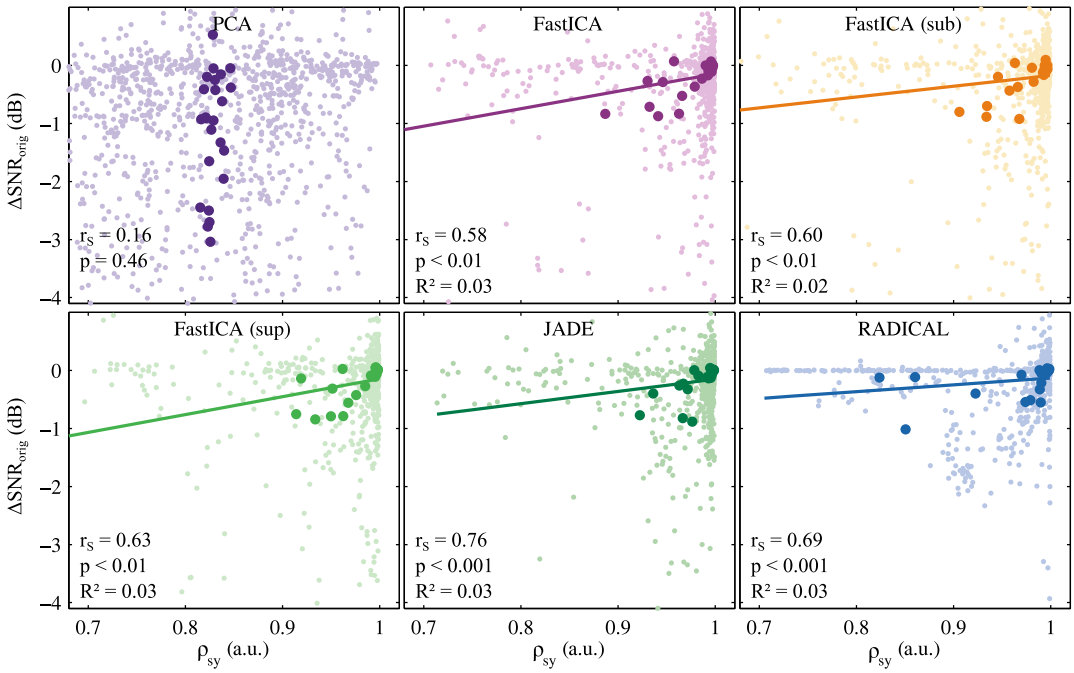

(b)

Figure 33: Relation between the BSS reliability measures U_{max} and ρ_{sy}, respectively, and the SNR, i.e. ΔSNR_{orig}. Full data distribution is shown in faint color, subject- and disturbance-type-wise averaged data (N = 24) is shown in bright color. An exemplary (log-)linear regression (incl. R^2) is calculated and drawn, if Spearman's rank partial correlation coefficient r_S (controlling for the disturbance type) indicates a significant correlation ($p \leq 0.05$).

6.1.2 *Mixture Signal Characteristics*

Hypothesis 2-1:
Different BSS algorithms show different performance (i.e. ΔSNR_{orig}, U_{max} and ρ_{sy}) on underdetermined mixtures ($\mathbf{s} : \{s_i \,|\, 1 \leq i \leq M\}, \mathbf{y} : \{y_j \,|\, 1 \leq j \leq N\}$ with $M > N$)

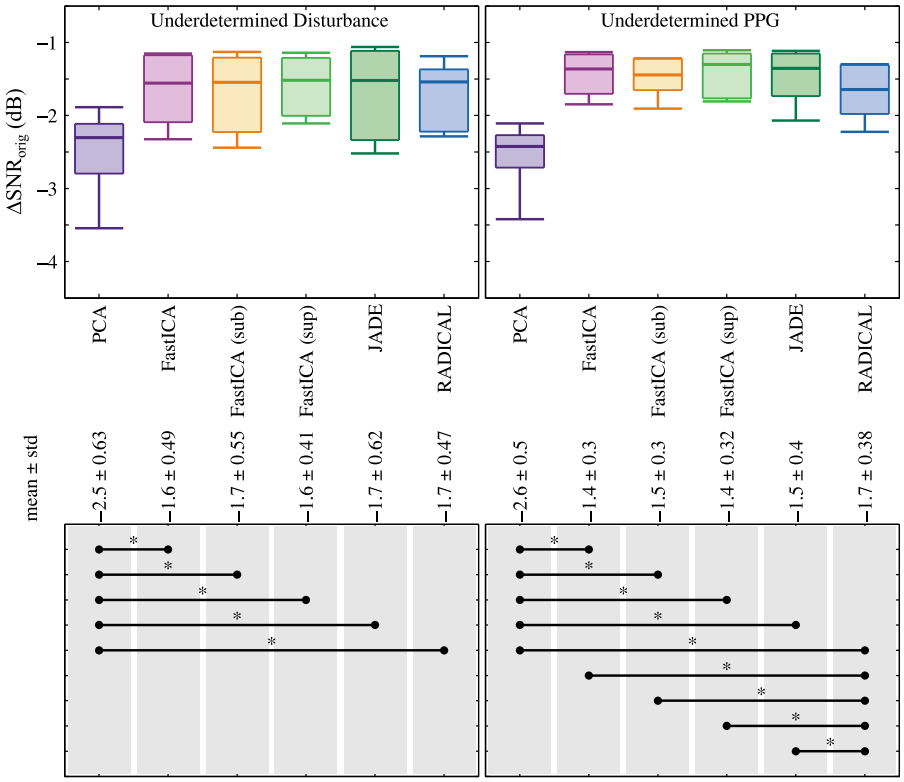

Figure 34: The SNR performance with respect to the BSS algorithm and disturbance type measured by ΔSNR_{orig} (in dB, subject-wise averaged, N = 6, whisker lengths 10 % and 90 % percentile). Horizontal lines in the lower boxes indicate pairwise significant post-hoc tests between the BSS algorithms ($^*p \leq 0.05$, $^{**}p < 0.01$).

The performance of the different BSS algorithms with respect to underdetermined mixtures using the BSS output measures ΔSNR_{orig}, U_{max} and ρ_{sy}, respectively, is assessed. Two cases are distinguished, i.e. (a) underdetermined mixtures containing an additional disturbance signal in the signal sources $\mathbf{s}$ (referring to as "underdetermined disturbance") and (b), underdetermined mixtures containing an additional PPG signal in the signal sources $\mathbf{s}$ (referring to as "underdetermined PPG"). The dependent samples of ΔSNR_{orig}, U_{max} and ρ_{sy}, respectively, are subject-wise averaged to ensure statistical independence (i.e. each 100 segments sampled using three physiological and three pathological RRI series give N = 6 averaged values per disturbance type). First, the homoscedasticity is validated by Brown-Forsythe-test. All data showed homoscedasticity. The Friedman test further indicates significant differences ($p \leq 0.05$) between the BSS algorithms of the evaluated

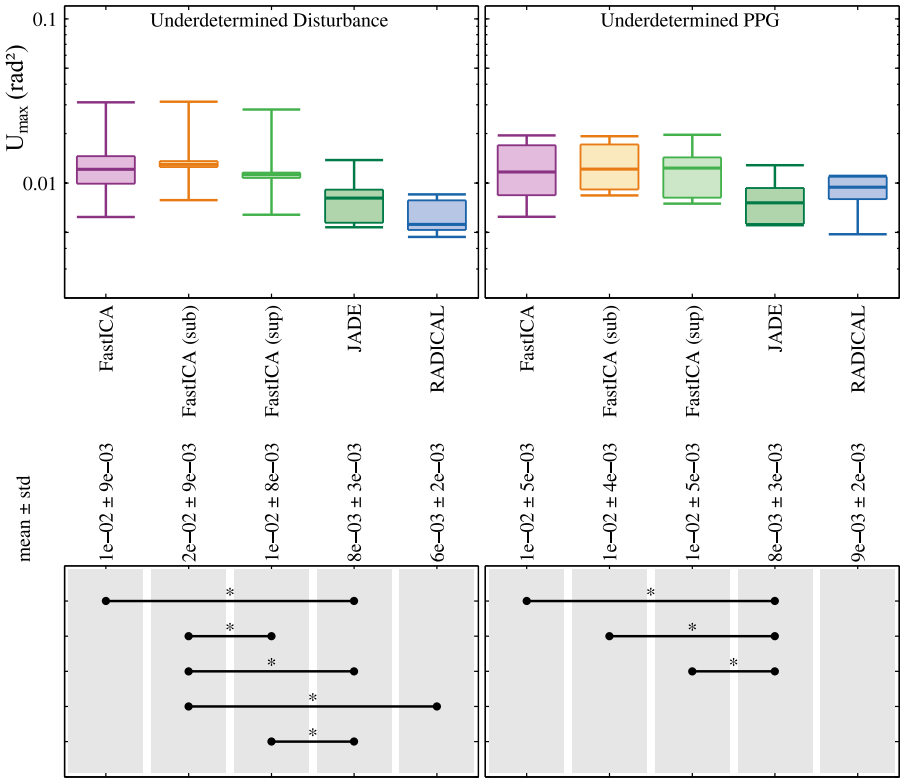

(a)

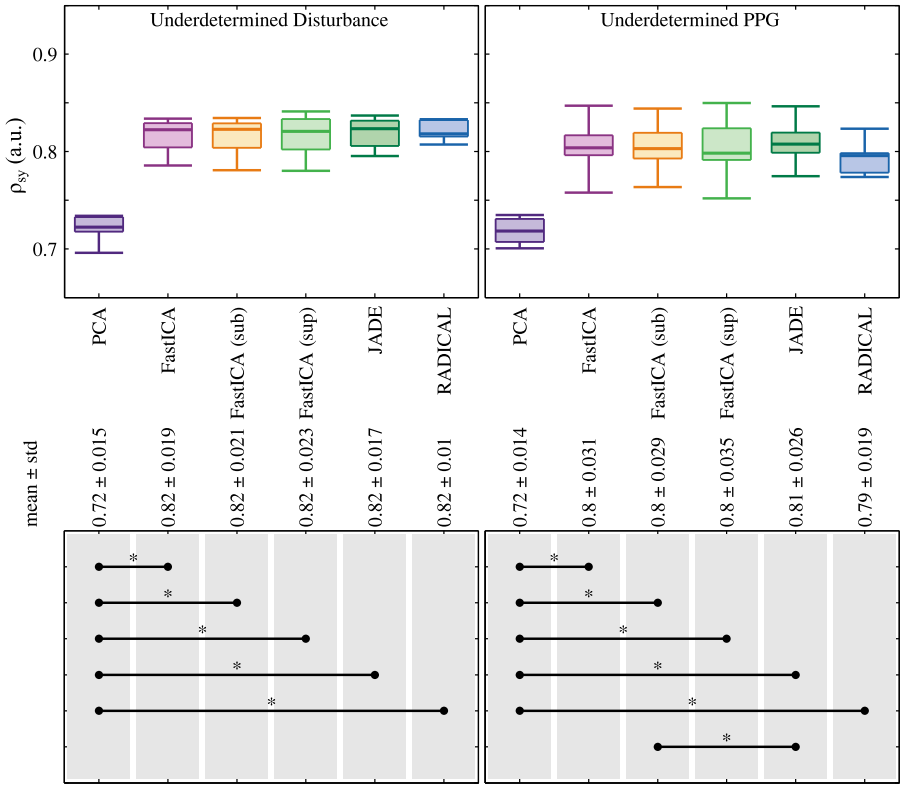

(b)

Figure 35: The reliability performance with respect to the BSS algorithm and underdetermined mixtures measured by U_{max} (rad^2) and ρ_{sy} (a.u.), respectively (subject-wise averaged, N = 6, whisker lengths 10 % and 90 %). Horizontal lines in the lower boxes indicate pairwise significant post-hoc tests between the BSS algorithms ($^*p \leq 0.05$, $^{**}p < 0.01$).

groups. Wilcoxon's signed rank test serves as post-hoc test to confirm significant differences amongst the pairs. See the Figures 34, 35a and 35b for the results. Also, see additional results in section A.3.2 (p.168).

Evaluating underdetermined mixtures with respect to the strength of the cardiac pulse ΔSNR_{orig} (i.e. does the strength of the cardiac pulse in the BSS output $\mathbf{y}$ attain the strength of the cardiac pulse in the original source signals $\mathbf{s}$) and the reliability ρ_{sy} (signal morphology match) shows that the PCA performs worse compared to all tested ICA algorithms. I.e. regardless of the nature of the underdetermined mixture (underdetermined disturbance or underdetermined PPG), applying the PCA causes a significantly lower output SNR and cross-correlation between original and estimated source signal. Moreover, the ΔSNR_{orig} tests show that RADICAL performs significantly worse compared to other ICA algorithms if the underdetermined mixtures contains another PPG signal. Also, the JADE results display a solution of $\mathbf{W}$ that is more stable (shows smaller U_{max}) compared to the FastICA solutions. However, this difference does not significantly affect ΔSNR_{orig} and ρ_{sy}.

Hypothesis 2-2:
Phase shifts among BSS input signals (i.e. phase shifts within PPG signal mixtures) do affect the strength of the cardiac pulse (i.e. the SNR), the reliability of the solution $\mathbf{W}$ (U_{max}) and the reliability of the solution $\mathbf{y}$ (ρ_{sy}).

Spearman's rank correlation is used to measure the relation of phase shifts within the signal mixtures to the BSS output measures. Figures 36a and 36b show the relation between the sample-wise time lag (τ_{PPG}, sampling frequency $f_s = 100\,\text{Hz}$) and the relative strength of the cardiac pulse ΔSNR_{orig} and the BSS's reliability measure ρ_{sy}, respectively. The underlying signal mixtures contained a PPG signal as well as its phase shifted version plus a noise signal (no additional disturbance). The PCA results (data not shown) does not show significant correlations with τ_{PPG}.

The SNR expresses a significant positive correlation with the increasing time lag τ_{PPG} for standard and super-Gaussian FastICA as well as SOBI. For neither U_{max} (except SOBI, data not shown) nor ρ_{sy}, a significant correlation can be proven. Solely, a positive correlation between increasing time lag τ_{PPG} and U_{max} ($r_s = 0.42, p < 0.01$) and thus, a decreasing $\mathbf{W}$-reliability finds. Moreover, all correlations fully vanish while further adding a disturbance signal to the signal mixture (as described as experiment (2)(b) in section 4.1.3, p.76: *Mixture Signal Characteristics*). However, while no significant correlations are expressed for the full interval of tested time lags τ_{PPG}, ρ_{sy} indicates correlation patterns related to partial time lag intervals (see Figure 36b).

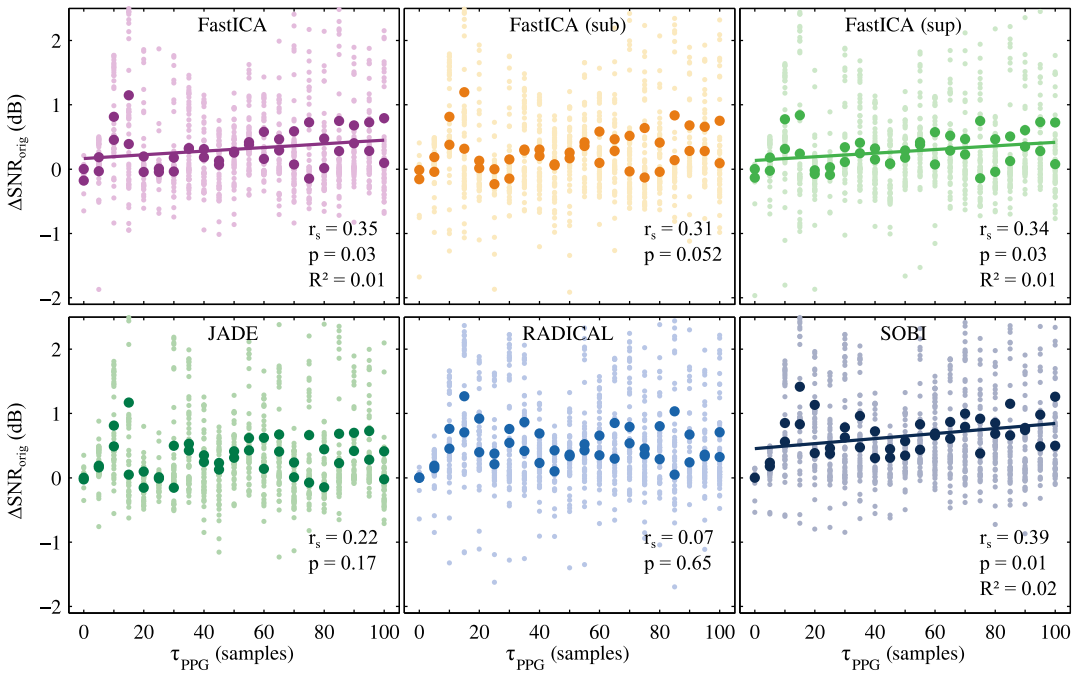

(a)

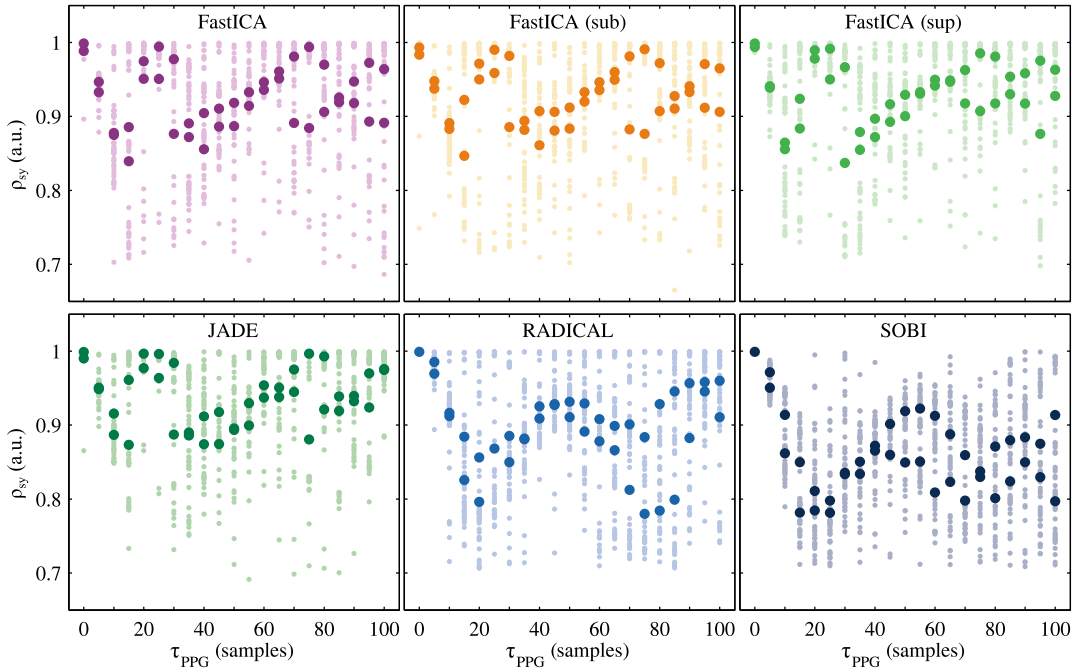

(b)

Figure 36: Relation between phase shifts (time lags τ_{PPG} with respect to the sampling frequency $f_s = 100\,\mathrm{Hz}$) among BSS input signals and $\Delta\mathrm{SNR}_{orig}$ and ρ_{sy}, respectively. Full data distribution is shown in faint color, subject- and time-lag-wise averaged data (N = 42) is shown in bright color. An exemplary linear regression (incl. R^2) is calculated and drawn, if Spearman's rank correlation coefficient r_S indicates a significant correlation ($p \leq 0.05$).

Furthermore, the performance of the different BSS algorithms in this experiment (adding PPG signals with different time lag to the BSS input) is compared amongst each other. Again, the BSS output measures ΔSNR_{orig}, U_{max} and ρ_{sy}, respectively, are assessed. Two cases are distinguished: (a) BSS inputs consisting only of phase-shifted PPGs and a white noise source and (b), an underdetermined mixture of the signals of (a) plus randomly adding a disturbance signal from {SIN,CHIRP,TREND,STEP}.

The dependent samples of ΔSNR_{orig}, U_{max} and ρ_{sy}, respectively, are subject-wise and time-lag-wise averaged to ensure statistical independence (i.e. each 50 PPG signals from each a physiological and a pathological RRI series averaged per time lag (N = 21) give N = 42 averaged values). Initially, the homoscedasticity is validated by Brown-Forsythe-test. To ensure homoscedasticity, the PCA data is excluded from experiment (a). Also in experiment (b), the U_{max} data is fully excluded from further analysis. The Friedman test afterwards indicates highly significant differences ($p < 0.001$) between the BSS algorithms of the evaluated groups. Wilcoxon's signed rank test serves as post-hoc test to confirm significant differences amongst the pairs. See Tables 23 - 27 in the appendix A.3.2 (p.168f) for the pairwise results. Whereas SOBI showed the significantly highest ΔSNR_{orig} compared to other ICA algorithms in experiment (a), the underdetermined conditions of experiment (b) caused SOBI to show the significantly lowest ΔSNR_{orig} amongst the ICA algorithms (only PCA reaches a lower SNR). In experiment (a), SOBI additionally show's the highest reliability of $\mathbf{W}$ (significantly higher than FastICA). However, SOBI also achieves the lowest $\mathbf{y}$-reliability among the ICA algorithms (again only PCA reaches a lower ρ_{sy}). With respect to the reliability of the BSS output components $\mathbf{y}$, i.e. ρ_{sy}, FastICA and JADE perform best in the phase shift experiments with a slightly (but significantly) better performance of JADE.

Hypothesis 2-3:
Different BSS algorithms perform different on heterogeneous (underdetermined) mixtures with respect to ΔSNR_{BSS} and the reliability of $\mathbf{W}$ (U_{max}).

The performance of the different BSS algorithms on heterogeneously underdetermined mixtures (mixtures consisting of BCG and PPG signals) using the BSS output measures ΔSNR_{BSS} and U_{max} is assessed. Figure 37 shows the according box plots. The dependent samples of ΔSNR_{orig} and U_{max}, respectively, are subject-wise averaged to ensure statistical independence and homoscedasticity (N = 4). RADICAL needs to be excluded from the ΔSNR_{BSS} results to ensure homoscedasticity. However, whereas homoscedasticity is confirmed by Brown-Forsythe-test (which only holds for subject-wise averaged data in this case), the Friedman test afterwards indicates no significant differences among the BSS algorithms (ΔSNR_{BSS}: $p = 0.075$, U_{max}: $p = 0.051$).

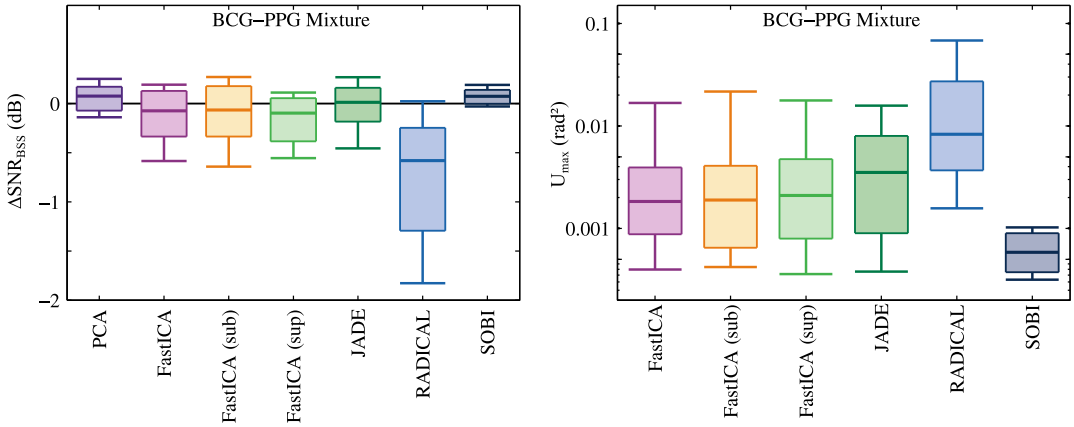

Figure 37: The SNR performance with respect to the BSS algorithm and disturbance type measured by ΔSNR_{BSS} in dB and the $\mathbf{W}$-reliability performance U_{max} in rad^2 (N = 100, whisker lengths 10 % and 90 % percentile).

6.1.3 *Mixture Signal Modification*

Hypothesis 3-1:
Batch processing of BSS inputs (i.e. processing only a partial amount of input signal samples $\mathbf{x}$ to compute $\mathbf{W}$) does affect the strength of the cardiac pulse (i.e. the ΔSNR_{orig}), the reliability of the solution $\mathbf{W}$ (U_{max}) and the reliability of the solution $\mathbf{y}$ (ρ_{sy}).

Spearman's rank correlation is used to measure the relation between the portion of samples processed by BSS within a batch and the BSS output measures. The Figures 38 and 39 show the relation between batch % (with respect to the sampling frequency $f_s = 100\,\text{Hz}$) and the relative strength of the cardiac pulse ΔSNR_{orig} as well as the BSS's reliability measures U_{max} and ρ_{sy}, respectively. The samples of ΔSNR_{orig}, U_{max} and ρ_{sy}, respectively, are subject-wise and batch %-wise averaged to ensure statistical independence. Namely, 100 PPG signals from each three physiological and three pathological RRI series are each averaged per used batch % (N = 6), thus giving N = 36 averaged values.

The SNRs show no correlation with the portion of samples processed within a batch for the tested batch sizes $\geq$ 10 %. On the contrary, U_{max} expresses a significant negative correlation with increasing batch size, i.e. the reliability of $\mathbf{W}$ increases while increasing the data portion in the batch. Also, the reliability of $\mathbf{y}$, ρ_{sy}, slightly but significantly increases while increasing the data portion in the batch (except for PCA). However, using a linear regression to express the correlation results in a relation of only a very small slope: $\delta\,\rho_{sy}/\delta\,\text{batch}\,\% < 0.0001$ with batch % $\in [10\,\%, 100\,\%]$.

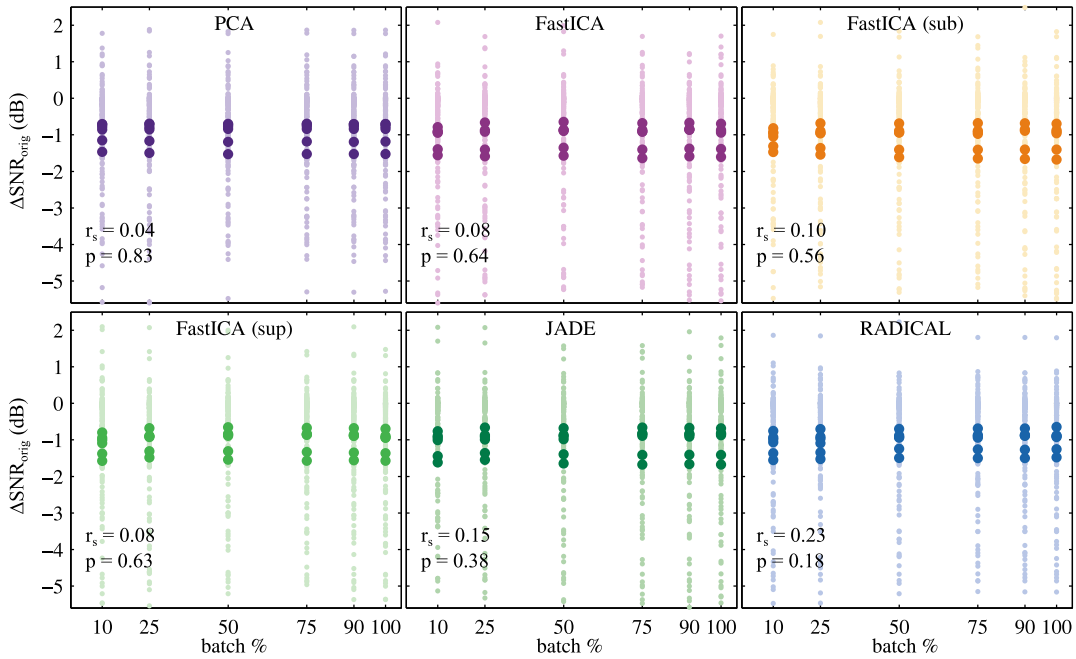

(a)

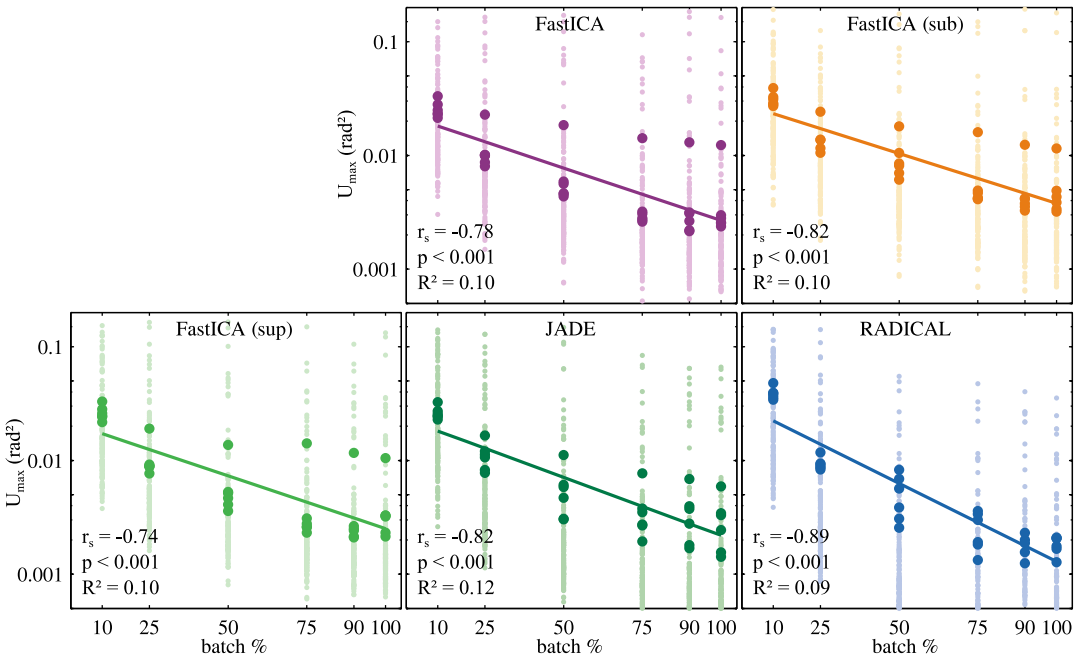

(b)

Figure 38: Relation between the percentage of samples used for batch processing of BSS (batch %, sampling frequency $f_s = 100\,\text{Hz}$) and ΔSNR_{orig} and U_{max}, respectively. Full data distribution is shown in faint color, subject- and batch %-wise averaged data (N = 36) is shown in bright color. An exemplary (log-)linear regression (incl. R^2) is calculated and drawn, if Spearman's rank correlation coefficient r_S indicates a significant correlation ($p \leq 0.05$).

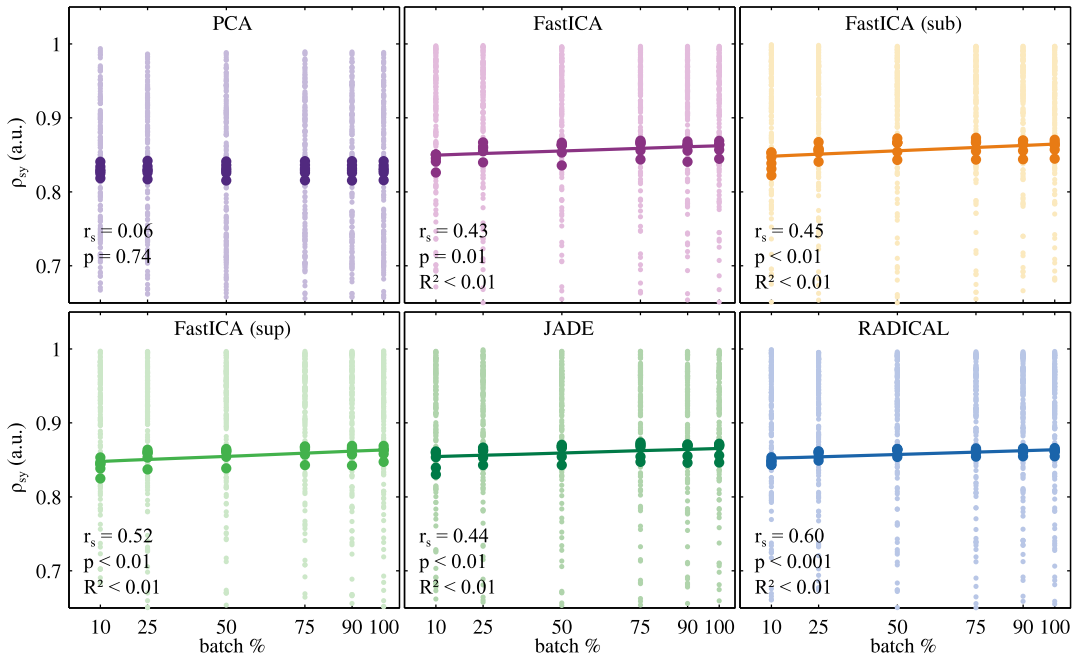

Figure 39: Relation between the percentage of samples used for batch processing of BSS (batch %, sampling frequency $f_s = 100\,\text{Hz}$) and ρ_{sy}. Full data distribution is shown in faint color, subject- and batch %-wise averaged data (N = 36) is shown in bright color. Also finds the corresponding Spearman's rank correlation coefficients r_S including their p-value. An exemplary linear regression (incl. R^2) is calculated and drawn, if Spearman's rank correlation coefficient r_S indicates a significant correlation ($p \leq 0.05$).

Hypothesis 3-2:
The spatio-temporal dimension *dim* of BSS inputs does affect the strength of the cardiac pulse (i.e. ΔSNR_{orig})

Spearman's rank correlation measures the relation between the spatio-temporal dimension *dim* used for BSS input generation and the relative strength of the cardiac pulse, i.e. ΔSNR_{orig}. Figure 40 shows the corresponding results (with respect to the sampling frequency $f_s = 100\,\text{Hz}$). The samples of ΔSNR_{orig} are subject-wise and *dim*-wise averaged to ensure statistical independence. Namely, 100 PPG signals from each three physiological and three pathological RRI series are each averaged per *dim* % (max. N = 7), thus giving N = 42 averaged values for FastICA and N = 24 for JADE.

The SNRs on average show a significant negative correlation with the spatio-temporal dimension *dim* for both BSS algorithms. However, the overall spread of all values ΔSNR_{orig} increases with increasing *dim*, thus higher output SNR (i.e. an amplification of the spectral strength of the cardiac pulse) as well as lower SNR (i.e. an attenuation of the spectral strength of the cardiac pulse) are possible with increasing *dim*. Moreover, despite the overall negative trend, Figure 40 indicates that ΔSNR_{orig} on average seems to profit from small increases of *dim* ($dim_{\text{FastICA}} \leq 5$, $dim_{\text{JADE}} \leq 2$).

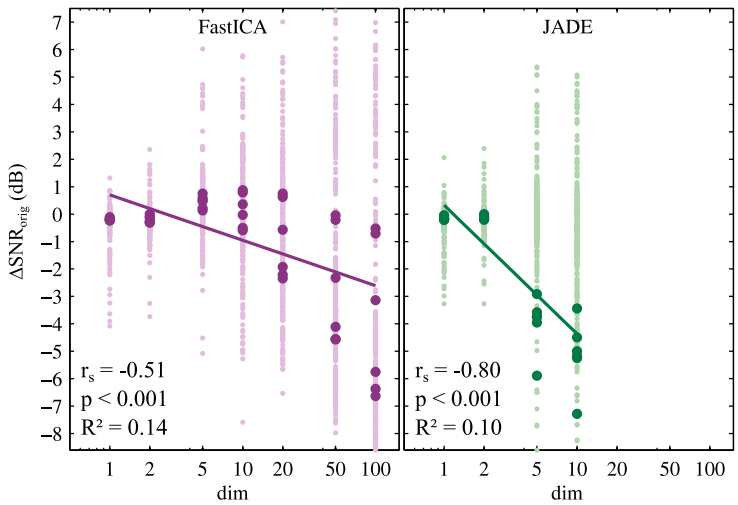

Figure 40: Relation between spatio-temporal dimension *dim* used for BSS input generation (with respect to the sampling frequency $f_s = 100\,\text{Hz}$) and ΔSNR_{orig}. Full data distribution is shown in faint color, subject- and *dim*-wise averaged data ($\text{N}_{\text{FastICA}} = 42$, $\text{N}_{\text{JADE}} = 24$) is shown in bright color. An exemplary log-linear regression (incl. R^2) is calculated and drawn, if Spearman's rank correlation coefficient r_S indicates a significant correlation ($p \leq 0.05$).

Hypothesis 3-3:
The spatio-temporal BSS can compensate for convolutive mixtures, i.e. it unmixes a convolutive mixture and provides an output component y_{PPG} of comparable strength of the cardiac pulse (i.e. the SNR) as present in the original source s_{PPG}.

The SNR performance of two spatio-temporally applied BSS algorithms FastICA and JADE on convolutive mixtures is assessed with respect to the spatio-temporal dimension *dim* of the BSS inputs.

The dependent samples of the BSS output SNRs and the original PPG source SNR are subject-wise averaged to ensure statistical independence (i.e. each 100 PPG signals from three physiological and three pathological RRI series give N = 6 averaged values per *dim*). Initially, the homoscedasticity is validated by Brown-Forsythe-test. To ensure homoscedasticity, $dim = 100$ is excluded from the FastICA results. The subsequent Friedman test indicates highly significant differences ($p < 0.001$) among the groups. Wilcoxon's signed rank test serves as post-hoc test to confirm, especially if significant differences exist between the BSS output SNR and the SNR of the original PPG source. Figure 41a shows the corresponding boxplots and statistical test results. See also the detailed statistical results in section A.3.3 (p.171f).

The results show that FastICA can compensate for the tested convolutive mixtures given $dim = 10$ (also $dim = 20$), because the SNR difference between the ICA output with $dim = 10$ and the original source SNR of s_{PPG} is non-significant. JADE shows signifi-

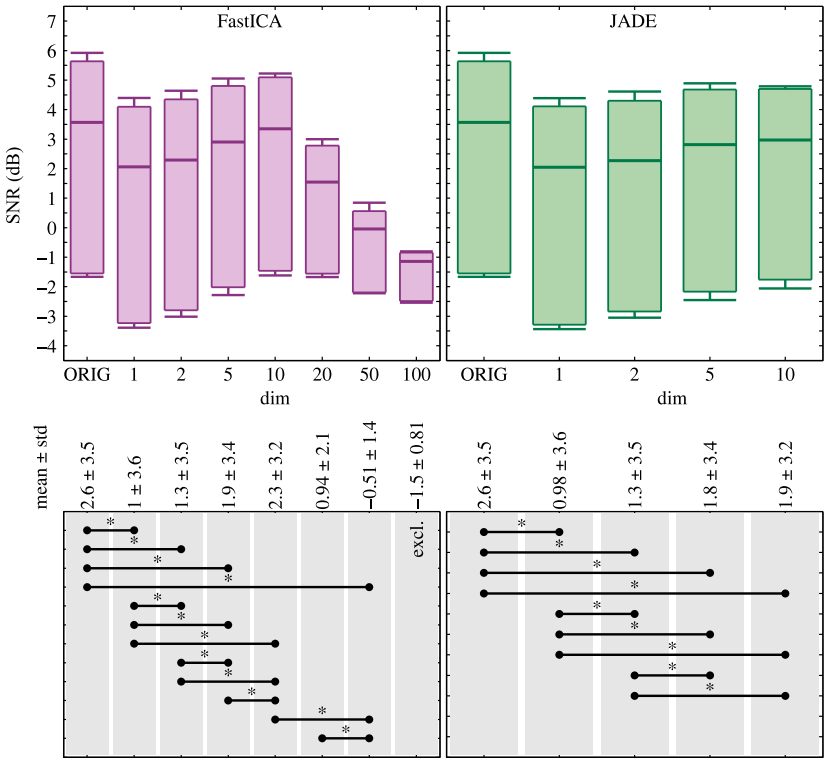

(a)

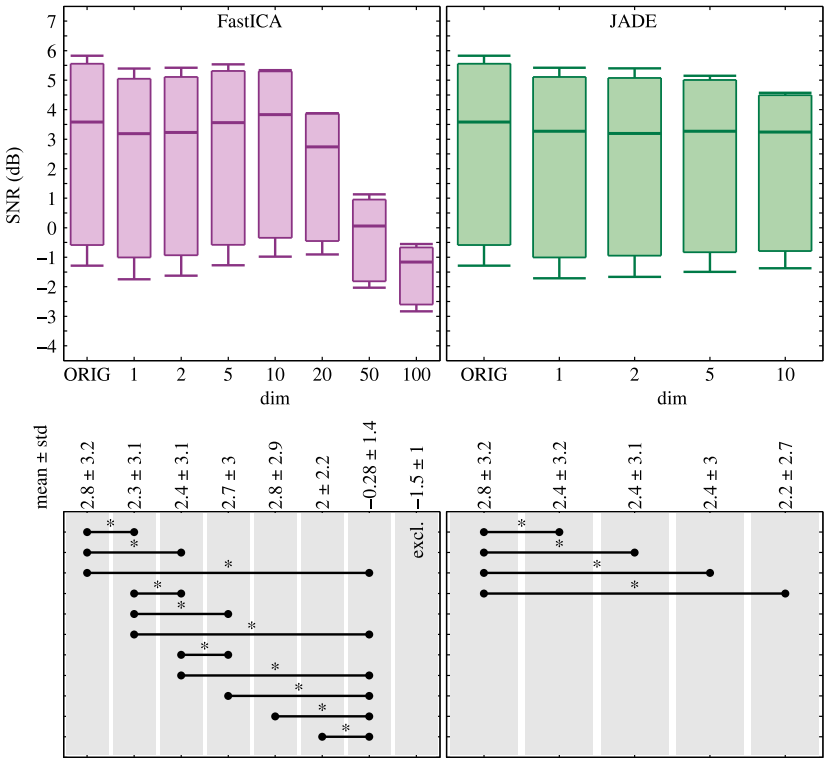

(b)

Figure 41: The SNR performance with respect to the spatio-temporal dimension *dim* of BSS inputs and convolutive (Figure 41a) and non-stationary mixtures (Figure 41b), respectively (subject-wise averaged, N = 6, whisker lengths 10 % and 90 % percentile). ORIG represents the SNR of the original PPG source. Horizontal lines in the lower boxes indicate pairwise significant post-hoc tests between the BSS algorithms ($^*p \leq 0.05$, $^{**}p < 0.01$).

cant SNR differences for all tested *dim* values and thus, cannot fully compensate for the convolutive mixtures with respect to the SNR.

Hypothesis 3-4:
The spatio-temporal BSS can compensate for non-stationary mixtures, i.e. it unmixes a non-stationary mixture and provides an output component y_{PPG} of comparable strength of the cardiac pulse (i.e. the SNR) as present in the original source s_{PPG}.

The performance in terms of SNR improvement of two spatio-temporally applied BSS algorithms FastICA and JADE on non-stationary mixtures is assessed with respect to the spatio-temporal dimension *dim* of the BSS inputs.

The dependent samples of the BSS output SNRs and the original PPG source SNR are subject-wise averaged to ensure statistical independence (i.e. each 100 PPG signals from three physiological and three pathological RRI series give N = 6 averaged values per *dim*). Initially, the homoscedasticity is validated by Brown-Forsythe-test. To ensure homoscedasticity, $dim = 100$ is excluded from the FastICA results. The subsequent Friedman test indicates significant differences ($p = 0.01$) among the groups. Wilcoxon's signed rank test serves as post-hoc test to confirm, if significant differences exist between the BSS output SNR and the SNR of the original PPG source. Figure 41b shows the corresponding boxplots and statistical test results. See also the detailed statistical results in section A.3.3, p.171.

The results show that FastICA can compensate for the tested non-stationary mixtures given $dim = \{5, 10\}$ (also $dim = 20$), because the SNR difference between the corresponding ICA output and the original source SNR of s_{PPG} is non-significant. JADE shows significant SNR differences for all tested *dim* values and thus, cannot fully compensate for the non-stationary mixtures with respect to the SNR.

6.1.4 *Spatial (Contextual) BSS Input Selection*

Hypothesis 4-1:
Varying BSS input sets S provide cbPPG of different SNR.

The comparison between input SNRs is addressed using one-way ANOVA on subject-wise averaged (N = 18) dependent samples after ensuring homoscedasticity by Brown-Forsythe-test. As post-hoc tests, a selection of 13 pairwise t-tests with Bonferroni-Holm correction is applied (see Table 2, for the test selection and pairwise results, see Figure 42 and Table 3, p.131 for SNR results). The selection contains pairwise comparisons of the deterministic small-sized ROIs (S^{mc1}, S^{mc2}, S^{ms1}, S^{ms2}) plus the tests of the random small-sized ROI selection matched with S^{mc1} and S^{ms1} (i.e. S^{mcR}, S^{msR}). Moreover, pairwise comparisons of all deterministic multispectral sets are conducted (S^{ms1}, S^{ms2}, S^{FhC}, S^{F}). Furthermore,

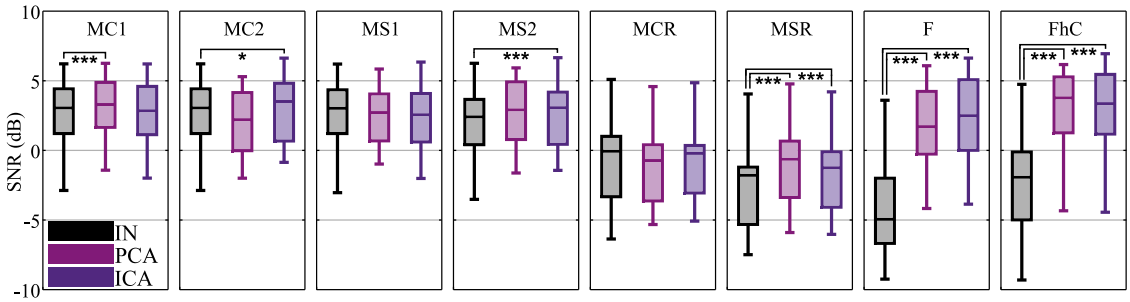

Figure 42: Input and output SNRs for BSS processing of cbPPGs of different sets S (in dB, subject-wise averaged, N = 18, whisker lengths 10 % and 90 % percentile). Significance of differences ΔSNR between output and input SNRs by pairwise t-tests is indicated between the boxes (in case of significance) denoting p-values as: $^{*}p \leq 0.05$, $^{**}p < 0.01$, $^{***}p < 0.001$). [286]

the effect size measure Hedges g [85] including the 95 % CI of g [104] is used as standardized mean difference between groups.

The ANOVA yields a highly significant difference between inputs ($p < 0.001$). According to Table 2, g shows consisted effects between various inputs as well as post-hoc t-tests confirm significant differences between various inputs.

The deterministic automated selection of 32 x 32 pixels input $\mathrm{ROI_n}$ and respective $\mathrm{cbPPG_{n,color}}$ (according to the selection algorithm described in Appendix A.2, p.162f) provides higher quality cbPPG compared to random selection of $\mathrm{ROI_n}$ of same size or standard $\mathrm{ROI_F}$ and $\mathrm{ROI_{FhC}}$, respectively. Omitting the random selection, an increased ROI size comes along with a decreased input SNR (for example on a multispectral input ROI (MS1 < MS2 < FhC < F)). Regarding the random selection of $\mathrm{cbPPG_{n,color}}$, the input signal quality in both cases, the monochrome and multispectral random case, is significantly worse than the one achieved by the deterministic selection.

Table 2: **Results of the SNR comparison for input sets.** Pairwise results: Bonferroni-Holm-corrected p-values from post-hoc pairwise t-tests, effect size g and 95 % confidence intervals of g [104] in brackets.

Set ID 1	Set ID 2	p-value	effect size g
MS1	F	< 0.001	2.01 [1.23,2.78]
MS2	F	< 0.001	1.86 [1.15,2.56]
MS1	MSR	< 0.001	1.57 [0.95,2.19]
MS1	FhC	< 0.001	1.34 [0.77,1.91]
MS2	FhC	< 0.001	1.21 [0.71,1.72]
MC1	MCR	< 0.001	1.09 [0.60,1.59]
MC1	MS2	0.06	0.14 [0.03,0.25]
MC2	MS2	0.06	0.14 [0.03,0.25]
MS1	MS2	0.06	0.12 [0.01,0.22]
MC1	MS1	0.01	0.02 [0.01,0.04]
MC2	MS1	0.01	0.02 [0.01,0.04]
MC1	MC2	n/a	n/a
F	FhC	< 0.001	-0.51 [-0.74,-0.27]

Hypothesis 4-2:
cbPPG input sets of varying constitution and quality cause BSS to provide source estimates $\mathbf{y}$ of different quality (i.e. SNR), i.e. BSS application shows an effect on the cbPPG signals' SNR that depends on the input set S.

For assessing the BSS performance on different cbPPG input sets S, the comparison of output SNR alone does not suffice, because the BSS performance $\Delta\text{SNR}_{\text{BSS}}$ (difference between output and input SNR) and the output SNR must be assumed to be heavily dependent on the input SNR. A statement, which bases solely on output SNRs, thus might favor the output featuring the highest input SNR and won't provide a meaningful statement on BSSs' performance. A dependence on the input SNR implies using the input SNR as covariate, i.e. ANCOVA. Suchlike analysis provides a meaningful statement on the benefit of applying BSS. However, poor input SNR will be favored by this analysis, as a large improvement can be obtained while the outcome still might be worse than using another input. For high input SNRs, on the other hand, the potential improvement which can be gained by BSS is limited as the output SNR is bounded. For such reasons, both analyzes, ANOVA and ANCOVA, are combined. An ANOVA to the output SNRs and respective post-hoc tests could be used as described before. For ANCOVA, the input SNR serves as covariate. As post-hoc tests for ANCOVA, t-tests with centered mean [102] are applied and Hedges g is calculated (again N = 18 subjects' means are used). The selection of post-hoc tests as applied for the input SNRs is also used for these results. For the pairwise comparison of two settings, one of them is regarded as superior and relevant for further discussion if ANOVA's and ANCOVA's post-hoc test show consistent effects with the same sign (both CI entirely positive or negative, for a detailed example see the result descriptions below). Additionally, the question if a significant $\Delta\text{SNR}_{\text{BSS}}$ could be achieved by applying a BSS algorithm to a single input is answered by pairwise t-tests of output and input SNR.

Figure 42 shows boxplots of individually taken BSS performances, namely the patient-wise averaged output and input SNRs including the statistical measure of the pairwise difference. Especially for low input SNR, statistically significant SNR improvements are obtained for both PCA and ICA. PCA moreover significantly improves the SNR of the monochrome set MC1 with equal dominant frequencies whereas ICA significantly improves the SNR of the monochrome set MC2 with different dominant frequencies. ICA also shows a high SNR improvement on MS2. Figure 43 illustrates a distinct dependence of the BSS performance, i.e. the obtained SNR difference $\Delta\text{SNR}_{\text{BSS}}$, on the input SNR. ANCOVA proves that there are no significant differences in the strength of that dependence (i.e. no differences in the slope of separate regression lines with $p = 0.27$ for PCA and $p = 0.15$ for ICA, Brown-Forsythe-test in addition proves homoscedasticity). ANCOVA further proves highly significant differences in terms of adjusted means (i.e. significant differences in the intercepts of parallel regression lines with $p < 0.001$ for PCA and ICA). ANCOVA post-hoc

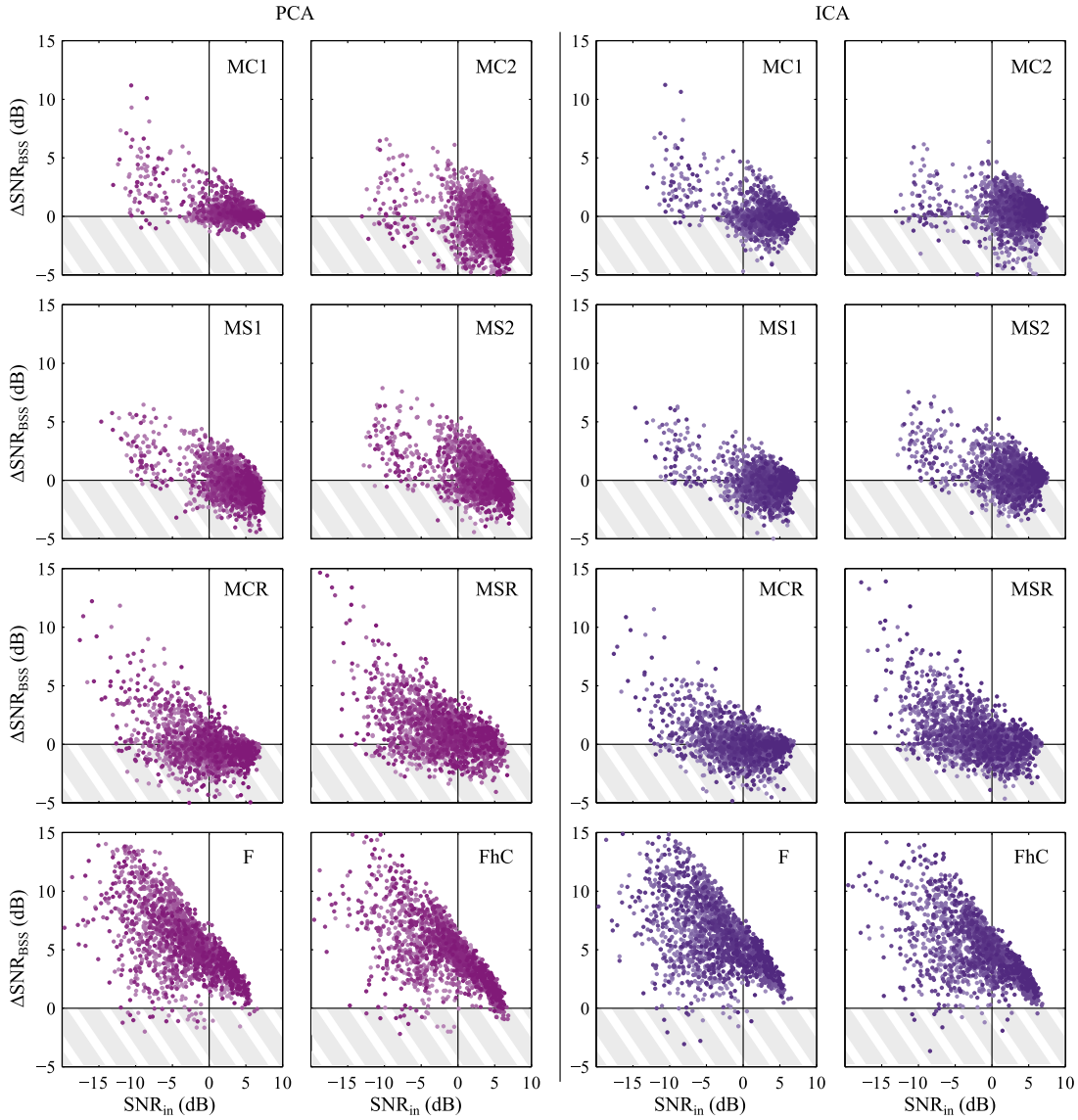

Figure 43: BSS performance $\Delta\mathrm{SNR}_{\mathrm{BSS}}$ with respect to the input SNR. Every point depicts the performance of a single 10 s segment. Color gradation indicates single patients. Each point below the x-axis indicates a SNR decrease due to BSS application. [286]

tests confirm significant differences between various outputs (see Figure 44). ANOVA for the BSS output SNR yields a highly significant difference between outputs ($p < 0.001$ for PCA and ICA). ANOVA post-hoc tests confirm significant differences between various outputs (see also Figure 44). Figure 44 gives a comprehensive overview on the post-hoc results of ANCOVA and ANOVA together with Hedges g including its 95 % CIs. As stated before, BSS's application can be considered as superior in a pairwise S comparison if g and its CI are consistent and show the same direction (sign of g) for both ANOVA and ANCOVA post-hoc tests.

As can be seen in Figure 44, not every pairwise comparison shows relevant differences. The comparison of ICA results for ANCOVA and ANOVA for the standard approaches of sets

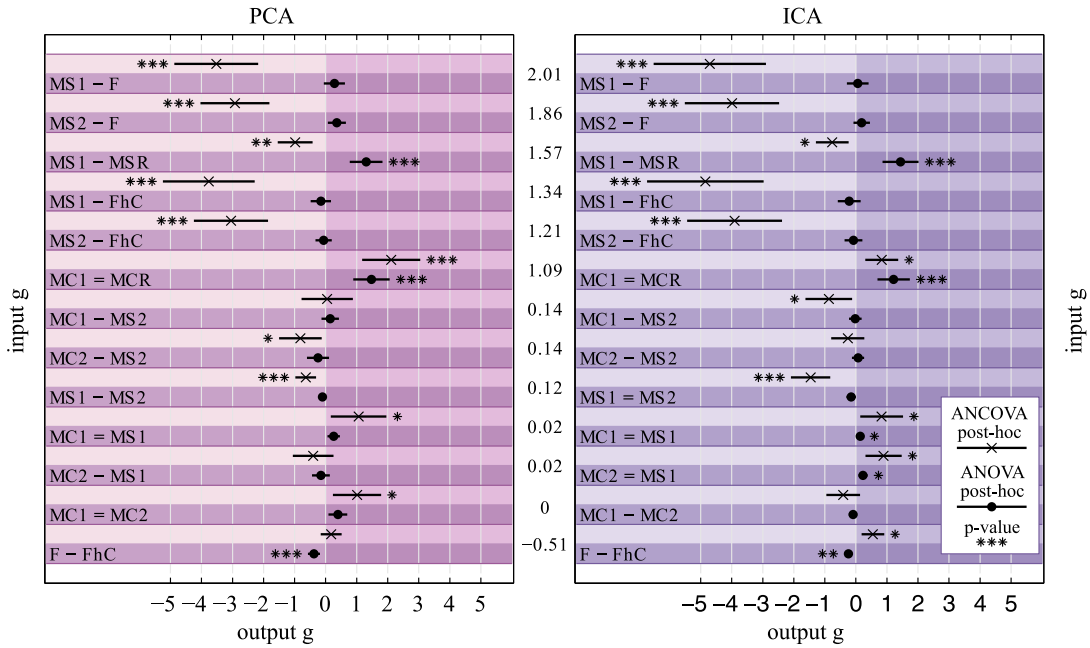

Figure 44: Pairwise t-test results (ANOVA) and pairwise t-test results using mean-centered independent variable (ANCOVA) of patient-wise averaged (N = 18) BSS output SNR. The results are characterized by its effect size g (• for ANOVA, x for ANCOVA) as well as the 95 % CI of g[104] stated as line length. Sign of g indicates the effect direction according to the mean difference obtained by always setting the second set as subtrahend. The set comparisons are vertically (y-axis) ordered according to the effect size g of the input comparison of the same sets. Significance according to the Bonferroni-Holm-corrected p-value is denoted by $^{*}p \leq 0.05$, $^{**}p < 0.01$, $^{***}p < 0.001$. Consistency of an effect is denoted by = between the set names, - otherwise. [286]

FhC and F may serve as an example for the interpretation of Figure 44. Both sets show significant differences in their input SNR (y-axis) with a negative effect size g = -0.51 (input SNR of S^{F} is smaller than input SNR of S^{FhC}). Considering the comparison of adjusted means, i.e. ANCOVA's post-hoc test, a consistent effect in favor of S^{F} was found (indicated by the entirely positive CI of g). Concerning the comparison of the output SNR without adjustment, i.e. ANOVA's post-hoc test, also a consistent effect was obtained. However, this time the CI is entirely negative, which indicates that S^{FhC} provides a significantly higher output SNR. Apparently, the lower input SNR of S^{F}, together with a bounded SNR, favors S^{F} within ANCOVA's post-hoc test. Accordingly, the ICA performance on cbPPG signals of $\mathrm{ROI_F}$ and $\mathrm{ROI_{FhC}}$, respectively, is depending on the input SNR and shows no unambiguous effect (i.e. no advantage of one ROI or another). As example for a pairwise comparison, which shows a relevant difference, one may be referred to MC1 vs. MCR using ICA: besides significantly differing input SNR (with g = 1.09, input SNR of S^{mc1} is higher than input SNR of S^{mcR}), both ANOVA and ANCOVA show consistent effects, either of them is positive. It indicates the better performance of ICA on homogeneous (frequency) inputs of best available SNR compared to homogeneous (frequency) input of random SNR regardless of the input SNR.

The results illustrated in Figure 44 can be summarized as follows. Consistent effect size measures according to the definition (i.e. fully positive, respective negative confidence interval of g) can be found for both, PCA and ICA, for example assessing the adjusted means (ANCOVA) of S^{FhC} when compared to high SNR inputs S^{ms1} and S^{ms2}. Thus, in case of poor input SNR, PCA and ICA both can be efficiently applied. However, relevant effects according to the definition, i.e. considering ANCOVA and ANOVA at the same time, are found for PCA with $S^{\mathrm{mc1}} > S^{\mathrm{mc2}}$ and $S^{\mathrm{mc1}} > S^{\mathrm{ms1}}$ as well as for ICA with $S^{\mathrm{mc1}} > S^{\mathrm{ms1}}$, $S^{\mathrm{mc2}} > S^{\mathrm{ms1}}$ and $S^{\mathrm{ms2}} > S^{\mathrm{ms1}}$. Accordingly, PCA is considered performing worse on inhomogeneous frequency input compared to homogeneous frequencies. Moreover, PCA and ICA are considered performing better on monochrome inputs compared to multispectral inputs of same ROI size. Increasing the ROI size (from S^{ms1} to S^{ms2}) also favors ICA performance.

Hypothesis 4-3:
Different BSS algorithms show different output SNR performance on different sets S.

The comparison between the BSS performance of different algorithms with the respect to the output SNR is assessed by pairwise t-tests of ICA and PCA outputs. Again, subjects means (N = 18) are used and Hedges g is concerned for measuring the effect size.

Table 3 shows the input and output SNR for all input sets and BSS techniques (PCA and ICA). Note that for equal dominant frequencies originally three different input sets were available but only the highest SNR is shown (independently from the used dominant frequency; in 44 % / 36 % / 20 % the first / second / third dominant frequency yielded the highest SNR). Comparing the performance of PCA and ICA on a given input shows that PCA works significantly better on homogeneous inputs S^{mc1} (dominant frequency, wavelength). ICA works significantly better on inhomogeneous inputs S^{mc2} (dominant frequency) as well as for inhomogeneous ROIs (S^{F}).

Table 3: **Pairwise comparison between ICA and PCA outputs.** SNR in dB shown as mean ± standard deviation, p-values from pairwise t-tests and effect size g and 95 % confidence intervals of g [104] in brackets.

Set ID	Input SNR	PCA	ICA	p-value	effect size g
MC1	2.56 ± 2.50	3.01 ± 2.21	2.69 ± 2.37	< 0.001	0.14 [0.07,0.20]
MC2	2.56 ± 2.50	2.10 ± 2.31	2.92 ± 2.48	< 0.001	-0.33 [-0.53,-0.13]
MS1	2.50 ± 2.52	2.45 ± 2.06	2.36 ± 2.33	0.53	0.04 [-0.08,0.16]
MS2	2.18 ± 2.76	2.68 ± 2.24	2.74 ± 2.56	0.67	-0.03 [-0.15,0.09]
MCR	-0.74 ± 3.34	-0.86 ± 2.88	-0.63 ± 2.94	< 0.01	-0.08 [-0.14,-0.02]
MSR	-2.33 ± 3.43	-1.09 ± 3.13	-1.60 ± 3.02	< 0.001	0.16 [0.09,0.24]
F	-4.05 ± 3.74	1.70 ± 2.99	2.18 ± 3.25	< 0.01	-0.15 [-0.25,-0.05]
FhC	-2.05 ± 3.97	2.85 ± 3.01	2.98 ± 3.16	0.32	-0.04 [-0.12,0.04]

6.2 APPROACHES TO PERMUTATION INDETERMINACY

In the following, the results and statistical evaluation of experiments, using ECG data of different origin, are described.

The heartbeat detection accuracy ACC serves as evaluation parameter. Since ACC is practically non-continuously distributed (because of the limited amount of heart beats within a segment) and furthermore bounded by 1 (100 %), it is expected to be distributed non-normal. That is why non-parametric statistical tests, i.e. rank based tests are utilized for the statistical assessment of the simulated data. Moreover, the effect size measure Cohen's U1 [104] is chosen to characterize the effect size of potentially significant differences. Since it assesses relative amounts of group elements being larger/smaller than opposing group maxima/minima, respectively, its interpretation is straightforward. A maximum effect (U1 = 1) is achieved if every group element of one group is larger than all elements of another group. No effect equals U1 = 0.

6.2.1 *Permutation Indeterminacy for ECG Signals*

Hypothesis 5-1:
Subsequent to a BSS processing by spatio-temporal FastICA, different BSS component selection algorithms automatically select components of different heartbeat detection ACC with respect to the underlying data tECG, cECG and aECG.

The statistical analysis of the accuracies is conducted separately for the textile, capacitive and arrhythmia ECG data. Besides the ACCs obtained by assessing the components selected by the respective algorithms, a benchmark comparison to the input data without the BSS processing is provided as the average ACC of all input leads of a segment using the same detector (Av.Input). The acquired groups of accuracies (Av.Input, each BSS component selector) are pairwise compared by Wilcoxon's signed-rank test after testing for significant differences between all groups by applying the Friedman test and requiring homoscedasticity of the groups evaluated by the Brown-Forsythe-test. To ensure independence within each group, the statistical analysis is calculated for subject-wise averaged accuracies (N = 10 respectively N = 48 for aECG data). As effect size measure for the p-values obtained from Wilcoxon's signed-rank test, Cohen's U1 including its 95 %-CI is calculated with bootstrapping (N = 1000) [104].

Figure 45 shows boxplots of the accuracies obtained after selecting a single output component after spatio-temporal BSS application by using five different selectors ($RCODE$, $PeriodTest$, $SKEW$, $KURT$, $CASCSEL$) for three different datasets (tECG, cECG, aECG) without subject-wise averaging. The boxplots also show the average input accuracy (Av.Input) before BSS application to highlight the potential of BSS application in the

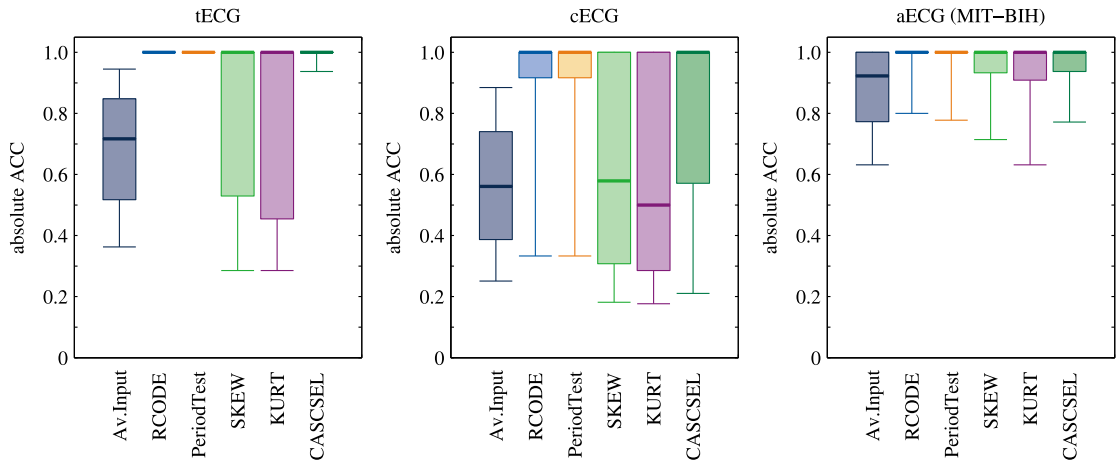

Figure 45: Heartbeat detection accuracy ACC for each segment and subject (N = 10 resp. N = 48 for aECG data). Shown are the average input ACC (Av.Input) of the respective ECG input leads and the selections results of the $RCODE$, $PeriodTest$, skewness ($SKEW$) , kurtosis ($KURT$) and Cascaded ($CASCSEL$) output component selectors. The whisker length is defined as 10 % and 90 % percentile, respectively. No outliers are shown. Subject-wise averaged results can be found in the appendix A.4.1, p.173. [287]

context of the component selection. Brown-Forsythe-test proves homoscedasticity for the cECG and aECG data. That is why pairwise tests are excluded for tECG data. However, Figure 45 qualitatively shows a superior performance of the newly introduced sparse code selectors $RCODE$ and $PeriodTest$ for tECG data with absolute accuracies ACC ≈ 1. The Friedman test on subject-wise averaged ACCs shows highly significant differences between the groups ($p < 0.001$) for cECG and aECG data. Pairwise post-hoc tests on subject-wise means including effect size measure Cohen's U1 and its 95 % CI for cECG and aECG data are shown in the appendix A.4.1 (p.173).

The pairwise comparisons between the average input accuracy (Av.Input) and any component selection after spatio-temporal BSS show an unambiguous benefit of the BSS application with the subsequent component selection. Despite the skewness and kurtosis selector for cECG data, highly significant ACC increases by the selected BSS component compared to the average of input channels are available. Large effects (effect sizes) are obtained especially for the peak-detection-based selectors (RCODE, PeriodTest) and the $CASCSEL$ selector in cECG data. However, for cECG data, the application of higher order moments selection ($SKEW$, $KURT$) is not able to provide significantly higher ACC after BSS compared to the average of input channels.

Pairwise comparison of the peak-detection-based selectors ($RCODE$, $PeriodTest$) with the other selectors based on higher order moments or frequency-domain-features shows that the peak-detection-based methods significantly outperform the other approaches for all datasets. Large effects can especially be proven for cECG data. No significant difference of the $RCODE/PeriodTest$ algorithm can be obtained in the case of the arrhythmia data in comparison to the skewness selector. However, the average difference achieved in the

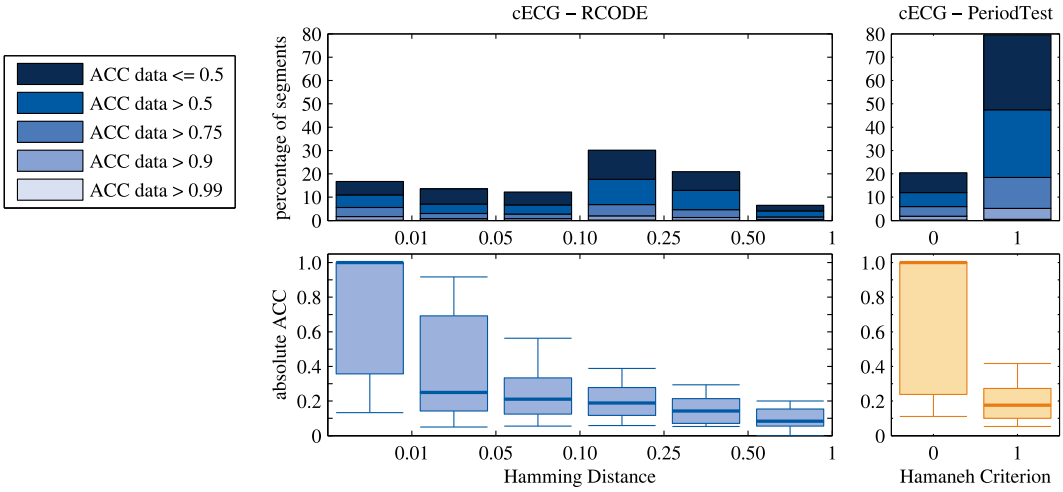

(a)

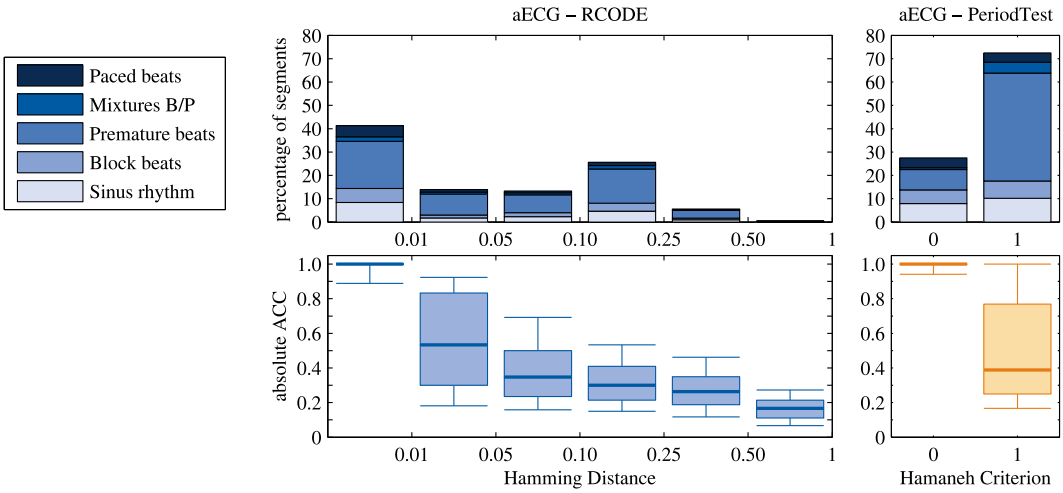

(b)

Figure 46: Relation between the modified Hamming distance gathered from the *RCODE* algorithm, respectively the periodicity criterion according to the *PeriodTest* algorithm (x-axis) and the heartbeat detection accuracy (y-axis) obtained for each distance measure. Shown are the results for cECGs (Figure 46a) and aECGs (Figure 46b), respectively (whisker lengths 10 % and 90 % percentile, no outliers). All available BSS output components are assessed (not only the selected components). Additionally, a histogram shows the data distribution with respect to the input data quality (average ACC of the multichannel measurement) for cECG in Figure 46a, respectively the beat/rhythm classifications present in the segments for aECG in Figure 46b. [287]

output ACC (see Table 33, p.173) between $RCODE/PeriodTest$ and $SKEW$ is 1.5 % and 1.2 %, respectively, in favor of the peak-detection-based methods. The skewness selector always significantly outperforms the kurtosis selector, too.

When comparing the peak-detection-based selectors ($RCODE$, $PeriodTest$) against each other, no significant difference between the obtained ACC of the respectively selected components can be found for cECG data. Despite being of very small absolute value, a significant difference in favor of $RCODE$ is achieved for the aECG data. An insight into the direct comparison between $RCODE$ and $PeriodTest$ and their respective selection criteria, modified Hamming Distance and the Hamaneh periodicity criterion, is given in Figure 46a and Figure 46b. The figures show the accuracy of any output component (i.e. its peak detections) given its selection measure for all available output components after BSS. The variance of the output ACC given $d_H/\mathrm{HC} = 0$ underlines the necessity of applying an additional criterion (i.e. $AltSkew$) for selecting among the components classified as suitable candidates by $RCODE/PeriodTest$. In the case of the cECG data (Figure 46a), the candidates for selection of the cardiac component (modified Hamming distance or Hamaneh criterion equals zero) show a higher first quartile in the according $RCODE$ boxplot (ACC $>$ 0.35) compared to the $PeriodTest$ boxplot (ACC $<$ 0.25). Figure 46b shows the same assessment for the aECG data. In this case, the $RCODE$ algorithm shows a slight advantage regarding the amount of data accessed as good cardiac component candidates. The histogram shows around 10 % more components achieving modified Hamming distance equal to zero compared to the components classified as periodic using the Hamaneh criterion with comparable ACC.

6.3 LINKING INPUT COMPOSITION AND OUTPUT PERFORMANCE OF BSS

Hypothesis 6-1:
The spatio-temporal dimension *dim* of BSS inputs affects the maximum reachable heartbeat detection accuracy $\mathrm{ACC}_{\mathrm{max}}$ of the BSS output.

Spearman's rank partial correlation is used to measure the relation of the maximum reachable heartbeat detection accuracy $\mathrm{ACC}_{\mathrm{max}}$ with the spatio-temporal BSS dimension *dim*. However, the relation, respectively correlation is only considered further if homoscedasticity can be proven by Browne-Forsythe-test on the subject-wise averaged data (N = 10 for tECG, cECG, N = 48 for aECG) with respect to a grouping according to *dim*. Figure 47 illustrates this relation for tECG, cECG and aECG data, respectively.

$\mathrm{ACC}_{\mathrm{max}}$ shows significant positive correlation with *dim* given $dim \in [1, 50]$ for cECG data. For tECG and aECG a potentially positive correlation cannot be proven due to heteroscedasticity among the *dim* groups. However, cECG data results show that an in-

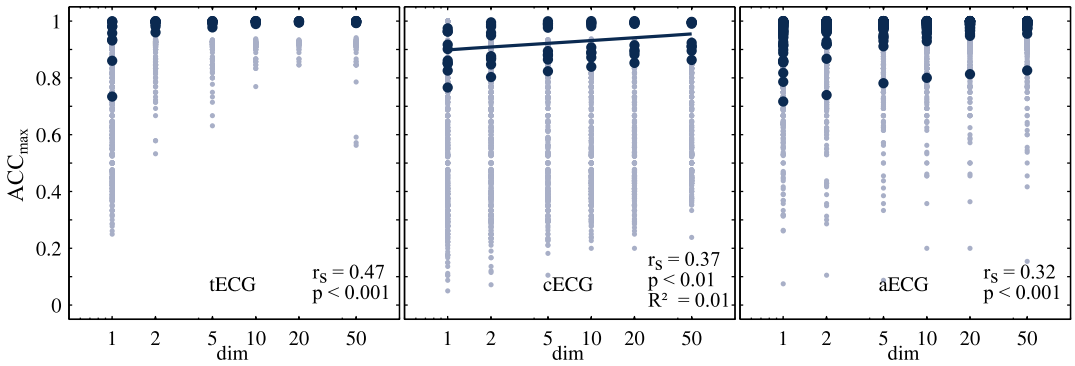

Figure 47: Relation between the spatio-temporal BSS dimension *dim* and the maximum heartbeat detection accuracy $\mathrm{ACC}_{\mathrm{max}}$ for tECG, cECG and aECG data. Full data distribution is shown in faint color, subject-wise averaged data (N = 10 for tECG, cECG, N = 48 for aECG) is shown in bright color. An exemplary linear regression (incl. R^2 for the non-averaged data) is calculated and drawn, if the data show homoscedasticity and Spearman's rank partial correlation coefficient r_S indicates a significant correlation ($p \leq 0.05$).

creasing spatio-temporal BSS dimension *dim* improves the quality of the BSS output, i.e. the maximum heartbeat detection accuracy among the BSS output components $\mathbf{y}$.

Hypothesis 6-2:
The spatio-temporal dimension *dim* of BSS inputs affects the relative heartbeat detection accuracy $\mathrm{ACC}_{\mathrm{rel}} = {}^{\mathrm{ACC}_{\mathrm{sel}}}/_{\mathrm{ACC}_{\mathrm{max}}}$ of the selected BSS output component.

Again, Spearman's rank partial correlation is used to measure the relation between the relative heartbeat detection accuracy $\mathrm{ACC}_{\mathrm{rel}}$ and the spatio-temporal BSS dimension *dim*. Thereby, $\mathrm{ACC}_{\mathrm{rel}}$ describes, how well a maximum heartbeat detection accuracy component among the BSS output can be selected by an automated BSS component selection algorithm given the spatio-temporal BSS dimension (which directly affect's the number of BSS outputs). However, the relation, respectively correlation is only considered further if homoscedasticity can be proven by Browne-Forsythe-test on the subject-wise averaged data (N = 10 for tECG, cECG, N = 48 for aECG) with respect to a grouping according to *dim*. The Figures 48a, 48b and 49 illustrate this relation for tECG, cECG and aECG data, respectively.

Whereas homoscedasticity among the *dim* groups can be proven for tECG and cECG and all selectors, no significant correlation is observed for the BSS output components of tECG. On the contrary, aECG BSS output components show heteroscedasticity among the *dim* groups which prohibits an evaluation of potentially negative correlations of $\mathrm{ACC}_{\mathrm{rel}}$ and *dim*. For cECG data, a significant negative correlation can be proven for the $SKEW$ and $KURT$ selector which indicates that BSS component selectors based on higher order moments are negatively affected by an increasing *dim*, i.e. select the best available (maximum ACC) component less effectively while increasing the number of output components.

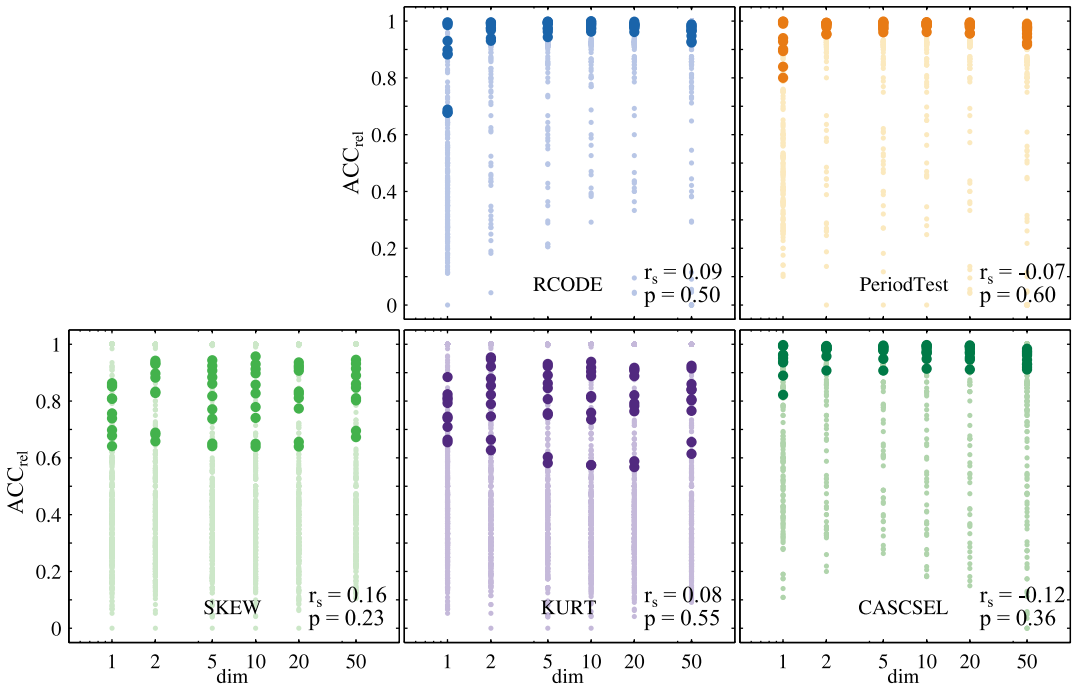

(a)

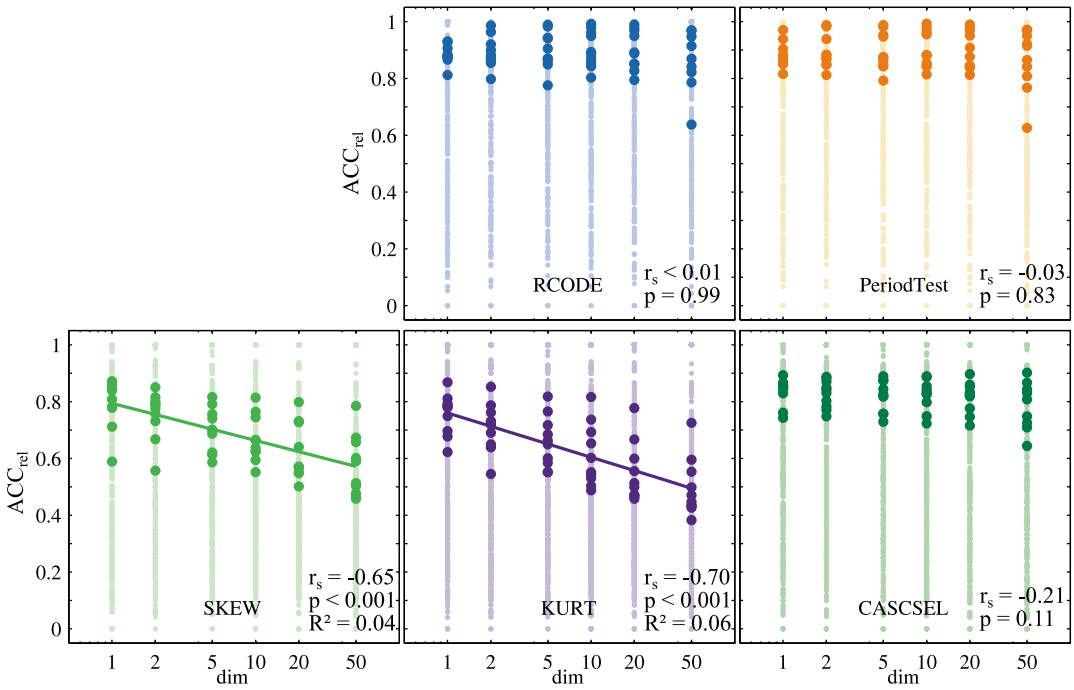

(b)

Figure 48: Relation between the spatio-temporal BSS dimension *dim* and the relative heartbeat detection accuracy ACC_{rel} for (a) tECG and (b) cECG data each given a BSS component selection algorithm. Full data distribution is shown in faint color, subject-wise averaged data (N = 10) is shown in bright color. An exemplary linear regression (incl. R^2 for the non-averaged data) is calculated and drawn, if the data show homoscedasticity and Spearman's rank partial correlation coefficient r_S indicates a significant correlation ($p \leq 0.05$).

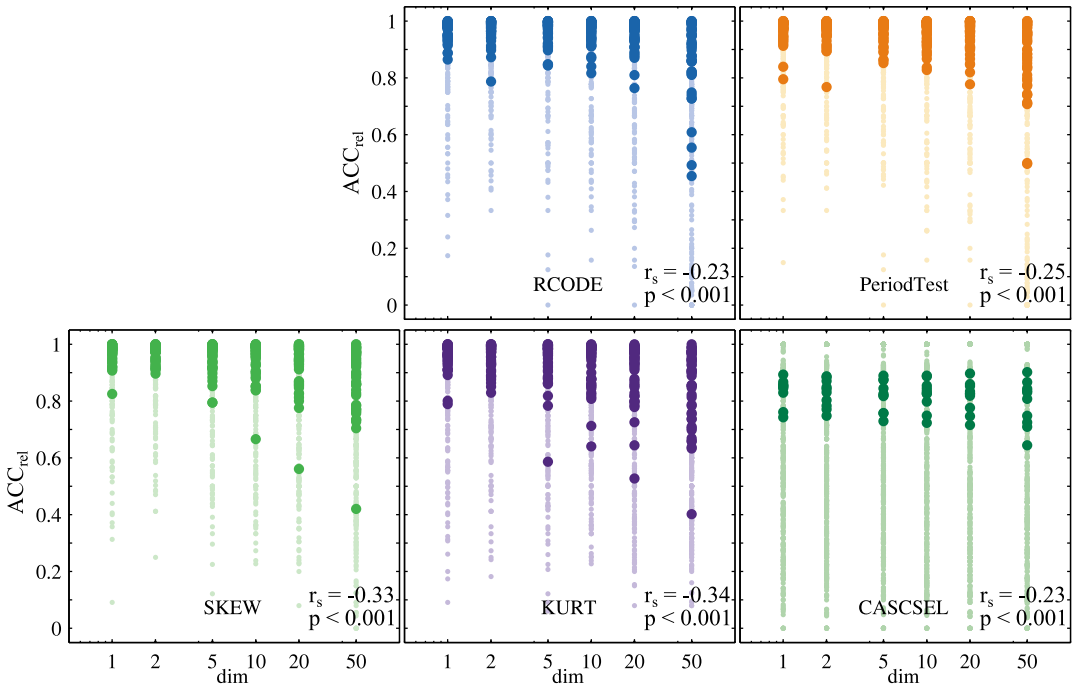

Figure 49: Relation between the spatio-temporal BSS dimension *dim* and the relative heartbeat detection accuracy $\mathrm{ACC}_{\mathrm{rel}}$ for aECG data each given a BSS component selection algorithm. Full data distribution is shown in faint color, subject-wise averaged data (N = 48) is shown in bright color. An exemplary linear regression (incl. R^2 for the non-averaged data) is calculated and drawn, if the data show homoscedasticity and Spearman's rank partial correlation coefficient r_S indicates a significant correlation ($p \leq 0.05$).

Additionally, selectors based on sparse coding (*RCODE*, *PeriodTest*) show no significant $\mathrm{ACC}_{\mathrm{rel}}$ correlation with *dim* for tECG and cECG data and thus, show a selection performance that is not affected by the number of output components ($dim \in [1, 50]$).

6.4 CHAPTER SUMMARY

The preceding section reports the results of a variety of experiments conducted based on simulated and real-world (cb)PPGs and ECGs of different kind, i.e. tECG, cECG and aECG.

The experiments utilizing simulated PPG data and a well-controlled experimental environment highlight the differences among different PCA and ICA algorithms with respect to their performance on source signal conditions (e.g. orthogonality) and signal mixtures featuring different noise types and underdetermined mixtures of different nature. Thereby, the results are represented by measuring SNRs as well as the reliabilities of the BSS solution $\mathbf{W}$ and the BSS output $\mathbf{y}$. Besides the core algorithmic differences, the experiments based on simulated PPGs result in insights regarding the modification of BSS algorithms. In this context, batch processing does negatively affect the reliability of $\mathbf{W}$ and $\mathbf{y}$ whereas the SNR is not significantly affected by such techniques. Also, spatio-temporal BSS is shown

to rather decrease cbPPG SNRs but partially performs beneficially for convolutive and non-stationary mixtures.

The experiments based on real-recorded cbPPGs follow the path of characterizing the BSS performance given controlled conditions about the BSS inputs where it is possible. These experiments show a BSS output performance, whose SNR is dependent on factors like the input SNR and the fundamental nature of the cbPPG mixture.

The subsequent experiments feature approaches to permutation indeterminacy based on ECG data. The results show that the newly introduced automated BSS component selection algorithms based on sparse coding outperform standard selectors based on higher order moments with respect to the absolute heartbeat detection accuracy and relative heartbeat accuracy, i.e. the select-ability of a maximum accuracy output. Moreover, these findings hold regardless of the spatio-temporal BSS dimension dim.

Cersei: "We pay you for truth, Lord Varys. Remember that, or this small council may grow smaller still."

— George R.R. Martin in *A Clash of Kings* p.529, A Song of Ice and Fire (1998)

7

DISCUSSION AND PROSPECTIVE

This chapter provides the discussion of the above described results. Section 7.1 discusses how different (cb)PPG data from synthesized and real camera-based origin influence BSS. Section 7.2 discusses the algorithms presented to solve permutation indeterminacy for ECG processing by BSS. Finally, section 7.3 discusses the comprehensive experiment about linking BSS inputs and output indeterminacy. Contents of this chapter partially appeared already in own publications, i.e. [284, 286, 287].

7.1 SELECTION OF BSS INPUT DATA

7.1.1 *Source Signal Characteristics*

In typical Blind Source Separation algorithms and applications, the orthogonal approach is utilized to computationally solve the BSS problem. Specifically, the estimated sources $\mathbf{y}$ are required to form an orthogonal system regardless of the orthogonality of the original sources $\mathbf{s}$. This constraint is intended to simplify the computations [123]. However, it cannot be guaranteed in principal that this constraint holds in real-world source signals (e.g. the original sources within cbPPG measurements). Therefore, the question is raised whether violations from the orthogonal approach affect the BSS results in the cbPPG context. First, it is verified that sources $\mathbf{s}$ assembled from PPGs and different artificial disturbance signals out of {SIN, CHIRP, TREND, STEP} together with noise express significant differences in their deviations from orthogonality $d_{\perp}$. This is taken as a justification to use these artificial signals together with PPGs in order to evaluate the influence of violations from the orthogonal approach onto BSS results. Furthermore, different commonly applied BSS algorithms, i.e. PCA and ICA (FastICA with different contrast functions, JADE, RADICAL), are assessed regarding their BSS results with respect to the violation from the orthogonal approach. ΔSNR_{orig} describes the change of the SNR of the PPG component due to BSS application. The reliability of $\mathbf{W}$, i.e. U_{max} assesses the stability of the BSS solution and the reliability of $\mathbf{y}$, i.e. ρ_{sy} assesses the morphology retention by BSS.

The quantitative results show that for each tested BSS algorithm there exists a significantly negative relation between ΔSNR_{orig} and increasing $d_{\perp}$, i.e. the output SNR and

thus strength of the cardiac pulse in the extracted PPG component y_{PPG} decreases while the violation from the orthogonal approach in the sources $\mathbf{s}$ increases. On the contrary, the reliability of $\mathbf{W}$ (U_{max}) is not significantly affected (despite for FastICA with only low variance explanation of $R^2 \approx 5\,\%$) by a increasing $d_\perp$. That indicates BSS showing stable solutions (i.e. stable transformations $\mathbf{W} \cdot \mathbf{x}$) with respect to changes in the orthogonality of the source system $\mathbf{s}$. Accordingly, in a real-world measurement scenario where the original source signals, and thus $d_\perp$ are not known a priori, the online-estimate U_{max} cannot be used to reveal deviations from the orthogonal approach in the source system formed by $\mathbf{s}$. Thus, U_{max} is only of limited use as an online indicator of the expected quality of the BSS solution, if the violation of the orthogonal should be considered. However, the online detection of such violation would be beneficial. Accordingly, the results of the relation between $d_\perp$ and the reliability of $\mathbf{y}$ (ρ_{sy}, see Figure 30b, p.111) show a significant inverse relation between increasing $d_\perp$ and ρ_{sy} for all ICA algorithms (not for PCA). This indicates that ICA decreasingly preserves the morphology of the original sources $\mathbf{s}$ in $\mathbf{y}$ with increasing deviation from the orthogonal approach. Thus, by forcing orthogonal output components, ICA potentially impairs morphology retention. Especially, RADICAL shows a high negative correlation $r_S = -0.83$ with high variance explanation $R^2 \approx 76\,\%$. RADICAL combines the entropy-based ICA approach known from e.g. FastICA with the compartementalized transformation optimization based each on pairs of the entries of the rotation matrix which is known e.g. from JADE. The combination of this two properties could be assumed to contribute to the increased sensitivity of RADICAL to deviations from the orthogonal approach compared to other ICA algorithms. Otherwise, ICA algorithms perform similar among each other, however, with JADE and RADICAL showing a slightly better reliability of $\mathbf{W}$ (lesser U_{max}, see Figure 32a, p.113) for CHIRP, TREND and STEP disturbances compared to FastICA. PCA in general shows a worse separation performance ($\Delta\mathrm{SNR}_{orig}$, $d_\perp$) compared to ICA given the selected source signals and symmetric random mixtures. In the cbPPG community [55, 99, 153], PCA is typically not directly compared to the performance of ICA where rather the ICA application is discussed against the originally measured signals. Still, Holton *et al.* [112] report heartrate estimates in PCA outputs showing higher absolute errors compared to ICA outputs which indirectly confirms the above findings. Nevertheless, the PCA performance with respect to cbPPG morphology retention shows a main difference compared to ECG processing, i.e. [49] reported PCA to maintain diagnostic morphology in the projected space rather then ICA.

In real-world cbPPG processing, the SNR difference between BSS inputs $\mathbf{x}$ and outputs $\mathbf{y}$ defines the benefit of a cbPPG processing algorithm since the original source signals $\mathbf{s}$ are not available. The question whether a higher SNR also coincides with a better morphology retention (ρ_{sy}) can be positively answered for ICA algorithms for the given synthesized data. Despite explaining only a small amount of variance ($R^2 \approx 3\,\%$), a significant positive correlation has been observed between $\Delta\mathrm{SNR}_{orig}$ and ρ_{sy} (see Figure 33b, p.115). U_{max} is not consistently related to $\Delta\mathrm{SNR}_{orig}$ across the BSS algorithms and shows positive

correlations (again of small variance explanation, see Figure 33a, p.115) for FastICA and RADICAL only. Accordingly, the online-estimate U_{max} cannot in general be utilized to decide whether a signal of maximum SNR has been extracted by BSS.

7.1.2 *Mixture Signal Characteristics*

In the previously discussed experiments on the influence of source signal characteristics, i.e. the influence of violations of the orthogonal approach on BSS results, a symmetrical and thus well-determined mixture $\mathbf{x} = \mathbf{A} \cdot \mathbf{s}$ was guaranteed by the experimental design. However, in real-world (cbPPG) measurements mostly utilizing three input signals prior to BSS processing as proposed by Poh *et al.* [212], it becomes likely that the measured mixtures present underdetermined mixtures. Thus, more source signals are incorporated into the measured mixture than mixture signals available.

The according experiments (see e.g. Figures 34 and 35, p.116f) on underdetermined mixtures show that both the strength of the cardiac pulse (ΔSNR_{orig}) as well as the PPG's signal morphology (ρ_{sy}) is preserved significantly worse in PCA compared to ICA algorithms. However, this confirms the results of the determined mixtures above. Comparing the ICA algorithms among each other reveals a comparable performance of different ICA algorithms on underdetermined mixtures. A detailed view also shows RADICAL causing outputs $\mathbf{y}$ of significantly less SNR compared to FastICA and JADE for underdetermined PPGs. These signal mixtures can be expected to show a distinct violation of the orthogonal approach since two different PPG segments from the same RRI series are assembled in the original sources $\mathbf{s}$. That increases the probability of correlation between the two PPG source signals. Moreover, JADE shows a higher reliability of $\mathbf{W}$ compared to FastICA for underdetermined mixtures, however as discussed for the determined problems above, U_{max} cannot be proven to provide an added value as an online-estimate of the BSS performance since it cannot be globally linked to SNR or ρ_{sy} improvements by BSS.

As can be seen from Figure 36 (p.119), underdetermined mixtures caused by phase shifts between multiple measurements of the same PPG signal within the signal mixture are affecting the BSS outcome in terms of the strength of the cardiac pulse (ΔSNR_{orig}) as well as the PPG's signal morphology retention (ρ_{sy}). However, the effect is strongly dependent on the particular time lag τ_{PPG}, which itself can be expected to be heavily dependent on the mean heartrate of the PPG segment. This particular relation is not further quantified within this thesis. Moreover, SOBI which is conceptually capable of compensating phase differences qualitatively shows a similar interference by phase shifts as other ICA algorithms if also disturbance signals are involved.

The experiments based on heterogeneous underdetermined mixtures (mixing PPG and BCG signals) reveal that despite there are no significant differences between the BSS algorithms, RADICAL shows the qualitatively worst performance on these mixtures with respect to SNR and the reliability of $\mathbf{W}$ (see Figure 37, p.121).

7.1.3 *Mixture Signal Modification*

Mixture signal modification provides the possibility to either achieve computational advantages by e.g. applying batch processing techniques or to apply more comprehensive (but computationally more demanding) BSS models by e.g. utilizing spatio-temporal BSS approaches. Both techniques are characterized in the context of cbPPG processing.

The experiments on batch processing (see e.g. Figures 38 and 39, p.122f) show that the preservation of the strength of the cardiac pulse (ΔSNR_{orig}) is not affected by batch processing, i.e. there exist no significant relation between the batch size and the SNR. However, there is a small positive relation between batch size and morphology retention (ρ_{sy}) whereas this correlation is of small absolute value ($r_S \approx 0.5$) and variance explanation ($\text{R}^2 \approx 1\,\%$). The reliability of $\mathbf{W}$ is strongly negatively affected (increasing absolute value U_{max}) by decreasing the batch size. This can be expected since the fewer samples involved in the computation, the more important are becoming single samples. Overall, batch processing seems to be a suitable computational tool for cbPPG processing with BSS.

The spatio-temporal BSS experiments (see e.g. Figure 40, p.124) show an inverse relation between the preserved strength of the cardiac pulse (ΔSNR_{orig}) and the increasing spatio-temporal dimension dim for both FastICA and JADE. Nevertheless, the subsequent experiments on convolutive mixtures reveal (see e.g. Figure 41, p.125) that spatio-temporal FastICA can compensate for convolutive mixtures by applying a spatio-temporal dimension dim equaling the dimension of the convolutive mixture itself. Specifically, the output SNR of y_{PPG} does not show a significant difference to the original SNR of s_{PPG} for $dim = 10$ (FastICA). On the contrary, spatial-only FastICA ($dim = 1$) and other configurations do not preserve the SNR, i.e. show a significant difference in the SNR. Simultaneously, JADE is not capable of compensating for convolutive mixtures in this spatio-temporal setup with respect to the SNR. In addition, FastICA but not JADE shows to cope with the tested non-stationary mixtures for the given dim selections. In summary, spatio-temporal FastICA if properly configured, i.e. incorporating a problem-matching dim, shows to successfully handle complex mixing scenarios like convolutive and non-stationary mixtures in the cbPPG domain. A suitable spatio-temporal dimension dim might be estimated in practical applications by delay embedding [240]. I.e. convergence of a state-space reconstruction [129] with respect to the measured signals can guide a dim selection. However, the reconstruction dimension d of a state-space reconstruction is not only effected by mixture complexity (addressed by dim) but also by the time-structure of the underlying source signals. An online-estimate of d might thus be larger than the required dim to separate a non-stationary mixture. For instance, Sun *et al.* [243] selects dim based on the time-structure and calculates dim based on the frequency content of interest. However, the results (see e.g. Figure 41, p.125) also show that increasing dim above the mixture complexity (larger then dim used for $\mathbf{A}$) does decrease the output SNR. Thus, a delay

embedding to estimate *dim* should address the complexity of the mixture $\mathbf{A}$ rather than the a state-space reconstruction of the signals $\mathbf{x}$.

7.1.4 *Spatial (Contextual) BSS Input Selection*

ROI SELECTION In real applications, ROIs for cbPPG extraction have to be selected by using automated video processing algorithms. Typically, rectangular ROIs using frontal face classifiers for detection and (stabilized) tracking of the complete face [212] or selective rectangular ROIs [79, 181] or non-rectangular ROIs [252] of smaller face parts further using facial landmarks are used. The contextual selection of BSS input signals from square ROIs utilized within this thesis does not require face detection. Yet, standard ROIs are compared to the contextual selection methods by simulating a perfect functioning face/face part detection by manual ROI selection (see Figure 22, p.99).

This comparison (see tables 2 and 3, p.127,131) shows that the automated spatial selection among small-sized squared $\mathrm{ROI_n}$ (S^{mc1} and S^{ms1}) outperforms the input SNR of selecting ROIs of the whole face or parts of it (forehead and cheeks) including consistent effect sizes g. Together with BSS, the output SNR (Figure 44, p.130) show inconsistent effects which will be discussed later.

However, the comparison of deterministic and random selection of $\mathrm{ROI_n}$ clearly motivates that assembling homogeneous input characteristics (wavelength, dominant frequency) for BSS processing is not sufficient to reach the best BSS outcome. Both, the deterministic as well as the random selection of ROIs make use of periodicity in terms of frequently occurring dominant frequencies. Accordingly, both sets S^{mcR} and S^{msR} contain signals of the same dominant frequency and thus, homogenous content from a frequency perspective should be present up to some extent. Still, input and output SNR of MCR and MSR of both BSS algorithms show absolute values below 0 dB (see tables 2, 3 and Figure 42, p.127 and 131). In addition, the BSS performance as a function of the input SNR (Figure 43, p.129) shows an inferior performance compared to deterministic selection of equally sized ROIs in terms of a broadened area of negative performance (performance below x-axis) which widely lasts into the range of negative input SNR. This finding underlines the necessity to process the best available input. Consequently, BSS is not necessarily able to compensate for lower input SNR under comparable conditions (ROI size, dominant frequency).

BSS PERFORMANCE Figures 50 and 51 show examples of selecting $\mathrm{cbPPG_{n,color}}$ according to the proposed BSS input selection and the further processing of these signals with PCA and ICA for the monochrome (MC1) and multispectral (MS1) case, respectively. In both cases, PCA and ICA are able to extract a distinct pulsatile component in the time domain. Focusing on the markedness of the spectral peak related to the heart rate in the spectra $X(f)$, it is worth noting that in the monochrome set (Figure 50), PCA and ICA

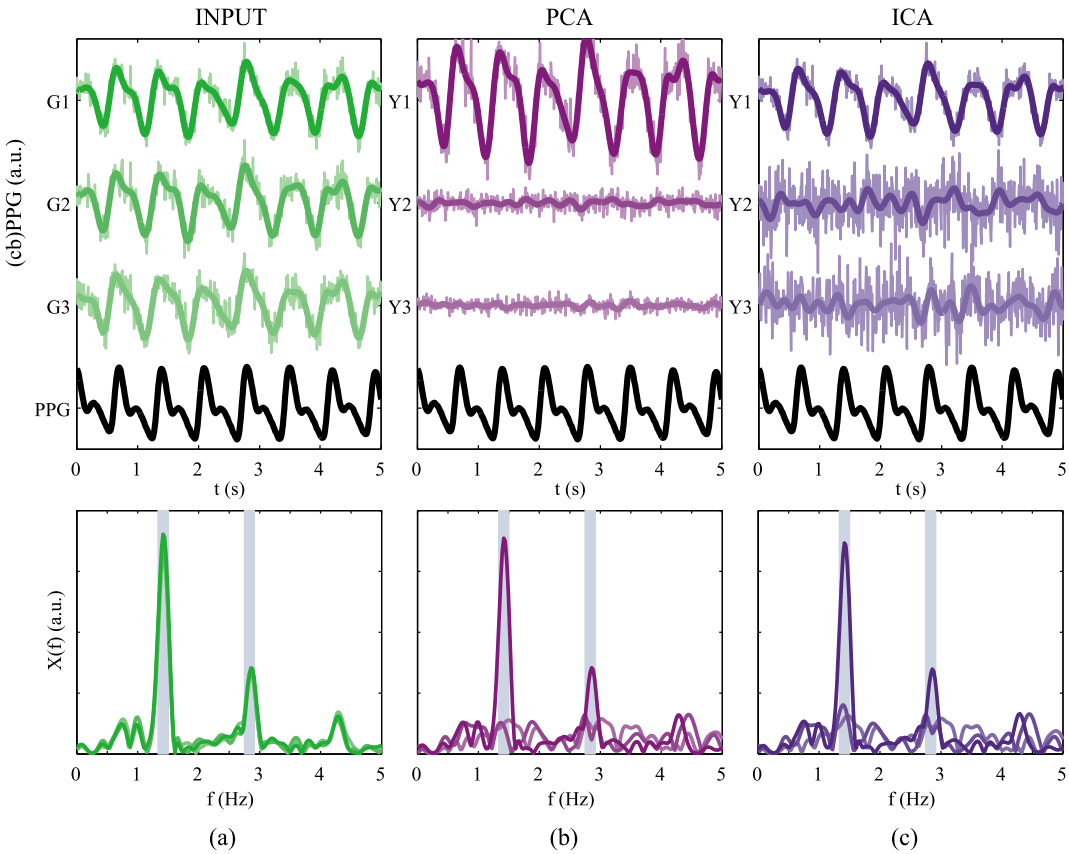

Figure 50: Sample signal excerpts (+ 4 Hz lowpass filtered (bold signal) versions) and amplitude spectra according to an automatically selected set S^{mc1}. (a): BSS input. (b): PCA output. (c): ICA output. The true heart rate from the reference and its harmonic (± 5 bpm) is indicated by the colored areas in the back of the spectra. Colors of the respective spectra are according to the time signals. [286]

are performing similar. On the contrary, in the multispectral set (Figure 51) PCA shows a decrease in the spectral power of the cardiac pulse compared to ICA. However, both examples and both BSS algorithms show at least one output component of proper quality regarding common postprocessing tasks (e.g. heart rate estimation). Accordingly, even a decrease in signal quality by application of BSS not necessarily renders post-processing impossible. Nevertheless, morphology retention through BSS should be considered carefully [13].

Several researchers have reported that BSS not necessarily improves cbPPG quality and outcome. ICA was found to, if any, only subtly decrease the heart rate error for a small-sized cheek ROI [55] and even (slightly) increase for rectangular face ROI [112, 153] compared to the BSS inputs. Moreover, PCA was found to perform worse on multispectral input compared to FastICA [112]. Since movements affect the input signal quality, it is worth relating these results to the movement conditions during recording. Christinaki *et al.* [55] allowed for small movements (facial expression) while extracting cheek ROIs, whereas face ROIs were extracted from subjects who were asked not to move [112, 153]. Accordingly, ICA showed a benefit for moderate motion scenarios but not for motionless

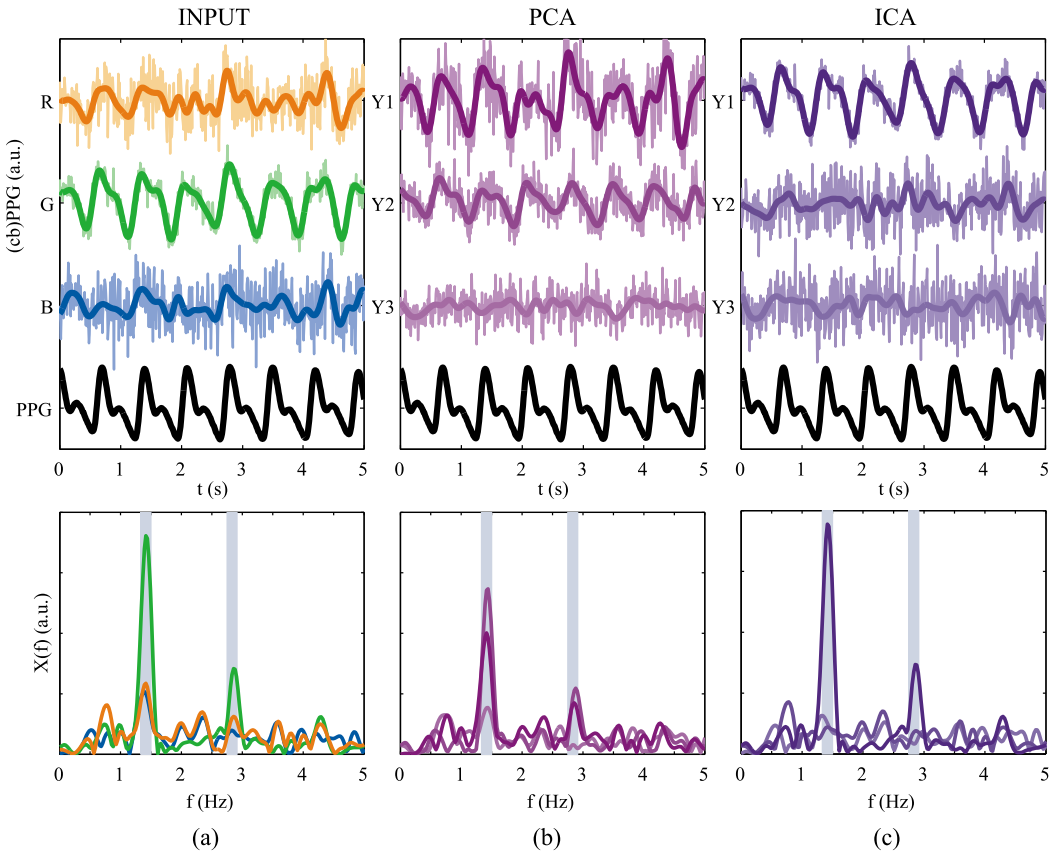

Figure 51: Sample signal excerpts (+ 4 Hz lowpass filtered (bold signal) versions) and amplitude spectra according to an automatically selected set S^{ms1}. (a): BSS input. (b): PCA output. (c): ICA output. The true heart rate from the reference and its harmonic (± 5 bpm) is indicated by the colored areas in the back of the spectra. Colors of the respective spectra are according to the time signals. [286]

setups. Also, improvements of Bland Altman heart rate measures for facial ROIs turned out to be higher for movement phases compared to no movement [212].

Such findings are in accordance with the results obtained by this thesis's investigations. Considering Figure 43 (p.129) which indicates an inverse relationship between input SNR and BSS performance (negative ΔSNR), the usage of BSS can even decrease the signal quality, its application thus should be considered with care. Particularly for small-sized ROIs after deterministic spatial selection (MC1, MC2, MS1, MS2), a SNR decrease mainly appears in case of high quality input (to the right of the y-axis) and is differently pronounced for different sets. On the contrary, especially the standard approaches using the face ROI and the forehead-cheeks ROI (Figure 43, p.129), respectively, are not showing this marked negative BSS performance, while the increase of SNR for good quality inputs is also limited.

ROI HOMOGENEITY Different factors of (in-)homogeneity of input signal sets to BSS are assessed in a controlled fashion by the experiments on contextual BSS input (ROI) selection.

First, the sensitivity of BSS algorithms regarding input of different dominant frequencies is analyzed. The results show that the ICA can take advantage of input signals comprising content with different dominant frequencies (output SNR MC2 > MC1) while PCA shows significantly worse performance on MC2 compared to ICA (see Table 3, p.131). One might infer that the concept of statistical independence as applied for ICA is rather suited to such content compared to the basic concept of decorrelation utilized for PCA. However, in case of a very homogeneous BSS input (MC1) comprising only one uniform wavelength and dominant frequency, PCA performs significantly better than ICA. As we used pre-whitening prior to ICA which is similar to PCA, one might deduce that the contrast applied for ICA, which is used to additionally transform the pre-whitened data, isn't well chosen to extract the cardiac pulse component. A potential application of the result that only PCA is able to preserve the SNR in very homogeneous (wavelength, dominant frequency) high quality inputs of small-sized ROIs could be the evaluation of ΔSNR of spatially distributed ROIs to address the spatial homogeneity of the cutaneous microcirculation. Two-dimensional statements of the microcirculation may provide clinical significance in critical care patients [217].

Second, the question of sensitivity of BSS algorithms regarding wavelength homogeneity could clearly be answered for same ROI size and equal dominant frequencies (MC1, MS2) in support of the monochrome approach. Both, PCA and ICA, showed a significantly higher output SNR (see Table 3, p.131) by using the monochrome input. Also consistent effects are found for both ANOVA and ANCOVA on outputs (Figure 44, p.130). Such findings support the idea that wavelength-dependent penetration depth into human skin imposes a non-linear problem [117], which BSS cannot consistently resolve. However, the results also confirm the better suitability of ICA compared to PCA for multispectral face ROI input (F) [112].

Another result giving insight into BSS input homogeneity is stated by the comparison between the multispectral sets MS1, MS2, FhC and F. While ROI size and input SNR show an inverse relationship, the output SNR of multispectral PCA and ICA shows proportionality to the ROI size except for the rectangular face ROI (see tables 2 and 3, p.127,131). Up to $\mathrm{ROI}_{\mathrm{FhC}}$ one might assume a homogeneous ROI augmentation since mostly homogeneous skin regions without marked edges and regions which do not necessarily contribute to a distinct cardiac pulse are consolidated with $\mathrm{ROI}_{\mathrm{FhC}}$. The same skin regions are principally addressed by the sets MS1 and MS2. The only exception gives $\mathrm{ROI}_{\mathrm{F}}$ where also less-suited regions like mouth and nose are included in the ROI, thus serving a inhomogeneous ROI augmentation. Consequently, homogeneous ROI augmentations seems to be beneficial for multispectral BSS, whereas inhomogeneous areas inside ROIs should be omitted in order to optimize the extraction of the cardiac pulse. This behavior could also be found regarding heart rate error measures after FastICA on 15 s cbPPGs of different ROIs [179]. Despite that investigation neglected the input quality, the FastICA output showed decreasing heart rate error measures while step-wise excluding the face surrounding and face borders

from the ROI. On the other hand, the heart rate error of outputs increased again while assessing ROI with highly edged face regions mostly containing nose and mouth structures. Nevertheless, the positive effect of homogeneity of the input seems to be limited especially considering monochrome inputs of high signal quality.

LINKING TO RESULTS OF SYNTHESIZED DATA The experiments on real cbPPG signals show that increasing ROI size (especially inhomogeneous augmentation) causes a decreasing SNR of the input signals prior to BSS. However, this can be expected since the small-size ROI selection is based on SNR. Also, this input SNR affects the BSS performance, i.e. $\Delta\mathrm{SNR}_{\mathrm{BSS}}$ (see e.g. Figure 43, p.129). For instance in small size ROIs many $\mathrm{SNR}_{\mathrm{in}} > 0\,\mathrm{dB}$ are available whereas further BSS processing causes a $\Delta\mathrm{SNR}_{\mathrm{BSS}} < 0\,\mathrm{dB}$. Such cases should be avoided in BSS applications. Only PCA can deal with high quality inputs but for homogenous sets only (MC1) where on average also the highest mean output SNR after BSS is obtained by this setup. For other sets the high input SNR is compensated (extinguished as can be seen by negative $\Delta\mathrm{SNR}_{\mathrm{BSS}}$ in Figure 43, p.129). Taking into account the input SNR (see combined ANOVA/ANCOVA statistics in Figure 44, p.130) some consistent effects can be proven. ICA shows a better BSS performance for monochrome sets MC1 and MC2 compared to the multispectral MS1. Also for PCA, MC1 outperforms MS1 whereas opposed to ICA this does not hold for MC2 (on the contrary MC1 > MC2). Comparing PCA and ICA (see Table 3, p.131), ICA performs significantly better on MC2 and F.

In homogenous good quality signals (like MC1), the mixtures $\mathbf{x}$ contain very similar disturbance-free signals, which can be separated in signals orthogonal to each other, e.g. a PPG and noise components (see e.g. Figure 50). However, in inhomogeneous sets (e.g. MC2, MS1) the different components do not necessarily form an orthogonal system. Nevertheless, both PCA and ICA algorithms have shown a relation between increasing deviation from orthogonality and decreasing SNR, yet, PCA has shown a worse performance compared to ICA in presence of disturbances as well as in underdetermined conditions for synthesized data. Especially in multispectral or otherwise inhomogeneous sets, underdetermined mixtures are likely. The output SNR comparison between PCA and ICA at MC2 and F, respectively, confirms that.

The experiments on synthesized data does not explain the ICA results on homogenous high quality inputs. This behavior might be attributed to the used ICA optimization contrast. MC1 consists of inputs which are as homogeneous as possible. The decorrelation transformation conducted by PCA is mostly able to preserve the SNR and shows the lowest number of segments with negative ΔSNR for high (positive) input SNR (see Figure 43, p.129). In comparison, the additional rotation introduced by ICA decreases the SNR for this set. However, the exclusive usage of PCA for high quality inputs is not sufficient if the input is not as homogeneous as assembled by MC1 as the results of MC2, MS1 and MS2 show. So far, a standard tanh-contrast for FastICA as well as symmetric optimization

for uniformity of the amount of output signals is used for the cbPPG signals. One should further test optimized contrasts or alternatively, let the demixing be guided by an expected cardiac pulse composition [95]. Regarding contrasts, Morris *et al.* [195] indicates utilizing the sub-Gaussian properties of the cbPPG component. The experiments on synthesized data, however, does not show a marked improvement of BSS performance for sub-Gaussian contrasts. Sub-Gaussian FastICA as other FastICA contrasts shares the dependency on deviations from the orthogonal approach and shows a comparable performance on different disturbance types and underdetermined mixtures.

Another possibility to avoid undesired SNR decrease, if no SNR preserving contrast for high input quality is available, could be an adaptive decision, whether a BSS algorithm should be applied or not. This decision could be based on the prior SNR estimate based on peak frequency detection which is done during the selection process of inputs. Alternatively, deflationary ICA could be applied to focus on single components instead of simultaneously calculating a rotation for the full set of input signals $\mathbf{x}$.

However, whereas the latter discussion focuses on high quality inputs and the avoidance of a SNR decrease in already good quality signals due to BSS, it is worth noting that still inputs of inferior quality (SNR) can be processed well with BSS, i.e. BSS facilitates a significant SNR increase for low input SNR (see e.g. Figure 43, p.129).

7.2 APPROACHES TO PERMUTATION INDETERMINACY

7.2.1 *Permutation Indeterminacy for ECG Signals*

THE POTENTIAL OF SPATIO-TEMPORAL BSS BSS in general is considered an appropriate tool for the processing of measurements imposing non-predictable and varying signal qualities across multiple ECG channels. Moreover, spatio-temporal BSS is a powerful processing technique which combines spatial-filtering of multichannel data with channel-wise adaptive FIR filtering all guided by the concept of statistical independence [204]. Although it has been proven to successfully compete against the standard BSS [290], its application to cardiac signal processing is addressed only by limited number of researchers, so far [204, 243, 281, 290]. This may be attributed to the lack of robust selectors of components of interest (i.e. the cardiac component), namely for solving permutation indeterminacy, a problem intrinsic to the BSS. Especially, spatio-temporal BSS generates a vast amount of output components after its usage. Particularly, a very large number of temporal filter coefficients is proposed in [243]. At the same time, even pure spatial BSS (standard BSS) often requires complex selection routines of cascaded structure or pre-computed thresholds. Pre-trained templates are seldom transferable over datasets of different nature [4, 101, 222]. On the other hand, using non-symmetric BSS approaches like projection pursuit [204] which estimates output components one-by-one still involves the problem of deciding whether the component of interest has already been extracted.

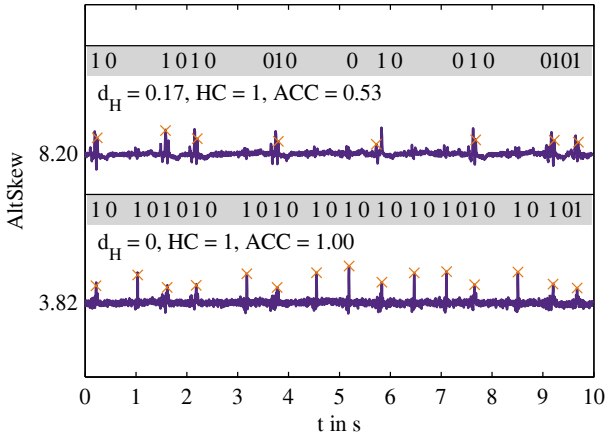

Figure 52: Two different BSS output component examples of one aECG recording. The lower panel shows the *RCODE* selection and the respective *PeriodTest* selection is depicted in the upper panel. The corresponding modified Hamming distance (d_H), Hamaneh criterion (HC) and beat detection ACC is provided. The sparse code sequence is indicated above each component and the QRS detections obtained from the customized peak detector are marked as orange crosses. The y-axis shows the *AltSkew* measure. [287]

It has been shown, that component selection methods based on peak detections (i.e. *RCODE* and *PeriodTest*) and their rhythm evaluation regarding potential cardiac behaviour are capable of handling spatio-temporal BSS outputs of different data nature (i.e. tECG, cECG, aECG). This can be seen from Figure 45 (p.133), where for tECG and aECG data both median and inter-quartile-range (IQR) show output accuracies of selected components being ACC = 1. Also, the highly distorted cECG data achieve an IQR ACC > 0.9. This finding is underlined by the pairwise comparisons of these selectors with the average input quality (section A.4.1, p.173f), always significantly increasing ACC. Efficient usage of spatio-temporal BSS, thus, becomes possible.

SELECTION STRATEGIES During automatic selection of a single (desired) BSS component, undesired components (e.g. artifact components) might resemble features initially chosen to characterize the desired component. In particular, higher order moments are heavily affected by outliers or time-/frequency based features [285]. Moreover, both types of features may vary in absolute and relative values between datasets of different origin [3], which renders an according feature selection to be even more complicated. The susceptibility of higher order moments to artifacts is especially observed in the minimal-conductive ECG datasets (tECG and cECG, see Figure 45, p.133), where artifacts are likely to occur (e.g. see Figure 25(a), p.102). In pairwise comparisons (section A.4.1, p.173) even a decrease in ACC after BSS application and the subsequent selection was obtained by using skewness or kurtosis selectors (with outlier removal). For an almost artifact-free ECG setting (aECG) the higher order moments (i.e. skewness) performed well and no significant difference compared to other selectors was observed. This highlights the limitations

of higher order moments as the BSS component selector in distorted ECG settings. Still, skewness showed better performance than kurtosis, which is in accordance with [290].

Nevertheless, a selector based on peak detections can also be misguided, since its performance is given by: (1) the detection performance prior to selection, and (2) the detection performance after selection. Both performances are not necessarily the same, since, e.g. prior to selection, the presented detector was designed to be more sensitive to artifacts compared to the post-selection detector. Also, periodic artifacts (such as those included in the measurement protocol of the assessed cECG data) can cause an artifact component being a good cardiac candidate according to the selection criterion. The large IQR (Figure 46a, p.134) of components showing Hamming distance or Hamaneh criterion equaling zero for the cECG data is a possible consequence. However, Figure 46a shows the detection accuracy in all available output components, whereas Figure 45 (p.133) illustrates the results only for the selected ones. The largely decreased IQR in Figure 45 (cECG) compared to Figure 46a (p.134) supports the usability of our additional selection criterion $AltSkew$ in the case of multiple cardiac component candidates after peak detection evaluation and underlines its necessity. In the case of arrhythmia, which can also hamper periodicity tests based on peak detections, the advantage of our advanced code manipulation and assessment ($RCODE$) compared to the simple periodicity test ($PeriodTest$) emerges. Figure 52 underlines this finding by means of two BSS components after processing aECG. The upper component was selected by $PeriodTest$ solely based on $AltSkew$, because no output component could be classified as periodic according to the Hamaneh criterion HC (HC = 1 $\forall$ components). Accordingly, using $AltSkew$ alone fails to select the proper component in this case. The lower component (Figure 52) was selected by $RCODE$ according to its modified Hamming distance $d_H = 0$ and shows maximum ACC = 1. Thus $RCODE$ shows a higher capability to select cardiac components in the case of arrhythmia. Also, $RCODE$ explicitly tries to compensate for arrhythmia originating from blocks before rhythm evaluation (but it doesn't compensate for fibrillation type arrhythmia). Whereas this is not relevant for the healthy subjects in the tECG and cECG data, for the aECG data is obtained a slightly but significantly higher output ACC using $RCODE$ (section A.4.1, Table 33, p.173). Moreover, around 10% more components (Figure 46b, p.134) can be exploited of the aECG data showing Hamming distance equal to zero compared to the PeriodTest-selected components. Nevertheless, it should be noted that the BSS analysis of the two-lead ECGs in the aECG data comprises a less complicated component selection problem in BSS's permutation indeterminacy, as compared to the analysis of the tECG and cECG data. However, it is assumed, that the equivalent BSS processing for all data using the same amount of time lags in BSS input construction brings along comparable BSS component characteristics as precondition for the selection problem. Accordingly, the aECG results are considered exemplary for arrhythmia data originating from contact-less techniques.

7.2.2 *Permutation Indeterminacy for PPG Signals*

In the cbPPG domain, permutation indeterminancy remains only unsatisfactorily solved. Wedekind *et al.* [284] showed that traditional component selection algorithms like utilizing a SNR measure (without ground truth) achieved a success rate of around $70 \pm 20\%$ among only three cbPPG components. Thereby, a success was defined by an automatic selection of the component with maximum SNR based on the ground truth. Better results were only theoretically obtained by using a combination of Markov models as a probabilistic selector. The above described sophisticated selection strategies applied to ECG processing thereby might contribute to a large improvement of the selection performance. The core part of the selection strategies of $RCODE$ and $PeriodTest$ is given by the rhythmical interpretation of heartbeat detections. Such strategies are highly transferable to other rhythmic signals of cardiac origin like the cbPPG. Still, a suitable beat detection algorithm adapted to the signal characteristics of a cbPPG would be needed, however, that is available in literature e.g. [30, 244].

7.3 LINKING INPUT COMPOSITION AND OUTPUT PERFORMANCE OF BSS

Spatio-temporal BSS modifies the measured signals and BSS inputs $\mathbf{x}$ by artificial augmentation using time-delayed version of the signals. This procedure has shown to improve the results of BSS processing in e.g. the ECG domain [290] as well as in the experiments on synthesized PPG data conducted within this thesis. Nevertheless, increasing the amount of input signals prior to BSS for the commonly applied symmetric BSS approaches also increases the amount of BSS output components in $\mathbf{y}$. This complicates solutions to permutation indeterminacy which are needed to automatically (e.g. for remote applications [4]) make any use of the BSS results for selecting components with improved SNR with respect to the original measurements. Accordingly, a potential improvement in signal quality due to BSS can only be utilized if the respective component in $\mathbf{y}$ can also be selected for further usage.

This relation is addressed for ECG data by the experiments regarding the hypotheses 6-1 and 6-2. Specifically, first a potential positive effect of increasing *dim* for spatio-temporal BSS is tested, i.e. if the maximum available accuracy $\mathrm{ACC}_{\mathrm{max}}$ among the BSS outputs $\mathbf{y}$ can be increased by increasing *dim*. Figure 47 (p.136) shows a valid positive effect of increasing *dim* at least for the cECG data. For tECG and aECG data, the measured positive effect cannot be considered further due to heteroscedasticity. The precondition for further utilizing this positive effect is a non-significant relationship between $\mathrm{ACC}_{\mathrm{rel}}$ and *dim*. $\mathrm{ACC}_{\mathrm{rel}}$ measures how an actually selected component (i.e. $\mathrm{ACC}_{\mathrm{sel}}$) matches the best available output component (i.e. $\mathrm{ACC}_{\mathrm{max}}$). This result is dependent on the actual selection algorithm. Figure 48 (p.137) especially for cECG finds a negative relation and thus a decreasing $\mathrm{ACC}_{\mathrm{rel}}$ while increasing *dim* for standard selectors $SKEW$ and $KURT$.

On the contrary, there are no significant correlations to *dim* for the selectors *RCODE*, *PeriodTest* and *CASCSEL* that have been newly proposed alongside this thesis. These sophisticated BSS component selection algorithms, thus, are capable of utilizing the BSS performance improvements possible by spatio-temporal BSS for ECG processing.

7.4 CHAPTER SUMMARY

The preceding section discusses the results gathered alongside the questions how BSS input influences the BSS performance as well as how the results of BSS processing can be exploited, i.e. what algorithms are suited to solve permutation indeterminacy.

Especially in the cbPPG domain, the benefit of processing cbPPG measurements with BSS in order to improve the signal quality has not yet been proven. Several experiments within this thesis approach this question by characterizing BSS performance under controlled BSS input conditions. Accordingly, it has been shown that both SNR and morphology retention is negatively affected by violations to the orthogonal approach that is underlying common BSS algorithms. Thereby, PCA performs worse compared to ICA on disturbances present alongside PPG signals as well as for underdetermined mixtures. Several ICA algorithms have been found to perform widely similar amongst each other in the tested setups. Despite some individual differences in certain experiments, however, FastICA shows some small advantages especially, because it can also be shown to successfully work with spatio-temporal ICA in the PPG domain. Moreover, cbPPG BSS performance has been found being dependent on the signal quality of the signal mixtures. Only PCA works as expected with high quality inputs, i.e. it preserves already high signal quality in the BSS input. However, as signal mixtures get content-wise inhomogeneous, ICA suits better than PCA. No single recommendation on what BSS algorithm should be used for cbPPG processing can be given. Adaptive algorithms could overcome the ambiguities. In this context, the online estimate U_{max}, i.e. the reliability of $\mathbf{W}$, has been tested if it is related to the output performance of BSS measured by the SNR or the morphology retention ρ_{sy}. Unfortunately, U_{max} has not shown a consistent relation to BSS output measures. U_{max} quantifies the influence of sample portions on the overall BSS solution. Potentially, violations of the orthogonal approach could rather be quantified by measures simultaneously addressing all available samples, e.g. distribution metrics like the pdf and the question how are the distribution metrics changed between BSS inputs $\mathbf{x}$ and outputs $\mathbf{y}$.

In the ECG domain spatio-temporal ICA allows for improvements in the processing performance, i.e. BSS outputs with increased heartbeat accuracy can be generated. This is necessary especially in remote measurements e.g. by contact-less measurement techniques. For these techniques, the signal quality is not likely to be kept at a high level across typical measurement scenarios. Spatio-temporal ICA has shown to cope with such scenarios. Most importantly, this potential can also be exploited by a successful solution to permutation indeterminacy. The application of the newly developed automated component

selection algorithms, especially the sparse coding based *RCODE*, show a high selection performance amongst BSS outputs of signals from different origin (tECG, cECG, aECG).

Cersei: "And you're quite certain, that Father is the lion?"
Tyrion grinned: "It's on all our banners."

— George R.R. Martin in *A Clash of Kings* p.321, A Song of Ice and Fire (1998)

8

CONCLUSION

BSS in biosignal processing aims at resolving an unknown signal mixture $\mathbf{x} = \mathbf{A} \cdot \mathbf{s}$ in order to improve the quality of the signals of interest. Contact-less measurement techniques typically involve significant distortions due to the nature of their measurement principles. Whether BSS contributes to an improvement of the signal quality depends on mainly two factors and the subsequent question if the chosen BSS algorithm presents a suitable match to each of these factors. One factor is given by the original source signals $\mathbf{s}$ and the question if the source model applied to extract $\mathbf{y} \approx \mathbf{s}$ matches the original sources present in the measurements. Common BSS algorithms follow the orthogonal approach and thus assume orthogonal sources. The second factor is given by the mixture $\mathbf{A}$, i.e. the question if the BSS model can compensate for complex (e.g. underdetermined, non-stationary, convolutive) mixtures.

This work has investigated the influence of these factors onto the BSS results for processing biosignals in the (cb)PPG domain. Moreover, the suitability of particular BSS algorithms given these factors was examined. In this context, this work has contributed a large selection of own synthesized PPG data and mixtures as well as real-world cbPPG data gathered during the *CardioVisio* project to facilitate cbPPG for clinical usage in critical care patients. Moreover, a candidate online estimate (U_{max}, i.e. the reliability of $\mathbf{W} = \mathbf{A}^{-1}$) to indicate poor BSS performance has been evaluated in the (cb)PPG context.

The results show that violations of the commonly applied orthogonal approach negatively affect the quality of the cardiac BSS output components, i.e. both the strength of the cardiac pulse SNR is decreased as well as the morphology retention is hampered by decreasing ρ_{sy}. Thus, common BSS application is negatively affected especially in those conditions, where different source signals are correlated, i.e. share significant amounts of variance. In these scenarios, one might consider non-orthogonal BSS approaches.

For the forced synthesized BSS model violations (e.g. orthogonal approach, underdetermined mixtures), PCA generally performed worse compared to different ICA algorithms. This behavior has also been found in real-world cbPPG where ICA showed better performance with inhomogeneous heterogeneous inputs. Thereby, inhomogeneous heterogeneous inputs are likely to contain underdetermined mixtures. On the contrary, considering the results of real-world cbPPG for the processing of homogeneous less-distorted signal mix-

tures (i.e. monochrome homogeneous high-quality cbPPG), the PCA outperformed ICA. ICA is even found to reduce signal quality in high-quality inputs. Thus, PCA seems to suit best in pure noise-reduction applications, i.e. where sufficient control and pre-selection of the BSS input is possible. However, real complex signal mixtures are rather addressed by ICA.

Many ICA algorithms have shown a comparable performance on different BSS model violations. For instance, the adaption of the FastICA contrast function towards sub- or super-Gaussian sources did not cause significant performance improvements. However, RADICAL has shown a higher sensitivity to violations of the BSS model. Distinct negative correlations between morphology retention and the violation of the orthogonal approach as well as a significantly worse SNR for underdetermined PPG mixtures were found compared to the other ICA algorithms. RADICAL seems not to be suited best in (cb)PPG BSS, accordingly.

Independent of the distinct violations of the BSS model, ICA showed stable solutions $\mathbf{W}$. U_{max} has not been proven being consistently related to violations of orthogonality, morphology retention and the SNR. The variance of $\mathbf{W}$ during bootstrapping of the components to be unmixed obviously is no indicator of the quality of $\mathbf{y}$, respectively, ICA serves stable solutions regardless the quality of $\mathbf{y}$. That is why U_{max} despite its potential as an online-estimate of BSS performance is proven as unsuitable to estimate the quality of the BSS output $\mathbf{y}$. Potentially, distribution metrics like the pdf and the relation of such distribution metrics between BSS inputs $\mathbf{x}$ and outputs $\mathbf{y}$ should be addressed in future works on online reliability measures of BSS that are intended to unmask violations of the orthogonal approach.

Advanced BSS techniques as batch processing and spatio-temporal FastICA has been found to successfully contribute to cbPPG processing. Batch processing of cbPPGs might help with fast processing in applications with limited computational power. On the other hand, spatio-temporal FastICA suits for complex (e.g. convolutive, non-stationary) mixing scenarios.

Whether the potential of a BSS algorithm in terms of signal quality improvements can be exploited in practice, depends on the availability of suitable algorithms to solve permutation indeterminacy.

Spatio-temporal BSS has shown high potential to process distorted ECG recordings as it is found in minimum- or non-contact ECG techniques (e.g. tECG, cECG) used for innovative mobile recording applications. The disadvantage of spatio-temporal BSS is a large number of output components obtained after processing which causes component selection after BSS to be difficult. Specifically, the automatic selection of the best available single component, i.e. the cardiac component of maximum signal quality, among the BSS output becomes challenging as the number of components increases. Within this thesis, different common selection strategies have been evaluated against newly developed approaches based on sparse coding.

Common component selection algorithms solving permutation indeterminacy simultaneously address feature extraction and component selection. For instance, higher order moments as kurtosis serve as a component feature and selector at the same time. On the contrary, sparse coding methods use features (e.g. peaks) to create an abstract representation of the BSS component. This representation later on is evaluated e.g. from a rhythmical point of view and thus, abstracts the component selection step from the handling of signal-specific features and differences (e.g. between ECGs of different origin). Thus, a selection based on sparse coding is transferable to any signal of cardiac origin. The application of sparse coding algorithms would only require the adaption of the extraction of a sparse code sequence (e.g. from a cbPPG signal), whereas the interpretation and thus selection algorithm would remain the same. Accordingly, a potentially re-usable selection algorithm part has been obtained what presents a main advantage compared to common algorithms based on higher order moments or frequency domain features.

Such newly developed component selection algorithm based on sparse coding ($RCODE$) has shown to outperform the common usage of higher order moments and frequency domain features. The availability of performant component selection algorithms being able to handle large amounts of BSS output components and, nevertheless, selecting the best cardiac component with high certainty, facilitates the usage of spatio-temporal BSS for processing highly distorted ECGs. This is particularly relevant since the results of this thesis also has shown that first, increasing the spatio-temporal dimension dim in highly distorted signal mixtures (cECG) also increases the maximum available heartbeat accuracy in the BSS output. Thus, the worse the starting condition for a selection algorithm (i.e. the higher the amount of BSS output components), the higher is the potential of a high quality cardiac component. Second, common selection algorithms based on higher order moments are not able to handle the increasing numbers of output components in this context. I.e., while increasing dim, higher order moments as skewness and kurtosis are decreasingly able to select the best available cardiac component among the outputs. Thus, sophisticated selection algorithms e.g. based on sparse coding are required to exploit the potential of spatio-temporal BSS.

Future work should address the transfer of the promising sparse coding selection algorithms to the cbPPG domain. The experiments on spatio-temporal BSS for PPG signals described within this thesis have shown the potential of advanced BSS techniques to resolve complex, i.e. non-stationary or convolutive signal mixtures also in the cbPPG domain. This potential now should be exploited by solving permutation indeterminacy in cbPPG BSS and adapting the sparse coding algorithms $RCODE$ and $PeriodTest$, accordingly.

Sam did not know how long it had been since last he'd slept, but scarce an inch remained of the fat tallow candle he'd lit when starting on the ragged bundle of loose pages that he'd found tied up in twine.

— George R.R. Martin in *A Feast for Crows* p.101, A Song of Ice and Fire (2005)

A

APPENDIX

A.1 PPG WAVEFORM SYNTHESIS

Table 4: PPG model parameters of a 24, 61 and 70 year old male subject according to the synthesis model in equation (83) and [119]. Given are mean ± standard deviation (STD).

index i	amplification a_i	distribution mean μ_i	distribution STD σ_i
24 year old male subject			
1	0.23611 ± 0.00064	0.17830 ± 0.00081	0.67751 ± 0.00234
2	0.00788 ± 0.00032	0.24193 ± 0.00108	0.11866 ± 0.00449
3	0.14237 ± 0.00074	0.41878 ± 0.00131	0.24789 ± 0.00351
4	0.04771 ± 0.00198	0.65103 ± 0.00552	0.13537 ± 0.00742
5	0.01540 ± 0.00212	0.77177 ± 0.00165	0.07312 ± 0.00437
61 year old male subject			
1	0.34075 ± 0.00638	0.28884 ± 0.00600	0.74016 ± 0.00734
2	0.03848 ± 0.00138	0.28353 ± 0.00225	0.20647 ± 0.00000
3	0.21446 ± 0.00827	0.54630 ± 0.01034	0.28774 ± 0.01534
4	0.06470 ± 0.01187	0.77861 ± 0.01477	0.15132 ± 0.01925
5	0.02181 ± 0.00617	0.93668 ± 0.00486	0.08740 ± 0.00821
70 year old male subject			
1	0.29437 ± 0.00586	0.27005 ± 0.00629	0.74839 ± 0.00863
2	0.05237 ± 0.00206	0.28000 ± 0.00000	0.24380 ± 0.00000
3	0.07547 ± 0.00000	0.43385 ± 0.00466	0.20867 ± 0.00734
4	0.07410 ± 0.00465	0.59554 ± 0.00816	0.17392 ± 0.00975
5	0.01678 ± 0.00306	0.75239 ± 0.00413	0.09058 ± 0.00862

A.2 CBPPG SELECTION

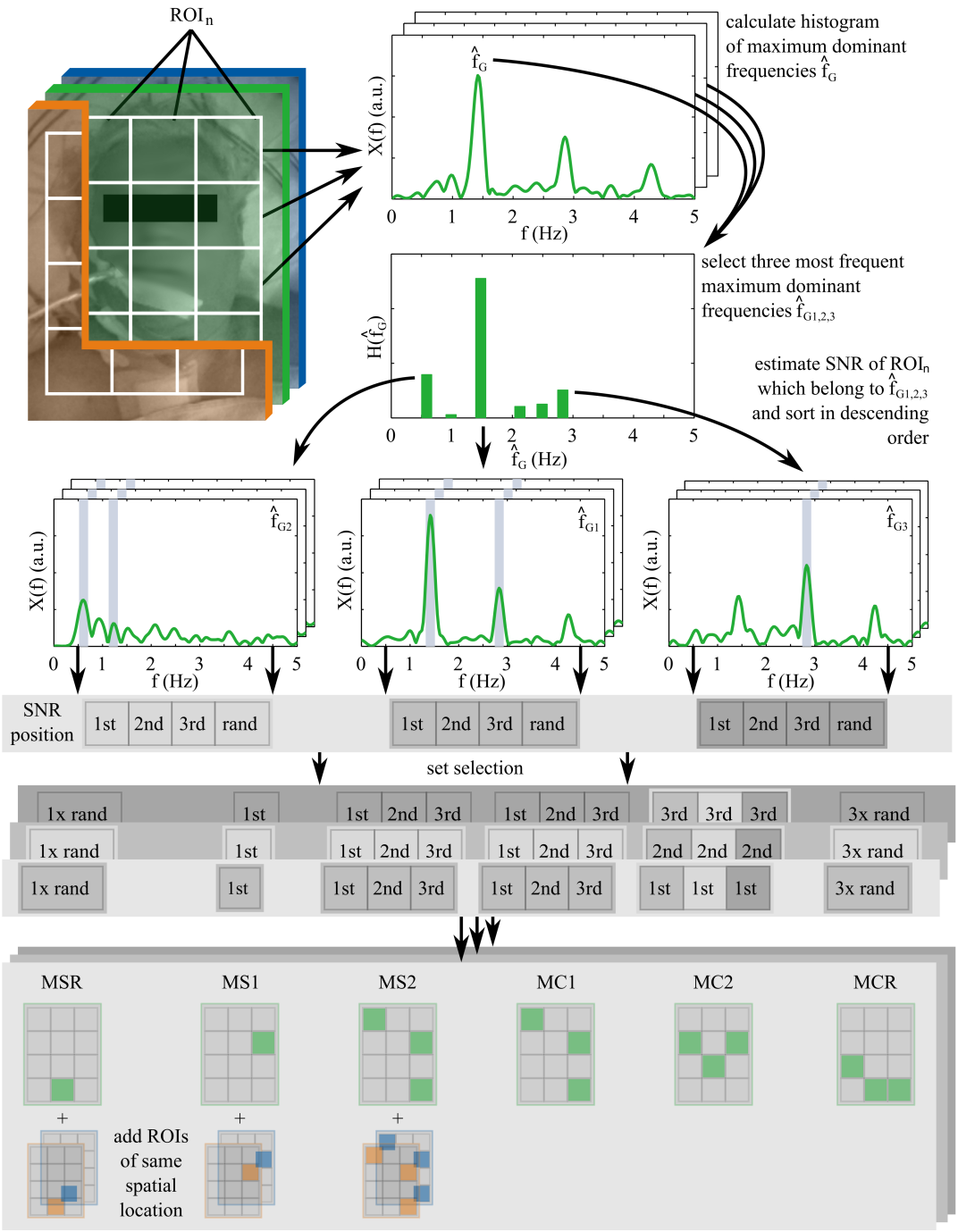

Figure 53: ROI selection based on the three most frequent dominant frequencies of the green wavelength. ROI assembly (MC#,MS#) based on signal quality inside dominant frequencies. [286]

ALGORITHM INPUT All available $\mathrm{cbPPG}_{\mathrm{n,color}}$ signals with $n = 1, 2, ..., 475$ and *color* $\in$ {R,G,B} serve as input to the input set selection algorithm. The selection is mainly based on evaluating peak frequencies $\hat{f}_{\mathrm{G}}$ and its grouping clusters $\tilde{f}_{\mathrm{i,G}}$ considered as the dominant frequency respectively periodic component of the amplitude spectrum $X(f)$ of a $\mathrm{cbPPG}_{\mathrm{n,G}}$.

1. The maximum peak frequency $\hat{f}_{\mathrm{n,G}}$ of the amplitude spectra $X(f) = \mathcal{F}\{\mathrm{cbPPG}_{\mathrm{n,G}}\}$ between [30,240] bpm is estimated for every ROI. The green wavelength is chosen for this selection according to the suitability for detecting the cardiac pulse inside this channel [265].

2. The histogram $H(\hat{f}_{\mathrm{G}})$ of peak frequencies $\hat{f}_{\mathrm{G}}$ for all 475 ROIs is estimated (see Fig. 53 for an example). Clusters of $\mathrm{cbPPG}_{\mathrm{n,G}}$ are formed according to peak frequencies $\hat{f}_{\mathrm{n,G}}$ of maximum spread of 10 bpm ($\pm$ 5 bpm). The cluster width adapts to the signal quality measure used for evaluation. In case of multiple possibilities for forming $\mathrm{cbPPG}_{\mathrm{n,G}}$ clusters due to a continuous range of peak frequencies $\hat{f}_{\mathrm{n,G}}$ with spread $>$ 10 bpm, always the cluster with maximum amount of $\mathrm{cbPPG}_{\mathrm{n,G}}$ is formed and the cluster limits to surrounding clusters are adjusted accordingly. The clustering according to peak frequencies in general addresses the search for highly periodic components as we expect the nature of the cardiac pulse.

3. The three largest clusters of $\mathrm{cbPPG}_{\mathrm{n,G}}$ of $H(\hat{f}_{\mathrm{G}}) \rightarrow \tilde{f}_{\mathrm{i,G}}$ with $\mathrm{i} \in \{1, 2, 3\}$ according to its central peak frequency $\tilde{f}_{\mathrm{i,G}}$ (see Fig. 53) are located.

4. In order to assess the strength of the periodic component defined by its peak frequency $\hat{f}_{\mathrm{n,G}}$ inside a $\mathrm{cbPPG}_{\mathrm{n,G}} \in \tilde{f}_{\mathrm{i,G}}$ with $\mathrm{i} \in \{1, 2, 3\}$ the $\mathrm{SNR}_{\mathrm{n,G}}^{\tilde{f}_{\mathrm{i}}}$ ($\mathrm{i} \in \{1, 2, 3\}$) of the $\mathrm{cbPPG}_{\mathrm{n,G}}$ is calculated using equation (76) and (77) while considering the peak frequency $\hat{f}_{\mathrm{n,G}}$ as usable signal frequency estimate f_{PPG} . Accordingly, $\mathrm{SNR}_{\mathrm{n,G}}^{\tilde{f}_{\mathrm{i}}} = \mathrm{SNR}^{f_{\mathrm{PPG}}}$ with $f_{\mathrm{PPG}} = \hat{f}_{\mathrm{n,G}}$ and $\hat{f}_{\mathrm{n,G}} \in \tilde{f}_{\mathrm{i,G}}$ ($\mathrm{i} \in \{1, 2, 3\}$).

5. Input sets S are principally formed of ROIs of identical size so approaches could equally benefit from spatial averaging. Exceptions are formed by the standard multispectral approaches using a face or a forehead-cheek ROI, respectively. Moreover, one multispectral set is build with larger ROI area to adapt to the area intrinsically formed by the monochrome approach.

MONOCHROME APPROACH (HOMOGENOUS FREQUENCY CONTENT) Assemble the green channel from appropriate ROIs inside a cluster $\tilde{f}_{\mathrm{i,G}}$ to three input sets according to ($\mathrm{i} \in \{1, 2, 3\}$):

$$\left\{\begin{array}{ll} \mathrm{cbPPG}_{\mathrm{n,G}} \text{ with} & \text{highest } \mathrm{SNR}_{\mathrm{n,G}}^{\tilde{f}_{\mathrm{i}}} \text{ subject to } \hat{f}_{\mathrm{n,G}} \overset{!}{=} \tilde{f}_{\mathrm{i}}, \\ \mathrm{cbPPG}_{\mathrm{n,G}} \text{ with} & \text{second highest } \mathrm{SNR}_{\mathrm{n,G}}^{\tilde{f}_{\mathrm{i}}} \text{ subject to } \hat{f}_{\mathrm{n,G}} \overset{!}{=} \tilde{f}_{\mathrm{i}}, \\ \mathrm{cbPPG}_{\mathrm{n,G}} \text{ with} & \text{third highest } \mathrm{SNR}_{\mathrm{n,G}}^{\tilde{f}_{\mathrm{i}}} \text{ subject to } \hat{f}_{\mathrm{n,G}} \overset{!}{=} \tilde{f}_{\mathrm{i}} \end{array}\right\} \rightarrow S_{\mathrm{i}}^{\mathrm{mc1}}$$

MONOCHROME APPROACH (HETEROGENEOUS FREQUENCY CONTENT) Assemble the green channel from appropriate ROIs inside a SNR positioning (of absolute SNRs) j for all three clusters $\tilde{f}_{\mathrm{i,G}}$ with $\mathrm{i} \in \{1, 2, 3\}$ to three input sets according to ($\mathrm{j} \in \{\text{first}, \text{second}\,\text{third}\}$):

$$\left\{\begin{array}{ll} \mathrm{cbPPG_{n,G}} \text{ with} & \mathrm{j} \text{ highest } \mathrm{SNR}_{\mathrm{n,G}}^{\tilde{f}_1} \text{ subject to } \hat{f}_{\mathrm{n,G}} \stackrel{!}{=} \tilde{f}_1, \\ \mathrm{cbPPG_{n,G}} \text{ with} & \mathrm{j} \text{ highest } \mathrm{SNR}_{\mathrm{n,G}}^{\tilde{f}_2} \text{ subject to } \hat{f}_{\mathrm{n,G}} \stackrel{!}{=} \tilde{f}_2, \\ \mathrm{cbPPG_{n,G}} \text{ with} & \mathrm{j} \text{ highest } \mathrm{SNR}_{\mathrm{n,G}}^{\tilde{f}_3} \text{ subject to } \hat{f}_{\mathrm{n,G}} \stackrel{!}{=} \tilde{f}_3 \end{array}\right\} \rightarrow S_{\mathrm{j}}^{\mathrm{mc2}}$$

MULTISPECTRAL APPROACH (HOMOGENOUS FREQUENCY CONTENT) Assemble the color channels from appropriate ROIs inside a cluster $\tilde{f}_{\mathrm{i,G}}$ to three input sets according to ($\mathrm{i} \in \{1,2,3\}$):

$$\left\{\begin{array}{ll} \mathrm{cbPPG_{n,R}} \text{ with} & \text{highest } \mathrm{SNR}_{\mathrm{n,G}}^{\tilde{f}_{\mathrm{i}}} \text{ subject to } \hat{f}_{\mathrm{n,G}} \stackrel{!}{=} \tilde{f}_{\mathrm{i}}, \\ \mathrm{cbPPG_{n,G}} \text{ with} & \text{highest } \mathrm{SNR}_{\mathrm{n,G}}^{\tilde{f}_{\mathrm{i}}} \text{ subject to } \hat{f}_{\mathrm{n,G}} \stackrel{!}{=} \tilde{f}_{\mathrm{i}}, \\ \mathrm{cbPPG_{n,B}} \text{ with} & \text{highest } \mathrm{SNR}_{\mathrm{n,G}}^{\tilde{f}_{\mathrm{i}}} \text{ subject to } \hat{f}_{\mathrm{n,G}} \stackrel{!}{=} \tilde{f}_{\mathrm{i}} \end{array}\right\} \rightarrow S_{\mathrm{i}}^{\mathrm{ms1}}$$

MULTISPECTRAL APPROACH (ROI AREA ADAPTION) Assemble the color channels from appropriate ROIs inside a cluster $\tilde{f}_{\mathrm{i,G}}$ containing the area ($\mathrm{ROI_n}$) of the three best SNR ROIs obtained by frame-wise averaging the respective ROIs located as in $S_{\mathrm{i}}^{\mathrm{mc1}}$ for three wavelengths each to three input sets according to ($\mathrm{i} \in \{1,2,3\}$) to match the ROI area of the monochrome approach:

$$\left\{\begin{array}{ll} \mathrm{cbPPG_{n,R}} \text{ with} & \text{highest } \mathrm{SNR}_{\mathrm{n,G}}^{\tilde{f}_{\mathrm{i}}} \text{ subject to } \hat{f}_{\mathrm{n,G}} \stackrel{!}{=} \tilde{f}_{\mathrm{i}}, \\ & \text{second highest } \mathrm{SNR}_{\mathrm{n,G}}^{\tilde{f}_{\mathrm{i}}} \text{ subject to } \hat{f}_{\mathrm{n,G}} \stackrel{!}{=} \tilde{f}_{\mathrm{i}}, \\ & \text{third highest } \mathrm{SNR}_{\mathrm{n,G}}^{\tilde{f}_{\mathrm{i}}} \text{ subject to } \hat{f}_{\mathrm{n,G}} \stackrel{!}{=} \tilde{f}_{\mathrm{i}} \\ \mathrm{cbPPG_{n,G}} \text{ with} & \text{highest } \mathrm{SNR}_{\mathrm{n,G}}^{\tilde{f}_{\mathrm{i}}} \text{ subject to } \hat{f}_{\mathrm{n,G}} \stackrel{!}{=} \tilde{f}_{\mathrm{i}}, \\ & \text{second highest } \mathrm{SNR}_{\mathrm{n,G}}^{\tilde{f}_{\mathrm{i}}} \text{ subject to } \hat{f}_{\mathrm{n,G}} \stackrel{!}{=} \tilde{f}_{\mathrm{i}}, \\ & \text{third highest } \mathrm{SNR}_{\mathrm{n,G}}^{\tilde{f}_{\mathrm{i}}} \text{ subject to } \hat{f}_{\mathrm{n,G}} \stackrel{!}{=} \tilde{f}_{\mathrm{i}} \\ \mathrm{cbPPG_{n,B}} \text{ with} & \text{highest } \mathrm{SNR}_{\mathrm{n,G}}^{\tilde{f}_{\mathrm{i}}} \text{ subject to } \hat{f}_{\mathrm{n,G}} \stackrel{!}{=} \tilde{f}_{\mathrm{i}}, \\ & \text{second highest } \mathrm{SNR}_{\mathrm{n,G}}^{\tilde{f}_{\mathrm{i}}} \text{ subject to } \hat{f}_{\mathrm{n,G}} \stackrel{!}{=} \tilde{f}_{\mathrm{i}}, \\ & \text{third highest } \mathrm{SNR}_{\mathrm{n,G}}^{\tilde{f}_{\mathrm{i}}} \text{ subject to } \hat{f}_{\mathrm{n,G}} \stackrel{!}{=} \tilde{f}_{\mathrm{i}} \end{array}\right\} \rightarrow S_{\mathrm{i}}^{\mathrm{ms2}}$$

RANDOM APPROACHES For testing against choosing only the highest SNRs, assemble analogous monochrome $S_{\mathrm{i}}^{\mathrm{mcR}}$ and multispectral $S_{\mathrm{i}}^{\mathrm{msR}}$ sets with respective random selection out of available $\mathrm{cbPPG_{n,color}}$ subject to $\hat{f}_{\mathrm{n,G}} \stackrel{!}{=} \tilde{f}_{\mathrm{i}}$ and $\mathrm{i} \in \{1,2,3\}$.

STANDARD APPROACHES For testing against standard multispectral BSS processing for cbPPG, form sets S^{F} and S^{FhC} from $\mathrm{cbPPG_{F,color}}$ and $\mathrm{cbPPG_{FhC,color}}$, respectively.

ALGORITHM OUTPUT Input sets $S_{\mathrm{i}}^{\mathrm{mc1}}$, $S_{\mathrm{j}}^{\mathrm{mc2}}$, $S_{\mathrm{i}}^{\mathrm{ms1}}$, $S_{\mathrm{i}}^{\mathrm{ms2}}$, $S_{\mathrm{i}}^{\mathrm{mcR}}$ and $S_{\mathrm{i}}^{\mathrm{msR}}$ with $\mathrm{i} \in \{1,2,3\}$ and $\mathrm{j} \in \{\text{first}, \text{second}, \text{third}\}$ (i.e. three input sets, containing three channels each for the multispectral and monochrome approach) as well as one set S^{F} and S^{FhC}, respectively.

A.3 ADDITIONAL RESULTS FOR SELECTION OF BSS INPUT DATA

A.3.1 *Source Signal Characteristics*

Table 5: **Pairwise $d_\perp$ results for disturbance types.** $d_\perp$ values are shown as mean ± standard deviation a.u., p-values of log-scaled $d_\perp$ (below main diagonal) from Mann–Whitney U test on subject-wise means (N = 6) and effect size (above main diagonal) Cohen's U1 and 95% CIs of U1 [104] (calculated with bootstrapping, N = 1000) in brackets.

$d_\perp$	GROUP	SIN	CHIRP	TREND	STEP
1.15 ± 0.37	SIN		1 [1,1]	1 [1,1]	1 [1,1]
0.43 ± 0.08	CHIRP	< 0.01		0.75 [0.5,1]	1 [1,1]
0.24 ± 0.08	TREND	< 0.01	< 0.01		0.42 [0.25,1]
0.25 ± 0.05	STEP	< 0.01	< 0.01	0.13	

In the following (Tables 6 - 9), SNRs are shown as mean ± standard deviation dB, p-values (below main diagonal) from Wilcoxon's signed-rank test on subject-wise means (N = 6) and effect size (above main diagonal) Cohen's U1 and 95% CIs of U1 [104] (calculated with bootstrapping, N = 1000) in brackets.

Table 6: **Pairwise SNR results for mixtures with SIN disturbances.**

ΔSNR_{orig}	GROUP	PCA	FASTICA	FASTICA (SUB)	FASTICA (SUP)	JADE	RADICAL
-1.77 ± 0.93	PCA		1 [1,1]	0.83 [0.5,1]	1 [1,1]	1 [1,1]	0.75 [0.58,1]
-0.54 ± 0.33	FastICA	0.03		0.25 [0.17,0.5]	0.17 [0.17,0.5]	0.17 [0.17,0.5]	0.17 [0.17,1]
-0.56 ± 0.33	FastICA (sub)	0.06	0.69		0.25 [0.17,0.5]	0.25 [0.17,0.5]	0.17 [0.17,0.83]
-0.55 ± 0.32	FastICA (sup)	0.03	0.84	1		0.17 [0.17,0.5]	0.17 [0.17,0.92]
-0.45 ± 0.33	JADE	0.03	0.44	0.03	1		0.17 [0.17,0.75]
-0.29 ± 0.38	RADICAL	0.03	0.22	0.22	0.16	0.44	

Table 7: **Pairwise SNR results for mixtures with CHIRP disturbances.**

ΔSNR_{orig}	GROUP	FASTICA	FASTICA (SUB)	FASTICA (SUP)	JADE	RADICAL
-1.14 ± 1.08	PCA	X	X	X	X	X
-0.12 ± 0.17	FastICA		0.17 [0.17,0.5]	0.25 [0.17,0.5]	0.42 [0.25,0.5]	0.33 [0.17,0.54]
-0.08 ± 0.13	FastICA (sub)	0.16		0.17 [0.17,0.42]	0.17 [0.17,0.5]	0.42 [0.33,1]
-0.13 ± 0.18	FastICA (sup)	0.56	0.09		0.25 [0.17,0.5]	0.33 [0.25,0.58]
-0.07 ± 0.07	JADE	0.56	0.69	1		0.42 [0.25,1]
-0.27 ± 0.24	RADICAL	0.03	0.03	0.03	0.06	

Table 8: **Pairwise SNR results for mixtures with TREND disturbances.**

ΔSNR_{orig}	GROUP	PCA	FASTICA	FASTICA (SUB)	FASTICA (SUP)	JADE	RADICAL
-0.68 ± 1.04	PCA		0.58 [0.5,1]	0.58 [0.5,1]	0.58 [0.5,1]	0.5 [0.5,1]	0.58 [0.5,1]
-0.13 ± 0.34	FastICA	0.03		0.25 [0.17,1]	0.33 [0.17,1]	0.17 [0.17,0.5]	0.25 [0.17,0.5]
-0.14 ± 0.33	FastICA (sub)	0.03	0.31		0.33 [0.25,1]	0.33 [0.25,1]	0.25 [0.17,0.58]
-0.11 ± 0.32	FastICA (sup)	0.03	0.16	0.06		0.17 [0.17,0.75]	0.17 [0.17,0.5]
-0.14 ± 0.31	JADE	0.03	0.84	0.44	0.31		0.25 [0.17,0.58]
-0.08 ± 0.23	RADICAL	0.03	0.44	0.31	0.84	0.56	

Table 9: **Pairwise SNR results for mixtures with STEP disturbances.**

ΔSNR_{orig}	GROUP	PCA	FASTICA	FASTICA (SUB)	FASTICA (SUP)	JADE	RADICAL
-0.85 ± 0.84	PCA		0.83 [0.67,1]	1 [1,1]	1 [1,1]	0.83 [0.67,1]	1 [1,1]
-0.07 ± 0.11	FastICA	0.03		0.17 [0.17,0.5]	0.17 [0.17,0.42]	0.17 [0.17,0.42]	0.25 [0.17,0.67]
-0.08 ± 0.08	FastICA (sub)	0.03	0.44		0.25 [0.17,0.5]	0.17 [0.17,0.42]	0.42 [0.17,0.75]
-0.05 ± 0.05	FastICA (sup)	0.03	1	0.16		0.17 [0.17,0.42]	0.33 [0.17,0.67]
-0.08 ± 0.10	JADE	0.03	0.16	0.56	0.16		0.42 [0.17,0.75]
-0.02 ± 0.03	RADICAL	0.03	0.84	0.56	0.56	0.56	

In the following (Tables 10 - 12), U_{max} are shown as mean ± standard deviation rad^2, p-values (below main diagonal) from Wilcoxon's signed-rank test on subject-wise means (N = 6) and effect size (above main diagonal) Cohen's U1 and 95% CIs of U1 [104] (calculated with bootstrapping, N = 1000) in brackets.

Table 10: **Pairwise W-reliability results for mixtures with CHIRP disturbances.**

U_{max}	GROUP	FASTICA	FASTICA (SUB)	FASTICA (SUP)	JADE	RADICAL
7.2e-03 ± 1e-02	FastICA		0.25 [0.17,0.5]	0.17 [0.17,0.5]	0.5 [0.5,1]	0.41 [0.25,1]
6.8e-03 ± 9e-03	FastICA (sub)	1		0.25 [0.17,0.5]	0.5 [0.5,1]	0.5 [0.33,1]
6.9e-03 ± 9e-03	FastICA (sup)	0.84	0.56		0.5 [0.5,1]	0.42 [0.25,1]
2.5e-03 ± 5e-03	JADE	0.03	0.03	0.03		0.5 [0.5,1]
2.1e-03 ± 8e-04	RADICAL	0.09	0.06	0.15	0.44	

Table 11: **Pairwise W-reliability results for mixtures with TREND disturbances.**

U_{max}	GROUP	FASTICA	FASTICA (SUB)	FASTICA (SUP)	JADE	RADICAL
9.1e-03 ± 2e-02	FastICA		0.42 [0.33,1]	0.25 [0.17,0.5]	0.42 [0.25,1]	0.75 [0.58,1]
1.1e-02 ± 2e-02	FastICA (sub)	0.03		0.5 [0.5,1]	0.5 [0.5,1]	1 [1,1]
8.0e-03 ± 2e-02	FastICA (sup)	0.03	0.03		0.42 [0.25,1]	0.75 [0.58,1]
3.1e-03 ± 5e-03	JADE	0.03	0.03	0.03		0.5 [0.33,1]
6.0e-04 ± 4e-04	RADICAL	0.03	0.03	0.03	0.09	

Table 12: **Pairwise W-reliability results for mixtures with STEP disturbances.**

U_{max}	GROUP	FASTICA	FASTICA (SUB)	FASTICA (SUP)	JADE	RADICAL
5.8e-03 ± 1e-02	FastICA		0.33 [0.25,1]	0.25 [0.17,0.5]	0.5 [0.5,1]	1 [1,1]
7.0e-03 ± 1e-02	FastICA (sub)	0.03		0.42 [0.33,1]	0.5 [0.5,1]	1 [1,1]
8.1e-03 ± 2e-02	FastICA (sup)	0.84	0.44		0.42 [0.33,1]	1 [1,1]
2.7e-03 ± 5e-03	JADE	0.03	0.03	0.03		0.58 [0.33,1]
5.0e-04 ± 3e-04	RADICAL	0.03	0.03	0.03	0.09	

In the following (Tables 13 - 16), ρ_{sy} are shown as mean ± standard deviation a.u., p-values (below main diagonal) from Wilcoxon's signed-rank test on subject-wise means (N = 6) and effect size (above main diagonal) Cohen's U1 and 95% CIs of U1 [104] (calculated with bootstrapping, N = 1000) in brackets.

Table 13: **Pairwise y-reliability results for mixtures with SIN disturbances.**

ρ_{sy}	GROUP	PCA	FASTICA	FASTICA (SUB)	FASTICA (SUP)	JADE
0.82 ± 0.007	PCA		1 [1,1]	1 [1,1]	1 [1,1]	1 [1,1]
0.958 ± 0.02	FastICA	0.03		0.17 [0.17,0.5]	0.17 [0.17,0.5]	0.17 [0.17,1]
0.959 ± 0.02	FastICA (sub)	0.03	0.56		0.17 [0.17,0.42]	0.25 [0.17,0.75]
0.960 ± 0.02	FastICA (sup)	0.03	0.09	1		0.17 [0.17,0.67]
0.969 ± 0.02	JADE	0.03	0.06	0.03	0.16	
0.904 ± 0.07	RADICAL	X	X	X	X	X

Table 14: **Pairwise y-reliability results for mixtures with CHIRP disturbances.**

ρ_{sy}	GROUP	PCA	FASTICA	FASTICA (SUB)	FASTICA (SUP)	JADE	RADICAL
0.828 ± 0.01	PCA		1 [1,1]	1 [1,1]	1 [1,1]	1 [1,1]	1 [1,1]
0.984 ± 0.01	FastICA	0.03		0.17 [0.17,0.42]	0.17 [0.17,0.42]	0.17 [0.17,0.75]	0.33 [0.21,0.5]
0.987 ± 0.01	FastICA (sub)	0.03	0.16		0.25 [0.17,0.5]	0.25 [0.17,0.58]	0.42 [0.33,1]
0.984 ± 0.01	FastICA (sup)	0.03	1	0.16		0.25 [0.17,0.75]	0.33 [0.17,0.5]
0.992 ± 0.007	JADE	0.03	0.06	0.06	0.16		0.5 [0.42,1]
0.985 ± 0.007	RADICAL	0.03	0.44	0.44	0.44	0.22	

Table 15: **Pairwise y-reliability results for mixtures with TREND disturbances.**

ρ_{sy}	GROUP	PCA	FASTICA	FASTICA (SUB)	FASTICA (SUP)	JADE	RADICAL
0.831 ± 0.01	PCA		1 [1,1]	1 [1,1]	1 [1,1]	1 [1,1]	1 [1,1]
0.977 ± 0.04	FastICA	0.03		0.33 [0.25,1]	0.33 [0.17,0.5]	0.33 [0.25,1]	0.33 [0.25,1]
0.978 ± 0.04	FastICA (sub)	0.03	0.44		0.42 [0.33,1]	0.42 [0.25,1]	0.58 [0.5,1]
0.983 ± 0.03	FastICA (sup)	0.03	0.03	0.03		0.33 [0.17,0.5]	0.25 [0.17,0.5]
0.983 ± 0.03	JADE	0.03	0.31	0.03	0.44		0.33 [0.17,0.5]
0.996 ± 0.003	RADICAL	0.03	0.03	0.03	0.09	0.84	

Table 16: **Pairwise y-reliability results for mixtures with STEP disturbances.**

ρ_{sy}	GROUP	PCA	FASTICA	FASTICA (SUB)	FASTICA (SUP)	JADE	RADICAL
0.832 ± 0.01	PCA		1 [1,1]	1 [1,1]	1 [1,1]	1 [1,1]	1 [1,1]
0.985 ± 0.03	FastICA	0.03		0.5 [0.5,1]	0.25 [0.17,0.5]	0.17 [0.17,0.58]	0.17 [0.17,0.5]
0.987 ± 0.02	FastICA (sub)	0.03	0.44		0.42 [0.33,1]	0.42 [0.25,1]	0.50 [0.5,1]
0.984 ± 0.03	FastICA (sup)	0.03	1	0.44		0.33 [0.25,0.83]	0.25 [0.17,0.5]
0.990 ± 0.01	JADE	0.03	0.84	0.03	0.56		0.25 [0.17,0.83]
0.995 ± 0.003	RADICAL	0.03	0.56	0.03	0.56	0.16	

A.3.2 *Mixture Signal Characteristics*

In the following (Tables 17 and 18), ΔSNR_{orig} are shown as mean ± standard deviation dB, p-values (below main diagonal) from Wilcoxon's signed-rank test on subject-wise means (N = 6) and effect size (above main diagonal) Cohen's U1 and 95% CIs of U1 [104] (calculated with bootstrapping, N = 1000) in brackets.

Table 17: **Pairwise SNR results for underdetermined disturbances.**

ΔSNR_{orig}	GROUP	PCA	FASTICA	FASTICA (SUB)	FASTICA (SUP)	JADE	RADICAL
-2.50 ± 0.63	PCA		0.58 [0.5,1]	0.5 [0.5,1]	0.67 [0.5,1]	0.50 [0.5,1]	0.58 [0.5,1]
-1.65 ± 0.49	FastICA	0.03		0.17 [0.17,0.42]	0.17 [0.17,0.42]	0.25 [0.17,0.5]	0.17 [0.17,0.42]
-1.68 ± 0.55	FastICA (sub)	0.03	0.44		0.25 [0.17,0.5]	0.25 [0.17,0.5]	0.17 [0.17,0.42]
-1.58 ± 0.41	FastICA (sup)	0.03	0.16	0.22		0.33 [0.17,0.5]	0.25 [0.17,0.5]
-1.68 ± 0.62	JADE	0.03	1	1	0.56		0.33 [0.17,0.5]
-1.69 ± 0.47	RADICAL	0.03	0.69	1	0.06	1	

Table 18: **Pairwise SNR results for underdetermined PPGs.**

ΔSNR_{orig}	GROUP	PCA	FASTICA	FASTICA (SUB)	FASTICA (SUP)	JADE	RADICAL
-2.57 ± 0.50	PCA		1 [1,1]	1 [1,1]	1 [1,1]	0.83 [0.67,1]	0.83 [0.67,1]
-1.43 ± 0.30	FastICA	0.03		0.25 [0.17,0.5]	0.17 [0.17,0.42]	0.17 [0.17,0.42]	0.42 [0.33,0.92]
-1.49 ± 0.30	FastICA (sub)	0.03	0.09		0.33 [0.17,0.5]	0.33 [0.21,0.5]	0.42 [0.29,0.63]
-1.41 ± 0.32	FastICA (sup)	0.03	0.56	0.16		0.17 [0.17,0.42]	0.42 [0.33,0.75]
-1.47 ± 0.40	JADE	0.03	0.31	0.84	0.56		0.33 [0.17,0.5]
-1.69 ± 0.38	RADICAL	0.03	0.03	0.03	0.03	0.03	

In the following (Tables 19 and 20), U_{max} results are shown as mean ± standard deviation rad^2, p-values (below main diagonal) from Wilcoxon's signed-rank test on subject-wise means (N = 6) and effect size (above main diagonal) Cohen's U1 and 95% CIs of U1 [104] (calculated with bootstrapping, N = 1000) in brackets.

Table 19: **Pairwise W-reliability results for underdetermined disturbances.**

U_{max}	GROUP	FASTICA	FASTICA (SUB)	FASTICA (SUP)	JADE	RADICAL
1.5e-02 ± 1e-02	FastICA		0.17 [0.17,0.5]	0.17 [0.17,0.5]	0.33 [0.25,1]	0.67 [0.42,1]
1.5e-02 ± 9e-03	FastICA (sub)	0.31		0.17 [0.17,1]	0.25 [0.17,1]	0.75 [0.58,1]
1.3e-02 ± 8e-03	FastICA (sup)	0.44	0.03		0.25 [0.17,1]	0.67 [0.42,1]
8.5e-03 ± 3e-03	JADE	0.03	0.03	0.03		0.5 [0.25,1]
6.2e-03 ± 2e-03	RADICAL	0.06	0.03	0.06	0.16	

Table 20: **Pairwise W-reliability results for underdetermined PPGs.**

U_{max}	GROUP	FASTICA	FASTICA (SUB)	FASTICA (SUP)	JADE	RADICAL
1.2e-02 ± 5e-03	FastICA		0.17 [0.17,0.42]	0.17 [0.17,0.42]	0.33 [0.25,0.83]	0.42 [0.25,1]
1.3e-02 ± 5e-03	FastICA (sub)	0.44		0.25 [0.17,0.5]	0.42 [0.33,1]	0.5 [0.33,1]
1.3e-02 ± 5e-03	FastICA (sup)	1	0.56		0.5 [0.33,1]	0.33 [0.17,0.75]
8.1e-03 ± 3e-03	JADE	0.03	0.03	0.03		0.17 [0.17,0.58]
8.9e-03 ± 3e-03	RADICAL	0.09	0.09	0.06	0.69	

In the following (Tables 21 and 22), ρ_{sy} are shown as mean ± standard deviation a.u., p-values (below main diagonal) from Wilcoxon's signed-rank test on subject-wise means (N = 6) and effect size (above main diagonal) Cohen's U1 and 95% CIs of U1 [104] (calculated with bootstrapping, N = 1000) in brackets.

Table 21: **Pairwise y-reliability results for underdetermined disturbances.**

ρ_{sy}	GROUP	PCA	FASTICA	FASTICA (SUB)	FASTICA (SUP)	JADE	RADICAL
0.720 ± 0.015	PCA		1 [1,1]	1 [1,1]	1 [1,1]	1 [1,1]	1 [1,1]
0.816 ± 0.019	FastICA	0.03		0.17 [0.17,0.42]	0.17 [0.17,0.5]	0.17 [0.17,0.42]	0.25 [0.17,0.5]
0.815 ± 0.021	FastICA (sub)	0.03	0.69		0.17 [0.17,0.5]	0.17 [0.17,0.42]	0.25 [0.17,0.5]
0.816 ± 0.024	FastICA (sup)	0.03	1	0.84		0.17 [0.17,0.42]	0.33 [0.25,0.5]
0.819 ± 0.017	JADE	0.03	0.06	0.06	0.56		0.25 [0.17,0.5]
0.821 ± 0.010	RADICAL	0.03	0.69	1	1	0.84	

Table 22: **Pairwise y-reliability results for underdetermined PPGs.**

ρ_{sy}	GROUP	PCA	FASTICA	FASTICA (SUB)	FASTICA (SUP)	JADE	RADICAL
0.718 ± 0.014	PCA		1 [1,1]	1 [1,1]	1 [1,1]	1 [1,1]	1 [1,1]
0.804 ± 0.032	FastICA	0.03		0.17 [0.17,0.42]	0.17 [0.17,0.5]	0.17 [0.17,0.42]	0.17 [0.17,0.83]
0.804 ± 0.029	FastICA (sub)	0.03	0.84		0.17 [0.17,0.42]	0.17 [0.17,0.5]	0.17 [0.17,0.71]
0.802 ± 0.035	FastICA (sup)	0.03	0.56	0.56		0.17 [0.17,0.5]	0.17 [0.17,0.67]
0.809 ± 0.026	JADE	0.03	0.06	0.03	0.16		0.17 [0.17,1]
0.795 ± 0.019	RADICAL	0.03	0.44	0.43	0.56	0.31	

In the following (Tables 23 and 24), ΔSNR_{orig} are shown as mean ± standard deviation dB, p-values (below main diagonal) from Wilcoxon's signed-rank test on subject-wise

means (N = 42) and effect size (above main diagonal) Cohen's U1 and 95% CIs of U1 [104] (calculated with bootstrapping, N = 1000) in brackets.

Table 23: **Pairwise SNR results for mixtures of phase-delayed PPGs.**

ΔSNR_{orig}	GROUP	FASTICA	FASTICA (SUB)	FASTICA (SUP)	JADE	RADICAL	SOBI
-0.42 ± 0.47	PCA	X	X	X	X	X	X
0.31 ± 0.30	FastICA		0.02 [0.02,0.07]	0.04 [0.02,0.1]	0.02 [0.02,0.1]	0.08 [0.05,0.2]	0.11 [0.06,0.34]
0.28 ± 0.31	FastICA (sub)	< 0.001		0.05 [0.02,0.11]	0.04 [0.02,0.11]	0.12 [0.07,0.24]	0.13 [0.08,0.37]
0.28 ± 0.31	FastICA (sup)	0.04	0.70		0.05 [0.02,0.11]	0.14 [0.08,0.24]	0.21 [0.14,0.39]
0.31 ± 0.30	JADE	0.35	0.02	0.05		0.10 [0.06,0.24]	0.12 [0.08,0.37]
0.48 ± 0.29	RADICAL	< 0.001	< 0.001	< 0.001	0.01		0.02 [0.02,0.14]
0.65 ± 0.32	SOBI	< 0.001	< 0.001	< 0.001	< 0.001	< 0.001	

Table 24: **Pairwise SNR results for mixtures of phase-delayed PPGs and disturbance.**

ΔSNR_{orig}	GROUP	PCA	FASTICA	FASTICA(SUB)	FASTICA(SUP)	JADE	RADICAL	SOBI
-1.48 ± 0.60	PCA		0.33 [0.27,0.43]	0.33 [0.27,0.44]	0.33 [0.27,0.42]	0.32 [0.26,0.42]	0.36 [0.31,0.45]	0.29 [0.21,0.39]
-0.83 ± 0.52	FastICA	< 0.001		0.02 [0.02,0.07]	0.02 [0.02,0.08]	0.02 [0.02,0.07]	0.07 [0.04,0.13]	0.12 [0.06,0.24]
-0.84 ± 0.52	FastICA (sub)	< 0.001	0.09		0.02 [0.02,0.08]	0.02 [0.02,0.08]	0.07 [0.04,0.13]	0.11 [0.05,0.23]
-0.81 ± 0.51	FastICA (sup)	< 0.001	0.07	< 0.01		0.02 [0.02,0.08]	0.06 [0.02,0.12]	0.11 [0.06,0.23]
-0.84 ± 0.54	JADE	< 0.001	0.84	0.33	0. 17		0.07 [0.02,0.13]	0.11 [0.06,0.25]
-0.82 ± 0.53	RADICAL	< 0.001	0.70	0.29	0.69	0.59		0.1 [0.06,0.2]
-0.97 ± 0.47	SOBI	< 0.001	< 0.001	< 0.01	< 0.001	< 0.001	< 0.001	

In the following (Table 25), U_{max} are shown as mean ± standard deviation rad^2, p-values (below main diagonal) from Wilcoxon's signed-rank test on subject-wise means (N = 42) and effect size (above main diagonal) Cohen's U1 and 95% CIs of U1 [104] (calculated with bootstrapping, N = 1000) in brackets.

Table 25: **Pairwise W-reliability results for mixtures of phase-delayed PPGs.**

U_{max}	GROUP	FASTICA	FASTICA (SUB)	FASTICA (SUP)	JADE	RADICAL	SOBI
7.3e-03 ± 6e-03	FastICA		0.07 [0.03,0.2]	0.02 [0.02,0.11]	0.12 [0.07,0.25]	0.08 [0.04,0.2]	0.12 [0.08,0.32]
8.5e-03 ± 7e-03	FastICA (sub)	0.08		0.02 [0.02,0.14]	0.18 [0.12,0.3]	0.14 [0.08,0.24]	0.24 [0.17,0.35]
6.8e-03 ± 5e-03	FastICA (sup)	0.61	0.03		0.12 [0.07,0.21]	0.08 [0.05,0.17]	0.20 [0.14,0.31]
5.5e-03 ± 5e-03	JADE	0.01	< 0.01	0.04		0.04 [0.02,0.13]	0.11 [0.06,0.20]
6.4e-03 ± 5e-03	RADICAL	0.47	0.14	0.68	0.44		0.10 [0.06,0.19]
5.0e-03 ± 5e-03	SOBI	0.02	< 0.01	0.02	0.37	0.25	

In the following (Tables 26 -27), ρ_{sy} are shown as mean ± standard deviation a.u., p-values (below main diagonal) from Wilcoxon's signed-rank test on subject-wise means (N = 42) and effect size (above main diagonal) Cohen's U1 and 95% CIs of U1 [104] (calculated with bootstrapping, N = 1000) in brackets.

Table 26: **Pairwise y-reliability results for mixtures of phase-delayed PPGs.**

ρ_{sy}	GROUP	FASTICA	FASTICA (SUB)	FASTICA (SUP)	JADE	RADICAL	SOBI
0.84 ± 0.02	PCA	X	X	X	X	X	X
0.926 ± 0.04	FastICA		0.05 [0.02,0.11]	0.02 [0.02,0.11]	0.05 [0.02,0.13]	0.1 [0.05,0.2]	0.23 [0.15,0.44]
0.928 ± 0.04	FastICA (sub)	0.20		0.04 [0.02,0.12]	0.07 [0.04,0.14]	0.1 [0.06,0.21]	0.23 [0.17,0.44]
0.930 ± 0.04	FastICA (sup)	0.17	0.43		0.07 [0.04,0.15]	0.1 [0.05,0.18]	0.21 [0.15,0.4]
0.937 ± 0.04	JADE	< 0.01	< 0.01	0.04		0.15 [0.09,0.29]	0.36 [0.3,0.61]
0.898 ± 0.05	RADICAL	0.11	0.05	0.03	< 0.01		0.02 [0.02,0.13]
0.861 ± 0.06	SOBI	< 0.001	< 0.001	< 0.001	< 0.001	< 0.001	

Table 27: **Pairwise y-reliability results for mixtures of phase-delayed PPGs and disturbance.**

ρ_{sy}	GROUP	PCA	FASTICA	FASTICA(SUB)	FASTICA(SUP)	JADE	RADICAL	SOBI
0.73 ± 0.03	PCA		0.61 [0.55,0.78]	0.56 [0.5,0.76]	0.64 [0.57,0.79]	0.62 [0.56,0.83]	0.29 [0.23,0.55]	0.21 [0.15,0.44]
0.81 ± 0.04	FastICA	< 0.001		0.04 [0.02,0.08]	0.05 [0.02,0.1]	0.02 [0.02,0.07]	0.05 [0.02,0.14]	0.14 [0.1,0.27]
0.81 ± 0.04	FastICA (sub)	< 0.001	0.34		0.05 [0.02,0.1]	0.04 [0.02,0.1]	0.05 [0.02,0.14]	0.12 [0.07,0.26]
0.81 ± 0.04	FastICA (sup)	< 0.001	0.16	0.48		0.02 [0.02,0.1]	0.06 [0.04,0.17]	0.14 [0.1,0.29]
0.82 ± 0.04	JADE	< 0.001	< 0.01	< 0.001	< 0.001		0.06 [0.04,0.2]	0.13 [0.09,0.33]
0.79 ± 0.05	RADICAL	< 0.001	< 0.001	< 0.001	< 0.001	< 0.001		0.05 [0.02,0.15]
0.77 ± 0.04	SOBI	< 0.001	< 0.001	< 0.001	< 0.001	< 0.001	< 0.001	

A.3.3 *Mixture Signal Modification*

In the following (Tables 28 - 31), SNRs are shown as mean ± standard deviation dB., p-values (below main diagonal) from Wilcoxon's signed-rank test on subject-wise means (N = 6) and effect size (above main diagonal) Cohen's U1 and 95% CIs of U1 [104] (calculated with bootstrapping, N = 1000) in brackets.

Table 28: **Pairwise results for convolutive mixtures with FastICA with respect to spatio-temporal BSS dimension *dim*.**

SNR	GROUP	ORIG	1	2	5	10	20	50
2.58 ± 3.50	ORIG		0.42 [0.25,0.5]	0.42 [0.25,0.5]	0.33 [0.17,0.5]	0.25 [0.17,0.5]	0.33 [0.17,0.5]	0.5 [0.5,1]
1.00 ± 3.59	1	0.03		0.25 [0.17,0.5]	0.33 [0.17,0.5]	0.42 [0.25,0.5]	0.42 [0.25,0.5]	0.42 [0.33,1]
1.29 ± 3.50	2	0.03	0.03		0.33 [0.17,0.5]	0.33 [0.25,0.5]	0.42 [0.25,0.5]	0.5 [0.5,1]
1.89 ± 3.36	5	0.03	0.03	0.03		0.33 [0.17,0.5]	0.42 [0.25,0.5]	0.42 [0.25,1]
2.32 ± 3.20	10	0.16	0.03	0.03	0.03		0.33 [0.17,0.5]	0.5 [0.5,1]
0.94 ± 2.14	20	0.06	1	0.44	0.16	0.06		0.42 [0.33,1]
-0.51 ± 1.40	50	0.03	0.16	0.16	0.06	0.03	0.03	
-1.49 ± 0.81	100	X	X	X	X	X	X	X

Table 29: **Pairwise results for convolutive mixtures with JADE with respect to spatio-temporal BSS dimension *dim*.**

SNR	GROUP	ORIG	1	2	5	10
2.58 ± 3.50	ORIG		0.42 [0.25,0.5]	0.42 [0.25,0.5]	0.33 [0.17,0.5]	0.42 [0.25,0.5]
0.98 ± 3.61	1	0.03		0.25 [0.17,0.5]	0.33 [0.17,0.5]	0.33 [0.21,0.5]
1.26 ± 3.51	2	0.03	0.03		0.33 [0.17,0.5]	0.33 [0.17,0.5]
1.76 ± 3.39	5	0.03	0.03	0.03		0.25 [0.17,0.5]
1.93 ± 3.20	10	0.03	0.03	0.03	0.09	

Table 30: **Pairwise results for non-stationary mixtures with FastICA with respect to spatio-temporal BSS dimension *dim*.**

SNR	GROUP	ORIG	1	2	5	10	20	50
2.77 ± 3.16	ORIG		0.25 [0.17,0.5]	0.25 [0.17,0.5]	0.17 [0.17,0.42]	0.25 [0.17,0.5]	0.33 [0.17,0.5]	0.5 [0.5,1]
2.34 ± 3.15	1	0.03		0.17 [0.17,0.42]	0.17 [0.17,0.42]	0.17 [0.17,0.5]	0.42 [0.25,0.5]	0.42 [0.25,1]
2.40 ± 3.12	2	0.03	0.03		0.17 [0.17,0.42]	0.17 [0.17,0.5]	0.33 [0.17,0.5]	0.5 [0.5,1]
2.68 ± 3.05	5	0.44	0.03	0.03		0.17 [0.17,0.42]	0.33 [0.17,0.5]	0.5 [0.5,1]
2.82 ± 2.93	10	0.84	0.06	0.06	0.22		0.33 [0.17,0.5]	0.5 [0.5,1]
1.97 ± 2.23	20	0.16	0.44	0.44	0.16	0.06		0.5 [0.5,1]
-0.28 ± 1.43	50	0.03	0.03	0.03	0.03	0.03	0.03	
-1.50 ± 1.04	100	X	X	X	X	X	X	X

Table 31: **Pairwise results for non-stationary mixtures with JADE with respect to spatio-temporal BSS dimension *dim*.**

SNR	GROUP	ORIG	1	2	5	10
2.77 ± 3.16	ORIG		0.25 [0.17,0.5]	0.25 [0.17,0.5]	0.25 [0.17,0.5]	0.33 [0.17,0.5]
2.38 ± 3.17	1	0.03		0.17 [0.17,0.42]	0.17 [0.17,0.42]	0.25 [0.17,0.5]
2.37 ± 3.12	2	0.03	0.84		0.17 [0.17,0.42]	0.25 [0.17,0.5]
2.39 ± 2.99	5	0.03	1	0.69		0.25 [0.17,0.5]
2.22 ± 2.75	10	0.03	0.69	1	0.56	

A.4 ADDITIONAL RESULTS FOR PERMUTATION INDETERMINACY

A.4.1 *Permutation Indeterminacy for ECG signals*

In the following (Tables 32 and 33), ACCs are shown as mean ± standard deviation, p-values (below main diagonal) from Wilcoxon's signed-rank tests on subject-wise means (N = 10 for tECG and cECG, N = 48 for aECG) and effect size (above main diagonal) Cohen's U1 and 95% CIs of U1 [104] in brackets.

Table 32: **Pairwise results for cECG data.**

ACC	Group	Av.Input	RCODE	PeriodTest	SKEW	KURT	CASCSEL
0.566 ± 0.136	Av. Input		0.85 [0.7,1]	0.9 [0.75,1]	0.25 [0.15,0.45]	0.1 [0.1,0.35]	0.7 [0.55,1]
0.867 ± 0.092	RCODE	< 0.01		0.1 [0.1,0.3]	0.7 [0.55,1]	0.8 [0.65,1]	0.3 [0.2,0.58]
0.868 ± 0.093	PeriodTest	< 0.01	0.77		0.7 [0.55,1]	0.8 [0.65,1]	0.3 [0.2,0.6]
0.629 ± 0.107	SKEW	0.08	< 0.01	< 0.01		0.3 [0.15,0.5]	0.6 [0.5,1]
0.584 ± 0.127	KURT	0.49	< 0.01	< 0.01	< 0.01		0.6 [0.5,1]
0.793 ± 0.064	CASCSEL	< 0.01	< 0.01	< 0.01	< 0.01	< 0.01	

Table 33: **Pairwise results for aECG (MIT-BIH) data.**

ACC	Group	Av.Input	RCODE	PeriodTest	SKEW	KURT	CASCSEL
0.871 ± 0.100	Av. Input		0.16 [0.10,0.33]	0.17 [0.12,0.30]	0.08 [0.05,0.23]	0.06 [0.03,0.19]	0.06 [0.03,0.23]
0.948 ± 0.065	RCODE	< 0.001		0.01 [0.01,0.04]	0.01 [0.01,0.08]	0.01 [0.01,0.17]	0.01 [0.01,0.09]
0.945 ± 0.067	PeriodTest	< 0.001	0.01		0.02 [0.01,0.07]	0.02 [0.01,0.14]	0.01 [0.01,0.09]
0.933 ± 0.083	SKEW	< 0.001	0.21	0.67		0.01 [0.01,0.10]	0.01 [0.01,0.08]
0.917 ± 0.095	KURT	< 0.001	< 0.01	0.02	< 0.001		0.01 [0.01,0.13]
0.942 ± 0.067	CASCSEL	< 0.001	0.01	0.16	0.91	0.06	

BIBLIOGRAPHY

[1] ANSI/AAMI. *American National Standard - Cardiac monitors, heart rate meters, and alarms EC13:2002*. 2002.

[2] L.A.M. Aarts, V. Jeanne, J.P. Cleary, C. Lieber, J.S. Nelson, S. Bambang Oetomo, and W. Verkruysse. "Non-contact heart rate monitoring utilizing camera photoplethysmography in the neonatal intensive care unit - A pilot study." In: *Early Human Development* 89.12 (2013), pp. 943–948. DOI: 10.1016/j.earlhumdev.2013.09.016.

[3] U.R. Acharya, K.P. Joseph, N. Kannathal, C.M. Lim, and J.S. Suri. "Heart rate variability: a review." In: *Medical & Biological Engineering & Computing* 44.12 (2006), pp. 1031–1051. DOI: 10.1007/s11517-006-0119-0.

[4] A. Acharyya, K. Maharatna, B.M. Al-Hashimi, and S. Mondal. "Robust channel identification scheme: solving permutation indeterminacy of ICA for artifacts removal from ECG." In: *Proc. 32nd Annu. Int. Conf. IEEE Eng. Med. Biol. Soc. (EMBC)*. Buenos Aires, Argentina, 2010, pp. 1142–1145. DOI: 10.1109/IEMBS.2010.5627133.

[5] V.X. Afonso, W.J. Tompkins, T.Q. Nguyen, and S. Luo. "ECG Beat Detection Using Filter Banks." In: *IEEE Transactions on Biomedical Engineering* 46.2 (1999), pp. 192–202. DOI: 10.1109/10.740882.

[6] J. Allen. "Photoplethysmography and its application in clinical physiological measurement." In: *Physiological measurement* 28.3 (2007), R1–39. DOI: 10.1088/0967-3334/28/3/R01.

[7] J. Allen and A. Murray. "Similarity in bilateral photoplethysmographic peripheral pulse wave characteristics at the ears , thumbs and toes." In: *Physiological measurement* 21.3 (2000), pp. 369–377. DOI: 10.1088/0967-3334/21/3/303.

[8] S. Amari and A. Cichocki. "Adaptive Blind Signal Processing - Neural Network Approaches." In: *Proceedings of the IEEE* 86.10 (1998), pp. 2026–2048. ISSN: 0018-9219. DOI: 10.1109/5.720251.

[9] R. Amelard, D.A. Clausi, and A. Wong. "A spectral-spatial fusion model for robust blood pulse waveform extraction in photoplethysmographic imaging." In: *Biomedical Optics Express* 7.12 (2016), pp. 4874–4885. DOI: 10.1364/BOE.7.004874.

[10] R. Amelard, C. Scharfenberger, A. Wong, and D.A. Clausi. "Illumination-compensated non-contact imaging photoplethysmography via dual-mode temporally coded illumination." In: *Proc. Multimodal Biomedical Imaging X (SPIE 9316)*. San Francisco, USA, 2015, 931607 (1–5). DOI: 10.1117/12.2078197.

[11] F. Andreotti, M. Riedl, T. Himmelsbach, D. Wedekind, N. Wessel, H. Stepan, C. Schmieder, A. Jank, H. Malberg, and S. Zaunseder. "Robust fetal ECG extraction and detection from abdominal leads." In: *Physiological measurement* 35.8 (2014), pp. 1551–1567. DOI: 10.1088/0967-3334/35/8/1551.

[12] F. Andreotti, A. Trumpp, H. Malberg, and S. Zaunseder. "Improved heart rate detection for camera-based photoplethysmography by means of Kalman filtering." In: *Proc. 35th IEEE Int. Conf. Electronics and Nanotechnology (ELNANO)*. Kyiv, Ukraine, 2015, pp. 428–433. DOI: 10.1109/ELNANO.2015.7146951.

[13] F. Andreotti, J. Behar, S. Zaunseder, J. Oster, and G.D. Clifford. "An open-source framework for stress-testing non-invasive foetal ECG extraction algorithms." In: *Physiological measurement* 37.5 (2016), pp. 627–648. DOI: 10.1088/0967-3334/37/5/627.

[14] J. Anemüller, T.J. Sejnowski, and S. Makeig. "Complex independent component analysis of freqency-domain electroencephalographic data." In: *Neural Networks* 16.9 (2003), pp. 1311–1323. DOI: 10.1016/j.neunet.2003.08.003.

[15] C.H. Antink, H. Gao, C. Brüser, and S. Leonhardt. "Beat-to-beat heart rate estimation fusing multimodal video and sensor data." In: *Biomedical Optics Express* 6.8 (2015), pp. 2895–2907. DOI: 10.1364/BOE.6.002895.

[16] L.J. Badra, W.H. Cooke, J.B. Hoag, A.A. Crossman, T.A. Kuusela, K.U. Tahvanainen, and D.L. Eckberg. "Respiratory modulation of human autonomic rhythms." In: *American Journal of Physiology. Heart and Circulatory Physiology* 280.6 (2001), H2674–2688. ISSN: 0363-6135.

[17] H.J. Baek, J.S. Kim, K.K. Kim, and K.S. Park. "System for Unconstrained ECG Measurement on a Toilet Seat Using Capacitive Coupled Electrodes: The Efficacy and Practicality." In: *Proc. 30th Annu. Int. Conf. IEEE Eng. Med. Biol. Soc. (EMBC)*. Vancouver, Canada, 2008, pp. 2326–2328. DOI: 10.1109/IEMBS.2008.4649664.

[18] H.J. Baek, G.S. Chung, K.K. Kim, and K.S. Park. "A smart health monitoring chair for nonintrusive measurement of biological signals." In: *IEEE Transactions on Information Technology in Biomedicine* 16.1 (2012), pp. 150–158. DOI: 10.1109/TITB.2011.2175742.

[19] J.Y. Baek, J.H. An, J.M. Choi, K.S. Park, and S.H. Lee. "Flexible polymeric dry electrodes for the long-term monitoring of ECG." In: *Sensors and Actuators, A: Physical* 143.2 (2008), pp. 423–429. DOI: 10.1016/j.sna.2007.11.019.

[20] G. Balakrishnan, F. Durand, and J. Guttag. "Detecting Pulse from Head Motions in Video." In: *Proc. 26th IEEE Computer Vision and Pattern Recognition Conference (CVPR)*. Portland, USA, 2013, pp. 3430–3437. DOI: 10.1109/CVPR.2013.440.

[21] A.K. Barros and A. Cichoki. "Extraction of Specific Signals with Temporal Structure." In: *Neural Computation* 13.9 (2001), pp. 1995–2003. DOI: 10.1162/089976601750399272.

[22] A.K. Barros, A. Mansour, and N. Ohnishi. "Removing artifacts from electrocardiographic signals using independent components analysis." In: *Neurocomputing* 22.1-3 (1998), pp. 173–186. DOI: 10.1016/S0925-2312(98)00056-3.

[23] G. Baselli, S. Cerutti, S. Civardi, D. Liberati, F. Lombardi, A. Malliani, and M. Pagani. "Spectral and cross-spectral analysis of heart rate and arterial blood pressure variability signals." In: *Computers and Biomedical Research* 19.6 (1986), pp. 520–534. DOI: 10.1016/0010-4809(86)90026-1.

[24] A.N. Bashkatov, E.A. Genina, V.I. Kochubey, and V.V. Tuchin. "Optical properties of human skin, subcutaneous and mucous tissues in the wavelength range from 400 to 2000 nm." In: *Journal of Physics D: Applied Physics* 38.15 (2005), pp. 2543–2555. DOI: 10.1088/0022-3727/38/15/004.

[25] A.J. Bell and T.J. Sejnowski. "An Information-Maximization Approach to Blind Separation and Blind Deconvolution." In: *Neural Computation* 7.6 (1995), pp. 1129–1159. DOI: 10.1162/neco.1995.7.6.1129.

[26] A. Belouchrani, K. Abed-Meraim, J.F. Cardoso, and E. Moulines. "A Blind Source Separation Technique Using Second-Order Statistics." In: *IEEE Transactions on Signal Processing* 45.2 (1997), pp. 434–444. DOI: 10.1109/78.554307.

[27] R.P. Betts and B.H. Brown. "Method for recording electrocardiograms with dry electrodes applied to unprepared skin." In: *Medical & Biological Engineering* 14.3 (1976), pp. 313–315. DOI: 10.1007/BF02478127.

[28] E.B. Blackford, J.R. Estepp, A.M. Piasecki, M.A. Bowers, and S.L. Klosterman. "Long-range non-contact imaging photoplethysmography: cardiac pulse wave sensing at a distance." In: *Proc. Optical Diagnostics and Sensing (SPIE 9715)*. Vol. 9715. San Francisco, USA, 2016, pp. 971512–1–17. DOI: 10.1117/12.2208130.

[29] V. Blažek, W. De Ruetten, and O. De Such. *Patent Application DE19741982A1: System for local noninvasive functional indicating of dermal blood perfusion*. 1996.

[30] T. Blöcher, J. Schneider, and M. Schinle. "An online PPGI approach for camera based heart rate monitoring using beat-to-beat detection." In: *Proc. 12th Sensors Applications Symposium (SAS)*. Glassboro, USA, 2017, p. 6. DOI: 10.1109/SAS.2017.7894052.

[31] M. Braer. "Entwicklung und Evaluation eines Messstands zur kontaktlosen Erfassung der Vitalparameter." Diploma thesis. TU Dresden, 2013, p. 83.

[32] C. Brüser, A. Kerekes, S. Winter, and S. Leonhardt. "Multi-channel optical sensor-array for measuring ballistocardiograms and respiratory activity in bed." In: *Proc. 34th Annu. Int. Conf. IEEE Eng. Med. Biol. Soc. (EMBC)*. San Diego, USA, 2012, pp. 5042–5045. DOI: 10.1109/EMBC.2012.6347126.

[33] C. Brüser, C.H. Antink, T. Wartzek, M. Walter, and S. Leonhardt. "Ambient and Unobtrusive Cardiorespiratory Monitoring Techniques." In: *IEEE Reviews in Biomedical Engineering* 8 (2015), pp. 30–43. DOI: 10.1109/RBME.2015.2414661.

[34] M.J. Butler, J.A. Crowe, B.R. Hayes-Gill, and P.I. Rodmell. "Motion limitations of non-contact photoplethysmography due to the optical and topological properties of skin." In: *Physiological measurement* 37.5 (2016), N27–N37. DOI: 10.1088/0967-3334/37/5/N27.

[35] J.L. Camargo-Olivares, R. Martin-Clemente, S. Hornillo-Mellado, M.M. Elena, and I. Román. "The Maternal Abdominal ECG as Input to MICA in the Fetal ECG Extraction Problem." In: *IEEE Signal Processing Letters* 18.3 (2011), pp. 161–164. DOI: 10.1109/LSP.2011.2104415.

[36] X.R. Cao and R.W. Liu. "General Approach to Blind Source Separation." In: *IEEE Transactios on Signal Processing* 44.3 (1996), pp. 562–571. DOI: 10.1109/78.489029.

[37] J.F. Cardoso. "Multidimensional Independent Component Analysis." In: *Proc. IEEE Int. Conf. Acoustics, Speech and Signal Processing (ICASSP)*. Seattle, USA, 1998. DOI: 10.1109/ICASSP.1998.681443.

[38] J.F. Cardoso. "High-order contrasts for independent component analysis." In: *Neural Computation* 11.1 (1999), pp. 157–192. DOI: 10.1162/089976699300016863.

[39] J.F. Cardoso and A. Souloumiac. "Blind beamforming for non-Gaussian signals." In: *IEE Proceedings F (Radar and Signal Processing)* 140.6 (1993), pp. 362–370. DOI: 10.1049/ip-f-2.1993.0054.

[40] J.F. Cardoso and A. Souloumiac. "Jacobi Angles for Simultaneous Diagonalization." In: *SIAM Journal on Matrix Analysis and Applications* 17.1 (1996), pp. 161–164. DOI: 10.1137/S0895479893259546.

[41] M. Catrysse, R. Puers, C. Hertleer, L. Van Langenhove, H. Van Egmond, and D. Matthys. "Towards the integration of textile sensors in a wireless monitoring suit." In: *Sensors and Actuators, A: Physical* 114.2-3 (2004), pp. 302–311. DOI: 10.1016/j.sna.2003.10.071.

[42] G. Cennini, J. Arguel, K. Akşit, and A. van Leest. "Heart rate monitoring via remote photoplethysmography with motion artifacts reduction." In: *Optics Express* 18.5 (2010), pp. 4867–4875. DOI: 10.1364/OE.18.004867.

[43] S. Challa and D. Koks. "Bayesian and Dempster – Shafer fusion." In: *Sadhana* 29.2 (2004), pp. 145–176. DOI: 10.1007/BF02703729.

[44] B. Chamadiya, S. Heuer, M. Wagner, and U.G. Hofmann. "Textile Capacitive Electrocardiography For An Automotive Environment." In: *Proc. Int. Conf. Biomed. Electr. Dev. (BIODEVICES)*. Rome, Italy, 2011, pp. 422–425. DOI: 10.5220/0003194504220425.

[45] B. Chamadiya, K. Mankodiya, M. Wagner, and U.G. Hofmann. "Textile-based, contactless ECG monitoring for non-ICU clinical settings." In: *Journal of Ambient Intelligence and Humanized Computing* 4.6 (2013), pp. 791–800. DOI: 10.1007/s12652-012-0153-8.

[46] P. Charlton, L. Camporota, J. Smith, M. Nandi, M. Christie, J.P. Aston, and R. Beale. "Measurment of Cardiovascular State Using Attractor Analysis." In: *Proc. 23rd Europ. Conf. Signal Processing (EUSIPCO)*. Nice, France, 2015, pp. 444–448. DOI: 10.1109/EUSIPCO.2015.7362422.

[47] M.P.S. Chawla. "Parameterization and R-Peak error estimations of ECG signals using independent component analysis." In: *Computational and Mathematical Methods in Medicine* 8.4 (2007), pp. 263–285. DOI: 10.1080/17486700701776348.

[48] M.P.S. Chawla. "Detection of indeterminacies in corrected ECG signals using parameterized multidimensional independent component analysis." In: *Computational and Mathematical Methods in Medicine* 10.2 (2009), pp. 85–115. DOI: 10.1080/17486700802193153.

[49] M.P.S. Chawla. "PCA and ICA processing methods for removal of artifacts and noise in electrocardiograms: A survey and comparison." In: *Applied Soft Computing* 11.2 (2011), pp. 2216–2226. DOI: 10.1016/j.asoc.2010.08.001.

[50] J.G. Chen and N. Ansari. "Adaptive Fusion of Correlated Local Decisions." In: *IEEE Transactions on Systems, Man and Cybernetics Part C: Applications and Reviews* 28.2 (1998), pp. 276–281. DOI: 10.1109/5326.669570.

[51] Y.M. Chi, T.P. Jung, and G. Cauwenberghs. "Dry-contact and noncontact biopotential electrodes: methodological review." In: *IEEE Reviews in Biomedical Engineering* 3 (2010), pp. 106–119. DOI: 10.1109/RBME.2010.2084078.

[52] F. Chiarugi, V. Sakkalis, D. Emmanouilidou, T. Kontiris, M. Varanini, and I. Tollis. "Adaptive Threshold QRS Detector with Best Channel Selection Based on a Noise Rating System." In: *Proc. 34th Computers in Cardiology Conf. (CinC)*. Durham, USA, 2007, pp. 157–160.

[53] S. Choi, A. Cichocki, and A. Beloucharni. "Second order nonstationary source separation." In: *Journal of VLSI Signal Processing Systems for Signal, Image, and Video Technology* 32.1-2 (2002), pp. 93–104. DOI: 10.1023/A:1016319502849.

[54] J. Christie, L.M. Sheldahl, F.E. Tristani, K.B. Sagar, M.J. Ptacin, and S. Wann. "Determination of stroke volume and cardiac output during exercise: comparison of two-dimensional and Doppler echocardiography, Fick oximetry, and thermodilution." In: *Circulation* 76.3 (1987), pp. 539–547. DOI: 10.1161/01.CIR.76.3.539.

[55] E. Christinaki, G. Giannakakis, F. Chiarugi, M. Pediaditis, and G. Iatraki. "Comparison of Blind Source Separation Algorithms for Optical Heart Rate Monitoring." In: *Proc. 4th Mobihealth*. Athens, Greece, 2014, pp. 339–342. DOI: 10.1109/MOBIHEALTH.2014.7015980.

[56] Y. Chuo, K. Tavakolian, and B. Kaminska. "Evaluation of a novel integrated sensor system for synchronous measurement of cardiac vibrations and cardiac potentials." In: *Journal of Medical Systems* 35.4 (2011), pp. 445–455. DOI: 10.1007/s10916-009-9380-8.

[57] A. Cichocki and S. Amari. *Adaptive Blind Signal and Image Processing*. Rev. 1st. Chichester, UK: John Wiley & Sons, Ltd, 2002, p. 586. DOI: 10.1002/0470845899.

[58] A. Cichocki and R. Unbehauen. "Robust neural networks with on-line learning for blind identification and blind separation of sources." In: *IEEE Transactions on Circuits and Systems I: Fundamental Theory and Applications* 43.11 (1996), pp. 894–906. DOI: 10.1109/81.542280.

[59] G.D. Clifford, F. Azuaje, and P.E. McSharry. *Advanced methods and tools for ECG data analysis*. 1st. Boston, London: Artech House, 2006. ISBN: 9781580539661.

[60] P. Comon. "Independent component analysis, A new concept?" In: *Signal Processing* 36.3 (1994), pp. 287–314. DOI: 10.1016/0165-1684(94)90029-9.

[61] R. Cooper, J.W. Osselton, and J.C. Shaw. *EEG Technology*. 2nd. London: Butterworth & Co. (Publishers) Ltd., 1974, p. 288. ISBN: 9780407160019. DOI: 10.1016/B978-0-407-16001-9.50001-8.

[62] J.P. Couderc, S. Kyal, L.K. Mestha, B. Xu, D.R. Peterson, X. Xia, and B. Hall. "Detection of atrial fibrillation using contactless facial video monitoring." In: *Heart Rhythm* 12.1 (2015), pp. 195–201. DOI: 10.1016/j.hrthm.2014.08.035.

[63] Y. Cui, C.H. Fu, H. Hong, Y. Zhang, and F. Shu. "Non-Contact Time Varying Heart Rate Monitoring in Exercise by Video Camera." In: *Proce. 7th Int. Conf. Wireless Communications & Signal Processing (WCSP)*. Nanjing, China, 2015, pp. 1–5. DOI: 10.1109/WCSP.2015.7341278.

[64] K. Das, S. Ali, K. Otsu, H. Fukuda, A. Lam, Y. Kobayashi, and Y. Kuno. "Detecting Inner Emotions from Video Based Heart Rate Sensing." In: *Proc. Int. Conf. Intelligent Computing (ICIC)*. Liverpool, UK, 2017, pp. 48–57. DOI: 10.1007/978-3-319-63315-2_5.

[65] B.M. Dawant and C. Garbay. "Special topic section on biomedical data fusion." In: *IEEE Transactions on Biomedical Engineering* 46.10 (1999), pp. 1169–1170. DOI: 10.1109/TBME.1999.790490.

[66] L. De Lathauwer and J. Castaing. "Blind Identification of Underdetermined Mixtures by Simultaneous Matrix Diagonalization." In: *IEEE Transactions on Signal Processing* 56.3 (2008), pp. 1096–1105. DOI: 10.1109/TSP.2007.908929.

[67] L. De Lathauwer, J. Castaing, and J.F. Cardoso. "Fourth-Order Cumulant-Based Blind Identification of Underdetermined Mixtures." In: *IEEE Transactions on Signal Processing* 55.6 (2007), pp. 2965–2973. DOI: 10.1109/TSP.2007.893943.

[68] T. Degen, S. Torrent, and H. Jackel. "Low-noise two-wired buffer electrodes for bioelectric amplifiers." In: *IEEE Transactions on Biomedical Engineering* 54.7 (2007), pp. 1328–1332. DOI: 10.1109/TBME.2006.889781.

[69] A.P. Dempster, N.M. Laird, and D.B. Rubin. "Maximum Likelihood from Incomplete Data via the EM Algorithm." In: *Journal of the Royal Statistical Society. Series B (Methodological)* 39.1 (1977), pp. 1–38. ISSN: 0035-9246.

[70] C. Di Maria, W. Duan, M. Bojarnejad, F. Pan, S. King, D. Zheng, A. Murray, and P. Langley. "An Algorithm for the Analysis of Fetal ECGs from 4-channel Non-invasive Abdominal Recordings." In: *Proc. 40th Computing in Cardiology Conf. (CinC)*. Zaragoza, Spain, 2013, pp. 305–309.

[71] H.H. Dickhuth, A. Nause, J. Staiger, T. Bonzel, and J. Keul. "Two-dimensional echocardiographic measurements of left ventricular volume and stroke volume of endurance-trained athletes and untrained subjects." In: *International Journal of Sports Medicine* 4.1 (1983), pp. 21–26. DOI: 10.1055/s-2008-1026011.

[72] K.L. Duffin and W.A. Barrett. "Spiders: a new user interface for rotation and visualization of n-dimensional point sets." In: *Proc. IEEE Conf. Visualization (VISUAL)*. Washington DC, USA, 1994, pp. 205–211. DOI: 10.1109/VISUAL.1994.346318.

[73] S.S. Dukhin. "Electrokinetic phenomena of the second kind and their applications." In: *Advances in Colloid and Interface Science* 35 (1991), pp. 173–196. DOI: 10.1016/0001-8686(91)80022-C.

[74] A. Dyszkiewicz and M. Tendera. "Vibration syndrome diagnosis using a cooling test verified by computerized photoplethysmography." In: *Physiological measurement* 27.4 (2006), pp. 353–369. DOI: 10.1088/0967-3334/27/4/003.

[75] M.H. Ebrahim, J.M. Feldman, and I. Bar-Kana. "A robust sensor fusion method for heart rate estimation." In: *Journal of Clinical Monitoring* 13.6 (1997), pp. 385–393. DOI: 10.1023/A:1007438224122.

[76] R. Erts, J. Spigulis, I. Kukulis, and M. Ozols. "Bilateral photoplethysmography studies of the leg arterial stenosis." In: *Physiological measurement* 26.5 (2005), pp. 865–74. DOI: 10.1088/0967-3334/26/5/022.

[77] J.R. Estepp, E.B. Blackford, and C.M. Meier. "Recovering pulse rate during motion artifact with a multi-imager array for non-contact imaging photoplethysmography." In: *Proc. IEEE Int. Conf. Systems, Man, and Cybernetics (SMC)*. Vol. 940. San Diego, USA, 2014, pp. 1462–1469. DOI: 10.1109/SMC.2014.6974121.

[78] J.M. Feldman, M.H. Ebrahim, and I. Bar-Kana. "Robust sensor fusion improves heart rate estimation: Clinical evaluation." In: *Journal of Clinical Monitoring* 13.6 (1997), pp. 379–384. DOI: 10.1023/A:1007476707284.

[79] L. Feng, L. Po, X. Xu, and Y. Li. "Motion Artifacts Suppression for Remote Imaging Photoplethysmography." In: *Proc. 19th Int. Conf. Digital Signal Processing (DSP)*. Hong Kong, China, 2014, pp. 18–23. DOI: 10.1109/ICDSP.2014.6900813.

[80] L. Feng, L.M. Po, X. Xu, Y. Li, and R. Ma. "Motion-resistant remote imaging photoplethysmography based on the optical properties of skin." In: *IEEE Transactions on Circuits and Systems for Video Technology* 25.5 (2015), pp. 879–891. DOI: 10.1109/TCSVT.2014.2364415.

[81] S.L. Fernandes, V.P. Gurupur, N.R. Sunder, N. Arunkumar, and S. Kadry. "A novel nonintrusive decision support approach for heart rate measurement." In: *Pattern Recognition Letters* (2017). DOI: 10.1016/j.patrec.2017.07.002.

[82] O. Fojt and J. Holcik. "Applying Nonlinear Dynamics to ECG Signal Processing." In: *IEEE Engineering in Medicine and Biology Magazine* 17.2 (1998), pp. 96–101. DOI: 10.1109/51.664037.

[83] J.H. Friedman. "Exploratory Projection Pursuit." In: *Journal of the American Statistical Association* 82.397 (1987), pp. 249–266. DOI: 10.1080/01621459.1987.10478427.

[84] J.H. Friedman and J.W. Tukey. "A Projection Pursuit Algorithm for Exploratory Data Analysis." In: *IEEE Transactions on Computers* 23.9 (1974), pp. 881–890. DOI: 10.1109/T-C.1974.224051.

[85] C.O. Fritz, P.E. Morris, and J.J. Richler. "Effect size estimates: Current use, calculations, and interpretation." In: *Journal of Experimental Psychology: General* 141.1 (2012), pp. 2–18. DOI: 10.1037/a0024338.

[86] M. van Gastel, S. Stuijk, and G. de Haan. "Motion Robust Remote-PPG in Infrared." In: *IEEE Transactions on Biomedical Engineering* 62.5 (2015), pp. 1425–1433. DOI: 10.1109/TBME.2015.2390261.

[87] L.A. Geddes and M.E. Valentinuzzi. "Temporal Changes in Electrode Impedance While Recording the Electrocardiogram with "Dry" Electrodes." In: *Annals of Biomedical Engineering* 1.3 (1973), pp. 356–367. DOI: 10.1007/BF02407675.

[88] P. Georgiev, F. Theis, and A. Cichocki. "Sparse Component Analysis and Blind Source Separation of Underdetermined Mixtures." In: *IEEE Transactions on Neural Networks* 16.4 (2005), pp. 992–996. DOI: 10.1109/TNN.2005.849840.

[89] A.L. Goldberger, L.A.N. Amaral, L. Glass, J.M. Hausdorff, P.C. Ivanov, R.G. Mark, J.E. Mietus, G.B. Moody, C.K. Peng, and H.E. Stanley. "PhysioBank, PhysioToolkit, and PhysioNet : Components of a New Research Resource for Complex Physiologic Signals." In: *Circulation* 101.23 (2000), e215–e220. DOI: 10.1161/01.CIR.101.23.e215.

[90] L. Grajales and I.V. Nicolaescu. "Wearable multisensor heart rate monitor." In: *Proc. Int. Workshop Wearable and Implantable Body Sensor Networks (BSN)*. Cambridge, USA, 2006, pp. 154–157. DOI: 10.1109/BSN.2006.58.

[91] P.J. Green and D.P. Taylor. "Dynamic Signal Enumeration Algorithm for Smart Antennas." In: *IEEE Transactions on Signal Processing* 50.6 (2002), pp. 1307–1314. DOI: 10.1109/TSP.2002.1003056.

[92] A. Gruetzmann, S. Hansen, and J. Müller. "Novel dry electrodes for ECG monitoring." In: *Physiological Measurement* 28.11 (2007), pp. 1375–1390. DOI: 10.1088/0967-3334/28/11/005.

[93] A.R. Guazzi, M. Villarroel, M.C. Frise, P.A. Robbins, and L. Tarassenko. "Non-contact measurement of oxygen saturation with an RGB camera." In: *Biomedical Optics Express* 45.2008 (2015), pp. 1764–1771. DOI: 10.1364/BOE.6.003320.

[94] G. de Haan and V. Jeanne. "Robust pulse-rate from chrominance-based rPPG." In: *IEEE Transactions on Biomedical Engineering* 60.10 (2013), pp. 2878–2886. DOI: 10.1109/TBME.2013.2266196.

[95] G. de Haan and A. van Leest. "Improved motion robustness of remote-PPG by using the blood volume pulse signature." In: *Physiological measurement* 35.9 (2014), pp. 1913–1926. DOI: 10.1088/0967-3334/35/9/1913.

[96] D.L. Hall and J. Llinas. "An Introduction to Multisensor Data Fusion." In: *Proceedings of the IEEE* 85.1 (1997), pp. 6–23. DOI: 10.1109/5.554205.

[97] D.L. Hall and J. Llinas. *Handbook of Multisensor Data Fusion*. 1st. Boca Raton, London, New York: CRC Press, 2001, p. 541. ISBN: 0849323797.

[98] M.B. Hamaneh, N. Chitravas, K. Kaiboriboon, S.D. Lhatoo, and K.A. Loparo. "Automated Removal of EKG Artifact From EEG Data Using Independent Component Analysis and Continuous Wavelet Transformation." In: *IEEE Transactions on Biomedical Engineering* 61.6 (2014), pp. 1634–1641. DOI: 10.1109/TBME.2013.2295173.

[99] M. A. Hassan, A.S. Malik, N. Saad, B. Karasfi, Y.S. Ali, and D. Fofi. "Optimal source selection for image photoplethysmography." In: *Proc. IEEE Int. Conf. Instrumentation and Measurement Technology (I2MTC)*. Taipei, Taiwan, 2016. ISBN: 9781467392204. DOI: 10.1109/I2MTC.2016.7520406.

[100] M. A. Hassan, A. S. Malik, D. Fofi, N. M. Saad, Y. S. Ali, and F. Meriaudeau. "Video-Based Heartbeat Rate Measuring Method Using Ballistocardiography." In: *IEEE Sensors Journal* (2017). DOI: 10.1109/JSEN.2017.2708133.

[101] T. He, G.D. Clifford, and L. Tarassenko. "Application of independent component analysis in removing artefacts from the electrocardiogram." In: *Neural Computing and Applications* 15.2 (2006), pp. 105–116. DOI: 10.1007/s00521-005-0013-y.

[102] E. C. Hedberg and S. Ayers. "The power of a paired t-test with a covariate." In: *Social Science Research* 50 (2015), pp. 277–291. DOI: 10.1016/j.ssresearch.2014.12.004.

[103] A. Henning. "Verfahren zur Messung der kardiopulmonalen Aktivität Ansätze zur Steuerung bildgebender Verfahren." PhD Thesis. TU Dresden, 2017, p. 228.

[104] H. Hentschke and M.C. Stüttgen. "Computation of measures of effect size for neuroscience data sets." In: *European Journal of Neuroscience* 34.12 (2011), pp. 1887–1894. DOI: 10.1111/j.1460-9568.2011.07902.x.

[105] J. Herault and C. Jutten. "Space or time adaptive signal processing by neural network models." In: *Proc. American Instistute of Physics (AIP) Conf. on Neural Networks for Computing*. Vol. 151. Snowbird, USA, 1986, pp. 206–211. DOI: 10.1063/1.36258.

[106] A.I. Hernández, G. Carrault, F. Mora, L. Thoraval, G. Passariello, and J.M. Schleich. "Multisensor fusion for atrial and ventricular activity detection in coronary care monitoring." In: *IEEE transactions on Biomedical Engineering* 46.10 (1999), pp. 1186–1190. DOI: 10.1109/10.790494.

[107] A.B. Hertzman. "The Blood Suppy of Various Skin Areas as Estimated by the Photoelectric Plethysmograph." In: *American Journal of Physiology* 124.2 (1938), pp. 328–340. ISSN: 0002-9513.

[108] C.W. Hesse and C.J. James. "Stepwise Model Order Estimation in Blind Source Separation Applied to Ictal EEG." In: *Proc. 26th Annu. Int. Conf. IEEE Eng. Med. Biol. Soc. (EMBC)*. Vol. 2. San Francisco, USA, 2004, pp. 986–989. DOI: 10.1109/IEMBS.2004.1403327.

[109] T. Hetzel. "Sensordatenfusion für die kontaktarme Erfassung der Herzaktivität." Master thesis. Hochschule Mittweida, University of Applied Science, 2013, p. 109.

[110] S. Heuer. "Ambiente kapazitive EKG-Messung Elektroden, Systeme und Konzepte." PhD thesis. Karlsruher Institut für Technologie (KIT), Germany, 2011, p. 186.

[111] K.P. Hoffmann and R. Ruff. "Flexible dry surface-electrodes for ECG long-term monitoring." In: *Proc. 29th Annu. Int. Conf. IEEE Eng. Med. Biol. Soc. (EMBC)*. Lyon, France, 2007, pp. 5739–5742. DOI: 10.1109/IEMBS.2007.4353650.

[112] B.D. Holton, K. Mannapperuma, P.J. Lesniewski, and J.C. Thomas. "Signal recovery in imaging photoplethysmography." In: *Physiological measurement* 34.11 (2013), pp. 1499–1511. DOI: 10.1088/0967-3334/34/11/1499.

[113] Y.C. Hsu, Y.L. Lin, and W. Hsu. "Learning-based heart rate detection from remote photoplethysmography features." In: *Proc. 39th Int. Conf. Acoustics, Speech and Signal Processing (ICASSP)*. Florence, Italy, 2014, pp. 4433–4437. DOI: 10.1109/ICASSP.2014.6854440.

[114] S. Hu, J. Zheng, V. Chouliaras, and R. Summers. "Feasibility of imaging photoplethysmography." In: *Proc. Int. Conf. Biomed. Eng. Inf. (BMEI)*. Sanya, China, 2008, pp. 72–75. DOI: 10.1109/BMEI.2008.365.

[115] S.C. Huang, H.Y. Jan, G.H. Lin, W.C. Lin, and K.P. Lin. "Decomposition Analysis of Digital Volume Pulse Signal Using Multi-Model Fitting." In: *Proc. 13th Mediterranean Conf. on Medical and Biological Engineering and Computing (Part of IFMBE Proc. Vol. 41)*. Paphos, Cyprus, 2013, pp. 670–673. DOI: 10.1007/978-3-319-00846-2_157.

[116] P.J. Huber. "Projection Pursuit." In: *The Annals of Statistics* 13.2 (1985), pp. 435–475. DOI: 10.1214/aos/1176349519.

[117] M. Hülsbusch and V. Blažek. "Contactless Mapping of Rhythmical Phenomena in Tissue Perfusion Using PPGI." In: *Proc. Medical Imaging 2002 (SPIE 4683)*. San Diego, USA, 2002, pp. 110–117. DOI: 10.1117/12.463573.

[118] K. Humphreys, T. Ward, and C. Markham. "Noncontact simultaneous dual wavelength photoplethysmography: A further step toward noncontact pulse oximetry." In: *Review of Scientific Instruments* 78.4 (2007), 044304 (1–7). DOI: 10.1063/1.2724789.

[119] M. Huotari, A. Vehkaoja, K. Määttä, and J. Kostamovaara. "Photoplethysmography and its detailed pulse waveform analysis for arterial stiffness." In: *Rakenteiden Mekaniikka (Journal of Structural Mechanics)* 44.4 (2011), pp. 345–362. ISSN: 0783-6104.

[120] J. Huppelsberg and K. Walter. *Kurzlehrbuch Physiologie*. 4th. Stuttgart, New York, Delhi and Rio: Thieme Verlagsgruppe, 2013, p. 373. ISBN: 9783131945341. DOI: 10.1055/b-002-96275.

[121] A. Hyvärinen. *New Approximations of Differential Entropy for Independent Component Analysis and Projection Pursuit - A47*. Tech. rep. Helsinki, Finland: Helsinki University of Technology, Laboratory of Computer and Information Science, 1997, pp. 1–12.

[122] A. Hyvärinen. "New Approximations of Differential Entropy for Independent Component Analysis and Projection Pursuit." In: *Advances in Neural Information Processing Systems* 10 (1998), pp. 273–279. ISSN: 1049-5258.

[123] A. Hyvärinen. "Fast and Robust Fixed-Point Algorithms for Independent Component Analysis." In: *IEEE Transactions on Neural Networks* 10.3 (1999), pp. 626–634. DOI: 10.1109/72.761722.

[124] A. Hyvärinen and E. Oja. "Independent Component Analysis: Algorithms and Applications." In: *Neural Networks* 13.4-5 (2000), pp. 411–430. DOI: 10.1016/S0893-6080(00)00026-5.

[125] A. Hyvärinen and P. Pajunen. "Nonlinear independent component analysis: Existence and uniqueness results." In: *Neural Networks* 12.3 (1999), pp. 429–439. DOI: 10.1016/S0893-6080(98)00140-3.

[126] A. Hyvärinen, J. Särelä, and R. Vigário. "Spikes and Bumps: Artefacts Generated by Independent Component Analysis with Insufficient Sample Size." In: *Proc. 1st Int. Conf. Independent Component Analysis and Signal Separation (ICA)*. Aussois, France, 1999, pp. 425–429.

[127] L. Iozzia, L. Cerina, and L. Mainardi. "Relationships between heart-rate variability and pulse-rate variability obtained from video-PPG signal using ZCA." In: *Physiological Measurement* 37.11 (2016), pp. 1934–1944. DOI: 10.1088/0967-3334/37/11/1934.

[128] M. Ishijima. "Monitoring of Electrocardiograms in Bed Without Utilizing Body Surface Electrodes." In: *IEEE Transactions on Biomedical Engineering* 40.6 (1993), pp. 593–594. DOI: 10.1109/10.237680.

[129] C.J. James and O.J. Gibson. "Temporally Constrained ICA: An Application to Artifact Rejection in Electromagnetic Brain Signal Analysis." In: *IEEE Transactions on Biomedical Engineering* 50.9 (2003), pp. 1108–1116. DOI: 10.1109/TBME.2003.816076.

[130] C.J. James and C.W. Hesse. "A Comparison of Time Structure and Statistically Based BSS Methods in the Context of Long-Term Epileptiform EEG Recordings." In: *Proc. 5th Int. Conf. Independent Component Analysis and Signal Separation (ICA)*. Granada, Spain, 2004, pp. 1025–1032. DOI: 10.1007/978-3-540-30110-3_129.

[131] C.J. James and C.W. Hesse. "Independent component analysis for biomedical signals." In: *Physiological measurement* 26.1 (2005), R15–R39. DOI: 10.1088/0967-3334/26/1/R02.

[132] C.J. James and D. Lowe. "Extracting multisource brain activity from a single electromagnetic channel." In: *Artificial intelligence in medicine* 28.1 (2003), pp. 89–104. DOI: 10.1016/S0933-3657(03)00037-X.

[133] M. Joho, H. Mathis, and R.H. Lambert. "Overdetermined blind source separation: Using more sensors than sources in a noisy mixture." In: *Proc. 2nd Int. Workshop Independent Component Analysis and Blind Signal Separation (ICA2000)*. Helsinki, Finland, 2000, pp. 81–86. ISBN: 9512250179.

[134] E. Jonathan and M. Leahy. "Investigating a smartphone imaging unit for photoplethysmography." In: *Physiological measurement* 31.11 (2010), N79–N83. DOI: 10.1088/0967-3334/31/11/N01.

[135] C. Jutten and J. Herault. "Blind separation of sources, part I: An adaptive algorithm based on neuromimetic architecture." In: *Signal Processing* 24.1 (1991), pp. 1–10. DOI: 10.1016/0165-1684(91)90079-X.

[136] A.A. Kamshilin, S. Miridonov, V. Teplov, R. Saarenheimo, and E. Nippolainen. "Photoplethysmographic imaging of high spatial resolution." In: *Biomedical Optics Express* 2.4 (2011), pp. 996–1006. DOI: 10.1364/BOE.2.000996.

[137] A.A. Kamshilin, V. Teplov, E. Nippolainen, S. Miridonov, and R. Giniatullin. "Variability of microcirculation detected by blood pulsation imaging." In: *PloS ONE* 8.2 (2013), e57117 (1–9). DOI: 10.1371/journal.pone.0057117.

[138] A.A. Kamshilin, E. Nippolainen, I.S. Sidorov, P.V. Vasilev, N.P. Erofeev, N.P. Podolian, and R.V. Romashko. "A new look at the essence of the imaging photoplethysmography." In: *Nature Scientific Reports* 5 (2015), 10494 (1–9). DOI: 10.1038/srep10494.

[139] T.H. Kang, C.R. Merritt, E. Grant, B. Pourdeyhimi, and H.T. Nagle. "Nonwoven fabric active electrodes for biopotential measurement during normal daily activity." In: *IEEE Transactions on Biomedical Engineering* 55.1 (2008), pp. 188–195. DOI: 10.1109/TBME.2007.910678.

[140] T. Kato, A. Ueno, S. Kataoka, H. Hoshino, and Y. Ishiyama. "An Application of Capacitive Electrode for Detecting Electrocardiogram of Neonates and Infants." In: *Proc. 28th Annu. Int. Conf. IEEE Eng. Med. Biol. Soc. (EMBC)*. New York, USA, 2006, pp. 916–919. DOI: 10.1109/IEMBS.2006.260362.

[141] B. Kaur, S. Moses, M. Luthra, and V.N. Ikonomidou. "Robustness of Remote Stress Detection from Visible Spectrum Recordings." In: *Proc. Sensing and Analysis Technologies for Biomedical and Cognitive Applications (SPIE 9871)*. Baltimore, USA, 2016, 987103 (1–9). DOI: 10.1117/12.2223933.

[142] B. Khaleghi, A. Khamis, F.O. Karray, and S.N. Razavi. "Multisensor data fusion: A review of the state-of-the-art." In: *Information Fusion* 14.4 (2013), pp. 28–44. DOI: 10.1016/j.inffus.2012.10.004.

[143] B.S. Kim and S.K. Yoo. "Motion Artifact Reduction in Photoplethysmography Using Independent Component Analysis." In: *IEEE Transactions on Biomedical Engineering* 53.3 (2006), pp. 566–568. DOI: 10.1109/TBME.2005.869784.

[144] K.K. Kim, Y.K. Lim, and K.S. Park. "The Electrically Non-Contacting ECG Measurement on the Toilet Seat Using the Capacitively-Coupled Insulated Electrodes." In: *Proc. 26th Annu. Int. Conf. IEEE Eng. Med. Biol. Soc. (EMBC)*. San Francisco, USA, 2004, pp. 2375–2378. DOI: 10.1109/IEMBS.2004.1403688.

[145] K.K. Kim, Y.K. Lim, and K.S. Park. "Common mode noise cancellation for electrically non-contact ECG measurement system on a chair." In: *Proc. 27th Annu. Int. Conf. IEEE Eng. Med. Biol. Soc. (EMBC)*. Shanghai, China, 2005, pp. 5881–5883. DOI: 10.1109/IEMBS.2005.1615828.

[146] R. Klinge. *Das Elektrokardiogramm*. 5th. Stuttgart, New York: Georg Thieme Verlag, 1987, p. 346. ISBN: 3135540057.

[147] L. Kong, Y. Zhao, L. Dong, Y. Jian, X. Jin, Bing Li, Y. Feng, M. Liu, X. Liu, and H. Wu. "Non-contact detection of oxygen saturation based on visible light imaging device using ambient light." In: *Optics Express* 21.15 (2013), pp. 17464–17471. DOI: 10.1364/OE.21.017464.

[148] J.M. Kortelainen, M. van Gils, and J. Pärkkä. "Multichannel Bed Pressure Sensor for Sleep Monitoring." In: *Proc. 39th Computing in Cardiology (CinC)*. Krakow, Poland, 2012, pp. 5–8.

[149] R. Krishnan, B.B. Natarajan, and S. Warren. "Two-Stage Approach for Detection and Reduction of Motion Artifacts in Photoplethysmographic Data." In: *IEEE Transactions on Biomedical Engineering* 57.8 (2010), pp. 1867–1876. DOI: 10.1109/TBME.2009.2039568.

[150] J.W. Krug, G. Rose, G.D. Clifford, and J. Oster. "ECG-based gating in ultra high field cardiovascular magnetic resonance using an independent component analysis approach." In: *Journal of Cardiovascular Magnetic Resonance* 15.104 (2013), pp. 1–13. DOI: 10.1186/1532-429X-15-104.

[151] J. Kuzilek and L. Lhotska. "Electrocardiogram beat detection enhancement using Independent Component Analysis." In: *Medical Engineering & Physics* 35.6 (2012), pp. 704–711. DOI: 10.1016/j.medengphy.2012.07.017.

[152] J. Kuzilek, V. Kremen, F. Soucek, and L. Lhotska. "Independent component analysis and decision trees for ECG holter recording de-noising." In: *PLoS ONE* 9.6 (2014), e98450–1–9. DOI: 10.1371/journal.pone.0098450.

[153] S. Kwon, H. Kim, and K. Suk Park. "Validation of heart rate extraction using video imaging on a built-in camera system of a smartphone." In: *Proc. 34th Annu. Int. Conf. IEEE Eng. Med. Biol. Soc. (EMBC)*. San Diego, USA, 2012, pp. 2174–2177. DOI: 10.1109/EMBC.2012.6346392.

[154] A. Lam and Y. Kuno. "Robust heart rate measurement from video using select random patches." In: *Proc. 15th IEEE Int. Conf. Computer Vision (ICCV)*. Santiago, Chile, 2015, pp. 3640–3648. DOI: 10.1109/ICCV.2015.415.

[155] R.H. Lambert. "Difficulty Measures and Figures of Merit for Source Separation." In: *Proc. Int. Symp. ICA and BSS (ICA'99)*. Aussois, France, 1999, pp. 133–138.

[156] F. Lang. *Pathophysiologie, Pathobiochemie*. 4th. Stuttgart: Ferdinand Enke Verlag, 1990, p. 484. ISBN: 343290374X.

[157] B. Lantz. "The large sample size fallacy." In: *Scandinavian Journal of Caring Sciences* 27.2 (2013), pp. 487–492. DOI: 10.1111/j.1471-6712.2012.01052.x.

[158] P.D. Larsen, C.D. Lewis, G.L. Gebber, and S. Zhong. "Partial Spectral Analysis of Cardiac-Related Sympathetic Nerve Discharge Partial Spectral Analysis of Cardiac-Related Sympathetic Nerve Discharge." In: *Journal of Neurophysiology* 84.3 (2000), pp. 1168–1179. ISSN: 0022-3077.

[159] E.G. Learned-Miller and J.W. Fisher III. "ICA Using Spacings Estimates of Entropy." In: *Journal of Machine Learning Research* 4 (2003), pp. 1271–1295. ISSN: 1532-4435.

[160] H.J. Lee, S.M. Lee, K.M. Lee, and K.S. Park. "Performance Evaluation of Electrocardiogram Measured Using Capacitive Textiles on a Bed." In: *Proc. Int. Conf. Biomed. Electr. Dev. (BIODEVICES)*. Rome, Italy, 2011, pp. 436–439. DOI: 10.5220/0003291604360439.

[161] J. Lee, K.L. Park, and K.J. Lee. "Temporally constrained ICA based foetal ECG separation." In: *Electronic Letters* 41.21 (2005), pp. 1158–1160. DOI: 10.1049/el:20052235.

[162] T.W. Lee, M. Girolami, and T.J. Sejnowski. "Independent Component Analysis Using an Extended Infomax Algorithm for Mixed Sub-Gaussian and Super-Gaussian Sources." In: *Neural Computation* 11.2 (1999), pp. 417–441. DOI: 10.1162/089976699300016719.

[163] G. Lempe, S. Zaunseder, T. Wirthgen, S. Zipser, and H. Malberg. "ROI Selection for Remote Photoplethysmography." In: *Bildverarbeitung für die Medizin* (2013), pp. 99–103. DOI: 10.1007/978-3-642-36480-8_19.

[164] S. Leonhardt and A. Aleksandrowicz. "Non-Contact ECG Monitoring for Automotive Application." In: *Proc. 5th Int. Summer School Symp. Med. Dev. Biosens. (ISSS-MDBS)*. Hong Kong, China, 2008, pp. 183–185. DOI: 10.1109/ISSMDBS.2008.4575048.

[165] S. Leonhardt, L. Leicht, and D. Teichmann. "Unobtrusive vital sign monitoring in automotive environments—A review." In: *Sensors (Switzerland)* 18.9 (2018), pp. 1–38. DOI: 10.3390/s18093080.

[166] M. Lewandowska, J. Ruminski, T. Kocejko, and J. Nowak. "Measuring Pulse Rate with a Webcam: a Non-contact Method for Evaluating Cardiac Activity." In: *Proc. Federate Conf. Computer Science and Information Systems (FedCSIS)*. Szczecin, Poland, 2011, pp. 405–410. ISBN: 9788360810354.

[167] Q. Li, R.G. Mark, and G.D. Clifford. "Robust heart rate estimation from multiple asynchronous noisy sources using signal quality indices and a Kalman filter." In: *Physiological measurement* 29.1 (2008), pp. 15–32. DOI: 10.1088/0967-3334/29/1/002.

[168] X. Li, J. Chen, G. Zhao, and M. Pietikäinen. "Remote Heart Rate Measurement From Face Videos Under Realistic Situations." In: *Proc. IEEE Conf. Computer Vision and Pattern Recognition (CVPR)*. Columbus, USA, 2014, pp. 4264–4271. DOI: 10.1109/CVPR.2014.543.

[169] Y.G. Lim, K.K. Kim, and K.S. Park. "ECG Measurement on a Chair Without Conductive Contact." In: *IEEE Transactions on Biomedical Engineering* 53.5 (2006), pp. 956–959. DOI: 10.1109/TBME.2006.872823.

[170] Y.G. Lim, K.K. Kim, and K.S. Park. "ECG Recording on a Bed During Sleep Without Direct Skin-Contact." In: *IEEE Transactions on Biomedical Engineering* 54.4 (2007), pp. 718–725. DOI: 10.1109/TBME.2006.889194.

[171] Y.G. Lim, K.H. Hong, K.K. Kim, J.H. Shin, S.M. Lee, G.S. Chung, H.J. Baek, D.U. Jeong, and K.S. Park. "Monitoring Physiological Signals Using Nonintrusive Sensors Installed in Daily Life Equipment." In: *Biomedical Engineering Letters* 1.1 (2011), pp. 11–20. DOI: 10.1007/s13534-011-0012-0.

[172] Y.K. Lim, K.K. Kim, and K.S. Park. "The ECG Measurement in the Bathtub Using the Insulated Electrodes." In: *Proc. 26th Annu. Int. Conf. IEEE Eng. Med. Biol. Soc. (EMBC)*. Vol. 4. San Francisco, USA, 2004, pp. 2383–2385. DOI: 10.1109/IEMBS.2004.1403690.

[173] W. Lu, C. Jagath, and C. Rajapakse. "ICA with Reference." In: *Neurocomputing* 69.16-18 (2006), pp. 2244–2257. DOI: 10.1016/j.neucom.2005.06.021.

[174] C. Lueangwattana, T. Kondo, and H. Haneishi. "A Comparative Study of Video Signals for Non-contact Heart Rate Measurement." In: *Proc. 12th Int. Conf. Electrical Engineering/Electronics, Computer, Telecommunications and Information Technology (ECTI-CON)*. Hua Hin, China, 2015, pp. 1–5. DOI: 10.1109/ECTICon.2015.7206971.

[175] R.C. Luo and M.G. Kay. "Data Fusion an Sensor Integration: State-of-the-art 1990s." In: *Data Fusion in Robotics & Machine Intelligence*. Ed. by M.A. Abidi and R.C. Gonzalez. 1st. Boston, San Diego, New York et al.: Academic Press Inc., 1992. Chap. 2, p. 130. ISBN: 0120421208.

[176] R.C. Luo, M.H. Lin, and R.S. Scherp. "Dynamic multi-sensor data fusion system for intelligent robots." In: *Robotics and Automation, IEEE Journal of* 4.4 (1988), pp. 386–396. DOI: 10.1109/56.802.

[177] R.C. Luo, C.C. Yih, and K.L. Su. "Multisensor fusion and integration: approaches, applications, and future research directions." In: *IEEE Sensors Journal* 2.2 (2002), pp. 107–119. DOI: 10.1109/JSEN.2002.1000251.

[178] J.V. Lyle, P.H. Charlton, E. Bonet-Luz, G. Chaffey, M. Christie, M. Nandi, and P.J. Aston. "Beyond HRV: Analysis of ECG signals using attractor reconstruction." In: *Proc. 44th Computing in Cardiology (CinC)*. Rennes, France, 2017, pp. 1–4. DOI: 10.22489/CinC.2017.091-096.

[179] K. Mannapperuma, B.D. Holton, P.J. Lesniewski, and J.C. Thomas. "Performance limits of ICA-based heart rate identification techniques in imaging photoplethysmography." In: *Physiological measurement* 36.1 (2015), pp. 67–83. DOI: 10.1088/0967-3334/36/1/67.

[180] T. Matsuda and M. Makikawa. "ECG Monitoring of a Car Driver Using Capacitively-Coupled Electrodes." In: *Proc. 30th Annu. Int. Conf. IEEE Eng. Med. Biol. Soc. (EMBC)*. Vancouver, Canada, 2008, pp. 1315–1318. DOI: 10.1109/IEMBS.2008.4649406.

[181] D. McDuff, S. Gontarek, and R.W. Picard. "Remote Detection of Photoplethysmographic Systolic and Diastolic Peaks Using a Digital Camera." In: *IEEE Transactions on Biomedical Engineering* 61.12 (2014), pp. 2948–2954. DOI: 10.1109/TBME.2014.2340991.

[182] D.J. McDuff, J.R. Estepp, A.M. Piasecki, and E.B. Blackford. "A Survey of Remote Optical Photoplethysmographic Imaging Methods." In: *Proc. 37th Annu. Int. Conf. IEEE Eng. Med. Biol. Soc. (EMBC)*. Milan, Italy, 2015, pp. 6398–6404. DOI: 10.1109/EMBC.2015.7319857.

[183] R. McKendall and M. Mintz. "Robust Fusion of Location Information." In: *Proc. IEEE 1st Int. Conf. Robotics and Automation*. Philadelphia, USA, 1988, pp. 1239–1244. DOI: 10.1109/ROBOT.1988.12231.

[184] D.D. McManus, J. Lee, O. Maitas, N. Esa, R. Pidikiti, A. Carlucci, J. Harrington, E. Mick, and K.H. Chon. "A novel application for the detection of an irregular pulse using an iPhone 4S in patients with atrial fibrillation." In: *Heart Rhythm* 10.3 (2013), pp. 315–319. DOI: 10.1016/j.hrthm.2012.12.001.

[185] F.C. Meinecke, A. Ziehe, M. Kawanabe, and K.R. Müller. "Estimating the reliability of ICA projections." In: *Advances in Neural Information Processing Systems*. Ed. by M.I. Jordan. 2001, pp. 1181–1188. ISBN: 9780262561457.

[186] N. Meziane, J.G. Webster, M. Attari, and A.J. Nimunkar. "Dry electrodes for electrocardiography." In: *Physiological measurement* 34.9 (2013), R47–R69. DOI: 10.1088/0967-3334/34/9/R47.

[187] J.X. Mi. "A Novel Algorithm for Independent Component Analysis with Reference and Methods for Its Applications." In: *PLoS ONE* 9.5 (2014), e93984–1–13. DOI: 10.1371/journal.pone.0093984.

[188] M. Milanesi, N. Vanello, V. Positano, M. Santarelli, R. Paradiso, D. De Rossi, and L. Landini. "Frequency Domain Approach to Blind Source Separation in ECG Monitoring by Wearable System." In: *Proc. 32nd Computers in Cardiology (CinC)*. Vol. 32. Lyon, France, 2005, pp. 767–770. DOI: 10.1109/CIC.2005.1588217.

[189] M. Milanesi, N. Martini, N. Vanello, V. Positano, M. Santarelli, and L. Landini. "Independent component analysis applied to the removal of motion artifacts from electrocardiographic signals." In: *Medical & Biological Engineering & Computing* 46.3 (2008), pp. 251–261. DOI: 10.1007/s11517-007-0293-8.

[190] H.B. Mitchell. *Multi-Sensor Data Fusion: An Introduction*. 1st. Berlin, Heidelberg, New York: Springer-Verlag, 2007, p. 281. ISBN: 9783540714637.

[191] A.V. Moço, S. Stuijk, and G. De Haan. "Ballistocardiographic Artifacts in PPG Imaging." In: *IEEE Transactions on Biomedical Engineering* 63.9 (2016), pp. 1804–1811. DOI: 10.1109/TBME.2015.2502398.

[192] A.V. Moço, S. Stuijk, and G. de Haan. "Motion robust PPG-imaging through color channel mapping." In: *Biomedical Optics Express* 7.5 (2016), pp. 1737–1754. DOI: 10.1364/BOE.7.001737.

[193] H. Molitor and M. Kniazuk. "A New Bloodless Method for Continuous Recording of Periphal Circulatory Changes." In: *Journal of Pharmacology and Experimental Therapeutics* 57.1 (1936), pp. 6–18. ISSN: 0022-3565.

[194] G.B. Moody and R.G. Mark. "The impact of the MIT-BIH arrhythmia database." In: *IEEE Engineering in Medicine and Biology Magazine* 20.3 (2001), pp. 45–50. DOI: 10.1109/51.932724.

[195] D. Morris, T.S. Saponas, D.S. Tan, M. Dixon, S. Khullar, and H. Vathsangam. *Patent Application WO2014137768A1: Determining pulse transit time non-invasively using handheld devices*. 2014.

[196] J. Muhuthuswamy. "Biomedical Signal Analysis." In: *Standard Handbook of Biomedical Engineering and Design*. New York, Chicago, San Francisco, Lisbon et al.: The McGraw-Hill Companies, Inc., 2003. Chap. 18, p. 30. ISBN: 9780071356374.

[197] J.H. Nagel. "Biopotential Amplifiers." In: *The Biomedical Engineering Handbook, Two Volume Set*. Ed. by J.D. Bronzino. 2nd. Boca Raton: CRC Press LLC, 1999. Chap. 70, p. 14. ISBN: 9781420049510.

[198] S. Nakagawa and I.C. Cuthill. "Effect size, confidence interval and statistical significance: A practical guide for biologists." In: *Biological Reviews* 82.4 (2007), pp. 591–605. DOI: 10.1111/j.1469-185X.2007.00027.x.

[199] M.R. Neumann. "Biopotential Electrodes." In: *The Biomedical Engineering Handbook, Two Volume Set*. Ed. by J.D. Bronzino. 2nd. Boca Raton: CRC Press LLC, 1999. Chap. 48, p. 12. ISBN: 9781420049510.

[200] I. Nishidate, A. Hoshi, Y. Aoki, K. Nakano, K. Niizeki, and Y. Aizu. "Noncontact imaging of plethysmographic pulsation and spontaneous low-frequency oscillation in skin perfusion with a digital red-green-blue camera." In: *Proc. Dynamics and Fluctuations in Biomedical Photonics (SPIE 9707)*. Vol. 9707. San Francisco, USA, 2016, pp. 97070L–1–9. DOI: 10.1117/12.2212558.

[201] M. Oehler, V. Ling, K. Melhorn, and M. Schilling. "A multichannel portable ECG system with capacitive sensors." In: *Physiological measurement* 29.7 (2008), pp. 783–793. DOI: 10.1088/0967-3334/29/7/007.

[202] C. Orphanidou, S. Fleming, S. A. Shah, and L. Tarassenko. "Data fusion for estimating respiratory rate from a single-lead ECG." In: *Biomedical Signal Processing and Control* 8.1 (2013), pp. 98–105. DOI: 10.1016/j.bspc.2012.06.001.

[203] N. Östlund, J. Yu, and J.S. Karlsson. "Adaptive spatio-temporal filtering of multichannel surface EMG signals." In: *Medical & Biological Engineering & Computing* 44.3 (2006), pp. 209–215. DOI: 10.1007/s11517-006-0029-1.

[204] N. Östlund, U. Wiklund, J. Yu, and J.S. Karlsson. "Adaptive spatio-temporal filtration of bioelectrical signals." In: *Proc. 27th Annu. Int. Conf. IEEE Eng. Med. Biol. Soc. (EMBC)*. Vol. 27. Shanghai, China, 2005, pp. 5983–5986. DOI: 10.1109/IEMBS.2005.1615854.

[205] J. Ottenbacher, M. Kirst, L. Jatobá, M. Huflejt, U. Grossmann, and W. Stork. "Reliable Motion Artifact Detection for ECG Monitoring Systems with Dry Electrodes." In: *Proc. 30th Annu. Int. Conf. IEEE Eng. Med. Biol. Soc. (EMBC)*. Vancouver, Canada, 2008, pp. 1695–1698. DOI: 10.1109/IEMBS.2008.4649502.

[206] F.Z. Padmadinata, J.J. Veerhoek, G.J.A. van Dijk, and J.H. Huijsing. "Microelectronic skin electrode." In: *Sensors and Actuators: B. Chemical* 1.1-6 (1990), pp. 491–494. DOI: 10.1016/0925-4005(90)80257-Z.

[207] P.J. Pan and W.J. Tompkins. "A Real-Time QRS Detection Algorithm." In: *IEEE Transactions on Biomedical Engineering* 32.3 (1985), pp. 230–236. DOI: 10.1109/TBME.1985.325532.

[208] H.C. Pape, A. Kurtz, and S. Silbernagl. *Physiologie*. 7th. Stuttgart, New York, Delhi and Rio: Thieme Verlagsgruppe, 2014, p. 1026. ISBN: 9783131950772. DOI: 10.1055/b-002-98019.

[209] R. Paradiso, G. Loriga, and N. Taccini. "A Wearable Health Care System Based on Knitted Integrated Sensors." In: *IEEE Transactions on Information Technology in Biomedicine* 9.3 (2005), pp. 337–344. DOI: 10.1109/TITB.2005.854512.

[210] M.S. Pedersen, J. Larsen, U. Kjems, and L.C. Parra. "A Survey of Convolutive Blind Source Separation Methods." In: *Springer Handbook of Speech Processing*. 1st. Berlin, Heidelberg: Springer-Verlag, 2007, pp. 1065–1094. DOI: 10.1007/978-3-540-49127-9_52.

[211] D.T. Pham. "Joint Approximate Diagonalization of Positive Definite Hermitian Matrices." In: *SIAM Journal on Matrix Analysis and Applications* 22.4 (2001), pp. 1136–1152. DOI: 10.1137/S089547980035689X.

[212] M.Z. Poh, D.J. McDuff, and R.W. Picard. "Non-contact, automated cardiac pulse measurements using video imaging and blind source separation." In: *Optics Express* 18.10 (2010), pp. 10762–10774. DOI: 10.1364/OE.18.010762.

[213] M.Z. Poh, D.J. McDuff, and R.W. Picard. "Advancements in Noncontact, Multiparameter Physiological Measurements Using a Webcam." In: *IEEE Transactions on Biomedical Engineering* 58.1 (2011), pp. 7–11. DOI: 10.1109/TBME.2010.2086456.

[214] M.Z. Poh and Y.C. Poh. "Validation of a Standalone Smartphone Application for Measuring Heart Rate Using Imaging Photoplethysmography." In: *Telemedicine and e-Health* 23.8 (2017), pp. 1–6. DOI: 10.1089/tmj.2016.0230.

[215] H. Qi, X. Chen, and Z.J. Wang. "Non-contact Driver Cardiac Physiological Monitoring Using Video Data." In: *Proc. 3rd IEEE China Summit Int. Conf. Signal and Information Processing (ChinaSIP)*. Vol. 3. Chengdu, China, 2015, pp. 418–423. DOI: 10.1109/ChinaSIP.2015.7230436.

[216] H. Qi, Z. Guo, X. Chen, Z. Shen, and Z.J. Wang. "Video-based human heart rate measurement using joint blind source separation." In: *Biomedical Signal Processing and Control* 31 (2017), pp. 309–320. DOI: 10.1016/j.bspc.2016.08.020.

[217] S. Rasche, A. Trumpp, T. Waldow, F. Gaetjen, K. Plötze, D. Wedekind, M. Schmidt, H. Malberg, K. Matschke, and S. Zaunseder. "Camera-based photoplethysmography in critical care patients." In: *Clinical Hemorheology and Microcirculation* 64.1 (2016), pp. 77–90. DOI: 10.3233/CH-162048.

[218] A. Rashid, I.M. Qureshi, and A. Saleem. "Electrocardiogram signal processing for baseline noise removal using blind source separation techniques: A comparative analysis." In: *Proc. 4th Int. Conf. Mach. Learn. Cybern. (ICMLC)*. Guilin, China, 2011, pp. 1756–1761. DOI: 10.1109/ICMLC.2011.6016962.

[219] J.M. Richardson and K.A. Marsh. "Fusion of Multisensor Data." In: *The International Journal of Robotics Research* 7.6 (1988), pp. 78–96. DOI: 10.1177/027836498800700607.

[220] P.C. Richardson. "The insulated electrod: A pasteless electrocardiographic technique." In: *Proc. 20th Annu. Conf. Eng. Med. Biol.* Vol. 9. Boston, USA, 1967, pp. 15–17.

[221] P.C. Richardson, F.K. Coombs, and R.M. Adams. "Some new electrode techniques for long-term physiologic monitoring." In: *Aerospace Medicine* 39.7 (1968), pp. 745–750. ISSN: 0001-9402.

[222] J.J. Rieta, F. Castells, C. Sánchez, V. Zarzoso, and J. Millet. "Atrial Activity Extraction for Atrial Fibrillation Analysis Using Blind Source Separation." In: *IEEE Transactions on Biomedical Engineering* 51.7 (2004), pp. 1176–1186. DOI: 10.1109/TBME.2004.827272.

[223] R. Sameni. *The Open-Source Electrophyiological Toolbox (OSET), version 2.1 (www.oset.ir)*. 2010.

[224] R. Sameni, C. Jutten, and M.B. Shamsollahi. "Multichannel electrocardiogram decomposition using periodic component analysis." In: *IEEE Transactions on Biomedical Engineering* 55.8 (2008), pp. 1935–1940. DOI: 10.1109/TBME.2008.919714.

[225] R. Sameni, M.B. Shamsollahi, C. Jutten, and M. Babaie-Zadeh. "Filtering noisy ECG signals using the extended kalman filter based on a modified dynamic ECG model." In: *Proc. 32nd Computers in Cardiology (CinC)*. Lyon, France, 2005, pp. 1017–1020. DOI: 10.1109/CIC.2005.1588283.

[226] L.K. Saul, J.B. Allen, T. Labs, P. Ave, and F. Park. "Periodic Component Analysis : An Eigenvalue Method for Representing Periodic Structure in Speech." In: *Advances in Neural Information Processing Systems 13: Proc. 14th Ann. Conf. Neural Information Processing Systems (NIPS)*. Vol. 13. Denver, USA, 2000, pp. 807–813. ISBN: 9780262122412.

[227] J. Schumm, C. Setz, M. Bächlin, M. Bächler, B. Arnrich, and G. Tröster. "Unobtrusive physiological monitoring in an airplane seat." In: *Personal and Ubiquitous Computing* 14.6 (2010), pp. 541–550. DOI: 10.1007/s00779-009-0272-1.

[228] E.P. Scilingo, A. Gemignani, R. Paradiso, N. Taccini, B. Ghelarducci, and D. De Rossi. "Performance Evaluation of Sensing Fabrics for Monitoring Physiological and Biomechanical Variables." In: *IEEE Transactions on Information Technology in Biomedicine* 9.3 (2005), pp. 345–352. DOI: 10.1109/TITB.2005.854506.

[229] C.G. Scully, J. Lee, J. Meyer, A.M. Gorbach, D. Granquist-Fraser, Y. Mendelson, and K.H. Chon. "Physiological Parameter Monitoring from Optical Recordings With a Mobile Phone." In: *IEEE Transactions on Biomedical Engineering* 59.2 (2012), pp. 303–306. DOI: 10.1109/TBME.2011.2163157.

[230] A. Searle and L. Kirkup. "A direct comparison of wet, dry and insulating bioelectric recording electrodes." In: *Physiological measurement* 21.2 (2000), pp. 271–283. DOI: 10.1088/0967-3334/21/2/307.

[231] D. Shao, Y. Yang, C. Liu, F. Tsow, H. Yu, and N. Tao. "Noncontact Monitoring Breathing Pattern, Exhalation Flow Rate and Pulse Transit Time." In: *IEEE Transactions on Biomedical Engineering* 61.11 (2014), pp. 2760–2767. DOI: 10.1109/TBME.2014.2327024.

[232] D. Shao, F. Tsow, C. Liu, Y. Yang, and N. Tao. "Simultaneous Monitoring of Ballistocardiogram and Photoplethysmogram Using Camera." In: *IEEE Transactions on Biomedical Engineering* prior Epub (2016), pp. 1–9. DOI: 10.1109/TBME.2016.2585109.

[233] P. Shi, V.A. Peris, A. Echiadis, J. Zheng, Y.S. Zhu, P.Y.S. Cheang, and S.J. Hu. "Non-contact Reflection Photoplethysmography Towards Effective Human Physiological Monitoring." In: *Journal of Medical and Biological Engineering* 30.3 (2010), pp. 161–167. ISSN: 1609-0985.

[234] I.S. Sidorov, R.V. Romashko, V.T. Koval, R. Giniatullin, and A.A. Kamshilin. "Origin of infrared light modulation in reflectance-mode photoplethysmography." In: *PLoS ONE* 11.10 (2016), pp. 1–11. DOI: 10.1371/journal.pone.0165413.

[235] P. Smaragdis. "Blind separation of convolved mixtures in the frequency domain." In: *Neurocomputing* 22.1-3 (1998), pp. 21–34. DOI: 10.1016/S0925-2312(98)00047-2.

[236] A. Sološenko, A. Petrėnas, V. Marozas, and L. Sörnmo. "Modeling of the photoplethysmogram during atrial fibrillation." In: *Computers in Biology and Medicine* 81 (2017), pp. 130–138. DOI: 10.1016/j.compbiomed.2016.12.016.

[237] L. Sörnmo and P. Laguna. *Bioelectrical signal processing in cardiac and neurological applications*. 1st. Burlington, San Diego, London: Elsevier Academic Press, 2005, p. 688. ISBN: 9780124375529.

[238] E. Spinelli and M. Haberman. "Insulating electrodes: a review on biopotential front ends for dielectric skin-electrode interfaces." In: *Physiological measurement* 31.10 (2010), S183–S198. DOI: 10.1088/0967-3334/31/10/S03.

[239] S. Šprager and D. Zazula. "Optimization of heartbeat detection in fiber-optic unobtrusive measurements by using maximum a posteriori probability estimation." In: *IEEE Journal of Biomedical and Health Informatics* 18.4 (2014), pp. 1161–1168. DOI: 10.1109/JBHI.2013.2282403.

[240] H. Stögbauer, A. Kraskov, S.A. Astakhov, and P. Grassberger. "Least-dependent-component analysis based on mutual information." In: *Physical Review E* 70.6 (2004), pp. 66123–1–18. DOI: 10.1103/PhysRevE.70.066123.

[241] R. Stricker, S. Müller, and H.M. Gross. "Non-contact Video-based Pulse Rate Measurement on a Mobile Service Robot." In: *Proc. 23rd IEEE Int. Symp. Robot and Human Interactive Communication (RO-MAN)*. Edinburgh, Scotland, 2014, pp. 1056–1062. DOI: 10.1109/ROMAN.2014.6926392.

[242] Y. Sun and N. Thakor. "Photoplethysmography Revisited: From Contact to Noncontact, from Point to Imaging." In: *IEEE Transactions on Biomedical Engineering* 63.3 (2016), pp. 463–477. DOI: 10.1109/TBME.2015.2476337.

[243] Y. Sun, S. Hu, V. Azorin-Peris, S. Greenwald, J. Chambers, and Y. Zhu. "Motion-compensated noncontact imaging photoplethysmography to monitor cardiorespiratory status during exercise." In: *Journal of Biomedical Optics* 16.7 (2011), 077010 (1–10). DOI: 10.1117/1.3602852.

[244] Y. Sun, C. Papin, V. Azorin-Peris, R. Kalawsky, S. Greenwald, and S. Hu. "Use of ambient light in remote photoplethysmographic systems: comparison between a high-performance camera and a low-cost webcam." In: *Journal of Biomedical Optics* 17.3 (2012), 037005 (1–11). DOI: 10.1117/1.JBO.17.3.037005.

[245] Y. Sun, S. Hu, V. Azorin-Peris, R. Kalawsky, and S. Greenwald. "Noncontact imaging photoplethysmography to effectively access pulse rate variability." In: *Journal of Biomedical Optics* 18.6 (2013), 061205 (1–10). DOI: 10.1117/1.JBO.18.6.061205.

[246] C. Takano and Y. Ohta. "Heart rate measurement based on a time-lapse image." In: *Medical Engineering and Physics* 29.8 (2007), pp. 853–857. DOI: 10.1016/j.medengphy.2006.09.006.

[247] T. Takatani, T. Nishikawa, H. Saruwatari, and K. Shikano. "SIMO-Model-Based Independent Component Analysis for High-Fidelity Blind Separation of Acoustic Signals." In: *Proc. 4th Int. Symp. ICA and BSS (ICA2003)*. Nara, Japan, 2003, pp. 993–998. ISBN: 4990153111.

[248] T. Tanaka and A. Cichocki. "Subband Decomposition Independent Component Analysis And New Performance Criteria." In: *Proc. 5th Int. Conf. Acoustics, Speech, and Signal Processing (ICASSP'04)*. Montreal, Quebec, Canada, 2004, pp. 541–544. DOI: 10.1109/ICASSP.2004.1327167.

[249] J.M. Tanskanen, J.J. Viik, and J.A. Hyttinen. "Independent component analysis of parameterized ECG signals." In: *Proc. 28th Annu. Int. Conf. IEEE Eng. Med. Biol. Soc. (EMBC)*. New York, USA, 2006, pp. 5704–5707. DOI: 10.1109/IEMBS.2006.260345.

[250] L. Tarassenko, L. Mason, and N. Townsend. "Multi-sensor fusion for robust computation of breathing rate." In: *Electronics Letters* 38.22 (2002), pp. 1314–1316. DOI: 10.1049/el:20020773.

[251] L. Tarassenko, M. Villarroel, A. Guazzi, J. Jorge, D.A. Clifton, and C. Pugh. "Noncontact video-based vital sign monitoring using ambient light and auto-regressive models." In: *Physiological measurement* 35.5 (2014), pp. 807–831. DOI: 10.1088/0967-3334/35/5/807.

[252] H.E. Tasli, A. Gudi, and M.D. Uyl. "Remote PPG Vased Vital Sign Measurement Using Adaptive Facial Regions." In: *Proc. 16th Int. Conf. Image Processing (ICIP)*. Paris, France, 2014, pp. 1–5. DOI: 10.1109/ICIP.2014.7025282.

[253] N.V. Thakor. "Biopotentials and Electrophysiology Measurement." In: *The Measurement, Instrumentation, and Sensors Handbook*. Ed. by J.G. Webster. 1st. Boca Raton: CRC Press LLC, 1999. Chap. 74. DOI: 10.1201/9780415876179.ch74.

[254] F.J. Theis. "Multidimensional Independent Component Analysis Using Characteristic Functions." In: *Proc. 13th IEEE Europ. Conf. Signal Processing*. Antalya, Turkey, 2005, pp. 1941–1944. ISBN: 9781604238211.

[255] A. Trumpp, H. Malberg, and S. Zaunseder. "Signal extraction in camera-based photoplethysmography using a modified Wiener filter." In: *Proc. 5th Dresdner Medizintechnik Symposium*. Dresden, Germany, 2014, pp. 105–107. ISBN: 9783956630187.

[256] A. Trumpp, S. Rasche, D. Wedekind, M. Rudolf, H. Malberg, K. Matschke, and S. Zaunseder. "Relation between pulse pressure and the pulsation strength in camera-based photoplethysmograms." In: *Current Directions in Biomedical Engineering* 3.2 (2017), pp. 489–492. ISSN: 2364-5504. DOI: 10.1515/cdbme-2017-0184.

[257] A. Trumpp, P. Bauer, S. Rasche, H. Malberg, and S. Zaunseder. "The Value of Polarization in Camera-Based Photoplethysmography accepted." In: *Biomedical Optics Express* 8.6 (2017), pp. 1124–1135. DOI: 10.1364/BOE.8.002822.

[258] G.R. Tsouri and M.H. Ostertag. "Patient-specific 12-lead ECG reconstruction from sparse electrodes using independent component analysis." In: *IEEE Journal of Biomedical and Health Informatics* 18.2 (2014), pp. 476–482. DOI: 10.1109/JBHI.2013.2294561.

[259] G.R. Tsouri, S. Kyal, S. Dianat, and L.K. Mestha. "Constrained independent component analysis approach to nonobtrusive pulse rate measurements." In: *Journal of Biomedical Optics* 17.7 (2012), pp. 077011–1–5. DOI: 10.1117/1.JBO.17.7.077011.

[260] G. Uppal, N.R. Prakash, and P. Kalra. "Heart Rate Measurement Using Facial Videos." In: *Advances in Computational Sciences and Technology* 10.8 (2017), pp. 2345–2358. ISSN: 0973-6107.

[261] S. Valaee and P. Kabal. "An Information Theoretic Approach to Source Enumeration in Array Signal Processing." In: *IEEE Transactions on Signal Processing* 52.5 (2004), pp. 1171–1178. DOI: 10.1109/TSP.2004.826168.

[262] M Varanini, G Tartarisco, L Billeci, A Macerata, G Pioggia, and R Balocchi. "A multi-step approach for non-invasive fetal ECG analysis." In: *Proc. 40th Computing in Cardiology Conf. (CinC)*. Zaragoza, Spain, 2013, pp. 281–284.

[263] S.V. Vaseghi. *Advanced Digital Signal Processing and Noise Reduction*. 4th. Chichester, New York, Weinheim et al.: John Wiley & Sons, Ltd, 2009, p. 544. ISBN: 9780470754061. DOI: 10.1002/9780470740156.

[264] C. Vayá, J.J. Rieta, C. Sánchez, and D. Moratal. "Performance Study of Convolutive BSS Algorithms Applied to the Electrocardiogram of Atrial Fibrillation." In: *Proc. 6th Int. Conf. Independent Component Analysis and Blind Source Separation (ICA)*. Charleston, USA, 2006, pp. 495–502. DOI: 10.1007/11679363_62.

[265] W. Verkruysse, L.O. Svaasand, and J. Stuart Nelson. "Remote plethysmographic imaging using ambient light." In: *Optics Express* 16.26 (2008), pp. 21434–21445. DOI: 10.1364/OE.16.021434.

[266] V. Vidhya and D. Unnikrishnan. "Synthetic ECG and PPG signal generation using pulse shaping technique." In: *Proc. 12th IEEE Annu. India Conf. on Electronics, Energy, Environment, Communication, Computer, Control: (INDICON)*. New Delhi, India, 2015, pp. 1–6. DOI: 10.1109/INDICON.2015.7443256.

[267] M. Villarroel, J. Jorge, C. Pugh, and L. Tarassenko. "Non-Contact Vital Sign Monitoring in the Clinic." In: *Proc. 12th IEEE Int. Conf. Automatic Face & Gesture Recognition (FG)*. Washington, USA, 2017, pp. 278–285. DOI: 10.1109/FG.2017.43.

[268] E. Vincent, R. Gribonval, and C. Févotte. "Performance Measurement in Blind Audio Source Separation." In: *IEEE Transaction on Audio, Speech, and Language Processing* 14.4 (2006), pp. 1462–1469. DOI: 10.1109/TSA.2005.858005.

[269] R. Vullings, B. De Vries, and J.W.M. Bergmans. "An adaptive Kalman filter for ECG signal enhancement." In: *IEEE Transactions on Biomedical Engineering* 58.4 (2011), pp. 1094–1103. DOI: 10.1109/TBME.2010.2099229.

[270] S.E. Walsh. "Some Nonparametric Tests of whether the Largest Observations of a Set are too Large or too Small." In: *Annals of Mathematical Statistics* 21.4 (1950), pp. 583–592. DOI: doi:10.1214/aoms/1177729753.

[271] M. Walter, B. Eilebrecht, T. Wartzek, and S. Leonhardt. "The smart car seat: Personalized monitoring of vital signs in automotive applications." In: *Personal and Ubiquitous Computing* 15.7 (2011), pp. 707–715. DOI: 10.1007/s00779-010-0350-4.

[272] L. Wang, L. Xu, S. Feng, M.Q.H. Meng, and K. Wang. "Multi-Gaussian fitting for pulse waveform using Weighted Least Squares and multi-criteria decision making method." In: *Computers in Biology and Medicine* 43.11 (2013), pp. 1661–1672. DOI: 10.1016/j.compbiomed.2013.08.004.

[273] W. Wang, S. Stuijk, and G. de Haan. "Exploiting Spatial Redundancy of Image Sensor for Motion Robust rPPG." In: *IEEE Transactions on Biomedical Engineering* 62.2 (2015), pp. 415–425. DOI: 10.1109/TBME.2014.2356291.

[274] W. Wang, B.D. Brinker, S. Stuijk, and G. de Haan. "Algorithmic Principles of Remote-PPG." In: *IEEE Transactions on Biomedical Engineering* 64.7 (2016), pp. 1479 –1491. DOI: 10.1109/TBME.2016.2609282.

[275] W. Wang, A.C. den Brinker, S. Stuijk, and G. de Haan. "Amplitude-selective filtering for remote-PPG." In: *Biomedical Optics Express* 8.3 (2017), pp. 1965–1980. DOI: 10.1364/BOE.8.001965.

[276] T. Wartzek, R. Elfring, A. Janssen, B. Eilebrecht, M. Walter, and S. Leonhardt. "On the Way to a Cable Free Operating Theater: An Operating Table with Integrated Multimodal Monitoring Methods Multimodal sensor." In: *Proc. 38th Computing in Cardiology Conf. (CinC)*. Hangzhou, China, 2011, pp. 129–132. ISBN: 9781457706127.

[277] T. Wartzek, T. Lammersen, B. Eilebrecht, M. Walter, and S. Leonhardt. "Triboelectricity in Capacitive Biopotential Measurements." In: *IEEE Transactions on Biomedical Engineering* 58.5 (2011), pp. 1268–1277. DOI: 10.1109/TBME.2010.2100393.

[278] T. Wartzek, C. Bruser, M. Walter, and S. Leonhardt. "Robust Sensor Fusion of Unobtrusively Measured Heart Rate." In: *IEEE Journal of Biomedical and Health Informatics* 18.2 (2014), pp. 654–660. DOI: 10.1109/JBHI.2013.2274211.

[279] M. Wax and T. Kailath. "Detection of signals by information theoretic criteria." In: *Acoustics, Speech and Signal Processing* 33.2 (1985), pp. 387–392. DOI: 10.1109/TASSP.1985.1164557.

[280] J.G. Webster, J.W. Clark, M.R. Neuman, W.H. Olson, R.A. Peura, F.P. Primiano, M.P. Siedband, and L.A. Wheeler. *Medical Instrumentation: Application and Design*. Ed. by J.G. Webster. 4th. Hoboken, USA: Jon Wiley & Sons, Inc., 2010, p. 736. ISBN: 97804716760003.

[281] D. Wedekind, H. Malberg, and S. Zaunseder. "Cascaded Output Selection for Processing of Capacitive Electrocardiograms by Means of Independent Component Analysis." In: *Proc. 8th Int. Workshop Sensor Data Fusion (SDF)*. Bonn, Germany, 2013, pp. 1–6. DOI: 10.1109/SDF.2013.6698267.

[282] D. Wedekind, H. Malberg, and S. Zaunseder. "Processing of Capacitive Electrocardiograms by Back Transformation of Selected Independent Components." In: *Proc. Workshop Innovative Verarbeitung bioelektrischer und biomagnetischer Signale (BBS)*. Berlin, Germany, 2014, pp. 31–32.

[283] D. Wedekind, A. Trumpp, F. Andreotti, F. Gaetjen, S. Rasche, K. Matschke, H. Malberg, and S. Zaunseder. "Assessment of Source Separation Techniques to Extract Vital Parameters from Videos." In: *Proc. 23rd European Conference on Signal Processing (EUSIPCO)*. Nice, France, 2015, pp. 434–438. DOI: 10.1109/EUSIPCO.2015.7362420.

[284] D. Wedekind, F. Gaetjen, S. Rasche, K. Matschke, H. Malberg, and S. Zaunseder. "Automated Identification of Cardiac Signals after Blind Source Separation for Camera-Based Photoplethysmography." In: *Proc. 35th Int. Conf. Electronics and Nanotechnology (ELNANO)*. Kyiv, Ukraine, 2015, pp. 422–427. DOI: 10.1109/ELNANO.2015.7146950.

[285] D. Wedekind, D. Kleyko, E. Osipov, H. Malberg, S. Zaunseder, and U. Wiklund. "Sparse Coding of Cardiac Signals for Automated Component Selection after Blind Source Separation." In: *Proc. 43rd Computing in Cardiology (CinC)*. Vancouver, Canada, 2016, pp. 1–4. DOI: 10.22489/CinC.2016.226-413.

[286] D. Wedekind, A. Trumpp, F. Gaetjen, S. Rasche, K. Matschke, H. Malberg, and S. Zaunseder. "Assessment of blind source separation techniques for video-based cardiac pulse extraction." In: *Journal of Biomedical Optics* 22.3 (2017), 035002 (1–14). DOI: 10.1117/1.JBO.22.3.035002.

[287] D. Wedekind, D. Kleyko, E. Osipov, H. Malberg, S. Zaunseder, and U. Wiklund. "Robust Methods for Automated Selection of Cardiac Signals after Blind Source Separation." In: *IEEE Transactions on Biomedical Engineering* 65.10 (2018), pp. 2248–2258. DOI: 10.1109/TBME.2017.2788701.

[288] B. Wei, C. Zhang, and X. Wu. "Comprehensive comparison study on different ICA/BSS methods in IPPG techniques for obtaining high-quality BVP signal." In: *Proc. 5th Int. Conf. Intelligent Information Processing (ICIIP)*. Beijing, China, 2016. DOI: 10.1145/3028842.3028890.

[289] F.P. Wieringa, F. Mastik, and A.F.W. van der Steen. "Contactless Multiple Wavelength Photoplethysmographic Imaging: A First Step Toward "SpO2 Camera" Technology." In: *Annals of Biomedical Engineering* 33.8 (2005), pp. 1034–1041. DOI: 10.1007/s10439-005-5763-2.

[290] U. Wiklund, M. Karlsson, N. Östlund, L. Berglin, K. Lindecrantz, S. Karlsson, and L. Sandsjö. "Adaptive spatio-temporal filtering of disturbed ECGs: a multi-channel approach to heartbeat detection in smart clothing." In: *Medical & Biological Engineering & Computing* 45.6 (2007), pp. 515–523. DOI: 10.1007/s11517-007-0183-0.

[291] J.O. Wisbeck, A.K. Barros, A.K.B. Yy, and R.G. Ojeda. "Application of ICA in the Separation of Breathing Artifacts in ECG Signals." In: *Proc. Int. Conf. Neural Information Processing (ICONIP)*. Kitakyushu, Japan, 1998, pp. 211–214. ISBN: 9784274902598.

[292] B.F. Wu, Y.W. Chu, P.W. Huang, M.L. Chung, and T.M. Lin. "A Motion Robust Remote-PPG Approach to Driver's Health State Monitoring." In: *Proc. 4th Asian Conf. Computer Vision Workshops (ACCV)*. Taipei, Taiwan, 2016, pp. 463–476. DOI: 10.1007/978-3-319-54407-6_31.

[293] H.Y. Wu, M. Rubinstein, E. Shih, J. Guttag, F. Durand, and W. Freeman. "Eulerian video magnification for revealing subtle changes in the world." In: *ACM Transactions on Graphics* 31.4 (2012), pp. 1–8. DOI: 10.1145/2185520.2185561.

[294] K.F. Wu and Y.T. Zhang. "Contactless and Continuous Monitoring of Heart Electric Activities through Clothes on a Sleeping Bed." In: *Proc. 5th Int. Conf. Technol. Appl. Biomed. (ITAB2008)*. Shenzhen, China, 2008, pp. 282–285. DOI: 10.1109/ITAB.2008.4570586.

[295] T. Wu, V. Blažek, and H.J. Schmitt. "Photoplethysmography Imaging: A New Noninvasive and Non-contact Method for Mapping of the Dermal Perfusion Changes." In: *Proc. Optical Techniques and Instrumentation for the Measurement of Blood Composition, Structure, and Dynamics 2000 (SPIE 4163)*. Amsterdam, The Netherlands, 2000, pp. 62–70. DOI: 10.1117/12.407646.

[296] H.H. Yang and S.I. Amari. "Adaptive Online Learning Algorithms for Blind Separation: Maximum Entropy and Minimum Mutual Information." In: *Neural Computation* 9.7 (1997), pp. 1457–1482. DOI: 10.1162/neco.1997.9.7.1457.

[297] L. Yang, M. Liu, L. Dong, Y. Zhao, and X. Liu. "Motion-compensated non-contact detection of heart rate." In: *Optics Communications* 357 (2015), pp. 161–168. DOI: 10.1016/j.optcom.2015.08.017.

[298] P. Yang, G.A. Dumont, and J.M. Ansermino. "Sensor fusion using a hybrid median filter for artifact removal in intraoperative heart rate monitoring." In: *Journal of Clinical Monitoring and Computing* 23.2 (2009), pp. 75–83. DOI: 10.1007/s10877-009-9163-2.

[299] W. Ye, S. Li, X. Wu, and J. Ye. "Detection of Multilead ECG Character Points and Assessment Based on a Reference Database." In: *Proc. 27rd Annu. Int. Conf. IEEE Eng. Med. Biol. Soc. (EMBC)*. Shanghai, China, 2005, pp. 3895–3898. DOI: 10.1109/IEMBS.2005.1615312.

[300] M.A. Yokus and J.S. Jur. "Fabric-Based Wearable Dry Electrodes for Body Surface Biopotential Recording." In: *IEEE Transactions on Biomedical Engineering* 63.2 (2015), pp. 423–430. DOI: 10.1109/TBME.2015.2462312.

[301] G. Yoon, J.Y. Lee, K.J. Jeon, K.K. Park, and H.S. Kim. "Development of a Compact Home Health Monitor for Telemedicine." In: *Telemedicine and e-Health* 11.6 (2005), pp. 660–667. DOI: 10.1089/tmj.2005.11.660.

[302] N. Zaproudina, V. Teplov, E. Nippolainen, J.A. Lipponen, A.A. Kamshilin, M. Närhi, P.A. Karjalainen, and R. Giniatullin. "Asynchronicity of Facial Blood Perfusion in Migraine." In: *PLoS ONE* 8.12 (2013), e80189 (1–9). DOI: 10.1371/journal.pone.0080189.

[303] S. Zaunseder, A. Henning, D. Wedekind, A. Trumpp, and H. Malberg. "Unobtrusive acquisition of cardiorespiratory signals. Available techniques and perspectives for sleep medicine." In: *Somnologie* 2 (2017), pp. 1–8. DOI: 10.1007/s11818-017-0112-x.

[304] S. Zaunseder, A. Trumpp, D. Wedekind, and H. Malberg. "Cardiovascular assessment by imaging photoplethysmography-a review." In: *Biomedizinische Technik* 63.5 (2018), pp. 529–535. DOI: 10.1515/bmt-2017-0119.

[305] Q. Zhang, Q. Wu, Y. Zhou, X. Wu, Y. Ou, and H. Zhou. "Webcam-based, non-contact, real-time measurement for the physiological parameters of drivers." In: *Measurement* 100 (2017), pp. 311–321. DOI: 10.1016/j.measurement.2017.01.007.

[306] Z. Zhang, C. Lall, and Y. Chen. "Stability Analysis of QRS Features to Evaluate Signal Quality For Multi-lead QRS Dectection." In: *Proc. 33rd Annu. Int. Conf. IEEE Eng. Med. Biol. Soc. (EMBC)*. Boston, USA, 2011, pp. 3768–3771. DOI: 10.1109/IEMBS.2011.6090643.

[307] F. Zhao, M. Li, Y. Qian, and J.Z. Tsien. "Remote Measurements of Heart and Respiration Rates for Telemedicine." In: *PLoS ONE* 8.10 (2013), e71384 (1–14). DOI: 10.1371/journal.pone.0071384.

[308] Y.L. Zheng, X.R. Ding, C.C.Y. Poon, B.Pi.L. Lo, H. Zhang, X.L. Zhou, G.Z. Yang, N. Zhao, and Y.T. Zhang. "Unobtrusive Sensing and Wearable Devices for Health Informatics." In: *IEEE Transactions on Biomedical Engineering* 61.5 (2014), pp. 1538–1554. DOI: 10.1109/TBME.2014.2309951.

[309] T. Zhu, A.E.W. Johnson, J. Behar, and G.D. Clifford. "Bayesian Voting of Multiple Annotators for Improved QT Interval Estimation." In: *Proc. 40th Computing in Cardiology, (CinC)*. Zaragoza, Spain, 2013, pp. 659–662.

[310] M. Zibulevsky and B.A. Pearlmutter. "Blind Source Separation by Sparse Decomposition in a Signal Dictionary." In: *Neural Computation* 13.4 (2001), pp. 863–882. DOI: 10.1162/089976601300014385.

[311] A. Ziehe and K.R. Müller. "TDSEP—an efficient algorithm for blind separation using time structure." In: *Proc. 8th Int. Conf. Artificial Neural Networks (ICANN)*. Skövde, Sweden, 1998, pp. 675–680. DOI: 10.1007/978-1-4471-1599-1_103.

[312] A. Ziehe, P. Laskov, K.R. Müller, and G. Nolte. "A linear least-squares algorithm for joint diagonalization." In: *Proc. 4th Int. Symp. Independent Component Analysis and Blind Signal Separation (ICA)*. Vol. 2. Nara, Japan, 2003, pp. 469–474. ISBN: 4990153103.

PUBLICATION LIST

Some ideas and figures have appeared previously in the following publications, I've contributed to as a first or co-working author:

[1] D. Wedekind, H. Malberg, and S. Zaunseder. "Cascaded Output Selection for Processing of Capacitive Electrocardiograms by Means of Independent Component Analysis" In: *Proc. 8th Int. Workshop Sensor Data Fusion (SDF)*. Bonn, Germany, 2013, pp. 1–6, *doi*: 10.1109/SDF.2013.6698267.

[2] F. Andreotti, M. Riedl, T. Himmelsbach, D. Wedekind, S. Zaunseder, N. Wessel, H. Malberg. "Maternal signal estimation by Kalman filtering and Template Adaptation for fetal heart rate extraction" In: *Proc. 40th Computing in Cardiology (CinC)*. Zaragoza, Spain, 2013, pp. 193-196, *ISBN*: 9781479908868.

[3] D. Wedekind, H. Malberg, and S. Zaunseder. "Processing of Capacitive Electrocardiograms by Back Transformation of Selected Independent Components" In: *Proc. Workshop Innovative Verarbeitung bioelektrischer und biomagnetischer Signale (BBS)*. Berlin, Germany, 2014, pp. 31-32.

[4] D. Wedekind, A. Trumpp, S. Zaunseder and H. Malberg. "CardioVisio - Non-contact estimation of hemodynamic quantities" In: *Poster at Bionection - Partnering Conference for Technology Transfer in Life Science*. Dresden, Germany, 2014.

[5] D. Wedekind, H. Malberg, and S. Zaunseder. "Cardiac Pulse Enhancement in Camera-Based Monitoring - A Spectral Analysis of Common Linear Transformations" In: *Proc. 5th Dresdner Medizintechnik Symposium (MTS)*. Dresden, Germany, 2014, pp. 108-110, *ISBN*: 9783956630187

[6] F. Andreotti, M. Riedl, T. Himmelsbach, D. Wedekind, N. Wessel, H. Stepan, C. Schmieder, A. Jank, H. Malberg, and S. Zaunseder. "Robust fetal ECG extraction and detection from abdominal leads." In: *Physiological measurement* 35.8 (2014), pp. 1551–1567, *doi*: 10.1088/0967-3334/35/8/1551.

[7] D. Wedekind, F. Gaetjen, S. Rasche, K. Matschke, H. Malberg, and S. Zaunseder. "Automated Identification of Cardiac Signals after Blind Source Separation for Camera-Based Photoplethysmography" In: *Proc. 35th International Conference on Electronics and Nanotechnology (ELNANO)*. Kyiv, Ukraine, 2015, pp. 422–427, *doi*: 10.1109/ELNANO.2015.7146950.

[8] D. Wedekind, A. Trumpp, F. Andreotti, F. Gaetjen, S. Rasche, K. Matschke, H. Malberg, and S. Zaunseder. "Assessment of Source Separation Techniques to Extract Vital Parameters from Videos" In: *Proc. 23rd European Conference on Signal Processing (EUSIPCO)*. Nice, France, 2015, pp. 434–438, *doi*: 10.1109/EUSIPCO.2015.7362420.

[9] S. Zaunseder, F. Andreotti, A. Trumpp, D. Wedekind, and H. Malberg. "Real-time heart rate measurement from video recordings using different Kalman filter models" In: *Abstract at DGBMT Annual Conference (BMT)*. Lübeck, Germany, 2015.

[10] S. Rasche, A. Trumpp, T. Waldow, F. Gaetjen, K. Plötze, D. Wedekind, M. Schmidt, H. Malberg, K. Matschke, and S. Zaunseder. "Camera-based photoplethysmography in critical care patients" In: *Clinical Hemorheology and Microcirculation* 64.1 (2016), pp. 77–90, *doi*: 10.3233/CH-162048.

[11] D. Wedekind, D. Kleyko, E. Osipov, H. Malberg, S. Zaunseder, and U. Wiklund. "Sparse Coding of Cardiac Signals for Automated Component Selection after Blind Source Separation" In: *Proc. 43rd Computing in Cardiology (CinC)*. Vancouver, Canada, 2016, pp. 1–4, *doi*: 10.22489/CinC.2016.226-413.

[12] D. Wedekind, A. Trumpp, F. Gaetjen, S. Rasche, K. Matschke, H. Malberg, and S. Zaunseder. "Assessment of blind source separation techniques for video-based cardiac pulse extraction" In: *Journal of Biomedical Optics* 22.3 (2017), 035002 (1–14), *doi*: 10.1117/1.JBO.22.3.035002.

[13] A. Trumpp, S. Rasche, D. Wedekind, M. Schmidt, T. Waldow, F. Gaetjen, K. Plötze, H. Malberg, K. Matschke, S. Zaunseder. "Skin Detection and Tracking for Camera-Based Photoplethysmography Using a Bayesian Classifier and Level Set Segmentation" In: *Proc. Bildverarbeitung für die Medizin, Informatik aktuell*. Heidelberg, Germany, 2017, pp. 43-48, *doi*: 10.1007/978-3-662-54345-0_16.

[14] A. Trumpp, S. Rasche, D. Wedekind, M. Rudolf, H. Malberg, K. Matschke, S. Zaunseder. "Relation between pulse pressure and the pulsation strength in camera-based photoplethysmograms" In: *Current Directions in Biomedical Engineering* 3.2 (2017), pp. 489-492, *doi*: 10.1515/cdbme-2017-0184.

[15] S. Zaunseder, A. Henning, D. Wedekind, A. Trumpp, H. Malberg. "Unobtrusive acquisition of cardiorespiratory signals. Available techniques and perspectives for sleep medicine" In: *Somnologie* 21.2 (2017), pp 93-100, *doi*: 10.1007/s11818-017-0112-x.

[16] M. Schubert, S. Friedrich, K. Bock, D. Wedekind, S. Zaunseder, H. Malberg. "3D printed flexible substrate with pneumatic driven electrodes for health monitoring" In: *Proc. 21st European Microelectronics and Packaging Conference (EMPC) & Exhibition*. Warsaw, Poland, 2017, pp. 1-5, *doi*: 10.23919/EMPC.2017.8346846.

[17] D. Wedekind, D. Kleyko, E. Osipov, H. Malberg, S. Zaunseder, and U. Wiklund. "Robust Methods for Automated Selection of Cardiac Signals after Blind Source Separation." In: *IEEE Transactions on Biomedical Engineering* 65.10 (2018), pp. 2248–2258, *doi*: 10.1109/TBME.2017.2788701.

[18] A. Trumpp, J. Lohr, D. Wedekind, M. Schmidt, A.R. Heller, H. Malberg, S. Zaunseder. "Camera-based photoplethysmography in an intraoperative setting" In: *BioMedical Engineering OnLine* 17.1 (2018), pp. 33 (1-19), *doi*: 10.1186/s12938-018-0467-7

[19] S. Zaunseder, A. Trumpp, D. Wedekind, H. Malberg. "Cardiovascular assessment by imaging photoplethysmography-a review" In: *Biomedizinische Technik /Biomedical Engineering* 63.5 (2018), pp. 529-535, *doi*: 10.1515/bmt-2017-0119.

Tyrion: He wished he'd been able to think of some rousing last words.
"Bugger you all" was not like to earn him much of a place in the histories.

— George R.R. Martin in *A Storm of Swords* p.1062, A Song of Ice and Fire (2000)